Modelling the progression of neurodegenerative diseases

Simão Laranjeira

Department of Engineering Science

University of Oxford

This dissertation is submitted for the degree of

Doctor of Philosophy

St Cross College

Hillary 2017

Dedication:

This work is dedicated to my oldest friend Rodrigo Dessa

Abstract

Neurodegenerative disease is an umbrella term for pathologies that primarily damage neurons. As their incidence increases with age it is becoming of a greater concern for the west, due to its aging population. Due to their chronic nature and the difficulty to create reliable and reproducible animal models of these diseases their pathophysiologies are still poorly understood.

For all these reasons, a mathematical modelling approach is suggested. The methodology of the work here consisted of identifying the state of the art models that describe the healthy behaviour of cells (e.g. metabolism and ionic regulation) and adapting them for pathological environments. With these models hypotheses provided by clinicians and pathologists were tested. The work focuses on developing models of mechanisms common to neurodegenerative diseases, which include: glutamate excitotoxicity, aquaporin water kinetics, inflammatory complement lysis and acute inflammation.

Glutamate excitotoxicity was modelled by creating a compartmental model of glutamate exchange between neurons and astrocytes. This model was the first model of glutamate kinetics validated in an ischaemic stroke context.

The aquaporin water kinetics and complement lysis models were developed in the context of the autoimmune disease Neuromyelitis Optica. Through this project a hypothesised trigger for the pathology was confirmed. Additionally, the first model of astrocytic cytotoxic oedema due to complement lysis was developed. Finally, a preventative drug for complement lysis was simulated.

Acute inflammation was explored in the context of understanding the potential of chemerin as a pro-resolving cytokine. To that effect, a model of acute inflammation was developed where pro-resolving mechanisms were included. This model was the first to attempt model the effects of an intervention in inflammation. The results indicated that there is a maximum inhibitory effect of chemerin on inflammation. Additionally, two preventive avenues for chronic inflammation were found.

With this work, the first attempts of capturing relevant mechanisms of neurodegenerative diseases were presented. These models can now be further developed and adapted to other pathological environments.

Acknowledgments

Firstly, I would like to thank my supervisor Professor Stephen Payne for always providing perspective to the work and for his patience with my development. A special mention is given to Dr Piotr Orlowski for providing the foundation for all the work developed in this thesis. Additionally, I would like to thank Dr Piotr Orlowski for his immense patience and availability when barriers were encountered throughout the development of the models; without which this work would not have been feasible.

This thesis was developed in partnership with different labs and departments, which deserve special mention. I would like to thank Dr Thomas Lillicrap from the University of New South Wales for his expertise on Glutamate excitotoxicity. Additionally, I would like to thank Dr Jacqueline Palace and Dr Mkael Symmonds from the Nuffield Department of Clinical Neurology for providing the aim and expertise in the development of the Neuromyelitis Optica project. Similarly, I would like to thank Professor David Greaves and Dr Asif Iqbal for aiding in the development of the model on the pro-resolving pathway of Chemerin. I would, also, like to thank Dr Daniel Regan-Komito for acquiring the data utilized in the development of the pro-resolving model created.

I cannot forget to mention my family to whom I am greatly indebted to for their encouragement and support throughout this journey. Finally, I would like to thank Charles Mingus, who died of a neurodegenerative disease, as his music was a great companion throughout the development of this work.

Content:

Front Matter

4. Mathematical model of glutamate release during ischaemic stroke ----------------- 106

Conference Abstracts

S. Laranjeira, P. Orlowski, T. Lillicrap, C. Lueck, A. Neely and S. J. Payne. Modelling glutamate dynamics and associated tissue temperature change in brain cells after stroke. Royal academy of Engineering: Young research future meeting on neuronal engineering 2012. UK, Warwick. September 2012. Presentation.

S. Laranjeira, M. Symmonds, J. Palace, S. J. Payne, P. Orlowski. Mathematical model of glutamate release during ischaemia. Brain 2013. Shanghai, China. May 2013. Poster.

S. Laranjeira, M. Symmonds, J. Palace, S. J. Payne, P. Orlowski. Determination of the role of AQP-4 channels in Neuromyelitis Optica through mathematical modelling VPH 2014, Trondheim, Norway. September 2014. Poster.

S. Laranjeira, M. Symmonds, J. Palace, S. J. Payne, P. Orlowski. Using mathematical modeling to test therapeutic potential of CD59 to mitigate astrocytic oedema due to Neuromyelitis Optica. Brain 2015. Vancouver, Canada. June 2015. Poster.

S. Laranjeira, D. Regan-Komito, A. Iqbal, D. Greaves, S. J. Payne, P. Orlowski. Towards optimising anti-inflammatory treatment with chemerin. VPH 2016. Amsterdam, Netherlands, September 2016. Presentation.

Chapter 1

Introduction

The pathophysiology of neurodegenerative diseases is marked by the loss of structure and consequently the function of the central and/or of the peripheral nervous system. These diseases include Parkinson's, Alzheimer's, frontotemporal dementia and amyotrophic lateral sclerosis. Currently, they affect 2% of the population in the developed world and they have a propensity to occur with an increase in age [1]. As the average age in developed and developing countries increases, there is a tendency for the incidence of these diseases to increase: as reported by United Nations [2] the number of people older than 60 will be larger than 2 billion people by 2050. Just looking at the case of Alzheimer's costs incurred to governments amounted to approximately 160 billion € in the EU for the year of 2008 and predicted to reach 250 160 billion € by 2030 [3].

Treatment and research of these diseases are difficult due to the location. As many of these diseases target the central nervous system (CNS) in order to prescribe a chemical intervention, it needs to transverse the blood-brain barrier (BBB), greatly reducing the amount of molecule compound available [4]. Additionally, their pathophysiology is not fully understood. In the case of Alzheimer's evidence has been compiled that demonstrates that its pathophysiology involves non-neuronal structures e.g. astrocytes and micro-glia [5].

An in vivo approach has been found to be limited when identifying novel therapies for these diseases due to their multi-cellular and complex pathophysiology [6]. Alternatively, in silico mathematical models have proven to be powerful tools to understand the molecular and cellular kinetics of complex diseases [7], [8]. They have also been successfully applied in the context of neurodegenerative diseases such as Alzheimer's [9]–[12] and Parkinson's [13].

The starting point for this thesis was the work by Orlowski *et al.* on pH kinetics [14] and cellular cytotoxicity during ischaemic stroke [15]. This model consisted of using established models of cellular metabolic and ionic regulation and expanding them in order to simulate cellular behaviour in pathological conditions. By being able to simulate cytotoxic oedema Orlowski and collaborators were able to model an important pathological mechanism during an ischaemic stroke. However, Orlowski *et al.* have yet to model cellular membrane depolarization, which is one of the main causes of cell death during ischaemic stroke. Other forms of cell death due to this disease are excitotoxicity, inflammation and apoptosis, as seen in Figure. 1.1.

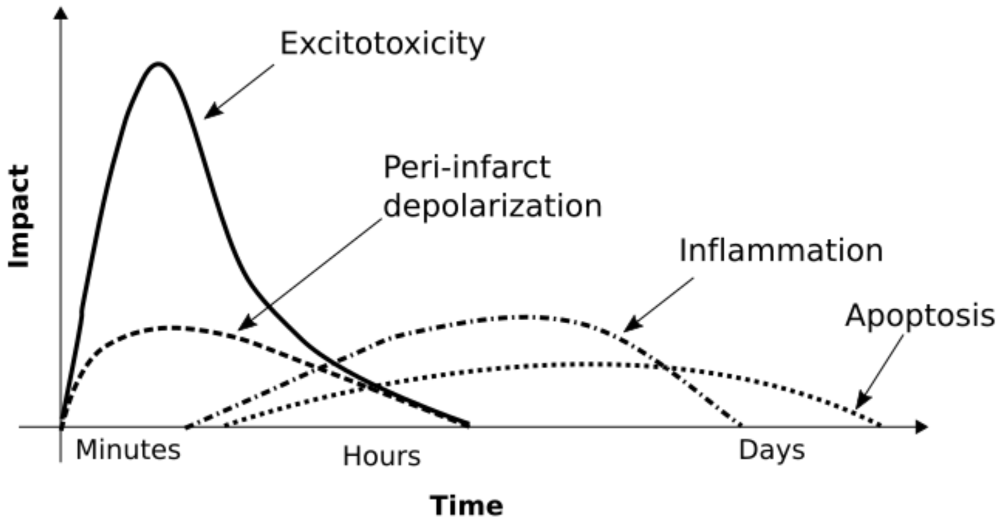

Figure 1.1: Summary of the cell death processes in ischaemic stroke.

These cell death processes are common to many other neurological pathologies besides ischaemic stroke. In the work here presented three are explored: excitotoxicity, membrane depolarization and inflammation. The first two involved expanding the work by Orlowski *et al.* [14], [15] to include glutamate kinetics as well as being able to model cellular oedema after membrane depolarization. In terms of inflammation, a different approach was required. In this context, the main concern is the recruitment and clearance of inflammatory cells. Therefore, it goes beyond intra and extra cellular kinetics. Instead, a one compartment model was created that includes inflammatory cell chemotaxis and phagocytosis.

Furthermore, an effort was made to apply these models to contexts that were of interest to experimental researchers. To that effect, collaborators were found that had data to validate and tests these models. Excitotoxicity was studied in the context of glutamate excitotoxicity in ischaemic stroke [16], as proposed by Thomas Lillicrap from the University of New South Wales. Cytotoxic oedema post depolarization was explored in the context of Neuromyelitis Optica (NMO) as proposed by Nuffield Department of Clinical Neurology (NDCN) at Oxford. This involved testing hypothesis that considered astrocytic water kinetics through channels called aquaporin-4 (AQP4) [17] as well as inflammatory complement [18]. Finally, the inflammatory context involved looking for data outside the central nervous system, as the only reproducible data found was of zymosan induced peritonitis in mice. The data was provided by the Sir William Dunn Department of Pathology at Oxford. Although inflammation response has marked differences between the central nervous system and other tissues the in diseases where there is vasculature damage such as stroke and NMO [17] the acute inflammatory response similar to that reported in non-neuronal tissue. For this work the models aimed at trying to understand the role of pro resolving mechanisms in the process of the resolution of acute inflammation.

The remainder of this chapter is divided into three sections. In Section 1.1 the evidence that the referred pathological mechanisms are present in many neurodegenerative diseases is reviewed. In Section 1.2 the structure of the thesis is described. Finally, in Section 1.3 a personal statement was included to explain why the work created cover a wide range of fields.

1.1 Proof of the universality of the mechanisms modelled.

The acquisition of data for the validation of the work developed involved sometimes going beyond the context of neurodegenerative diseases. This is the case of the cytotoxic oedema project where the work was placed in an NMO environment. In this environment AQP4 water flow is of great importance as well as inflammatory complement. Although specific pathological mechanisms are being analysed they are mechanisms common to many neurodegenerative diseases. In this section proof of the universality of the mechanisms here studied is presented. In Section 1.1.1 glutamate excitotoxicity is shown to be involved in many neurodegenerative diseases**.** Section 1.1.2 describes the role of aquaporins and in particular AQP4 in a variety of brain diseases. Then the role of complement lysis and the availed avenues for therapeutic prevention of it are described in Section 1.1.3. The potential of pro-resolving mechanisms as avenues for understanding the pathophysiology of neurodegenerative diseases and identifying novel treatments is presented in Section 1.1.4.

1.1.1 Glutamate excitotoxicity

Glutamate is an amino acid and the principal excitatory neurotransmitter in the CNS [19]. This is evidenced by the large concentration of glutamate inside neurons (from 3mM [20] to 10mM [21]). For a full description of the physiology of glutamate regulation please refer to Chapter 2. In this section, the focus is to present how the topic of glutamate excitotoxicity relates to the thesis title.

The concept of glutamate excitotoxicity was first presented by Olney *et al*. [22]. It is described as being a process by which this amino acid and others involved in the excitatory mechanisms are responsible for the death of neurons in acute and chronic diseases of the CNS. The cell death process involves the over stimulation of glutamate receptors and it results in the loss of post synaptic structures such as dendrites and cell bodies [22], [23]. Evidence amounts of the presence of excitotoxicity in acute cases such as ischaemic stroke and traumatic brain injury [24].

In the chronic case where neuronal tissue dies over a long period of time, the proof has been harder to acquire due to the difficulty to develop an experimental model that mimics the behaviour of a neurodegenerative disease. However, it has been demonstrated that small increase (as low as 10%) of extracellular glutamate leads to functional changes in cerebral tissue structure and function leading to nerve cell impairment [25], [26]. Additionally, animal and human studies have shown that toxins that inhibit receptors that glutamate stimulates induce excitotoxicity and lead to a slow development of neuronal deterioration [27], [28].

Furthermore, neurodegenerative diseases have been found to lead to glutamate excitotoxicity through a variety of mechanisms. In three cases the evidence is clear. There is the disease Amyotrophic Lateral Sclerosis (ALS) where several pathways have been hypothesised that result in the accumulation of glutamate in the ECS. It has been shown that glutamate extraction mechanisms from the ECS are down-regulated [29] and those release mechanisms are up-regulated [30]. In addition, there is an increased expression of amino acids that trigger glutamate release mechanisms [31]. Alzheimer's (AD) also presents glutamate excitotoxicity as a cell as the pathology is marked by a higher neuronal sensitivity to excitotoxicity [32] and as ALS there is a down-regulation of channels responsible for glutamate uptake [33] and an increase in channels that release it [34]. Finally, there is the case of Huntington's disease where it has been found that channels of glutamate uptake are redistributed which might result in the triggering of glutamate release and accumulation [35].

As the evidence amounts there is a need to test the hypothesis that arises in a prompt, cheap and ethical way. It is here argued that mathematical modelling of the known glutamate regulatory mechanism it is possible to satisfy the criteria stated.

1.1.2 The role of AQP4 in neuron degeneration [36]

AQP4 is a water channel located at a cerebral type of cell called astrocyte. These cells are responsible for ensuring the homoeostasis of cerebral tissue by, as an example, extracting neurotransmitters released by neurons after stimulation [37]. In terms of water kinetics, the astrocyte has been shown, through AQP4 channels but not exclusively, to interact with the BBB. This interaction is titled glymphatic system [38]. Through this system, it has been shown that the ECS hydrostatic pressure is modulated, which has been shown to ensure the homeostatic levels of potassium [39].

Due to its critical role in the interaction between cerebral tissue and the BBB AQP4 is believed to initiate or be a component in the pathophysiology of neurodegenerative diseases. Evidence has been compiled in three cases. AD is characterised by the build-up of beta-amyloid plaque in the tissue. This deregulates the tissue structure and function. It is hypothesised that the accumulation of plaque is a result of, in part, the failure of the glymphatic system [38]. Additionally, it has been shown that plaque clearance in the AQP4 knock out mice is reduced by 50-65% compared to wild-type mice [40], [41]. Therefore, it is hypothesised that the impairment of the glymphatic system is involved in the pathophysiology of AD and that AQP4 expression might be affected.

Other neurodegenerative diseases have demonstrated AQP4 involvement in their pathophysiology. These include Parkinson's and ALS. In terms of the former, it has been found that the characteristic reduction of dopamine production is important for the expression of AQP4 [42]. ALS, in turn, is a disease marked by the failure of muscle function that has been linked to a reduction in AQP4 expression in neuromuscular cells [43]. Additionally, ALS is marked by the breakdown of the BBB. Experimental work using animal models has shown that the breakdown is mediated, in part by loss, of AQP4 [44].

The newly identified glymphatic system has been proposed to play important roles in ensuring the homeostatic state of the brain. The disruption of this system has been linked to a variety of neurodegenerative diseases. As the evidence compiled AQP4 plays a crucial role in this system and therefore studying its expression and function might reveal pathological mechanisms and potential therapeutic strategies. As it was shown experimental models are limited and costly and therefore an experimental modelling approach is here proposed to study it. The pathology chosen was neuromyelitis optica as the role of AQP4 is clearer and therefore it's the best to create a proof of concept [45].

1.1.3 Inflammatory complement role in neurodegenerative pathologies.

Inflammatory complement is a system of proteins that aims at recruiting inflammatory cells and forming holes in the membranes of targeted bodies. The protein complex that forms the holes is termed membrane attack complex (MAC). Many neurodegenerative diseases have been shown to present a neuron inflammatory component in their pathophysiology and, additionally, proteins involved in the complement process have been measured [46], [47].

The evidence of the involvement of inflammatory complement is more prominent in the case of AD, as it has been reported that there is the activation of a variety of complement proteins [48], [49]. Furthermore, a range of complement proteins, including MAC, have been found in areas marked by beta-amyloid deposition [48], [50]. Besides being a route to understand the development of the disease [51], understanding the involvement of complement in the pathology might also be an avenue to identify new therapies for the disease. There are several complement inhibitors that regulate complement production. The one most prominently expressed in cell membranes in the nervous system is the protein CD59. It has been shown by Yang *et al.* [52] that there is a significantly lower expression of CD59 in the frontal cortex and hippocampus in Alzheimer's patients compared to controls.

Although less thoroughly explored there is evidence that there is an increase of expression of complement proteins in the presence of the Parkinson's pathology [47], [53]. It is characteristic of the disease for nerve cells in the substantia nigra area of the brain to die [53]. At this location, the work by Loeffler *et al.* [53] was able to identify, through staining, the presence of a variety of complement proteins including the deposition of proteins responsible for MAC. Therapeutic avenues using complement inhibitors have, however, yet to be tested.

As neurodegenerative diseases are characterised by presenting inflammatory mediators it is reasonable to assume that complement may play a part in the development of these diseases. In fact, as the evidence compiled has shown, complement and complement lysis might play a crucial role in the cell death process of these diseases. Experimentally, as the in vivo models are able to fully reproduce the full spectrum of these diseases [54] and the pool of patients required for statistically significant results is difficult to mobilise [55]. Therefore, in this thesis, a mathematical approach is presented that tries to model the mechanisms of complement lysis in astrocytes and to evaluate the therapeutic efficiency of CD59. All these tests are performed in the context of NMO where its role is better understood and characterised.

1.1.4 Pro-resolving strategies in the context of neurodegeneration

As demonstrated in Section 1.3, inflammation is a key feature of neurodegenerative diseases. This occurs independently of the natural protection that the brain has with the BBB to prevent the penetration of cells into the CNS [56]. However, during the neurodegenerative pathophysiologies the cells that experience apoptosis need to be cleared and therefore inflammatory cells are recruited [57]. In fact, it has been shown that AD and PD experience an increase in inflammatory cell recruitment mediators [58], [59].

The development of acute inflammation is a natural response and aims to prevent further tissue damage. However, it is evident that in the presence of these pathologies acute inflammation degenerates into chronic inflammation. Until recently it was believed that the clearance of inflammatory cells after an event was due solely to diffusion. Now it is known that clearance of these cells involves active mechanisms. The failure of these pro-resolving mechanisms is now hypothesised to be the reason for the development of chronic inflammation. Neurodegenerative diseases have also demonstrated that the failure of pro-resolving mechanisms is involved in their pathology. The chronic inflammation observed in Alzheimer’s has been linked to dysfunction in a pro-resolving mechanism as certain mediators were found to decrease [60]. Additionally, therapies have been proposed for AD that aims at enhancing or re-establishing these mediators [61].

This is a novel field that might aid in the understanding of the pathophysiology of these diseases and provide new therapeutic strategies. In order to test these, it is here proposed that mathematical modelling should be used, the first mathematical model to test a pro-resolving mechanism was created. With it, an intervention was tested and optimised in the effort to exploit a pro-resolving system to prevent the degeneration of acute inflammation into chronic inflammation.

1.2 Thesis structure

The aim of the work here developed is to test brain pathological hypothesis. The approach taken was to model physiological mechanisms and to test how these are perturbed, resulting in pathological symptoms. To justify the choice of the physiological mechanisms considered, Chapter 2 presents the most relevant nervous system physiology and the pathological mechanisms. These include neuronal and glial function, glutamate neurotransmission, AQP4 expression and function and ischaemic stroke, NMO and chronic inflammation pathologies.

The models developed are based on cellular metabolic and ionic concentration regulation. In Chapter 3 the evolution of the literature of the mathematical models considered is presented. More specifically the chapter focuses on the evolution of models of cellular metabolism as defined by Aubert *et al.* [62] and cellular ionic regulation initiated by Hodgkin-Huxley [63]. This family of models has been expanded to consider AQP4 water kinetics [64] and the impact of osmotic pressure has on cellular volume [65]. Additionally, the field of models of acute inflammation is described based on the work initiated by Laufenberg and Kennedy [66]. Furthermore, Chapter 3 describes all the tools and methods used to develop the model: the compilers of code used (e.g. OpenCell [67]), the methods used to fit parameters (e.g. simplex [68]) and the sensitivity analysis algorithms implemented (e.g. Morris method [69]).

Chapter 4 describes all the work done in the context of glutamate excitotoxicity in the presence of ischaemic stroke. It consists of expanding the model of cytotoxic oedema in the presence of ischaemic stroke by Orlowski *et al.* [15] to include glutamate regulation mechanisms. The model was validated using microdialysis measurements of ECS glutamate concentration in mice brains. The work done was developed in collaboration with Dr Mkael Symmonds and Dr Jacqueline Palace from the NDCN at Oxford. Both collaborators provided physiological expertise in the field.

Chapter 5 centres on the mathematical model created of the hypothesised triggers for NMO. The model developed consists of expanding the Orlowski *et al.* [15] model by integrating the effects of AQP4 water kinetics and the impact of astrocyte membrane complement lysis on volume of the cells. Besides testing pathological hypotheses, the work aims to test the therapeutic potential of CD59 to prevent the astrocytic cytotoxic oedema observed in the context of this disease. This work was also developed with the collaboration with the NDCN. Their expertise provided the aims of the work as well as guidance throughout the development of the work. Finally, this chapter also presents all the strategies used to try and simplify the integration of models with a large number of equations. These included using the Morris method [69] and the genetic based symbolic regression method provided by Allgaier and McDevitt [70].

Finally, Chapter 6 describes the work developed on the inflammatory pro-resolving mechanism of chemerin/ChemR23 as described by Cash *et al.* [71] . The work was done in collaboration with the group of Professor Greaves from the Willis Department of Physiology. Through the work of his student Dr Daniel Regan-Komito it was found that when extra chemerin is injected there is a significant reduction in cell recruitment in an in vivo model of peritonitis. The aims of the work were then to identify the optimal time and concentration for the injection of extra-chemerin in order to achieve maximal inhibition of inflammatory cell recruitment. In this work, sensitivity analysis was, also, implemented to identify the most relevant parameters that need to be measured in order to improve the predictions of the model.

1.3 Personal statement

The methodology chosen to create models of pathological mechanisms consisted in collaborating with experimental and pathological departments to acquire data to validate and place the models into a more established theoretical basis. Three different projects were developed, which involved three different collaborations.

Modelling glutamate excitotoxicity was first proposed by Dr Thomas Lillicrap from the University of New South Wales. With such a model it was expected to find if exacerbated glutamate release was responsible for the fever experience by a cohort of ischaemic stroke patients [72]. During the project development, it was found that glutamate could not be responsible for the increase of temperature experienced. Taking the theoretical knowledge provided by Dr Lillicrap the focus was, then, directed to create a validated model of glutamate release in stroke. The data used for validation was taken from the literature and it consisted on *in vivo* microdialysis measurements [73], [74].

By having a functioning model of cytotoxic oedema attracted the attention of Nutfield Department of Clinical Neurology at Oxford. In particular by Dr Jacqueline Palace and Dr Mkael Symmons. From meeting with these two doctors a project presented in Chapter 5 on NMO was defined. They proposed the use of mathematical modelling as way to test the main pathological mechanism behind astrocytic swelling during NMO, as identified by Saadoun *et al*. [17].

From the work done on inflammation, it was possible to approach research groups that acquire data on acute inflammation. This was done to create the models presented in Chapter 6. Our work was discussed with the group of Professor Greaves from the Sir William Dunn department of physiology at Oxford. It was possible to get access to data compiled by Dr Regan-Komito on a pilot intervention study where the pro-resolving pathway of the chemokine chemerin was tested. The modelling approach had to be adapted to match the data received. The model created moved from a four compartment model brain tissue to a 1 compartment inflammation recruitment and clearance of inflammatory cells, as described in chapter 6.

Chapter 2

Literature review: Biological principles

This chapter aims at presenting the main concepts behind the mathematical models developed. As the thesis focuses on pathologies of the nervous system, this chapter starts by giving an overview of the relevant nervous system pathology. Then the following topics are explored: 1. glutamate excitotoxicity during stroke; 2. glial swelling during NMO; and 3. neutrophil and leukocyte recruitment during peritonitis.

2.1 Nervous system physiology [75]

This section focuses on presenting the most relevant physiology of the nervous system that was the basis for the mathematical models developed. The physiology described is presented at two levels: tissue (section 2.1.1) and cellular (neurons in section 2.1.2.1 and astrocytes in section 2.1.2.2).

2.1.1 Main structures

The nervous system is responsible for human motility, thought and emotion. There are two main structures in the nervous system, the brain and the spinal column, which comprise the central nervous system (CNS). Additionally, there is the peripheral nervous

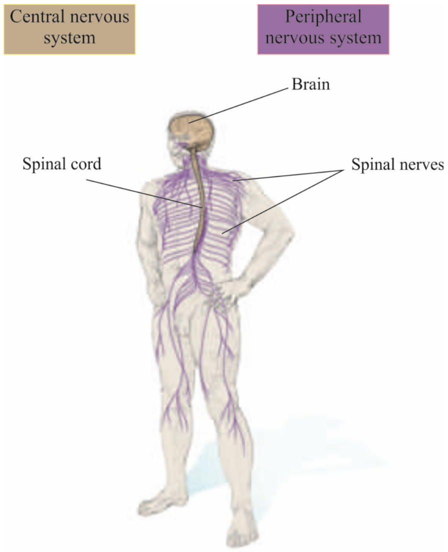

Figure 2.1: The CNS (brain and spinal cord) and PNS (spinal and cranial nerves); adapted from **[75]**

system (PNS), which consists of all the nerves that connect the spine to the remaining organs. This is summarized in Figure 2.1.

The brain is where all the information collected from all the systems in the human body is processed. This organ is organized into the cerebral hemisphere, the brain stem and the cerebellum. Then each of these structures is divided depending on the type of information being processed. Using the cortex as an example, it is divided into the frontal, the parietal, the occipital and the temporal lobes. Additionally, certain areas of the cortex have been mapped as having particular functions, e.g. the primary auditory cortex and the primary visual cortex. A summary of the ontology of the cortex is presented in Figure 2.2.

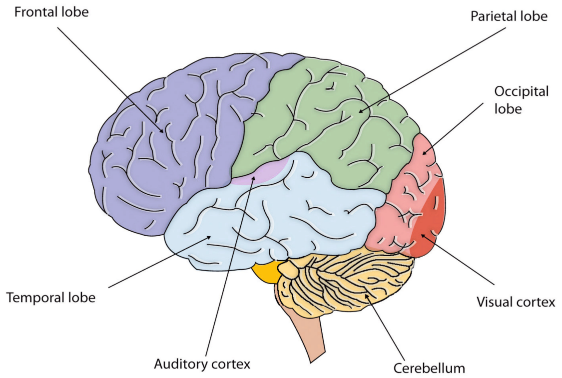

Figure 2.2: The brain cortex is divided into four lobes (frontal, temporal, occipital and parietal) and the cerebellum. Two examples of function primary cortex are also presented: auditory and visual; adapted from [75]

Furthermore, four systems are responsible for ensuring that the cells are maintained at a homeostatic state to perform their function: the ventricular system, the meninges, the brain's circulatory system and the brain blood barrier (BBB). The first of these consists of a series of interconnected, fluid-filled spaces that cover the whole CNS. These spaces are filled with cerebral spinal fluid (CSF). This fluid is formed at every ventricle in a vascular structure titled the choroid plexus. The fluid travels along the ventricular system moving to the sub arachnoid space through a perforation in the fourth ventricle. Here there are specialized structures called arachnoid villi or granules through which the CBF returns to the venous circulation.

The ventricle system consists of the lateral ventricles, which are the first and second ventricles. From these, the CBF moves to the third ventricle through the interventricular foramen. The third ventricle is followed by the cerebral aqueduct that opens into the fourth ventricle. The latter then has a canal that opens into the spinal cord. The function of this fluid is not yet fully understood. Currently, the following functions have been identified: it operates as a damper to absorb forces when the head suffers any sort of impact; it regulates intracranial pressure, and it is responsible for the clearance of metabolic waste. A description of the different pathological structures of the CBF circulatory system is presented in Figure 2.3.

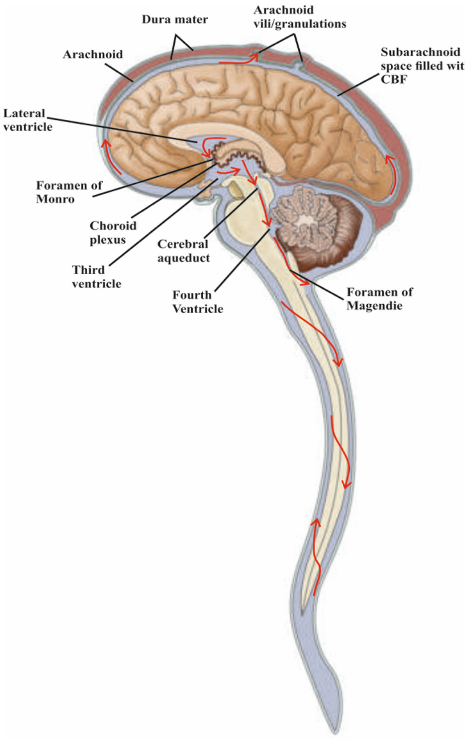

Figure 2.3: The structures of the CBF circulatory system, adapted from [75].

The subarachnoid space is named as such because it is under the arachnoid. The latter is one of the three protective layers surrounding the brain that make up the meninges. The other two are the dura mater and the pia mater. These layers can be seen in Figure 2.3.

The brain's blood circulatory system ensures that the nutritional needs of the brain are met. All blood flow to the brain and the spinal column is supplied by two sets of branches from the dorsal aorta: the vertebral arteries and the internal carotid arteries. The vertebral arteries combine and form the basilar artery. The latter then joins the blood supply of the internal carotids forming an arterial ring called the circle of Willis. By combining the two sources of the blood it is hypothesized that it functions as a safety mechanism that ensures that there is blood supply even if one of the sources is blocked. These three structures (internal carotid artery, vertebral artery and circle of Willis) supply blood to the arteries that in turn deliver blood to the different areas of the brain. The internal carotid arteries branch to form two major cerebral arteries, the anterior and middle cerebral arteries. These give rise to branches that supply the cortex and structures that penetrate the basal surface of the brain and deliver blood to deep structures such as the basal ganglia, the thalamus and the internal capsule. In addition, there is a set of arteries that constitutes the posterior circulation that supplies blood to the posterior cerebral cortex, the midbrain and the brain stem. It consists of arterial branches that arise from the posterior cerebral, basal and vertebral arteries. The blood circulatory system can be seen in Figure 2.4.

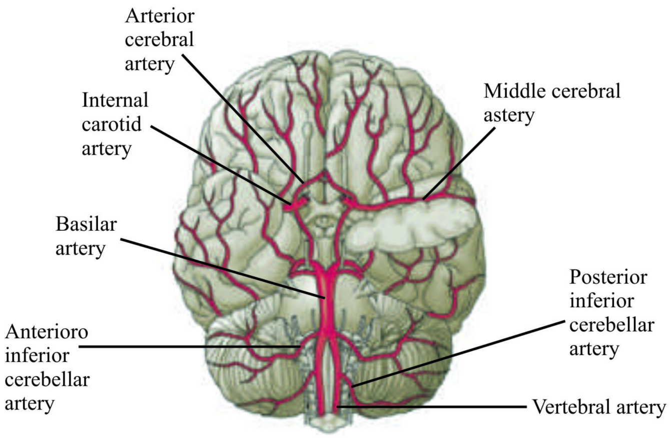

Figure 2.4: Description of the brain blood circulatory system; adapted from [75].

The brain, more than any other organ needs to shield itself from ionic changes as well as from toxic molecules such as those that get into the blood circulation due to ingestion, infection and other means. This shield exists in the form of the BBB, which is composed of specialized endothelial cells. These restrict the passage of ions and molecules much more than in other areas of the body by having a tight junction between them. However, essential molecules for tissue function like glucose do get through due to the presence of specific transporters. Furthermore, endothelial cells are surrounded by astrocytic endfeet. The full extent of the relationship between astrocytes and the BBB through the endothelial-astrocytic junction is still being researched. Currently, astrocytes have been identified to influence BBB features such as the flow through it; the expression and polarized localization transporters and expression of specialized enzyme systems. The main constituents of the BBB are shown in Figure 2.5.

The spinal column, in turn, is constituted of a series of bone structures, the vertebra, that are connected with cartilage and that are responsible for maintaining humans' upright posture. Furthermore, these ensure structural stability for the nervous system connections between the brain and the rest of the body. In particular, it ensures the connections responsible for the regulation of heart rate, breathing rate and all the thoracic organs. This fact is of particular interest as the spinal column has been identified as being one of the initial sites where patients who suffer from NMO experience lesions. Consequently, through damage to the spine, patients might experience further organ deregulation or even organ failure. In particular, respiratory failure has been commonly experienced by NMO patients.

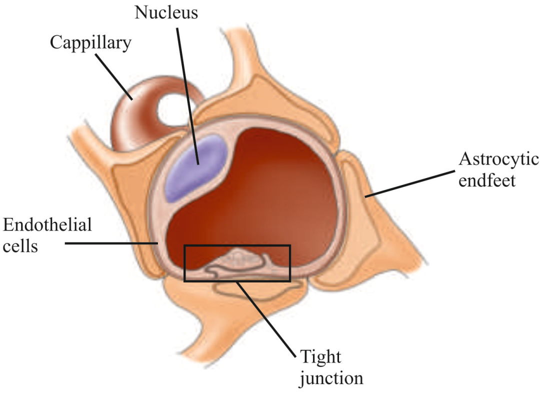

Figure 2.5: Breakdown of the main components of the BBB; adapted from [75]

2.1.2 Cellular components [19], [75]

All the information processed by the nervous system is due to the interactions between two types of cells: neurons and the astrocytes. In this section, all the relevant physiology of these cells and their functions are presented.

2.1.2.1 Neuron

These cells are specialized to exchange information through electrical and chemical means. They have three distinct sections: the cell body where the cell nucleus lies and electrical signals are triggered; the axon, which carries the electrical signals; and the axon terminals, where communication with other neurons occurs. The neuronal structures mentioned are summarized in Figure 2.6. In order to encode and to transfer information, neurons employ several types of electrical signals. When not excited the neuron maintains a resting membrane potential of -40 mV to -90 mV. Several types of stimuli have been characterized depending on how they momentarily (of the order of milliseconds) change the resting potential of neurons. In the case of sensory stimulation, e.g. light, heat and sound, they have been characterized as receptor potentials. Then there are the synaptic potentials, which are responsible for the transmission of information between neurons. Finally, there is a third type of electrical signal that ensures that no information is lost when signals need to travel long distances.

These signals are called action potentials (AP) and function as amplifiers of the signal in order to overcome the poor electrical conductivity of a neuron.

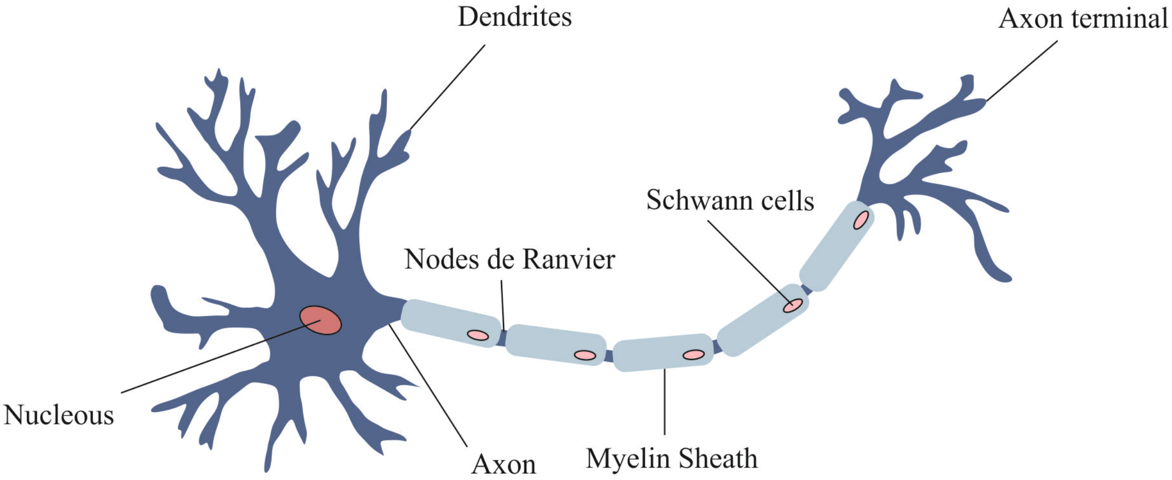

Figure 2.6: Description of the physiology of a neuron. [75]

The AP has two particular characteristics that explain how information is coded in the brain. Firstly, in order to induce an action potential, the membrane potential needs to be driven above a certain threshold, called the threshold potential, otherwise, it simply falls back to its resting state. Secondly, independent of the voltage dispensed, when the potential goes above the threshold it always produces an action potential with the same amplitude. Consequently, if continuously stimulated, a train of identical APs is formed. Therefore, information is coded not by the amplitude of APs but by their frequency.

All the electrical potentials mentioned are derived from ionic movements across the membrane. This movement is driven by electrostatic and diffusion forces induced by differences in ion concentrations between the intra and extra cellular fluids and by the selective permeability of the cellular membrane to ions. These two effects are in turn governed by two kinds of proteins in the cell membrane: the ion channels which are selectively permeable to ions that transverse it passively and the active transporters that actively move ions into or out of the cell against their concentration gradient.

There are several relevant ions that are responsible for neuronal behaviour. Here four are chosen based on the cellular physiological mechanisms that will be captured in the model developed later. These are used in this section to explain the ionic behaviour behind cellular signalling. They are sodium (Na^+), potassium (K^+), calcium (Ca^{2+}) and chloride (Cl^-). Typical intra and extra cellular concentrations are presented in Table 2.1.

Table 2.1: Extracellular and intracellular mammalian ion concentrations [75]

	Concentration (mM)	
Ion	**Intracellular**	**Extracellular**
Potassium (K^+)	140	5
Sodium (Na^+)	5-15	145
Chloride (Cl^-)	4-30	110
Calcium (Ca^{2+})	0.0001	1-2

Diffusion forces ions to move from the space with the largest concentration to the lowest. Therefore, Na^+, Ca^{2+} and Cl^- would be pushed into the cell with K^+ pushed outside the cell. However, the membrane potential is maintained at its resting potential of -70 mV due to two mechanisms. The first, as in the case of Cl^- and K^+, is that the electrostatic pressure exerts a force against the diffusion force. In the case of Ca^{2+} and Na^+, both diffusion and the electrostatic pressure push it inside the cell and therefore the membrane resorts to active ion transporters. One transporter of special relevance is the K^+/ Na^+ pump. It has a stoichiometry of 2 K^+ ions moved in for every 3 Na^+ ions pushed out and to operate it approximately 40% of the neuron's metabolic resources are consumed. Therefore, the healthy behaviour of the brain is dependent on the maintenance of the K^+/ Na^+ pump. The transport dependent ion gradients are the basis for the neuronal membrane potential and the action potential. The breakdown of the forces involved in the movement of ions through the membrane is shown in Figure 2.7.

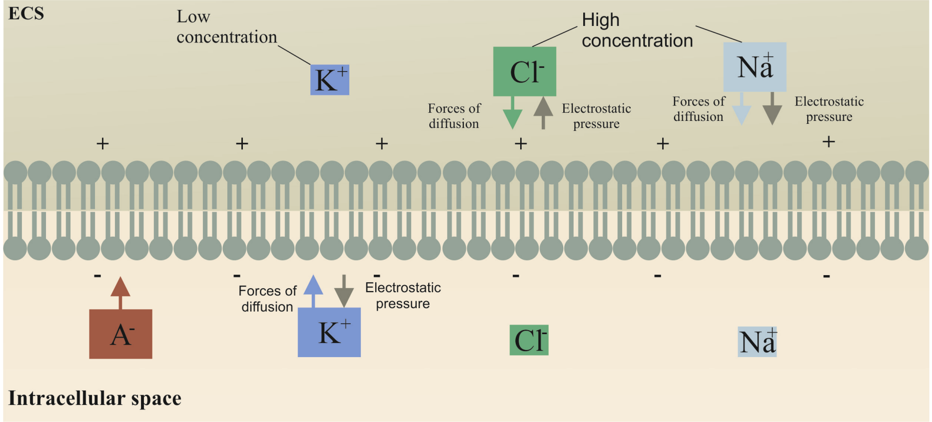

Figure 2.7: Description of the forces that explain the movement of ions across cellular membranes.[19]

The resting potential can be explained by the equilibrium potential of each ion. The latter can be calculated using the Nernst equation, which states that the equilibrium potential (V_{ion}) is proportional to the natural logarithm of the ratio of the extracellular (S_{ex}) over the intracellular (S_{in}) ion concentration as summarized in Equation 2.1.

$$V_{ion} = \frac{RT}{z_{ion}F} ln\left(\frac{S_{ex}}{S_{in}}\right), \tag{2.1}$$

where, R, T, F and z_{ion} are the gas constant, the temperature, Faraday's constant and the ion valence respectively. Since the resting potential of the membrane is approximately -70 mV, K^+ is the ion that is closest to being in electrochemical equilibrium. Therefore, the resting potential rises from both the fact that the membrane is more permeable to K^+ than to other ions, as experimentally confirmed by Hodgkin and Katz in 1949 and the fact that the K^+ ionic gradient is maintained by active accumulation of K^+ inside the cell.

The action potential is explained by a transient (of the order of 10 msec) increase in the membrane's permeability to ions. This increase is managed by voltage dependent ions that are open when the membrane potential reaches particular thresholds. It is initiated with the opening of Na^+ ionic channels when the neuron membrane crosses the threshold of excitation. As aforementioned both diffusive and electrostatic forces push sodium inside the cell, therefore, an increase in permeability results in a rush of Na^+ into the cell. This induces a rapid change of the membrane potential from -70 mV to +40 mV. Within this period of depolarization, at a larger threshold, K^+ voltage dependent channels also open. Initially, K^+ will also permeate the cell.

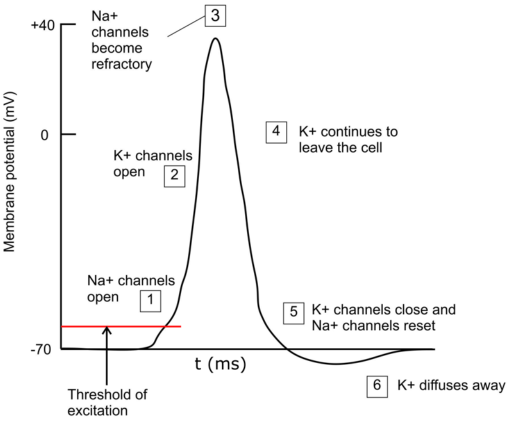

Figure 2.8: Description of how the membrane permeability changes during AP stimulation [19]

When the AP reaches its peak (in approximately 1 msec) value the sodium channels become blocked and cannot open until the membrane returns to its resting potential. This behaviour of the sodium channels is responsible for the refractory period. As the inside of the cell becomes positive the electrostatic force drives K^+ outside the cell. This removal of K^+ progressively causes the membrane potential to decrease. Before it goes back to its resting potential the AP is marked by an overshoot where the potential decreases to about -80 mV. This event is due to the extra permeability to K^+ incurred by the voltage dependent channels. Then the membrane goes back to its resting potential and only now can a new AP be induced. A description of the changes in membrane permeability in the presence of an AP is summarized in Figure 2.8.

Besides K^+ and Na^+ there are Ca^{2+} and Cl^- voltage dependent channels that also open during an AP event. The Ca^{2+} voltage dependent channels in some neurons can be responsible for driving AP in much the same way as Na^+. In other neurons, Ca^{2+} channels modulate the shape of the AP generated principally through Na^+ conductance changes. More generally, Ca^{2+} channels control the concentration of intracellular calcium, which regulates a range of biochemical processes, perhaps the most important of which is its role in regulating the release of neurotransmitters. This function will be further explained in Section 2.3. The Cl^- channels, in turn, have been found to control excitability, to contribute to the resting membrane potential and to help regulate cellular volume.

A model of an AP has been developed by Hodgkin and Huxley. This model assumes that the membrane's conductivity (g) obeys Ohm's Law. Hence the ionic currents (I_{ion}) induced by an AP are of the form:

$$I_{ion} = g_{ion}(V_m - E_{ion}), \tag{2.2}$$

where V_m is the membrane potential and E_{ion} is the equilibrium potential for the ion flow through the channel with conductance g_{ion}. From this simple relationship Hodgkin and Huxley were able to model the ionic currents of Na^+ and K^+. From voltage clamp experiments and knowing the intra and extra cellular concentrations of these ions they were able to measure the steady state values of g_K and g_{Na} as well as V_K and V_{Na}. Additionally, they characterized the voltage dependence of the ion channels conductance. Moreover, they found that an extra current was required in order to fully represent the AP behaviour, which they called the leak current. The latter accounted for the movement of all the other ions present in the extracellular space.

As aforementioned an AP is a form by which neurons communicate with each other. After initiation, the AP needs to travel down the axon to deliver the information to its required location.

While it travels through the axon the amplitude of the AP always remains the same. However, the axon is not made of electrically conductive material. In order to overcome this limitation, the axon is coated with an isolating material called myelin. The maintenance and replenishment of myelin are ensured by one type of glial cells called oligodendrocytes. Despite this coating, the signal, like in any electrical cable, will diminish as it travels through it. The loss of signal is overcome by amplifying the signal throughout the axon. This is done by interspersing myelinated segments with areas called nodes of Ranvier where the axons are exposed to the extracellular space. Here, there are voltage dependent Na^+ and K^+ ion channels which, when a fading AP arrives after traversing a myelinated area, open and regenerate the AP to go through another myelinated section.

Such conductance where APs appear to hop from node to node is called saltatory conduction. This type of conduction confers two advantages. The first has to do with energy efficiency. The Na^+ that comes in during AP depolarization has to be actively transported out. Therefore, by having areas isolated with myelin that ensures that less Na^+ enters the cell, consequently less energy is used to maintain the membrane potential. Secondly, it increases the speed. This is because the conduction of the electrical signal in the myelinated segment is much faster.

After the signal travels down the axon it arrives at the synapse. This is where neurons can communicate with each other through a process called synaptic transmission. The synapse is composed of a pre-synaptic membrane, located at the end of the terminal button, and the post-synaptic membrane, which is the membrane of the neuron that receives the signal. There are two types of synapses: electrical, where electrical signals can transverse to the postsynaptic neuron passively; and chemical, where the electrical signals are translated into a chemical form. The former are in the minority.

Electrical synapses have the two membranes connected by a gap junction that maintains the pre-synaptic ion channel and the post-synaptic ion channel alignment. Each channel pair forms a pore where not only ions but also larger molecules such as ATP can move between neurons. The passive flow is generated by the difference in potential between the two membranes driven locally by APs. Due to this arrangement, these synapses allow for bi-directional flow and the exchange can almost be perceived as instantaneous. Furthermore, these synapses allow for the synchronization of electrical activity among populations of neurons. Additionally, as the junction allows for the movement of large molecules it also permits electrical synapses to coordinate the intracellular signalling and metabolism of coupled cells. This property can be particularly important for glial cells, as it has been found that they form large intracellular signalling networks through the gap junction.

Chemical synapses are more common in the nervous system and have a larger gap between the neurons' membranes than the electrical synapses. This gap is called the synaptic cleft and it has on average a length of 20 nm. In order for the signal to transverse this gap the pre-synaptic neuron releases neurotransmitters. Approximately 100 different neurotransmitters have been identified. These are characterized as either small molecules or peptides. Additionally, different neurotransmitters elicit responses individual to each neuron, e.g. while for some neurons a certain neurotransmitter is excitatory for others it might be inhibitory. Furthermore, the different types of neurotransmitters allow for heterogeneous signal speeds; while small molecules mediate rapid synaptic actions, peptides modulate slower synaptic function. The two types of synapses can be visualized in Figure 2.9.

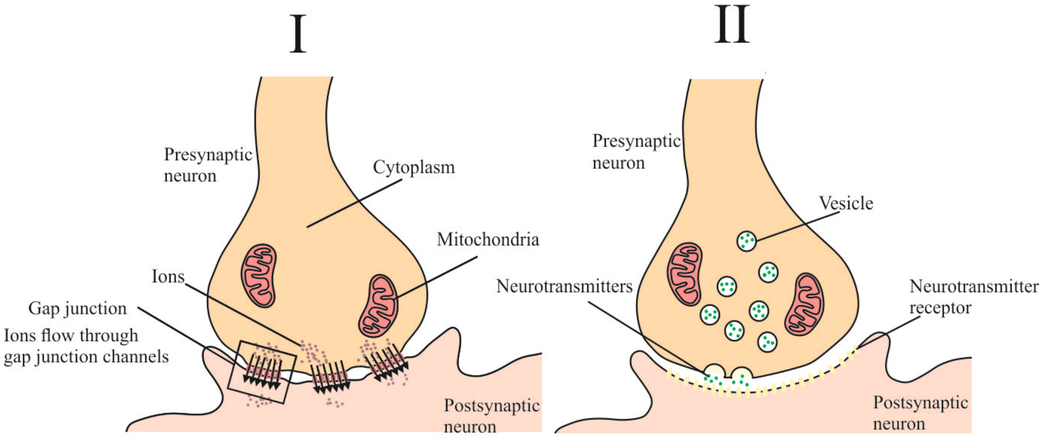

Figure 2.9: Description of the how the two types of synapses function: electrical (I) and chemical (II) [75]

Inside the neurons, these chemicals sit inside small membrane bound organelles called synaptic vesicles. These have an average diameter of 50 nm and each carries around 10,000 molecules of neurotransmitters. These vesicles are separated into pools that are organized depending on the species and on the type of neuron. In the work by [76] two types of mammalian neurons are analysed: hippocampal neurons and calyx of held neurons. In both cases the vesicles are organized into three pools: the reserve pool RP (80 to 90 % of vesicles) the recycling pool RC (5 to 10% of vesicles) and the ready release pool RRP (1 to 5% of vesicles). [76] presents evidence that the calyx of held and hippocampal neurons have approximately 200 and 300,000 vesicles respectively.

The RRP gets its name from the fact that its vesicles have docked to the membrane and have adhered through a process called priming to the pre-synaptic membrane. This ensures a fast release of neurotransmitters after stimulation. Depending on the frequency of stimulation the vesicle pools are recruited progressively from the smallest to the largest. The movement of vesicles between pools is also arranged depending on the type of neuron. Hippocampal neurons allow for vesicles to be exchanged between the three pools. In turn, the RRP of the Calyx of Held does not mix with other pools and RRP vesicles only join other pools after release. The movement of vesicles between the three pools is summarized in Figure 2.10.

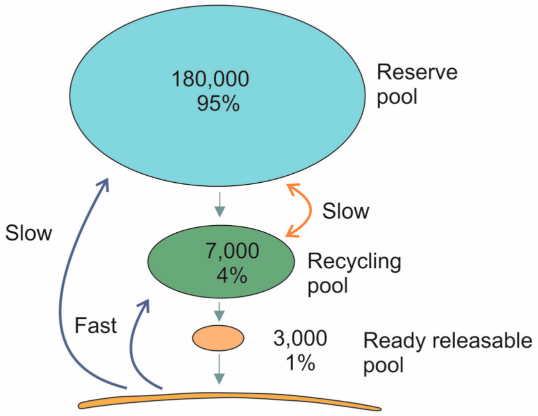

Figure 2.10: Diagram of the different types of synaptic vesicles pools and how vesicles move between them [74]

The AP induces exocytosis of neurotransmitters through an ionic mediator, Ca^{2+}. When the pre-synaptic membrane depolarizes Ca^{2+} voltage dependent channels open allowing for the influx of Ca^{2+}. The extra Ca^{2+} triggers the release of the contents of vesicles primed to the pre-synaptic membrane. The process of release is called vesicle fusion.

Depending on the frequency of stimulation a number of vesicles will release their content. The average concentration of neurotransmitters inside the vesicles, or quantal size and the number of vesicles released in response to one AP, or quantal content, are used to characterize synapses. Three forms of neurotransmitter release have been identified [77]: 1. fast, low frequency triggered synchronous release; 2. slow, high frequency AP train triggered asynchronous release; and 3. spontaneous release. Fast and slow neurotransmitter release is Ca^{2+} dependent. Conversely, the mechanisms behind spontaneous release are still not fully understood.

After the release of neurotransmitters, vesicles are recycled. There are three pathways: the “kiss-and-run” where after release vesicles undock from the membrane and are readily available to be refilled and join one of the 3 vesicle pools; the “kiss-and stay” where vesicles are refilled while still attached to the membrane; and a third pathway where vesicles are broken down and become part of an endosome from which new vesicles are produced. These three mechanisms of vesicle recycling are presented in Figure 2.11.

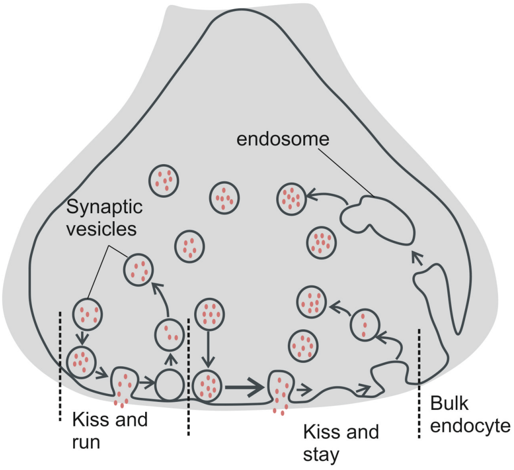

Figure 2.11 : Description of the three ways by which vesicles are recycled after exocytosis of neurotransmitters. [19]

At the synapse, neurotransmitters are responsible for activating post-synaptic receptors that in turn open post-synaptic ion channels. There are two types of ion channels. The most common are the inotropic channels, also called ligand-gated ion channels, which directly open or close ion channels when activated. Additionally, there are the metabotropic channels. Their name stems from the fact that they require cells to expend energy. Furthermore, the receptor does not trigger the channel to open directly. Instead, a “molecular switch” is activated, called a G-protein, that will bind with an ion channel and open it. There are also cases where the activation of the G-protein triggers a protein and enzymatic cascade that results in the release of a second messenger that is responsible for opening the channel. The two types of ion channels are depicted in Figure 2.12.

After the channels are opened, they allow ions to permeate the post-synaptic membrane inducing a postsynaptic potential. These can be depolarizing (excitatory) or hyperpolarizing (inhibitory). The nature of the potential is not determined by the neurotransmitter. Instead, the ionic channels that are sensitive to that particular neurotransmitter characterize the potential. Excitatory postsynaptic potentials (EPSP) are invoked by either the opening of Na^+ or Ca^{2+} channels, as there is a larger concentration of both ions outside the cell than inside and they both have a positive charge.

Hence, they increase the membrane potential and consequently increase the probability of the membrane reaching the threshold of excitation which would lead to the propagation of the AP. Conversely, if K^+ and Cl^- channels are opened, an inhibitory postsynaptic potential (IPSP) is generated. The increase of the membrane's permeability to K^+, as there is a larger concentration inside than outside, causes K^+ to move outside. This results in making the postsynaptic potential more negative. In addition, when Cl^- channels open Cl^- moves inside and it also makes the membrane potential more negative. By reducing the membrane potential, the probability of an AP being induced is reduced.

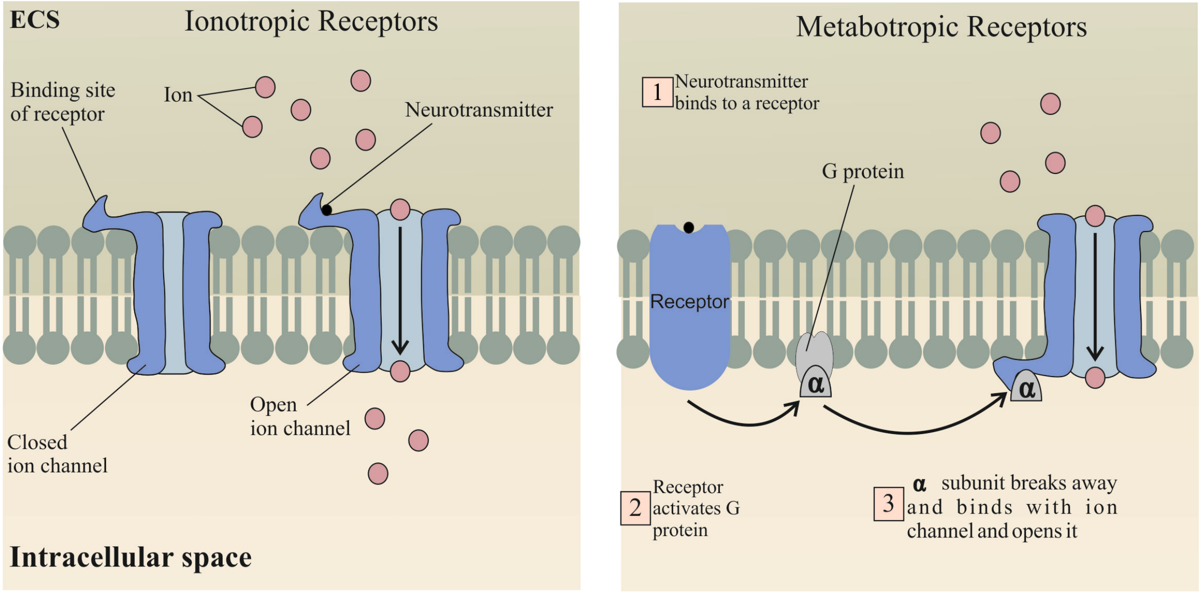

Figure 2.12: There are two types of postsynaptic channels: ionotropic channels and metabotropic channels. [19]

Besides participating in the modulation of postsynaptic potentials, Ca^{2+} has been found to be an important neuronal intracellular messenger. This was suggested by the discovery of a series of cellular organelles that are able to induce Ca^{2+} currents [78]. In particular the Endoplasmic Reticulum (ER) has active (SERCA Ca^{2+} pump) and passive (inositol (1,4,5)-triphosphate receptors - IP_3Rs - and ryanodine receptors - RyRs) Ca^{2+} transport channels in its membrane. The Ca^{2+} currents generated by the ER have been associated with many functional and structural changes in nerve cell circuits like neurite growth and synaptogenesis. Additionally, it has been shown that, when in close proximity, there are Ca^{2+} currents moving from ER into the mitochondria. Inside the mitochondria, Ca^{2+} levels have been related to energy production. Furthermore, the nucleus can also generate Ca^{2+} signals.

These have been found to influence gene expression. Hence, Ca^{2+} levels are an integral factor to maintain the normal function and behaviour of the nervous system. When excessive levels of Ca^{2+} are present in the cytoplasm, cellular apoptosis can be triggered. Ca^{2+} concentrations have also been found to play a crucial role in the pathophysiology of neurodegenerative diseases. Alzheimer's and Parkinson's diseases, for example, have been linked to abnormalities of ER-mediated Ca^{2+} signalling [78].

The aim of this section was to present the importance of ionic, metabolic and neurotransmission regulation for the healthy functioning of cerebral tissue. The mathematical models developed later in the thesis aim to capture these mechanisms. Then these models are used to mimic how these mechanisms are perturbed in the presence of pathological environments. Additionally, there is another set of mechanisms that were found important when considering pathologies in the brain, which regulate ionic and neurotransmission exchanges between neurons and astrocytes. In the following section, their physiology and function are presented.

2.1.2.2 Glial cells

Glial cells are the other type of cells in the brain besides neurons. They execute a variety of functions during brain development and during normal behaviour that ensures the efficiency of neuronal transmission [79]. There are several types of glial cells that vary when considering the CNS or the PNS. In the latter, there are the Schwann cells while in the CNS there are the oligodendrocytes and the astrocytes [79]. These cells are constituted by two main structures depending on which structure they form an interface with. There are the cell soma and cytoplasm that are commonly found in close proximity to the synapse and there are the endfoot processes that interact with capillaries. The first identified function of these cells was the production and maintenance of the Ranvier Nodes. In the CNS this function is performed by the oligodendrocytes.

More recently [80] has found that astrocytes have direct control of the synaptic function. It has been reported that glial cells have neurotransmitter receptors. These receptors have been found to open during brain activity leading to the increase of glial intracellular Ca^{2+} that in turn triggers the release of glial neurotransmitter stores, which feed back into neurotransmission. Furthermore, it has been shown that these Ca^{2+} currents can be propagated between astrocytes over long distances, therefore adding an extra level of complexity to synaptic transmission.

Astrocytes are also responsible for maintaining the brain tissue in a homeostatic state. This function is evidenced in two different contexts. The first consists of ensuring that neurotransmitters do not accumulate in the ECS after synaptic activity. These cells possess pumping mechanisms and enzymes that extract neurotransmitters like glutamate and GABA and metabolize them [80]. The second involves the reuptake of ions that are released during synaptic activity. It has been found that neurons alone cannot perform this action efficiently, leading to accumulation. K^+ is of particular relevance as if it accumulates it can disrupt the electrical activity of neurons.

Besides ionic channels and ionic pumps, the astrocytes are able to ensure the homeostatic state of brain tissue by being able to regulate the hydrostatic pressure in the tissue through water flux control between the blood and the brain through water specific channels called aquaporin-4 (AQP4) [81]. These channels have a high selectivity to transporting water. Three specializations of AQP4 have been identified that explain its selectivity to water. Firstly, the pore monomer diameter is about 2.8 Å and therefore molecules larger than water cannot permeate it. Secondly, an arginine residue coats the pore that blocks the entrance of protonated water and other cations. Thirdly, there are dipoles in the centre of the channel that prevent proton flow and reorient water molecules. There are several AQP4 isoforms that have been identified. The most commonly studied isoforms are M1 and M23 [81]. They show similar water transport capacities. However, the shorter transcript M23 is able to form square arrays. Furthermore, these channels have a 10 fold larger concentration at the endfoot processes of the astrocyte than the remaining membrane, therefore attesting to the polarized nature of astrocytes.

Water transport by the astrocyte has been hypothesized to be involved in a variety of brain tissue properties. Of particular interest is that it might help to explain the reported extra cellular space (ECS) volume reduction of 5% to 30% during high frequency activation of excitatory pathways [81]. The mechanisms behind this reduction have not been described in detail. Recently, it has been proposed that this reduction is due to water movement from the ECS into the astrocyte through water transport coupled with ion and neurotransmitter cotransport. It seems a promising hypothesis as water cotransport has been identified through NKCC1 channels (channels with a stoichiometry of

$Na^+/K^+/2CL^-/H_2O$) and the glutamate transporter (for every glutamate/$3Na^+/H^+/H_2O$ that go in the cell and mole of K^+ is pushed out). Additionally, AQP4 is also believed to play a role in terms of ECS shrinkage. Although mostly expressed at the endfeet processes there have been reported AQP4 pools in those delicate astrocytic processes that are close to excitatory synapses. Furthermore, it is still unclear if the expression of AQP4 is responsible for either extracting water from the ESC or preventing further shrinkage by allowing water flux into the ECS. The latter seems more promising. A mathematical model has suggested that this theory is correct by showing that during synaptic activity the NKCC1 channel is responsible for allowing water to enter the astrocyte while AQP4 would allow water to leave the cell [81].

Additionally, AQP4 water regulation has also been linked to K^+ homeostasis [81]. A further process of K^+ uptake has been identified called spatial buffering. Through this process, K^+ is redistributed along the concentration gradient. It has been found that K^+ uptake by the perisynaptic astrocyte membrane is coupled to K^+ efflux through Kir4.1 channels located at the endfoot membrane. In essence, K^+ is transported from areas of high synaptic activity to remote liquid compartments. As the endfoot has high concentrations of both Kir4.1 and AQP4 it is hypothesized that AQP4 might affect K^+ conductance indirectly. This effect might come either as a molecular interaction between the two channels or through volume changes resulting in membrane stretches. The latter has also been proposed by mathematical modelling simulations from the work of [82]. All the functions of astrocytes outlined are here shown detailed in Figure 2.13.

Furthermore, the astrocyte has been found to be an integral element in the newly defined glymphatic system [81]. This is an anatomical pathway responsible for exchange between interstitial cerebral fluid (ICF) and the cerebral spinal fluid (CSF). This system has been hypothesized as a mechanism to clear interstitial solutes, e.g. metabolites, from the ECS. This mechanism has three components: a para-arterial CSF influx route; a para-venous ISF clearance route and a trans-parenchymal pathway that is dependent on glial water transport via the astrocytic AQP4 water channel. This system has been found to be a key mechanism for clearance of soluble amyloid β (Aβ), which is a substance that in Alzheimer's patients have been found to form plaques. These plaques are then believed to be produced by the accumulation of Aβ due to impairment of the glymphatic system.

Additionally, it has been shown by [40] that AQP4 null mice have a radiolabelled Aβ clearance reduction of approximately 65% that of wild type mice. Therefore, it is suggested that AQP4 dependent flow along the glymphatic pathway constitutes a key mechanism of soluble Aβ clearance.

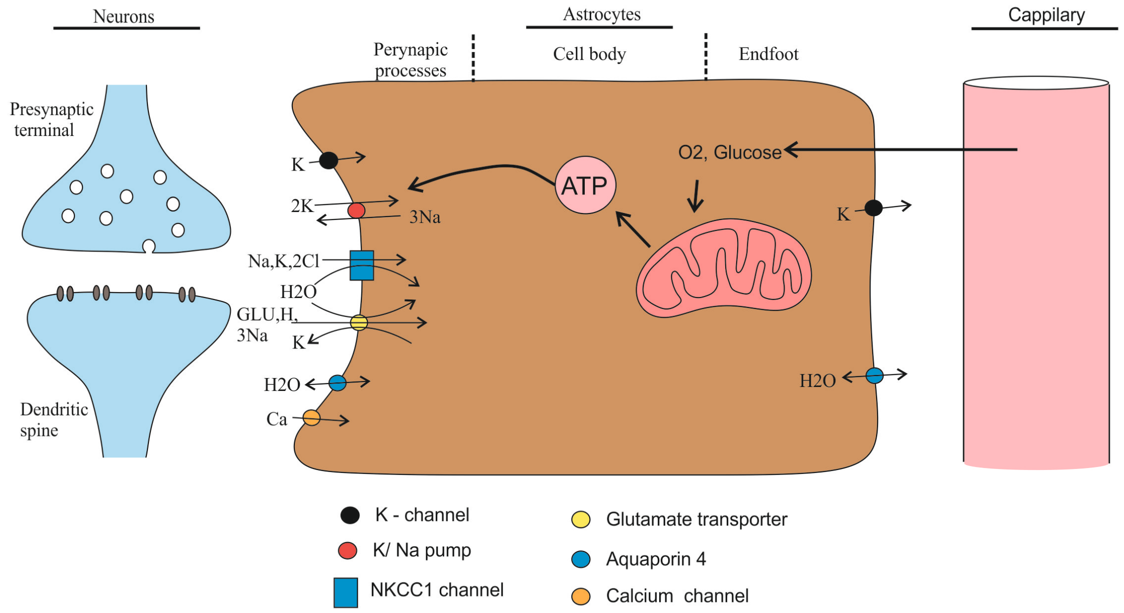

Figure 2.13: The astrocyte has mechanisms that interact with both neurons and the capillary [79].

2.1.3 Conclusion

From this analysis, it has been shown that the synapse is a tripartite entity. Previously it was considered as being constituted of pre- and post-synaptic membranes and the synaptic cleft. However, it has been shown that the astrocyte plays an integral role in regulating and maintaining homeostatic levels of ions and more importantly neurotransmitters. In the following section, the interactions between these two cells in terms of glutamate regulation are presented as well as its potential as a biomarker for cell death in cerebral pathological states.

2.2 The glutamate system

Glutamate is the neurotransmitter with the largest concentration in the brain (90% of neurons are glutaminergic [83]). Therefore, it is regarded as the principal excitatory transmitter in the nervous system. The maintenance of healthy levels of glutamate both intracellularly and in the ECS requires a complex regulatory system that involves neurons and astrocytes, and energy resources dispensed. Such a system is required because glutamate accumulation at the synaptic cleft leads to excitotoxicity: a mechanism responsible for cell death in many vascular, neurodegenerative and inflammatory brain pathologies. In this section, the case is made for the importance of having a mathematical model of glutamate release validated in a disease environment. Firstly, the glutamate system is described (Section 2.2.1). Then in Section 2.2.2 the role of glutamate excitotoxicity in a variety of diseases is discussed. In Section 2.2.3 the state of the art of *in vivo* measuring of glutamate is presented. Finally, in Section 2.2.4 it is explained how a model of glutamate fits into the overall research of the pathophysiology and treatment of neurological diseases.

2.2.1 Glutamate/glutamine cycle

Glutamate, like all the other neurotransmitters, is located inside the neuron in vesicles. In a healthy situation glutamate is released when an AP arrives and opens Ca^{2+} voltage dependent channels allowing Ca^{2+} to permeate the pre synaptic membrane [19]. In the presence of pathologies like ischaemic stroke glutamate has also been found to be released by the reverse function of the glutamate transporter, by swelling-activated anion channels and by an indomethacin-sensitive process in astrocytes. The first has been found to have particular relevance in the case of stroke as stated by [83]. The glutamate transporter is a voltage dependent channel that uptakes 1 molecule of glutamate with three molecules of sodium and releases one molecule of potassium [75]. However, in the presence of ischaemia as the membrane depolarizes, its stoichiometry is inverted leading to the exacerbation of glutamate release [83].

At the synaptic cleft, glutamate is responsible for the activation of a family of ionotropic receptors such as the N-methyl-D-aspartate (NMDA), the α-amino-3-hydroxy-5-methyl-4-isoxazolepropionic acid (AMPA) and the kainite receptors [19]. The AMPA receptor is the most common glutamate receptor. It controls a Na^+ channel that, when glutamate attaches to it, produces EPSPs. The kainate receptor has a similar function. The NAMD has particular characteristics that might inform future therapies that aim at mitigating excitotoxicity. It has 5 binding sites where four are exterior and one is inside the channel [19]. The exterior ones consist of glutamate, polyamine, zinc and glycine. For the channel to open both glutamate and glycine need to be attached to it. The latter is another neurotransmitter that in some areas of the nervous system acts as an inhibitor. Polyamine and zinc have been found to have a facilitator and an inhibitor effect respectively on NMDA activity. Inside the channel, the binding site is for magnesium, which blocks the channel even if glycine and glutamate are attached. For it to be removed the membrane needs to depolarize. Only then can Ca^{2+} and Na^{+} go through. As previously explained, when Ca^{2+} permeates the post-synaptic membrane it plays a principal role in the mechanisms responsible for synaptic growth and learning. Therefore, glutamate is integral to brain function.

From the synaptic cleft, the re-uptake of glutamate is mostly performed by astrocytes [21]. These have very sensitive glutamate transporters at the membrane. When inside the astrocyte, glutamate is metabolized into glutamine. Furthermore, the conversion requires ammonia (NH_3) and α-KG. The former is provided by the capillary or by the neuron while the latter is a product of the astrocytic TCA cycle. Glutamine is an amino acid that does not have any neurotransmitter function [83]. Therefore, it is safer to pump it to neurons without any concerns of excitotoxicity. At the neuron, glutamine is then converted back to glutamate through the release of ammonia. After this conversion glutamate is ready to be released again when an AP arrives. In Figure 2.14 the current understanding of the glutamate cycle is presented.

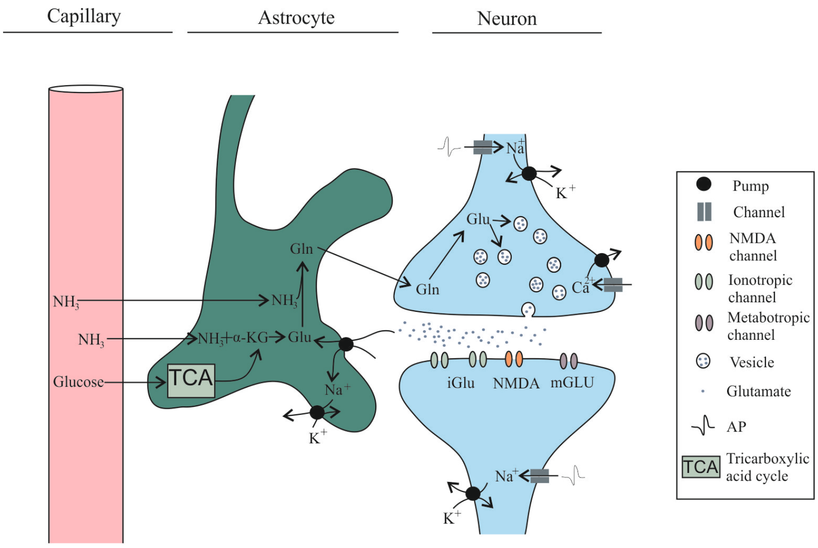

Figure 2.14: Characterization of the glutamate cycle including production; the exchange between astrocytes and neurons and activation of post synaptic receptors. This diagram is based on the work of [83].

2.2.2 Glutamate role in brain pathologies

The brain has in place several mechanisms that ensure that glutamate does not accumulate at the synaptic cleft. If any of these mechanisms fail, glutamate opens a larger number of receptors than is required for a longer period of time. This will, in turn, allow for an uncontrolled perfusion of Na $^{2+}$ and Ca $^{2+}$ into the post-synaptic neuron. The excess concentration of these ions has been found to be responsible for the production of apoptotic factors and oxidative stress. These processes have been linked with cell death mechanisms for many brain diseases. In this section, the role of glutamate in the pathophysiology of three different types of diseases (vascular, neurodegenerative and inflammatory) is presented. Additionally, the state-of-art research that aims to investigate the therapeutic potential of modulating the glutamate cycle is discussed in all three cases.

Glutamate was first determined as a toxin in the context of ischaemic stroke. In fact, it was found to be the principal agent responsible for cell death [84]. Consequently, researchers have hypothesized that inhibiting the glutamate system might be an ideal avenue for therapy. The initial targets proposed have been: the glutamate ionotropic and metabotropic receptors; and the calcium channels that trigger glutamate release and inhibition of mitochondrial products due to excitotoxicity like free radicals and nitric oxide [84]. However, it has been found that promising results from animal models are poorly translated into humans. Therefore, more complex models of excitotoxicity are currently being explored. These consist in inhibiting processes indirectly related to excitotoxicity. Researchers have explored inhibiting other Ca^{2+} channels like the sodium-calcium exchanger and the sodium, calcium and magnesium TRP channels as they exacerbate the intracellular levels of Ca^{2+} during stroke. However, no human studies have yet been performed [84].

Additionally, as glutamate has been found to take part in the mechanisms responsible for learning and memory it has been hypothesized that deregulation of the glutamate system might explain the extent of cell death due to neurodegenerative diseases. The most common neurodegenerative disease is Alzheimer's disease with a worldwide incidence of 44 million people in 2015 [85]. Glutamate excitotoxicity has been identified as one of the main causes of cell death. Alzheimer's is characterized by the accumulation of Aβ and the formation of a plaque in the ECS, which is hypothesized to lead to osmotic and hydrostatic pressure deregulation. This pressure deregulation leads to uncontrolled glutamate release. In fact, many therapies for Alzheimer's have been proposed that target the glutamate system. One of the principal targets has been the NMDA receptor. The most promising drug found has been Memantine, a channel blocker, and this is currently commonly prescribed for Alzheimer's disease patients [86]. However, its efficacy is still questionable [86]. Other promising drugs have been found in the family of non-competitive antagonists of the NMDA channel (substances that bind to the channel which does not block the binding site of glutamate and glycine [87]) in animal models [86]. As the evidence of glutamate excitotoxicity involvement in the pathology of Alzheimer's disease mounts [86], it is likely that new therapies will be developed.

Furthermore, brain inflammatory diseases might also have an excitotoxicity component to them. The particular case of multiple sclerosis (MS) has been explored. This disease is characterized by oligodendrocytes death and axonal demyelination [73]. Evidence has been compiled by [73] that glutamate levels increase in brains afflicted by MS, which is also marked by up-regulation of expression of the glutamate ionotropic receptor. Expression of glutamate transporters is also altered with particular relevance to the correlation between loss of transporters in cortical regions and microglia activation and neuronal damage. From this evidence, researchers have presented MS therapies through inhibition of ionotropic receptors. In fact, drugs like Memantine have been shown to ameliorate the symptoms of the disease by reducing oligodendrocyte and neuronal damage.

From the bulk of the evidence presented here, it has been shown that glutamate has a direct or indirect role in many of the main neurological diseases that afflict society today. However, before therapies that mitigate excitotoxicity can be prescribed, further experimental proof is required that will take time and be costly. Thus, in order to facilitate the work required a mathematical model of glutamate release was developed and this is presented in Chapter 3. Stroke was the disease chosen as this is the disease where the excitotoxic pathway is better understood. With such a model, it is showed how mathematical modelling can be used to test hypotheses about pathology progression and to investigate new therapies in a more cost effective and ethical manner.

2.2.3 Measuring glutamate

Glutamate plays an integral role in many neurological pathologies and so it has been proposed as a biomarker. Currently four procedures have been developed to measure glutamate *in vivo*: microdialysis probe measurement [74], [88], [89], the use of positron emission tomography (PET) or single photon computed emission computed tomography (SPECT) tracers for glutamate receptors [90], H magnetic resonance spectroscopy (H-MRS) and chemical exchange saturation transfer (CEST) MRI [91], [92]. The one most commonly used in a research setting is microdialysis as it is the least expensive. It is commonly used in animal models and it consists of the extraction of CBF (dialysate) from animals at certain time intervals using a probe and analysing the dialysate for its constituents. In a clinical environment, this is unsuitable as the probe needs to be inserted across the skull [74], [88], [89].

Starting with PET and SPECT, it has been found that imaging modalities can be used to quantify glutamate brain receptor concentration and can also be used to determine the occupancy of these receptors [90]. Therefore, they provide an efficient approach to develop new drugs and to evaluate their effect on brain function. Several ligands are being developed to quantify the metabotropic and ionotropic glutamate receptors with different levels of success. However, PET and SPECT require exposing patients to radiation, which is not ideal.

H-MRS and CEST MRI are safer for patients in that regard. H-MRS is an imaging modality that uses the same physical principles as magnetic resonance imaging (MRI) [91]. However, instead of originating from proton shifts of water it uses the magnetic resonance signal of hydrogen to determine the concentration of metabolites. While MRI has the ability to reveal anatomical structure, H-MRS offers biochemical information about living tissue. H-MRS is currently implemented to measure glutamate concentration in studies that look at schizophrenia. However, it requires long acquisition times and has poor spatial resolution.

To overcome those limitations CEST MRI has been developed for glutamate [91]. The modality provides higher spatial and temporal resolution compared with H-MRS. The underlying principles of CEST consist of using selective radiofrequency (RF) to saturate exchangeable solute protons that resonate at a frequency different from the bulk water protons. The saturation is then transferred to bulk water when solute protons exchange with water protons and the water signal becomes slightly attenuated. As there is a much larger concentration of the water pool than the saturated solute proton pool, each exchanging saturated solute proton is replaced by a non-saturated water proton, which is again saturated. Prolonged irradiation leads to a substantial enhancement of this saturation effect; this is visible in the water signal, making it possible to image low-concentration solutes. This modality has already shown promise, for example as shown in a study by [92] that aims to understand the loss of brain function during tauopathies (a class of diseases that have a pathological mechanism the accumulation of tau protein in the ECS). Using CEST MRI this work was able to quantify glutamate in tau transgenic mice with the P301S mutation (n=9) versus wild type mice (n=8). They found that there is a reduction in glutamate in the CA and thalamus where there was also synapse loss. Therefore, glutamate CEST MRI is presented by [92] as a potential modality to diagnose tauopathies.

2.2.4 Conclusion

From this analysis, it has been shown that through the understanding of how the nervous system regulates glutamate, it might be possible to explain the cell death process during many neurological conditions. This is not surprising as glutamate is the main excitatory neurotransmitter. Many of the mechanisms that regulate glutamate are connected directly or indirectly to the systems governing osmotic and hydrostatic regulation and metabolism. Consequently, glutamate has also been proposed as a biomarker of these diseases. With that in mind, researchers have developed methods to measure glutamate *in vivo*. At a research level microdialysis gives reliable data and is relatively cheap. For a clinical setting, the use of magnetic resonance technology using MRS or CEST procedures has been able to measure glutamate concentration.

2.3 Ischaemic stroke [93]

The process of excitotoxicity in this work is investigated in an ischaemic stroke environment. The disease was chosen as it is one whose pathophysiology is reasonably well understood and where the role of glutamate is more prominent. In this section, the pathophysiology is described (Section 2.3.1). Additionally, in section (2.3.2) the state of the art therapies for ischaemic stroke currently being prescribed as well as the most promising therapies still at the research stage are presented.

2.3.1 Ischemic stroke pathology

Ischaemia is a word that comes from the Greek *iskhein* that means restrict. Therefore, ischaemic stroke describes a disease where the brain vasculature is restricted. This leads to the reduction of blood flow that starves brain tissue of nutrients and energy. Consequently, the processes of cell death are initiated. Clinically, the tissue damaged can fall into two categories. The first is called the stroke core that consists of the tissue whose blood supply has been cut. The second is called the penumbra and it consists of the tissue that immediately surrounds the stroke core. Here the tissue still has a percentage of its blood supply and can still be salvageable if clinical intervention is effective. However, in order for the therapy to be effective five cell death processes need to be taken into account that have different time scales (minutes to days) and characteristics in the two stroke areas. These are as follows:

1. Excitotoxicity and ionic imbalance: The regulation of ionic osmotic balances depends on the availability of ATP. Without it, the sodium-potassium pump is unable to function, which leads to osmotic pressure deregulation, neurotransmitter release and inhibition of reuptake of ions and neurotransmitters. The principal neurotransmitter responsible for cell death during a stroke is glutamate. As previously explained this neurotransmitter is the one with the largest concentration in the brain and it is responsible for the activation of the NMDA and AMPA receptors. The excess of glutamate in the synapse during stroke leads to the over stimulation of the postsynaptic membrane resulting in uncontrolled permeability of Ca^{2+}. In the post synaptic neuron, the extra Ca^{2+} can trigger

phospholipases and proteases responsible for the degradation of the cellular membrane, putting the cellular integrity at risk.

2. Oxidative / nitrosative stress: Mitochondrial ATP production requires electron transport, which results in the formation of oxygen free radicals. However, the production of free radicals becomes unregulated when high concentrations of Ca^{2+}, Na^{+} and ADP are present in the intracellular space during an ischaemic stroke. The oxidative species start damaging the tissue due to the inability of brain oxidant enzymes to cope with the excess concentration. These reactive oxygen species have been found to damage proteins, lipids, nucleic acids and carbohydrates. Additionally, oxygen radicals and oxidative stress facilitate the formation of mitochondrial transition pores (MTP), which dissipate the proton motive force required for ATP production. Due to MTP, the mitochondria start to release apoptotic factors and other intra-mitochondrial constituents. These mechanisms have been found to be of relevance when considering tissue reperfusion. This is because the arrival of extra oxygen might exacerbate the damage since the tissue is already vulnerable. The first two mechanisms of cell death detailed here are shown in Figure 2.15.

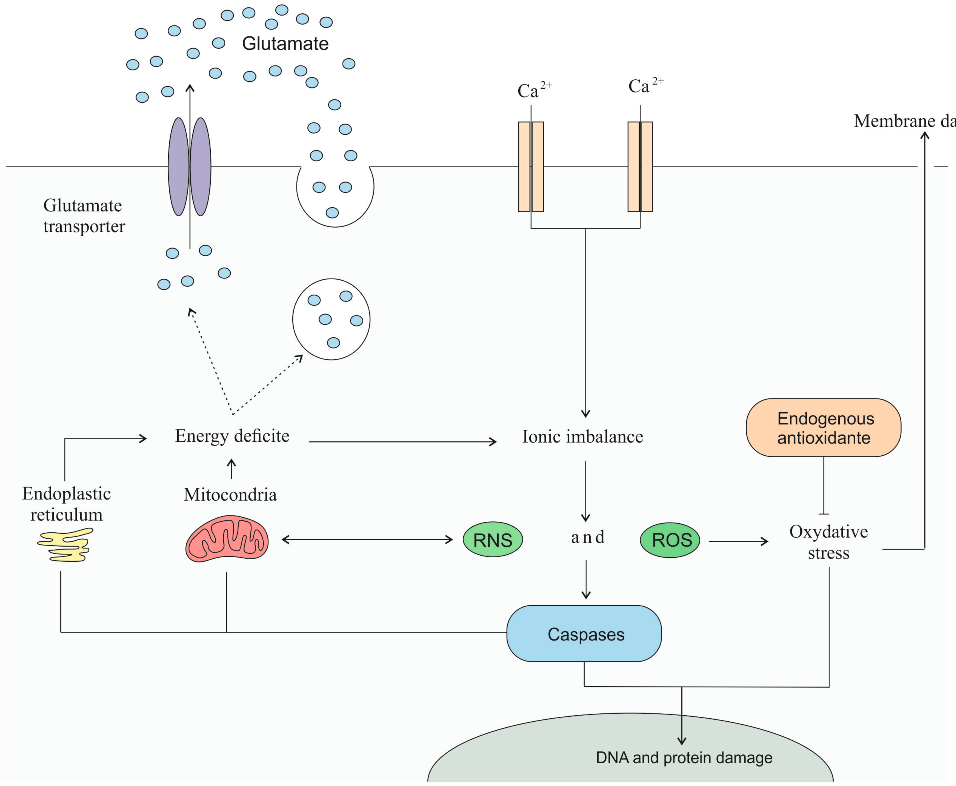

Figure 2.15: Diagram describing the different mechanisms involved in the initial stages of the ischaemic pathology. [93]

3. Inflammation: Throughout the ischaemic stroke pathophysiology process, inflammatory agents are produced at several stages. Starting with the vessel occlusion, it has been found that inflammation within the artery promotes atherosclerosis and arterial thrombosis. From this stage forward there are two waves of inflammation that promote tissue damage. The first is during the acute phase (minutes to hours) of the stroke, which is marked by injured tissue releasing ROS and pro-inflammatory mediators, e.g. cytokines and chemokine. These mediators promote the expression of adhesion molecules, which leads to the transendothelial migration of leukocytes. During the sub-acute phase (hours or even days) the leukocytes that have permeated into the tissue start to release cytokines and chemokines resulting in the further infiltration of leukocytes, which eventually leads to the breakdown of the BBB, brain oedema and neuronal death.

4. Apoptosis: This process is also called programmed cell death and it consists of caspase dependent and independent mechanisms. Caspases are cysteines that are responsible for the cleaving of cellular proteins. To perform their function, caspases require ATP. Therefore apoptosis is more prominent in the penumbra than in the core of the stroke. Several triggers for apoptosis have been reported: oxygen free radicals, death receptor ligation, DNA damage and possibly lysosomal protease activation. Additionally, ionic imbalance and mechanisms such as NMDA receptor-mediated K^+ efflux have been found to induce apoptosis under certain conditions. Therefore, inhibiting glutamate excitotoxicity might also prevent long-term cell death.

Apoptosis is a natural process; therefore, there are basal values of caspases present in neurons. These are responsible for the first wave of apoptosis. In the case of mitochondrial damage, the second wave of apoptosis might be generated. This organelle in a healthy situation plays an integral role in modulating apoptosis through the release of molecules. Therefore, during ischaemic stroke these molecules start releasing uncontrollably by the mitochondria, aggravating tissue damage.

In order to mitigate apoptosis caspase inhibitors were developed. However, it has been found that this does not fully protect neurons. This is because there are also caspase independent apoptotic mechanisms. One of these is promoted by the NMDA receptor perturbation, which results in the formation of apoptosis-inducing factors (AIF) by the mitochondria. The latter then move to the nucleus, bind to DNA and initiate the cell death process. Therefore, in order to fully prevent apoptosis a combination of treatments is required.

5. Peri-infarct depolarization: At the stroke core the deregulation of the ionic concentrations causes brain tissue depolarization and irreversible damage. This process is called anoxic depolarization. From the core the ions diffuse to neighbouring tissue leading to the propagation of an electrochemical wave at a rate of 2-5 mm/min that further depresses brain tissue. Consequently, glutamate and potassium release are also triggered, leading to further damage. These waves are called peri-infarct depolarisations (PID) and they result in the step-wise increase of the core-infarcted tissue into the penumbra.

The timescales of all the mechanisms involved in the pathophysiology of ischaemia are summarized in Figure 1.1.

2.3.2 Therapies for stroke

Although there is information available on the pathophysiology of stroke, the therapies currently implemented are still rudimentary. The main aim of all treatments is to re-establish blood flow to the penumbra in order to salvage as much brain tissue as possible. Treatments come in the form of intravenous thrombolytic therapy (e.g. intra-arterial thrombolysis – IA – and tissue plasminogen activator – tPA) and intra-arterial mechanical thrombectomy with stent retriever devices [94]. Additionally, drugs such as aspirin and anticoagulants are also commonly prescribed. All of these treatments have been found to incur a risk that might end up causing further damage to patients. As one example, in a study that looks at 111 patients that received thrombectomy treatment, 69% experienced full recanalization while 15 of 111 suffered intracranial haemorrhage [94]. Of those 10 were symptomatic. Similarly, aspirin has also been found to have a risk of inducing further haemorrhaging. A study that compiled the results of a number of experimental studies estimated that there is an occurrence of further haemorrhage in 0.2 per 1000 patients a year [95].

In order to mitigate the number of deaths due to clinical intervention, doctors utilize tools that aid in the process of demarking the penumbral area. The one most commonly used is diffusion/perfusion mismatch (PDM) MRI. However, there is no clinical consensus either on what perfusion weighted imaging (PWI) parameter should be used to identify the PDM accurately or on how to measure the PDM [96]. CBF maps are commonly used to visualize the brain of stroke patients [97]–[99]. From them, measurements are made to predict the size of the infarct. There is no agreement as to which measurement is superior between for example time to peak (TTP) and mean transit time (MTT). However, both of these have been shown to overestimate the ischaemic lesion [100], [101].

Clinically, there are two processes to estimate the PDM. The first consists in visually estimating the PWI-derived parametric maps and DWI from MRI console software. The second involves applying post-processing methods to derive the PWI maps and DWI based on region-of-interest calculations. For the latter, the PDM can be defined as either as diffusion lesion volume of >1.2, or as a difference of >10-50 mL volumes of abnormalities between PWI and DWI [102], [103]. Both processes have been found to overestimate the area of the ischaemic core [103], [104]. Therefore, patients might be misdiagnosed.

To overcome this limitation researchers have tried to find other penumbral biomarkers besides CBF. Three biomarkers have been singled out as promising tools to demarcate the penumbral area, the first of which is pH. pH weighted imaging considers the fact that at the penumbra the tissue experiences anaerobic metabolism, leading to the formation of lactate and a decrease in pH [105]. The second is temperature: it has been found that approximately 50% of ischaemic stroke patients experience fever [106], [107]. Temperature can be measured non-invasively through magnetic resonance spectroscopy imaging. From this imaging modality [108] it has been found that the infarct core is hotter than the surrounding tissue. Finally, the third is oxygen [109]: this comes from the finding that the oxygen extraction fraction (OEF) is significantly increased in the penumbra.

The current gold standard to identify the penumbra consists of using positron emission tomography (PET). The penumbra is defined here as the area with increased OEF. However, in practice, it has been found to be difficult to determine the absolute penumbral threshold values as the calculation requires arterial blood sampling [110], [111].

Clinically stroke is hard to diagnose and treat not only because of the imaging limitations but also because there is a limited time window for intervention. This window is of approximately 4.5

hours. As imaging resources at hospitals are often scarce it is difficult to ensure that patient's brains are imaged at the optimal time to ensure an accurate diagnosis. Therefore, researchers have been trying to develop procedures and drugs that will extend the time window and mitigate tissue damage. As presented, ischaemic stroke pathophysiology involves several pathways. Each of these pathways presents several possible targets for therapy which have proved to be successful at reducing ischaemic injury in animals, e.g. free radical scavenger NXY-059 [112], recombinant erythropoietin [113], the competitive NMDA antagonist selfotel [114] and non-competitive NMDA antagonist [115], [116]. However, there are several barriers to the efficacy of these drugs. At a research level, it has been found difficult to translate results acquired with animal models to clinical practice. The reason for this is that the human has different brain structure, function and vascular anatomy when compared to the brains of gerbils and rats. Additionally, the mice used are genetically engineered to ensure reproducibility of the results. Such genetic homogeneity does not exist when considering humans as age and comorbidities (diabetes and hypertension) have been found to affect the outcome of these novel therapies. Furthermore, the way therapeutic viability is evaluated in animal models and humans is different. While in animals, success is quantified in terms of infarct volume, for stroke patients, recovery is considered based on the NIH stroke scale, Barthel index, etc. In addition, therapeutic outcomes have different scales when considering animals (days) and humans (months).

The development of neuroprotective drugs is further aggravated by several barriers to be overcome before arriving at the stroke core. First, there is, evidently, a reduced CBF above 5-10% at the ischaemic core and 30-40% at the penumbra when compared to the baseline [93]. Secondly, drugs have to traverse the BBB that restricts the exchange between the vasculature and the parenchyma. Thirdly, the oedema characteristics of the stroke pathophysiology lead to an increase in intracranial pressure, which impairs efficient delivery. Currently, strategies are being developed to aid drugs to traverse the BBB through intracerebral and interventricular delivery, hyperosmolar substances and pharmacological agents. The later facilitate the osmolar opening and the development of carrier-mediated transport systems. All these strategies appear to be promising. However, they are still at early stages of development.

As has been shown, the pathophysiology of stroke involves many mechanisms and patients express a variety of levels of severity. Therefore, researchers have been trying to define combinations of treatments that are introduced at once or in series in accordance with the pathological timeline presented in Figure 2.16. A case that has been shown to have promising results in humans is the administration of neuroprotective drugs in combination with thrombolytic drugs. This combination has been shown to reduce reperfusion injury and to inhibit downstream targets in cell-death cascades. Examples of neuroprotective drugs that have been shown to provide synergetic additive effects in combination with thrombolysis can be found in oxygen scavengers, AMPA and NMDA receptor antagonists, MMP inhibitors, citicoline, topiramate, antileukocytic adhesion antibodies and antithrombotilitics. Other combinations of drugs that have been shown to have promising results in animal models consist of co-administration of NMDA receptor antagonists with GABA receptor agonists, free radical scavengers, citiclohexamide, caspase inhibitors or growth factors. Combinations of these drugs may decrease the dosage of each agent required and therefore avoid their individual adverse effects.

Furthermore, researchers are exploring non-pharmacological strategies as neuroprotective therapies. Here 6 proposed treatments are presented, based on the analysis by [93]:

1. Ischaemic preconditioning: This consists of inducing transient, non-damaging ischaemic insults to the brain that have been shown to up regulate endogenous pathways that increase resistance to injury. Evidence has been accumulated that the severity of ischaemia is reduced in patients that have suffered a previous stroke. This is believed to be due to preconditioning. In a diffusion perfusion study with 65 patients, the ones that had experienced a previous stroke (n=16) were found to have smaller initial diffusion lesions and final infarct volumes. The tolerance induced by preconditioning can be of two forms, acute or delayed. The former only lasts a few minutes and is mediated by post-translational protein modification while the former might last several hours and consists of changes in gene expression and new protein synthesis. From current understanding of ischaemia preconditioning, it may provide further insights into the molecular mechanisms responsible for endogenous neuroprotection.

2. Magnesium: The administering of extra magnesium intravenously in rats 6 hours after stroke onset has been shown to reduce the lesion volume. Magnesium has been found to mitigate many of the pathophysiological mechanisms of stroke in rats. During stroke it acts as a calcium channel antagonist, an inhibitor of glutamate release, a NMDA receptor blocker and it maintains cerebral blood flow. However, in humans the effects of prescribing magnesium as a therapy are still controversial. In a clinical study with approximately 2,500 patients, magnesium was injected within 12 hours after stroke onset and no therapeutically effects were identified. Currently, studies are trying to understand if injecting magnesium earlier might generate similar effects as those found in rat models.

3. Albumin infusion: This is a treatment commonly given to patients with liver disease and has also been found to have therapeutic effects in rat models. It enhances red cell perfusion and suppresses thrombosis and leucocyte adhesion within the brain microcirculation. Additionally, albumin reduces the erythrocyte volume fraction in the blood, improving circulation, viscosity of plasma, and cell deformability as well as oxygen transport capacity. Furthermore, reductions in infarct size and cell oedema have been reported. All these effects in rat models are currently being explored in clinical studies.

4. Hypertension: Researchers have found that the ischaemic penumbra that suffers from autoregulation impairment during stroke is sensitive to blood pressure manipulation. In animal models it has been found that by inducing hypertension through an increase in mean arterial pressure improves cerebral perfusion within the penumbra and consequently a faster return to basal electric activity. In the core, improvements were also observed in terms of cerebral blood flow and oxygen metabolism. Recently, induced hypertension has been tested in patients with acute stroke. The patients chosen presented significant diffusion-perfusion mismatch on MRI, large vessel occlusive disease and fluctuating neurological deficits. From these clinical trials it was found that perfusion did improve and that this correlated well with improvements in the corresponding cortical regions. However, this treatment incurs the risk of inducing intracerebral haemorrhage and worsening the symptoms experienced during reperfusion. Furthermore, cardiac complications might arise that are common to people with hypertension, e.g. myocardial ischaemia and cardiac arrhythmias. Therefore, this form of

ischaemic treatment is better advised for prescription to patients that do not fit the criteria for thrombolytic therapy.

5. Hypothermia: Temperature has been found to modulate several processes involved in stroke pathology. It has been reported that hypothermia has the potential to increase the resistance to many of the cell death pathways involved in ischaemic stroke, including oxidative stress and inflammation. Additionally, it was observed that as, most biological processes exhibit a Q_{10} (the temperature sensitivity of an enzymatic reaction rate or physiological due to an increase of 10 C^o [117]) of approximately 2.5, a reduction in temperature of 1^oC leads to an approximate 10% reduction in oxygen consumption. Additionally, it slows the rate of pathological processes such as lipid peroxidation, as well as the activity of certain cysteine or serine proteases. In animal models it has been found that small decreases in core temperature of about 1 - 4^oC substantially reduce neuronal death. Moderate hypothermia (reduction of core temperature by 5 to 9^oC) has also been tested but it has been found to be technically difficult to induce and to provoke further complications. Clinically results have shown to be promising. In a study with 25 patients that suffered complete middle cerebral artery infarction where their core temperature was reduced to 33^oC for 48-72 hours significant reductions in morbidity were observed. Currently further experimental tests are being performed to evaluate the efficacy of the treatment.

6. Hyperoxia: The reduction in tissue oxygenation plays a primary and secondary role in many stroke cell death mechanisms. Therefore it is hypothesized that inducing an increase in oxygen concentration might ameliorate ischaemic stroke symptoms. Additionally, oxygen possesses characteristics that make it more adequate than other drugs to treat stroke: it is able to traverse the BBB easily and it can be prescribed with no dose limiting side effects (except in the case of patients with chronic obstructive disease). This therapy was tested in animal and humans through a process called hyperbaric oxygen therapy (HBO). There were promising results in animal models, however these did not translate into the clinical setting. Alternatively, normobaric hyperoxia therapy (NBO) has been tested with much more successful results: in animals, it improved blood flow and inhibited peri-infarct depolarization while in humans, improvements were observed using diffusion-MRI in a clinical study with acute ischaemic stroke. When comparing NBO and HBO it is also found that NBO has particular

characteristics that make it more suitable for the clinical treatment of stroke: it is non-invasive, it can be implemented by paramedics, ensuring quick response times, and it is inexpensive. However, theoretically an increase in oxygen concentration might also induce further damage by promoting the production of oxygen free radicals. Therefore, further studies are required to ensure safety of the procedure. Furthermore, existing data show that oxygen benefits are transient and can only be maintained if the tissue is reperfused. Consequently, perhaps hyperoxia is better suited as an initial intervention that extends the time window for thrombolysis therapy.

2.3.3 Conclusion

The analysis presented here shows the complexity of pathophysiology of stroke. It is a cascade of events that after triggering cannot be reversed but instead only mitigated. From Figure 2.16 the two initial symptoms of ischaemic stroke are glutamate excitotoxicity and peri-infarct depolarization, which occur in the first few hours post stroke. The first 4.5 hours is the period for which surgical interventions are prescribed. Consequently, any model developed must capture these two symptoms. With such a model, it is possible that it might be used to test future therapies for stroke without requiring the expenditure and the animal sacrifice common to experimental work.

2.4 Inflammation

2.4.1 Overview of the inflammatory physiology [56]

Inflammation is the process involved in killing and clearing foreign bodies from the body. However, the inflammatory components responsible for microbes and dead tissues can also damage healthy tissue. Injury occurs if the inflammatory reaction is severe, prolonged or inappropriate (e.g. when it targets self-antigens as in the case of autoimmune diseases as NMO). This process involves the confluence of many types of cells: blood leukocytes and plasma proteins, endothelial cells of the vascular walls and extracellular matrix of the surrounding connective tissue.

There are two types of inflammation, acute and chronic. Acute inflammation is characterized by plasma protein exudation and a predominantly neutrophil leukocyte accumulation. This type of inflammation normally has the time scaled of a few hours to as long as a few days. Alternatively, chronic inflammation is of longer duration that can go from days to years. Here, the predominant feature is the influx of lymphocytes and macrophages, which then causes vascular proliferation and fibrosis. The arrival of all these cells to the site of acute inflammation can be externally identified due to heat, redness and swelling. Additionally, patients commonly complain of pain and loss of function.

Acute inflammation aims to rapidly deliver leukocytes and plasma proteins to the site of injury to clear microbes, other foreign bodies and necrotic tissue. The trigger for inflammation might take many forms as many types of inflammation e.g. bacterial, viral, fungal or parasitic; trauma and physical and chemical agents; tissue necrosis e.g. caused by ischaemia; penetration of foreign bodies e.g. splinters and finally autoimmune triggers. These triggers elicit the activation of two sets of mechanisms: vascular changes and cellular recruitment and clearance.

In the initial stages of inflammation, the arterioles dilate which leads to an increased volume of blood flow. Therefore, there is a rise in hydrostatic pressure resulting in the movement of fluid from the capillaries into the ECS. This fluid is called transudate and consists of blood and plasma ultra-filtrated containing no large molecules such as proteins. However, it does contain ions, leading to osmotic deregulation in the tissue. Consequently, there is a breakdown of the mechanisms that ensure capillary stability resulting in an increase of the vascular permeability. This allows for a fluid rich in proteins and cells (called exudate) to move into the ECS. The increase in permeability may be due to a variety of factors; such as: 1. endothelial cell contraction, which occurs due to chemical mediators like histamine and leukotriene; 2. endothelial injury that causes leakage that can persist for hours until the damaged vessels are thrombosed or repaired; 3. leukocyte-mediated endothelial injury that is caused by accumulation of leukocytes in the vascular wall; 4. increase in the expression of certain mediators such as vascular endothelial growth factors (VEGF), which augment venular permeability and 5. one of the tissue repair mechanisms is the formation of new blood vessels that are leaky until the endothelial cells are able to mature.

Although increasing the permeability of the vasculature might lead to tissue damage it is essential to allow leukocytes to arrive at the inflammatory site. Leukocytes ingest offending agents, kill bacteria and other microbes and eliminate necrotic tissue. The process by which leukocytes are recruited from the vasculature into the ECS involves a series of steps. It all starts by a process called margination by which leukocytes are pushed to the walls of the vasculature. This occurs because as blood moves from the capillaries into the post-capillaries laminar flow moves cells into the vessel wall. Additionally, leukocytes are normally pushed outside the central axial column of flow because of their larger size compared to red blood cells. Then, when in contact with the vessel wall the leukocytes start to tumble and the drag slows them down. This process is called rolling. In the inflammation areas, the vasculature expresses cell adhesion molecules called selectins. These will lead to an increase in drag in the vessel wall, reduction of the velocity of leukocyte rolling and sticking of the cells to the wall.

The next step of leukocyte recruitment consists of the firm adhesion of leukocytes to the wall. This process is mediated by another type of cellular adhesion molecules called integrins. Both endothelial cells and leukocytes need to express integrins in order for the adhesion process to be successful. The expression of these molecules is activated by chemokines. These are chemoattractant cytokines that are secreted by many cells in the sites of inflammation. These attach themselves to endothelial cells and are displayed on its surface. When the leukocytes encounter these chemokines, they are activated and their integrins undergo conformational changes and they cluster which leads to an increase in affinity of the cell to attach to the wall.

Due to the integrins, the cells become attached to the endothelial cells and are ready to migrate into the ECS. Migration occurs by diapedesis, which comprises of leukocytes squeezing through intercellular junctions. This movement is stimulated by chemokines. The leukocytes travel in the direction of their concentration gradient. In addition, this movement is mediated by a cellular adhesion molecule called PECAM-1.

After migration from the blood into the ECS, the movement of leukocytes towards the site of infection is mediated by the gradient of chemokines concentration. Chemokines can take the form of endogenous or exogenous substances, which include: bacterial products; cytokines; complement derived proteins; and products of the metabolism of arachnoid acid. The chemotactic molecules bind to specific receptors on the surface of the membrane of leukocytes. The region where there is a larger number of activated receptors suffers a series of structural changes responsible for leukocyte motility. These changes consist of the extension of pseudopods that anchor to the extracellular matrix and pull in the direction of the extension.

The types of leukocytes that are recruited are dependent on the duration of the inflammatory event and how it is triggered. The development of acute inflammation has a common progression. In the first 6 to 24 hours neutrophils infiltrate the tissue and then they are replaced by monocytes within the next 24 to 48 hours. This sequence can be explained by the different characteristics of the type of cells. Neutrophils are the first to be recruited because compared to monocytes they have a larger concentration in the blood; they have a larger number of receptors for cytokines and therefore are more sensitive to their presence, and they have more adhesion molecules making their extravasation mechanisms faster. Furthermore, their life span is smaller than monocytes. They tend to die by apoptosis after 24 to 48 hours and are then removed. Conversely, monocytes can live for days. The mechanism by which leukocytes are recruited is summarized in Figure 2.17.

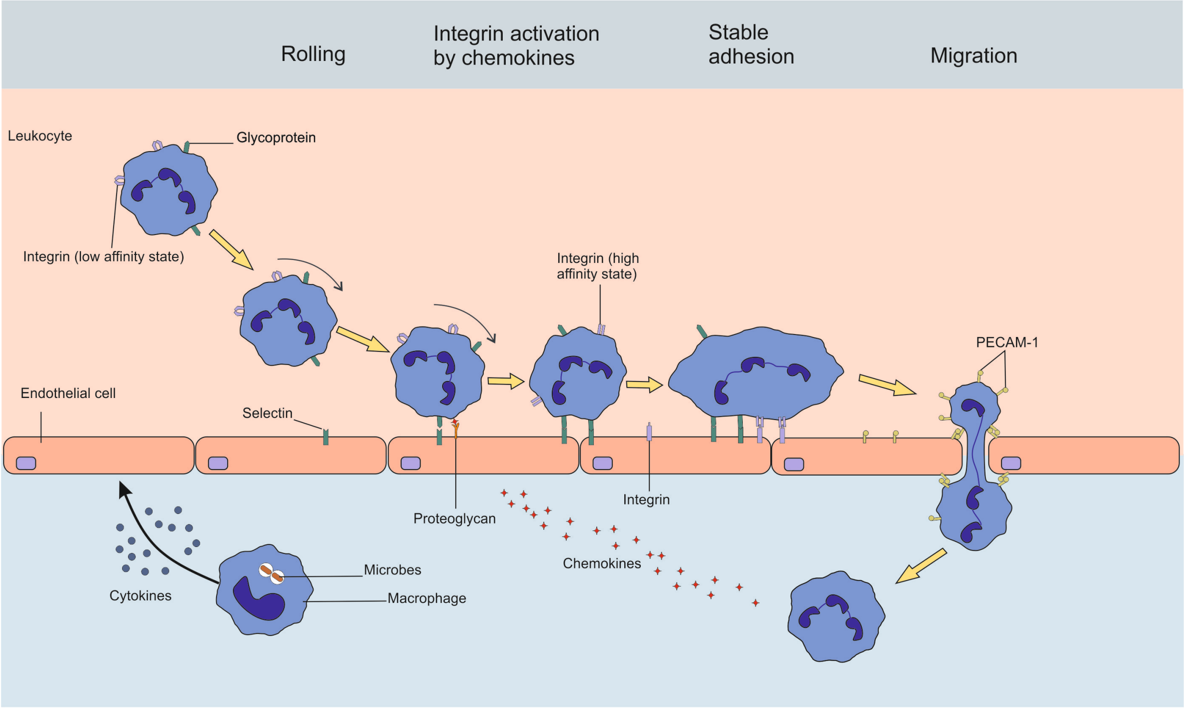

Figure 2.17: Description of how leukocytes are recruited and how they move into the ECS. [56]

After the leukocytes permeate into the tissue they follow the chemokine gradient in the direction of the inflammatory area. However, they still need to be activated to execute their functions. Leukocytes express receptors on their surface that sense the presence of microbes. The engagement of these receptors leads to leukocyte activation that comprises of: phagocytosis; the production of substances that destroy phagocytosed microbes and dead tissue; production of mediators that amplify the inflammatory reaction. The process of phagocytosis involves three steps: 1. detection and attachment of microbes and particles to the leukocyte; 2. engulfment of the microbe, which is then placed inside a phagocytic vacuole; and 3. killing and digestion of the ingested material.

In order for leukocytes to recognize the microbes or debris, they are first coated with proteins called opsonins through a process called opsonization. The most relevant types of opsonins are the antibodies of the class immunoglobin G (IgG). These bind to the surface of microbes and start to breakdown the complement proteins present in the plasma, which result in the formation of C3 and carbohydrate binding lectins called collectins. Leukocytes bind to the opsonins which trigger engulfment. Engulfment consists in the leukocyte extending pseudopods that surround the object being engulfed. These are then placed inside a phagocyte vacuole. Then the leukocyte produces microbicidal substances and places them inside lysosomes. Both the phagocyte vacuole and the microbicidal lysosome then meet and fuse, exposing the microbe to the destructive mechanisms of the leukocyte. The most important microbicidal substances are reactive oxygen species (ROS) and lysosomal enzymes. A summary of this process can be seen in Figure 2.18.

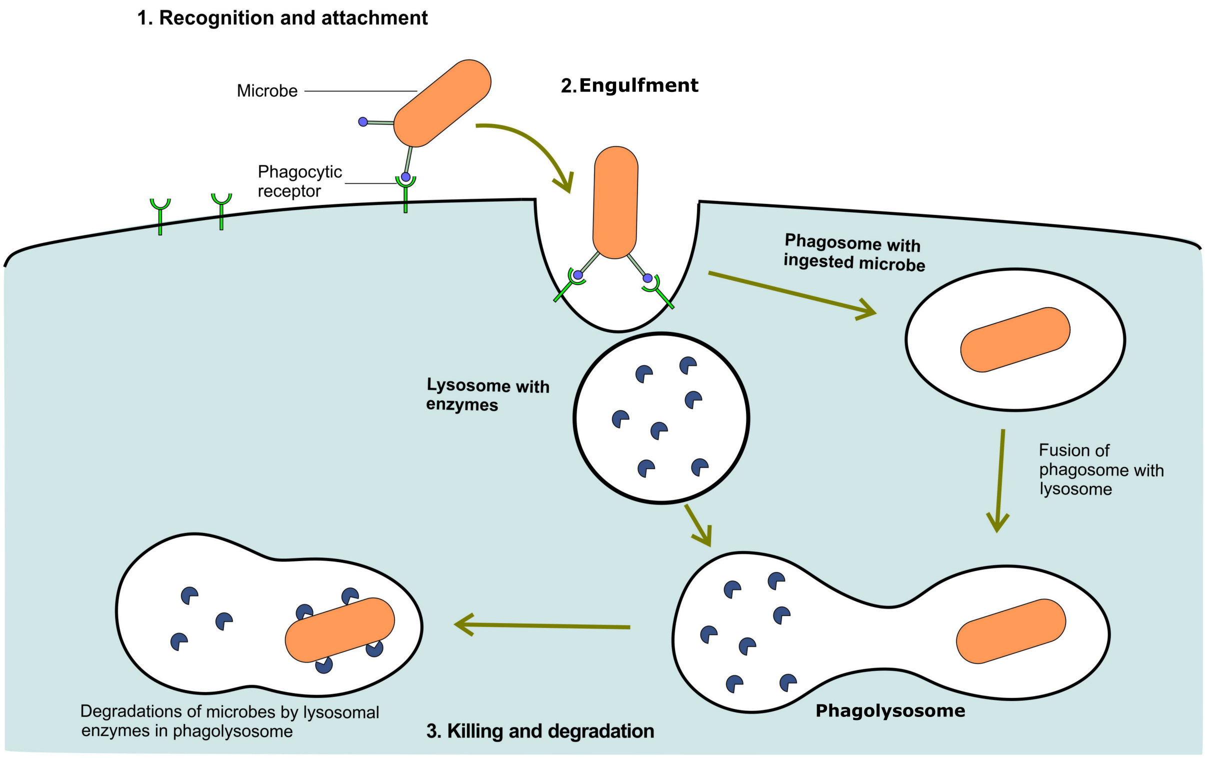

Figure 2.18: Overview of the process of phagocytosis. [56]

After inflammatory activation, acute inflammation can have one of two outcomes. The first consists of the resolution of the acute inflammatory response and restoration of the tissue's function and histology. This involves the death of neutrophils through apoptosis; the degradation of chemical mediators and restoration of basal levels of capillary permeability. Additionally, leukocytes start producing mediators that inhibit inflammation. Eventually, all the apoptotic neutrophils and necrotic tissue are cleared through macrophage ingestion and lymphatic drainage.

Acute inflammation, if not resolved, can give rise to chronic inflammation. This form of inflammation is characterized by: 1. the infiltration of mononuclear cells e.g. monocytes, lymphocytes and plasma cells; 2. tissue damage mostly due to inflammatory cell products; and 3. uncontrolled formation of new vessels (angiogenesis), which results in fibrosis. Additionally, abscesses may form which may result in tissue scarring. Chronic inflammation is present when the inflammatory response targets the host tissue, e.g. in multiple sclerosis, or where it reacts excessively against non-toxic environmental substances, e.g. allergies.

The inflammatory system involves a series of vascular changes and the recruitment of several types of cells. All of the mechanisms require the release of chemical mediators that are already present in the plasma or that are released by cells. The plasma mediators are synthesized in the liver and travel in the plasma as inactive precursors. At the site of inflammation, they are activated. Cell mediators are normally stored in intracellular granules and are released upon cellular activation. There are, a plethora of mediators that might have a singular purpose or they might interact with a variety of inflammatory mechanisms.

All the cells involved in the inflammatory process produce inflammatory mediators; this includes macrophages, leukocytes, mast cells and endothelial cells. The mediators have many different functions that include:

- Inducement of pain and triggering of the inflammatory process e.g. amines (serotonin), neuropeptides, platelet-activating factor (PAF).
- Vasodilation and increase in capillary permeability e.g. amines, neuropeptides and PAF.
- Activation of macrophages e.g. tumour necrosis factor (TNF) and interleukin1 (IL-1).
- Chemoattractant e.g. cytokines, chemokines and leukotrienes.
- Cellular adhesion to the capillary e.g. PAF, TNF and IL-1.
- Platelet aggregation e.g. PAF.
- Microbicidal e.g. ROS, Nitric oxide (NO) and the lysosomal enzymes leaked by leukocytes.
- Inhibitory e.g. NO and Lipoxins.

This is a very superficial overview of the types of mediators released during inflammation and only serves to show the complexity of this system. Here, only the functions of cytokines are explored, as they are the only ones within the scope of the work developed in this thesis.

Cytokines influence many stages of the inflammatory process. Some cytokines are responsible for stimulating the bone marrow to produce more cytokines. Alternatively, there are others that regulate for the communication between leukocytes. The major cytokines are the interleukin IL-1, the TNF and the chemoattractant cytokines called chemokines.

Activated macrophages, mast cells and endothelial cells predominantly produce TNF and IL-1. Their principal role is to stimulate the expression of adhesion molecules, which will increase the binding, and recruitment of leukocytes. Additionally, TNF increases the thrombogenicity of endothelium and causes the activation of neutrophils. The IL-1, in turn, activates tissue fibroblasts. Chemokines are a family of small structurally related proteins that act primarily as chemoattractants for different subsets of leukocytes. These proteins can be very specific and only recruit a particular type of cell to the inflammation site. Furthermore, chemokines, as shown previously, activate leukocytes, which increase the affinity of the leukocytes interleukins to dock to the endothelial interleukins. Chemokines are broken down into four families dependent on the arrangement of their proteins. The two most relevant are the CXC and the CC families, which act primarily on neutrophils and monocytes respectively.

In terms of plasma mediators, three types have been identified: 1. the coagulation system, 2. the Kinin system and 3. the complement protein cascade. The first is ultimately responsible for activating thrombin, which in turn activates platelets and endothelial cells. By binding to endothelial cells they activate them and promote leukocyte adhesion. Additionally, thrombin also increases vascular permeability and is chemotactic for leukocytes. The Kinin system generates bradykinin that like histamine causes the increase of vascular permeability.

The third and final system, the complement protein cascade, is one of the main focuses of this work. This system is involved in many mechanisms such as innate and adaptive immunity as well as tissue regeneration and tumour growth [56]. Proteins, that are numbered from C1 to C9 form it. These molecules travel inactivated in the plasma. These are then activated through three different pathways: alternative, triggered by bacterial polysaccharides and other cell-wall components; classical, which is initiated when protein C1 attaches itself to the antibody-antigen complex; and lectin, which is activated when either mannose binding lectin or Ficolin bind to carbohydrate moieties on the surface of pathogens. In each of these pathways, the proteins are sequentially broken down and agglomerated.

All three pathways converge to the formation of C3 convertase that breaks down C3 into C3a and C3b. The latter deposits at the surface of microbes and further proteins attach to forming a C5 convertase. This convertase breaks down C5 into C5a and C5b. The remaining proteins C6-C9 then attach to C5b to form the membrane attack complex (MAC). The latter complex forms a pore by inserting itself into the cell membrane, resulting in cell lysis [118].

The C3a, C3b and C5a molecules produced by the three pathways are responsible for a variety of functions in the inflammatory process. C3a and C5a increase vascular permeability by promoting mast cells to release histamine. C5a also activates neutrophils and macrophages to release more inflammatory mediators. Additionally, C5a activates leukocytes, increasing their adhesion to endothelium. Also, C5a is a potent chemoattractant agent for neutrophils and monocytes. Furthermore, C3b when attached to a microbial surface act as opsonins augmenting phagocytosis by neutrophils and macrophages. An overview of the discussed pathways and outcomes of inflammatory complemented is presented in Fig. 2.19.

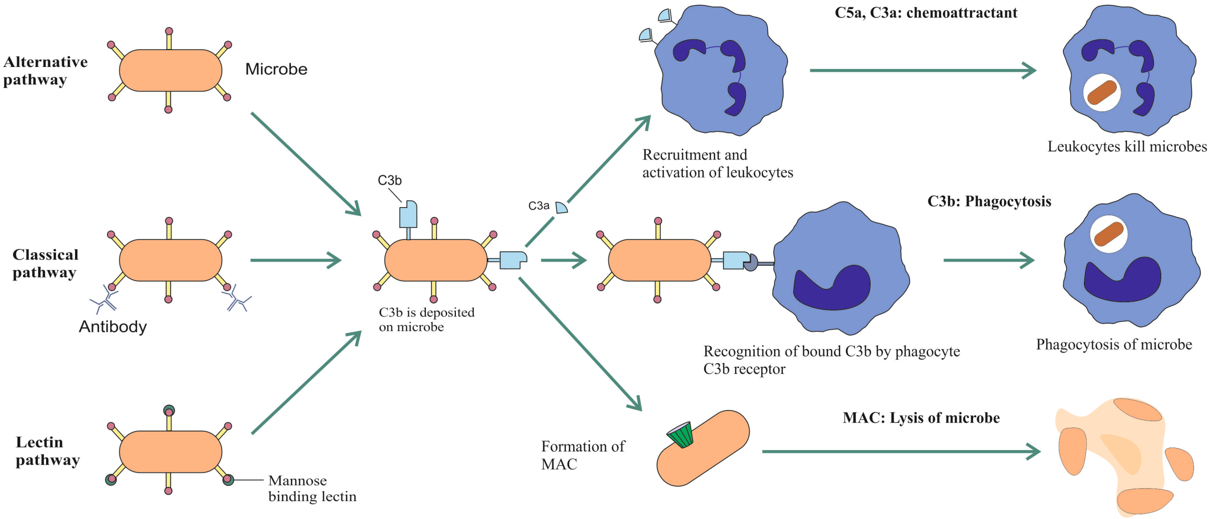

Fig.2.19: Summary of the pathways that activate complement and their possible outcomes. [56]

Due to the complexity of the complement and the potential effects, it can exert there are many mechanisms in place to tightly regulate it. Activation of the complement is regulated by preventing the assembly of C3 convertase or by inhibiting its activity. This is done by a series of decay accelerators that act upon different proteins. The ones currently reported are: DAF; CD55; C4 binding protein (C4BP) and Factor H. In addition, there are chemical agents that inhibit the phlogistic potential of C3a and C5a like C-terminal Arginine. There also chemical mediators that inactivate C3b and C4b by the protease Factor I. Finally, MAC formation is regulated by S protein, which is a plasma glycoprotein, vimentin that is a cytoskeletal protein and CD59 by blocking its formation. The complement pathways and the chemicals that modulate its activity can be seen in Fig. 2.20.

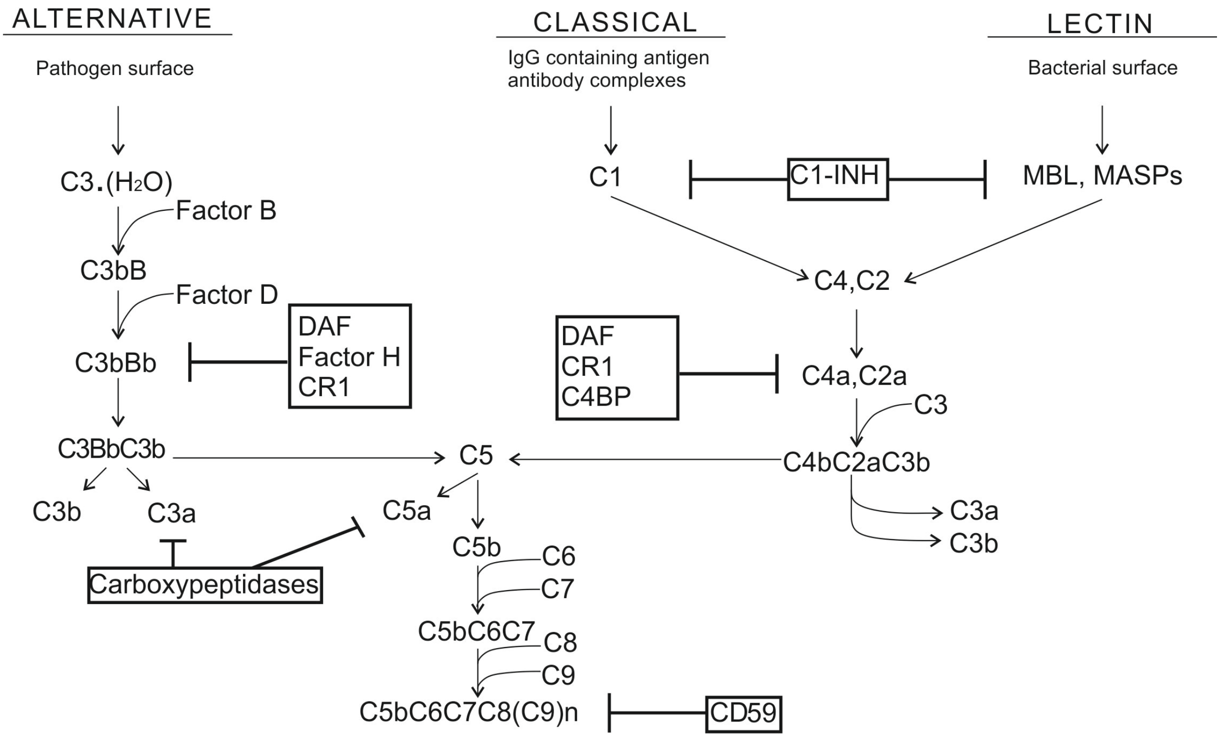

Fig.2.20: Full breakdown of the complement protein cascade. Additionally, the known complement inhibitors are also present**. [118]**

The inflammatory mechanisms explored here are leukocyte and monocyte recruitment and the complement system. However, this is a very simplistic analysis of the inflammatory process as there are many processes (e.g. monocyte activation of monocytes by T-cells, tissue damage by granulomatous inflammation, B-cell function, etc.) that have been omitted as they are beyond the scope of this work.

2.4.2 NMO pathophysiology [45]

NMO is a neuro inflammation disease that has until recently been treated as a more acute form of multiple sclerosis (MS). This occurs because both diseases incur lesions marked by demyelination and macrophage and neutrophil recruitment. However, in 2004 the Mayo clinic identified an antibody specific to NMO, which was termed NMO-IgG. Additionally, NMO has been found to target the spinal cord and the optic nerve more aggressively. Furthermore, the NMO is the first neuro inflammation disease where the antigen has been identified. The antigen was found to be the astrocytic water channel AQP4. Due to this latter finding the antibody has been renamed AQP4-IgG. There are levels of severity of the disease. The severity is evaluated in terms of how frequently lesions are formed. Based on these criteria NMO is characterized as monophasic (when the demyelination events happen once) or it is relapsing. It has been found by [119] that patients that suffer from relapsing NMO had a mean survival rate of 5 years (n=48).

Although severe the disease is rare, having a worldwide incidence of 1 per 100,000. However, when its epidemiology is broken down in some parts of the world it can have a higher incidence than MS. This is the case for African and East Asian countries. Conversely, in white populations MS is approximately 40 times more common than NMO. Furthermore, it has a higher incidence in women than in men as presented by [120] (e.g. in China it has a female to male ratio of 9:1). Moreover, the age of onset is variable with cases having been reported in patients 14 to 55 years old.

In order to clinically distinguish MS and NMO, Wingerchuk *et al.* [121] have developed diagnosis criteria which consist of two sets: absolute (optic neuritis and acute transverse myelitis) and three supportive (brain MRI lesions that do not match MS lesions, T2-weighted spinal MRI with signal abnormalities over more than two vertebra and AQP4-IgG seropositive status). NMO is then diagnosed when patients present both absolute criteria and at least two of the supportive criteria. In addition, there are patients that present AQP4-IgG positive serum (AQP4-IgG$^+$) and those that do not (AQP4-IgG$^-$). In the case of AQP4-IgG$^+$ but not satisfying enough NMO criteria these patients are diagnosed as suffering from a NMO spectrum disease. As the pathophysiology of the disease is better understood the criteria will be updated. Distinguishing between the two inflammatory diseases is clinically relevant as treatments and, more importantly, some treatments that are commonly prescribed to MS patients might exacerbate NMO. This was the case of IFN-β, which was found to increase relapse rate [122] and to promote severe exacerbation of NMO symptoms [123].

The current working hypothesis of the pathophysiology of NMO is that AQP4-IgG permeates the capillary from the plasma into the ECS and binds to the AQP4 channels on the perivascular astrocytic endfeet. This then triggers the classical complement pathway resulting in marked granulocyte and macrophage infiltration. These cells cause secondary oligodendrocyte damage, demyelination and neuronal death. The proposed description of NMO is summarized in Figure 2.21. This hypothesis is supported by the work of [124] where mice were injected alternatively with AQP4-IgG and human complement into brain tissue. It was found that NMO lesions were only formed when both were injected in mice. The same conclusion has also been verified in human studies [121], [125], [126] .

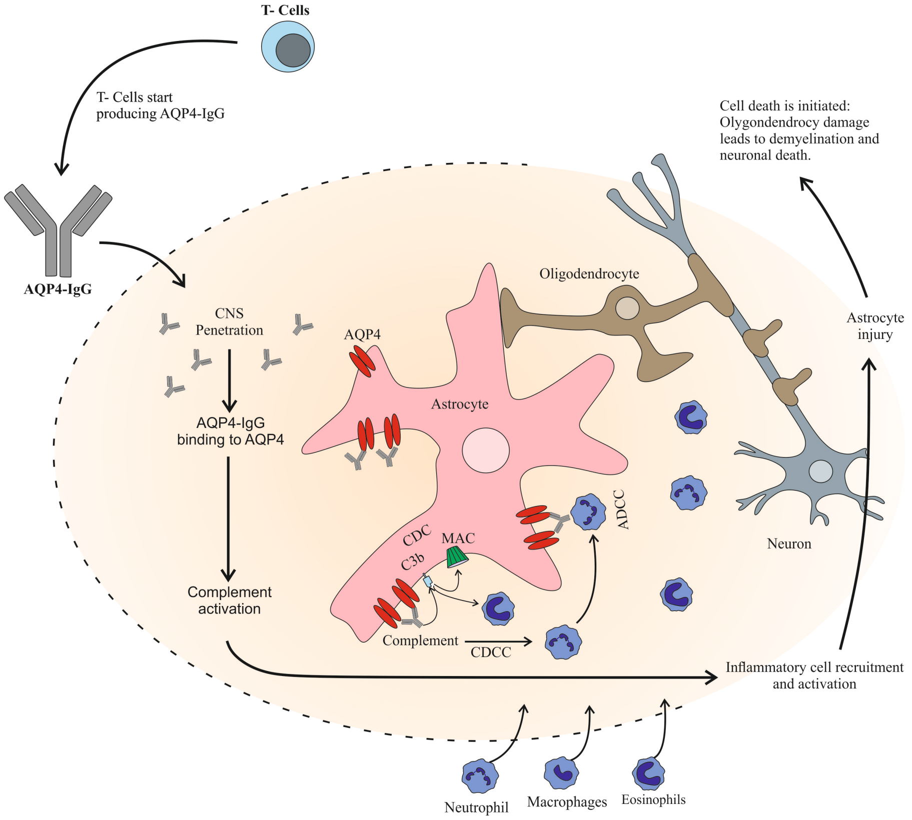

Figure 2.21: Description of the understanding of the pathophysiology of NMO [45].

The pathophysiology of the disease is still being uncovered. However, crucial mechanisms of the disease are still unexplained. In particular the system behind the initial production of AQP4-IgG in patients is not known. Researchers have presented several theories. One speculation is that, as described by [127], a form of molecular mimicry might be involved. This mechanism is here activated by the fact that AQP4 share structural homology with certain bacterial species such as *clostridium perfringens*. Therefore, it is believed that T-cells react as if they are in the presence of a pathogen and start producing AQP4-IgG. Additionally, a viral component might be involved in the pathogenesis of the disease. This has been verified by [128] who found that various viral infections can be associated with the development of NMO during the early stages of the illness.

Another concern about the pathophysiology of NMO is to understand how AQP4-IgG enters the CNS. Evidence shows [126] that the concentration of AQP4-IgG is 500 times more concentrated in the plasma than in the CSF. This suggests that the antibody is produced peripherally and then enters the CNS. Additionally, patients might present AQP4-IgG$^+$ plasma for several years before disease onset. One hypothesis [129] suggests that the AQP4-IgG initially targets the circumventricular organs as these express AQP4 and do not have a BBB. This theory is supported by the observed involvement of areas such as the area postrema and the posterior hypothalamus and the symptoms of nausea, vomiting and uncontrolled antidiuretic hormone [45].

The reason for why the disease predominantly targets the optic nerve and the spinal column is less understood. Both structures have a BBB, which in theory should prevent the presence of AQP4-IgG. It is hypothesized that the BBB might not be fully developed in the preliminary portion of the optic nerve and in the root entry zones in the spinal cord. Therefore, it is easier for the AQP4-IgG to traverse the BBB in these areas compared to elsewhere in the CNS. A further explanation for why these two areas are targeted is that inflammation in these regions precedes the movement of AQP4-IgG. This hypothesis has been suggested by [128], [129] and has shown that 25-33% of patients had experienced viral infection at the spinal cord and optic nerve prior to the NMO onset.

The PNS also expresses AQP4 channels, however only the CNS experiences NMO lesions. Several reasons for this differentiation have been presented. Firstly, as shown by [130]–[133] AQP4-IgG has a higher tendency to bind to M23-AQP4 than to M1-AQP4, also there is a higher expression of M1-AQP4 than M23-AQP4 in the PNS and therefore this might explain the preferential CNS targeting; secondly, the negligible importance of AQP4-expressing cells for tissue function in the PNS compared to the astrocytes in the CNS. Finally, there is a low concentration of AQP4 in the PNS compared to the CNS. All of these are theoretically reasonable, however, there has yet to be any supporting evidence to justify them.

An alternative justification is that there might be a reduced concentration in complement regulating proteins (CD55, CD59) in the astrocyte foot processes compared with the peripheral AQP4-expressing cells. Therefore, the latter would have a higher resistance to complement-dependent cytotoxicity. Furthermore, the reason for the lack of lesions in the PNS might simply reside in the fact that there is an absence of cells involved in the neuroinflammatory process, e.g. microglia.

When antibodies bind to antigens this induces several effects: modification of the target's function; target internalization; reducing surface expression; complement activation and potential cell death by complement dependent cytotoxicity and activation of effector cells such as natural killer cells which can lead to cell mediated cytotoxicity. In the case of AQP4 and AQP4-IgG, some of these effects have been reported. In a study by [133], antigen-antibody binding was observed to impair AQP4 permeability. However, a study by [132] in mice found no impact on AQP4 permeability.

Internalisation has also been reported in response to AQP4-IgG and AQP4 binding using HEK293 cells. Conversely, when using mouse cortical astrocytes cultures little to no internalisation was reported. The most dramatic effect of antibody-antigen binding is complement activation. This is evidenced by [17] where it was reported that NMO lesions in rat brains were only formed when human AQP4-IgG and complement were injected into the CNS. Therefore, complement cytotoxicity is probably the major mechanism by which NMO develops.

Despite the strides in understanding the disease in AQP4-IgG^{+} patients the lesions formed in AQP4-IgG^{-} patients are harder to explain. Evidence shows that seropositive NMO differs clinically and epidemiologically from the seronegative disease – more severe clinical attacks, higher spinal cord lesions and more frequent relapses. Additionally, the sensitivity of human leukocyte antigens in seronegative patients is more closely related to MS than the seropositive disease. Another possibility for the presence of the lesions is that the assays used to detect AQP4-IgG are not sensitive enough to identify the low concentrations present in seronegative patients. This has been shown in a series of cases where patients were diagnosed as presenting AQP4-IgG plasma [134]. Additionally, antigens might be targeting a different structure of the astrocyte. Therefore, there might be other antibodies that trigger NMO. A study by [130] has reported on the presence of IgG antibodies that can mediate complement dependent cytotoxicity in AQP-IgG^{-} disease. In addition [130] also found that the patients experienced optic neuritis, longitudinally extensive transverse myelitis, MS and lupus. The compiled literature points to the fact that seronegative patients are being misdiagnosed. Perhaps these patients fall into a heterogeneous group that includes patients with MS, seropositive, some that have the disease triggered by other antibodies and some whose disease is not antibody mediated.

Current treatments are prescribed based on two consensus papers published by panels of experts in the field [135], [136]. The overall approach to treat NMO is to minimize and ameliorate the neurological damage caused by acute attacks and to reduce the frequency of attacks. Clinically, the therapies offered aim at mitigating the damage caused by acute attacks. The most common treatments prescribed are intravenous methylprednisolone (IVMP) and plasma exchange. These are treatments that have been commonly prescribed to patients that suffer from MS, transverse myelitis and optic neuritis. IVMP is a corticosteroid, which has several anti-inflammatory effects that include the reduction of plasma concentration of lymphocytes and monocytes; decreased expression of cell adhesion molecules and altered transcription of pro-inflammatory cytokines [137]. In the case of NMO, cytokines such as IL-17A, IL-6 and IL-23p19 are down regulated by corticosteroids [138]. Plasma exchange, in turn, has been shown to reduce the concentration of AQP4-IgG in the plasma as well as cytokines and T and B cells [139].

The general prescription of these treatments follows the protocol of delivering IVMP for 3-5 days and then, if symptoms persist, plasma exchange is administered. Retrospective studies have shown that patients experienced marked recovery in terms of visual and neurological function [140], [141]. However, these studies were performed without considering if the patients were AQP-IgG$^+$ [141].

In terms of preventive therapies, the strategies considered aim to: deplete immune cell populations; diminish circulation of AQP4-IgG; and interfere with immune cell proliferation or activation. The most successful strategies consist of administering azathioprine (a study with n=99 of NMO or NMOSD patients found that patients experienced a reduction in annualized relapse rates (ARR) from 2.20 to 0.52 [142]), mycophenolate (n=24 reduction of ARR from 1.28 to 0.09 [143]) and rituximab (n=23 reduction of ARR from 1.87 down to 0 [144]). All these strategies target lymphocytes without consistent effects on AQP4-IgG.

Further therapies have been tested. These include methotrexate (n=14 of NMO and NMOSD experienced an ARR reduction from 1.39 to 0.18 [145]), mitoxantrone (n=20 of NMO and NMOSD patients had an ARR reduction of 2.8 to 0.7 [146]) and cyclophosphamide (n=4 with NMOSD had an expanded disability status scale (EDSS) reduction from 8 to 5.75 [147]). However, the latter treatments might be found to be toxic to some patients.

As the pathophysiology of the disease is now better understood, researchers have proposed treatments that target specific mechanisms of NMO. In particular there are several therapies currently prescribed for other conditions that might be repurposed for NMO. This is the case for complement inhibitors. As previously discussed, complement activation appears to be an integral part of the pathology. A C5 inhibitor is commonly used when treating diseases like paroxysmal nocturnal haemoglobinuria called eculizumab. It is a humanized IG2/4 antibody that binds to C5 preventing cleavage into C5a and C5b. This inhibitor was given to 14 NMOSD patients and it was found that ARR dramatically reduced and it stabilized or reduced EDSS levels [148].

Another pathological NMO target that has been considered is interleukin-6 (IL-6). In clinical trials humanized murine has been found to act as an anti-IL-6 receptor monoclonal antibody in patients. Several studies have reported a reduced relapse rate [149]–[151].

Furthermore, treatments are being proposed whose target is the function and recruitment of inflammatory cells. Two types of cells have been targeted: neutrophils and eosinophils. For the latter, silvelestat has been proposed, which has been approved for the treatment of acute respiratory distress in Japan [152]. Reports have shown that it is an inhibitor of neutrophil elastase [153], which can potentially reduce neutrophil recruitment and tissue damage [154]. Eosophils, in turn, are cells that have been found in demyelination lesions in NMO, which is in contrast to MS lesions where they are absent. Eosibophil inhibitors can be found in second-generation antihistamines cetirizine and ketotifen. These two components were found to greatly reduce cytotoxicity mediated by AQP4-IgG and eosinophils [155]. Therefore, finding agents that reduce the number and activity of these cells might be a good avenue to mitigate the symptoms of NMO.

Intravenous immunoglobulin (IVIg) is a therapy commonly prescribed to treat many immune-mediated demyelinating diseases of the nervous system (e.g. multifocal motor neuropathy, diabetic polyneuropathy, myasthenia gravis [143]). It consists of injecting patients with IgG antibodies taken from more than 1,000 blood donors [156]. This therapy has been found to act on several inflammatory mechanisms including: autoantibody neutralization; blockage of antibody binding sites; acceleration of antibody clearance; inhibition of dendritic cell activation and leukocyte migration; complement inhibition and blocking of Fcγ receptors [143]. When applied to an NMO context it has been found to reduce ARR from 1.8 to 0.006 (n=8, P= 0.01) [157].

Besides appropriating current therapeutic procedures applied to other diseases the singular mechanisms associated with the disease might be exploited. At all the stages of the pathophysiology therapies have been proposed to modulate the disease. The disease trigger is believed to be by AQP4-IgG and AQP4 binding. Therefore, researchers have hypothesized that if this antibody and antigen are prevented from binding it will reduce tissue damage by complement dependent cytotoxicity (CDC) and antibody dependent cell-mediated cytotoxicity (ADCC). Two components have been proposed. The first is called aquaporumab and it is generated from a recombinant monoclonal AQP4-IgG. This agent competitively displaces AQP4-IgG in the serum of patients with NMO. Aquaporumab has been tested *in vitro* and *in vivo* and has been found to greatly reduce ADCC and other aspects of the NMO pathology [158].

Alternatively, by screening several target based molecules for their affinity to AQP4 potential drugs and natural products that reduce AQP-IgG binding to AQP4 have been identified (e.g. arbidol and neutraceutical berbamine [159]). However, further research is required as the compounds identified have a relatively weak affinity to AQP4 and unfavourable pharmacological properties for use in NMO.

Another potential therapeutic strategy is antibody inactivation. There are several bacterial enzymes that selectively target IgG-class antibodies. Some of these enzymes disable the complement binding site such as the C1q, consequently, neutralizing the Fc-effector function that is involved in CDC. Additionally, they also target the Fcγ receptor, which is involved in ADCC. Examples of these compounds that have had success in an NMO context *in vitro* and *in vivo* were found in endoglycodiase S (EndoS) [160]. After acting on AQP4-IgG it was found to displace pathogenic AQP4-IgG, therefore converting the antibody into a therapeutic blocking agent.

Another enzymatic bacterium derived from S pyogenes enzyme (IdeS) has been found to degrade IgG. It selectively cleaves IgG antibodies into Fc and Fcγ fragments. When applied in an NMO environment it was found to abolish CDC and ADCC *in vitro* and NMO pathology *in vivo* [161].

Besides inhibiting C5 the complement protein cascade can be targeted at many other stages. Furthermore, C5 inhibiting eculizumab has been found to induce infection. This is hypothesised to occur because besides the desired inhibition of the classical complement pathway eculizumab also inhibits the alternative and the lectin pathways [162]. Consequently, the body loses an essential anti-bacterial mechanism. Therefore, inhibitors that target the complement classical pathway have been proposed. C1-inhibiting antibodies have proven to be effective in both *in vitro* and *in vivo* NMO models [160]. Furthermore, they have several therapeutic effects: they prevent the generation of C3a and C3b, which participate in CDC and block the mechanisms of classical pathway amplification part of the alternative pathway.

In addition, the complement cascade can be blocked at the levels of MAC formation. The most common inhibitor of this nature present in astrocytes is the CD59 protein. This complement inhibitor binds to either C5b-8 or C5b-9 blocking the addition of further membrane piercing C9 proteins. Its function is illustrated in Fig.2.22. Several diseases have been found to be induced by the lack of CD59 and other MAC regulating proteins such as membranoproliferative glomerulonephritis and dense deposit diseases [45]. In two proof of concept studies, it was found that following deletion or neutralization of CD59 the severity of the disease increased substantially [163], [164].

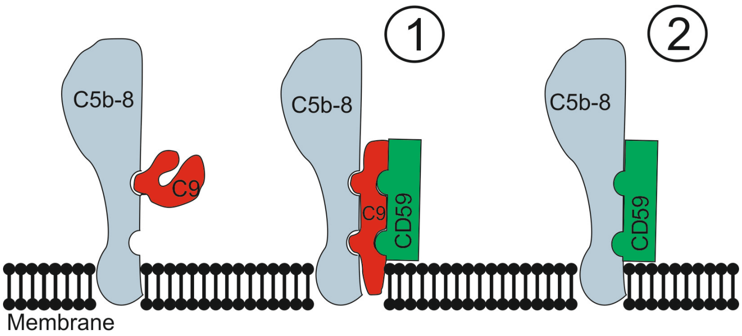

Figure 2.22: Diagram that explains how CD59 inhibits the formation of MAC complex [165].

All previous therapies focus on the cellular mechanisms involved in CDC. Researchers have also focused on trying to mitigate ADCC. The latter mechanism is triggered when AQP4-IgG binds to the Fcγ receptor on effector cells. This results in phagocytosis and degranulation of the cell. Moreover, this mechanism has been found to not only be responsible for cell death but also to act as a trigger for the pathophysiology of NMO [166]. In mice models of NMO, it has been found that neutralizing the Fcγ receptor antibody reduced NMO pathology [167].

Within the ADCC mechanisms, another structure that might be a potential therapeutic target is the BBB. Although the mechanisms behind the BBB disfunction during NMO are not clear, an increase endothelial growth factor (VEGF) has been detected. A clinical trial is currently under way, trying to understand if VEGF inhibitor is able to reduce the BBB opening due to NMO [168].

Finally, as the antibody that triggers the pathology is known one might envisage the development of antigen tolerance against AQP4. This can be done through a series of methods including DNA vaccination, altered peptide ligands, and low dose oral and nasal antigen administration. Similar studies have been developed in the context of MS. These have proven unsuccessfull due, in part, because a disease specific antigen and antibody are not known. Therefore, NMO presents a unique oportunity and this practice might yield more-substantial clinical and immunological effects.

With the same aim of generating antigen tolerance against AQP4, the use of haematopoietic stem cell transplantation (HSCT) has been proposed. This procedure has shown great promise when applied to MS [169] and systemic lupus erythematosus [170]. However, this procedure has been found to be risky with considerable mortality rate.

From this analysis, it has been shown that there is a plethora of strategies that have been proposed to try to mitigate the symptoms of NMO. Nevertheless, there are many challenges that clinical trials need to overcome in order to develop effective NMO therapies. Firstly, NMO has a high mortality rate and therefore impedes the compilation of a longitudinal study. Secondly, establishing therapeutic success criteria has proven difficult. Thirdly, although severe, the disease is rare and therefore a combined effort between labs is required. Finally, there are ethical concerns to take into account when considering the placebo arm of the trial. In Figure 2.23 an overview of the state of the art of NMO drug development described can be found.

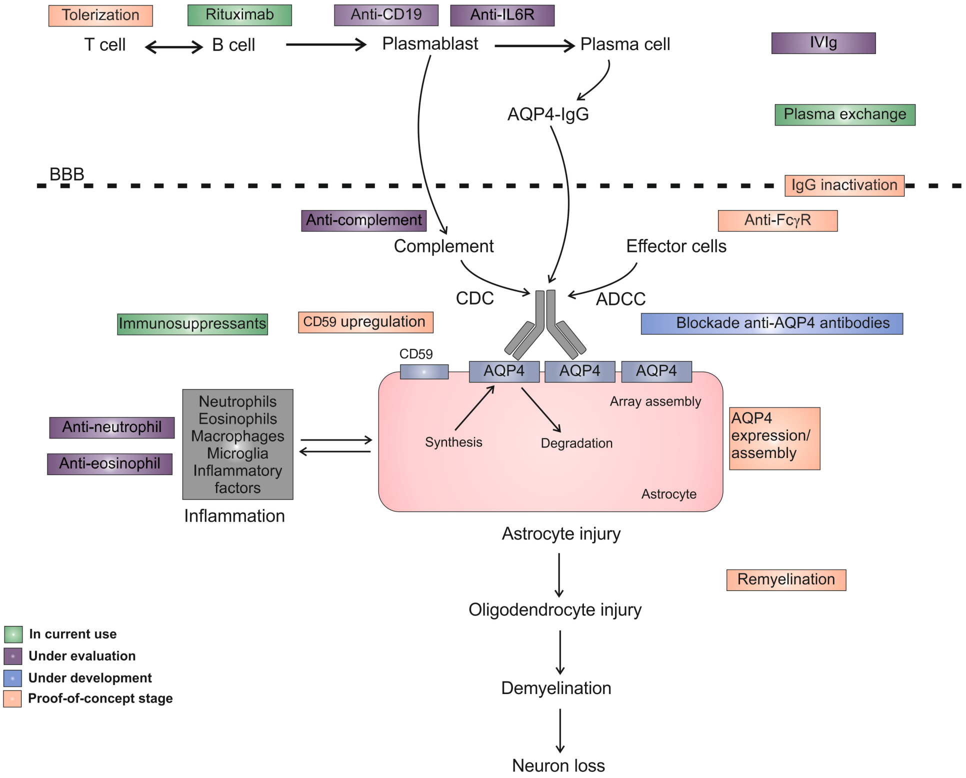

Figure 2.23: Overview of all proposed therapies for NMO, which pathological mechanism they target and their stage of development [45].

2.4.3 Chemerin role in inflammatory resolution [171]

The inflammatory process aims at the removal of harmful stimuli such as pathogens. Then all the cells recruited and the debris formed needs to be removed in order to restore normal function of the tissue. Until recently it was thought that the restoration process occurred passively. Experimental proof has been compiled that shows that there are endogenous anti-inflammatory mechanisms that ensure an appropriate inflammatory response and resolution. Additionally, this could suggest that chronic inflammation might develop, in part, due to the absence or malfunction of this pro-inflammatory resolution pathway. Therefore, understanding the endogenous anti-inflammatory systems might aid in the understanding of pathologies as well as guiding novel therapeutic pathways.

Several agents are involved in modulating the anti-inflammatory pathways: gaseous mediators; protease inhibitors; lipids that include resolvins, protectins, maresins and cyclopentenone prostaglandins; proteins and peptides. The work here presented focuses on the pro-resolving mechanism that involves a subset of membrane anti-inflammatory G protein receptors (GPCR) called ChemR23 and the mediators that activate it, which are chemerin peptides.

Chemerin is a chemoattractant protein that is found in the circulation and in inflammatory exudates. It is inactive when secreted. In order to generate the active chemoattractant proteins, it needs to undergo C-terminal proteolytic cleavage, which is performed by serine proteases. The enzymes responsible for the cleavage include those of the coagulation (factor VII) and fibrinolytic (plasmin) cascades and those derived post-neutrophil degranulation (elastase and cathepsin G) [172]–[174]. Chemerin has many functions as it acts as a plasmacytoid dendritic cell, as a natural killer cell and macrophage (MΦ) chemoattractant. The work here presented focuses on the chemoattractant capabilities of chemerin. Besides the ChemR23 GPRC, it also can bind to chemokine (C-C motif) receptor 2 (CCRL2). The latter is a chemokine receptor present on activated MΦ. The binding of chemerin to each of the mentioned has receptors is yet to be found. However, the synthesized chemerin-derived peptide C15 has been found to mediate MΦ behaviour through the ChemR23 receptor. C15 has been found to have several anti-inflammatory effects including: inhibits MΦ activation; suppressing neutrophil and monocyte recruitment and inhibiting expression of pro-inflammation cytokines and chemokines [171].

Importantly, C15 contributes to the MΦ clearance of apoptotic neutrophils and microbial particles. They recognize phagocytosis and kill microbial agents. Efficient clearance of pathogenic material by MΦ is important in limiting the duration and extent of the inflammatory response [171]. However, MΦ secretes and activates pro-inflammatory cytokines when identifying and engulfing microbial particles. Conversely, when MΦ ingest apoptotic cells they do not release pro-inflammatory mediators. In fact, it has been associated with suppression of pro-inflammatory mediators and up-regulation of anti-inflammation mediators such as TGF-β [175], [176], [177], [178]. Therefore, inefficient clearance of apoptotic cells promotes a persistent state of inflammation as seen in atherosclerosis and diabetes [179]–[181].

The interaction between C15 and ChemR23 is further evidenced by the work of [71], [182]. Here it was shown that ChemR23$^{-/-}$ cells and mice are unresponsive to the peptide. However, conclusive proof of the hypothesized C15 effects has not yet been presented [183], [184]. Furthermore, the work by [183] has not been able to reproduce any of the data obtained with C15. Instead, it concluded that C15 did not displace chemerin from its binding site on ChemR23. Therefore, a more complex model is required to explain this anti-inflammatory mechanism beyond the one ligand one signal hypothesis. Three alternative scenarios have been proposed by [184]: 1. C15 binds to an alternative and the yet unidentified site on a ChemR23 alternative to that of chemerin; 2. C15, in fact, displaces chemerin and it interacts with other GPCR residues triggering other signalling pathways; and 3. another CPCR could heterodimerize with ChemR23 and hence allow binding of C15 without fully diminishing the ChemR23 downstream effects.

From this analysis two main questions have arisen: 1. does chemerin get naturally cleaved into C15?; and, 2. what is the exact mechanism by which C15 exerts its effects on ChemR23? A better understanding of this pro-resolving pathway might suggest further therapeutic targets for chronic inflammation. In Figure 2.24 the hypothesized C15 synthesis and effects on MΦ behaviour are presented.

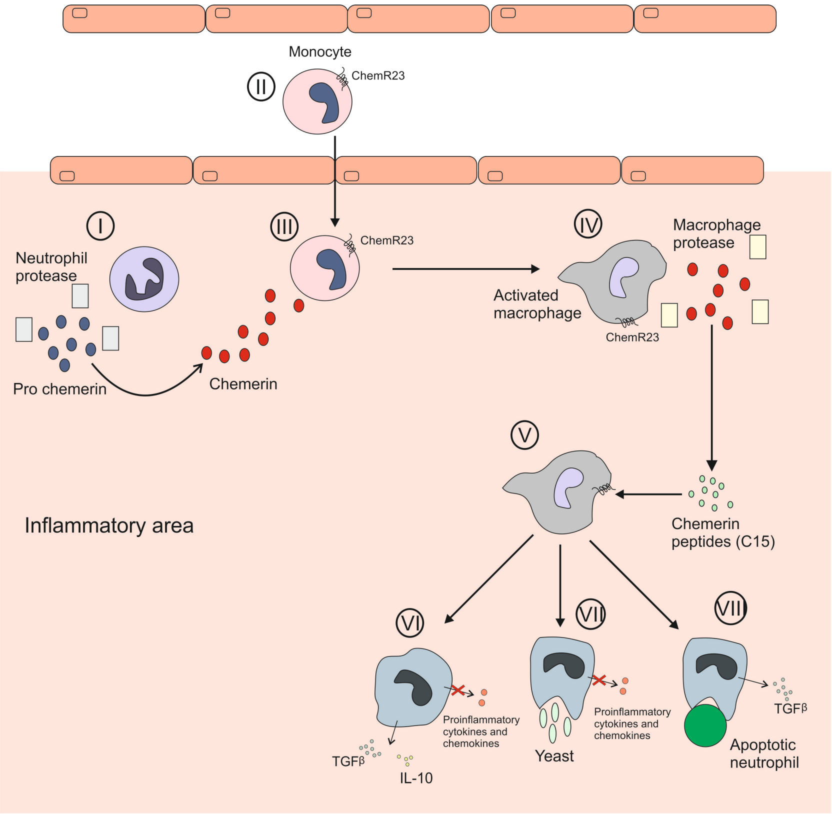

Figure 2.24: The hypothesized pro-resolving pathway where macrophage ingestion of apoptotic cells and release of anti-inflammatory cytokines are promoted by the activation of the ChemR23 receptor by chemerin peptide C15. [171]

2.5 Summary

In this chapter, an overview was presented of the mechanisms responsible for cell death in a pathological environment: excitotoxicity, peri-infarct depolarization inflammation apoptosis. Throughout the analysis made across vascular diseases (ischaemic stroke) and inflammatory diseases (NMO), these mechanisms have been identified. Additionally, several avenues for treatments for these diseases were presented that aim at mitigating and preventing these mechanisms.

Although, in many cases, the pathological mechanisms of the diseases are known, testing these and investigating new treatments have proven to be difficult. The main reasons for this has to do with its location; it sits inside the skull. Furthermore, in order to treat these diseases, it is required that the therapy does not perturb the pressure and blood flow mechanisms of the brain. Finally, some of the diseases that have the harshest symptoms have a low incidence rate. For all the reasons, it is hard to develop experimental studies that will achieve reliable results.

Here an alternative approach is presented where mathematical modelling is used to test theories for neurological pathologies and to test therapies. In the following chapter the literature that was the basis for the mathematical models developed is presented.

Chapter 3

Literature review: Mathematical modelling

The work developed here aims at creating mathematical models of complex biological contexts, such as ischaemic stroke and neuronal inflammation, that are poorly understood and have little data to characterize them. Therefore, the whole endeavour can be contested. To justify the approach chosen section 3.1 presents a critical analysis of mathematical modelling underlining the limitations and strengths of such an approach.

Although this works aims at covering a variety of pathologies the cellular death mechanisms e.g. oedema and inflammation, are shared between them. In this chapter, the individual mechanisms are thus presented. The following sections of this chapter will be divided into the three areas that the work created falls into. Section 3.2 examines the literature behind all the models that were combined to create the glutamate release model. Section 3.3 covers the state-of-art in terms of models of astrocytic water regulation (3.3.1) as well as complement lysis (3.3.2). In section 3.4 the existing models on neutrophil and monocyte recruitment in an acute inflammation context are presented and compared. Finally, this chapter also outlines the available methods and software packages for the creation of the models developed in Section 3.5.

3.1 Introduction

The work here presented aims to test hypothesis for the pathophysiology of neurodegenerative diseases. Many experimental procedures have been able to identify many of the triggers and pathological pathways for these diseases, as presented in chapter 2. However, these diseases present particular barriers for experimental models to effectively evaluate them. There are difficulties in developing reliable a reproducible *in vivo* and *in vitro* model. Additionally, compiling statistically significant numbers of patients is difficult and costly [185]. Mathematical modelling has an opportunity to aid the development of this research in order to avoid the unethical process of sacrificing large numbers of animals and exposing patients to placebo tests [186].

Mathematical modelling has proven to be a valuable tool to evaluate several biological systems at a variety of scales. In the particular case of brain physiology, there are examples of models since 1950's e.g. the Hodgkin and Huxley work on action potentials and ion movement [63]. Hodgkin and Huxley started by first measured the electrical capacitance of the membrane of the neuron to ions during stimulation. Then they assumed that the behaviour of the membrane could be modelled as an electrical circuit with a capacitor and three parallel series of batteries and resistances. Each battery describes the driving current for Na^+, K^+ and a leak current as calculated by the Nernst equation while each resistor represents the conductivity of the membrane to each ion.

With such a model, it was possible to simulate a variety of behaviour in the squid as well as neurons in general. Hence, through the process of using known physical and chemical equations allied to boundary conditions taken from the data, Hodgkin and Huxley were able to derive features of action potentials [187]. However, Hodgkin and Huxley have contradicted such a conclusion by stating that: "An equally satisfactory description of the voltage clamp data could no doubt have been achieved with equations of very different form, which would probably have been equally successful in predicting the electrical behaviour of the membrane.". Therefore, even in one of the most successful cases of the mechanistic approach to mathematical modelling of physiology, the concern is set if the model should be taken only as a data summary or is it a predictive tool and a heuristic guide to future theorizing [188]. Craver in his work "Physical Law and Mechanistic Explanation in the

Hodgkin and Huxley Model of the Action Potential" argues that it is all of the above.

The main concern then is if the equation and all the parameters chosen are all required and if they are biological sound. With current developments in mathematics, a phenomenological approach (black box approach) could have been applied and a model would be developed that has all the benefits presented without having to justify the choices of equations [189]. In this context, the mechanistic approach has proven, as it is demonstrated in Section 3.2.2, that from the equations derived by Hodgkin and Huxley researchers have been able to characterize and identify a variety of cellular behaviour.

The benefits of building upon validated have been established. Currently, there are databases, such as Biomodel Database [190], that promote the exchange and aggregation of mathematical models of physiology. Additionally, there is the project Virtual Physiological Human (VPH) that aims at the development of multi-scale models and to promote the exchange of data between research groups [191]. However, this approach raises further concerns that have been characterised by Brown and Sethna as "sloppy" models [192].

These models are defined by Brown and Sethna [192] as having: 1. a large number of poorly determined or completely unknown parameters; 2. simplified dynamics that is a form of coarse-graining and 3. murky topology due to lack of knowledge of underlying kinetics that has yet to be discovered or measured. Although, computational modelling is seen as an invaluable tool for understanding physiology the prediction of models cannot be trusted if they rely heavily on the uncertainty of parameters.

This characteristic of mathematical modelling has been found to be present in a variety of contexts by Gutenkunst *et al*. [193]. The later work looked at 17 system biology models from the literature and examined the sensitivity of the model to parameter changes. All these models appeared to demonstrate "sloppy" parameter sensitivity. Furthermore, Gutenkunst *et al*. [193] state that common strategies to overcome this limitation of mathematical modelling are unproductive e.g. focusing on measuring precise values for parameters. They have found that for parameter measurement to be efficient they must both be very precise and complete. This is further expanded on the work by Apgar *et al*. [194], which states that the perturbation of the experimental procedure used is intimately linked to the success of parameter estimations. Gutenkunst *et al.* [193] suggest that researchers should focus not on the quality of the parameter values but try and perform collective parameter fits to different sets of data and focus on the quality of predictions of the model.

The work developed aims at capturing complex pathological behaviour with little data and uses models with a large number of parameters. Therefore, they are prime candidates for “sloppy” behaviour. However, these are models of pilot studies to address novel contexts and new hypotheses. Additionally, all the assumptions made to develop the model are clearly presented. Furthermore, as described in Section 3.5.3 and 3.5.4 efforts were made to present the parameters to which the models are most sensitive to and methods used to reduce the number of parameters by reducing the models to its essential components. Through this methodology, it is proposed that these models answer the questions within their contexts, which of course will constrain their scope. From their results, the limitations of the models are presented and experimental procedures to improve the model suggested.

3.2 Modelling glutamate excitotoxicity

To model glutamate excitotoxicity a series of well-founded areas of literature were combined, which are here described. These include: cellular metabolism (Section 3.2.1), cellular ionic regulation (Section 3.2.2) and the glutamate cycle (Section 3.2.3). Additionally, the only known model of glutamate release during a stroke is analysed in Section 3.2.4.

3.2.1 Metabolism mathematical models

Cellular metabolism has been thoroughly described under homeostatic conditions. This is the process by which cells transform glucose into adenosine triphosphate (ATP), which is the main source of energy for cells. This process involves two main reactions: glycolysis and the Krebs cycle also called the Citric acid cycle. The former occurs in the cytoplasm while the latter occurs inside the mitochondria. A full breakdown of the healthy cellular metabolic mechanism is given in Figure 3.1.

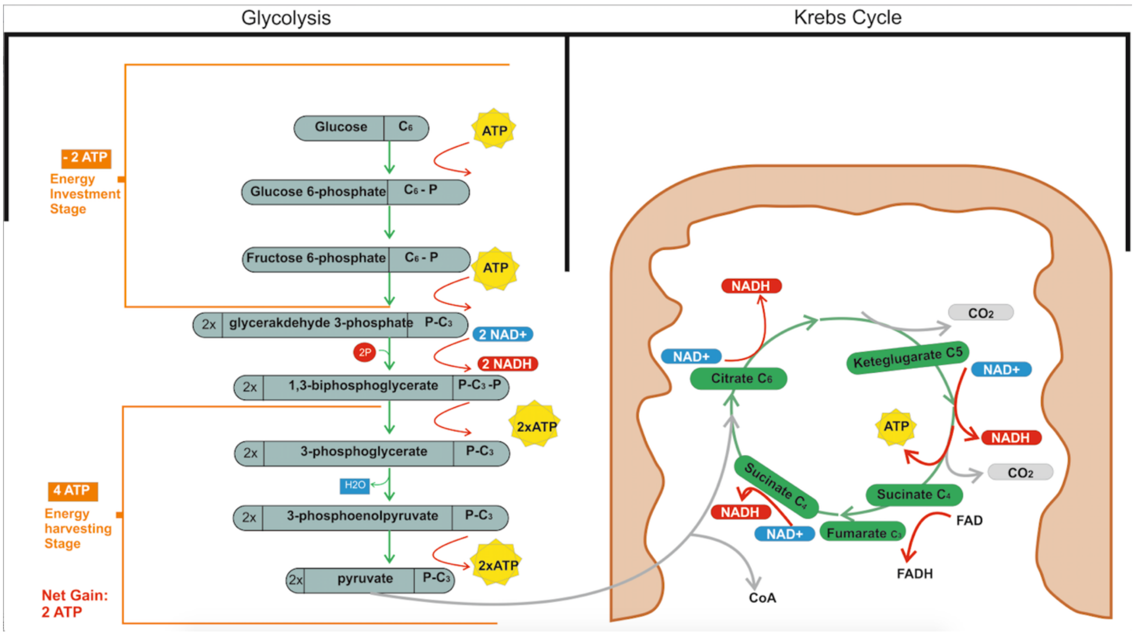

Figure 3.1: Diagram that presents the different reactions involved in both glycolysis and the Krebs cycle [56].

Maintaining sufficient levels of ATP is essential to ensure the proper functioning of cells. Therefore, cells have developed ways of energy storage and alternative forms of ATP production in order to survive periods of glucose starvation [195], such as the case of ischaemia. In this particular case of the brain, there is a mechanism that involves both neurons and astrocytes. The latter is able to store the product of glycolysis, glucose-6-phosphate, in the form of glycogen. Then when there is neuronal energetic requirements glycogen can be converted back to glucose-6-phosphate. Instead of going through the Krebs cycle to produce ATP, then is converted into lactate. It is hypothesized that the lactate is then transported through the lactate shuttle to the neuron where it is used to produce ATP. The glycolysis/lactate shuttle hypothesis is presented in Figure 3.2.

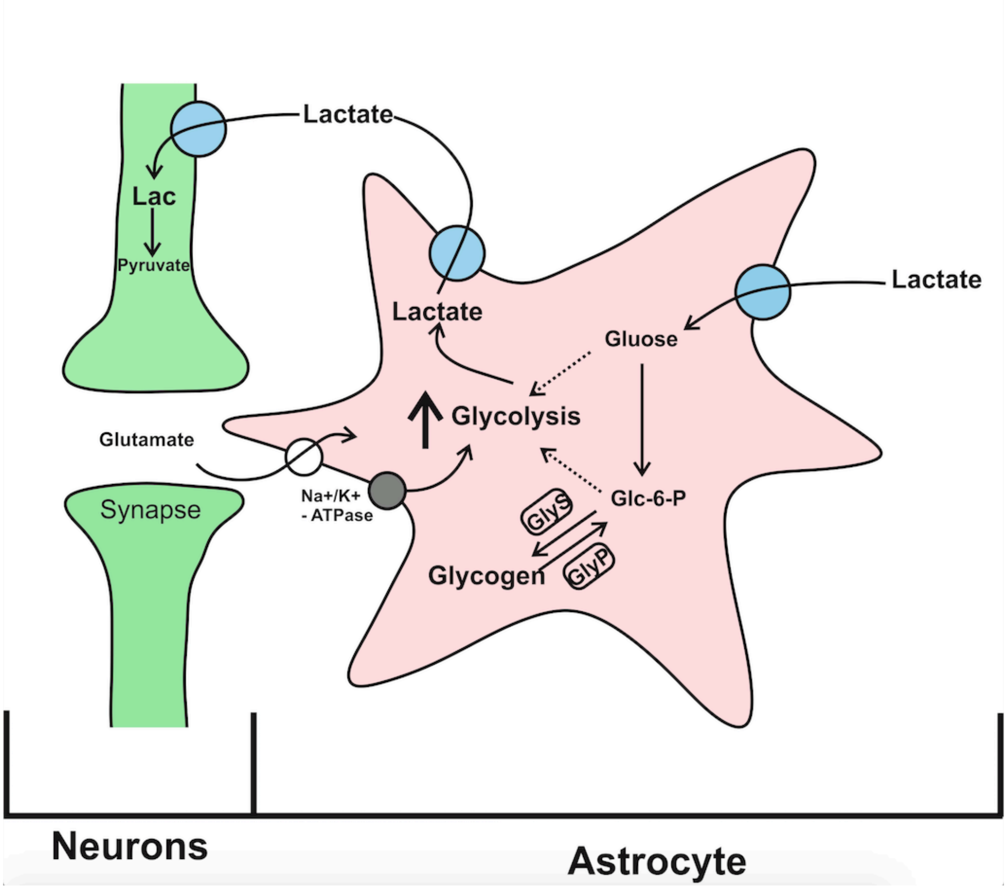

Figure 3.2: Diagram of the lactate shunt between astrocytes and neurons based on the work by [195].

In the literature, the models available vary depending on the context considered and the data available. This is because it is a highly complex process with several mechanisms that will have relative importance dependent upon on the aim of the model. Therefore, the literature is populated with models with a variable number of ODE's and compartments. Here, a focus is made on models that consider both astrocytes and neurons.

The work by Aubert and colleagues in the period 2001-2005 [62], [196], [197] has been the basis for the state-of-the-art models on the metabolic interactions between astrocytes and neurons. A diagram of the 2005 model is shown in Figure 3.3 taken from [197].

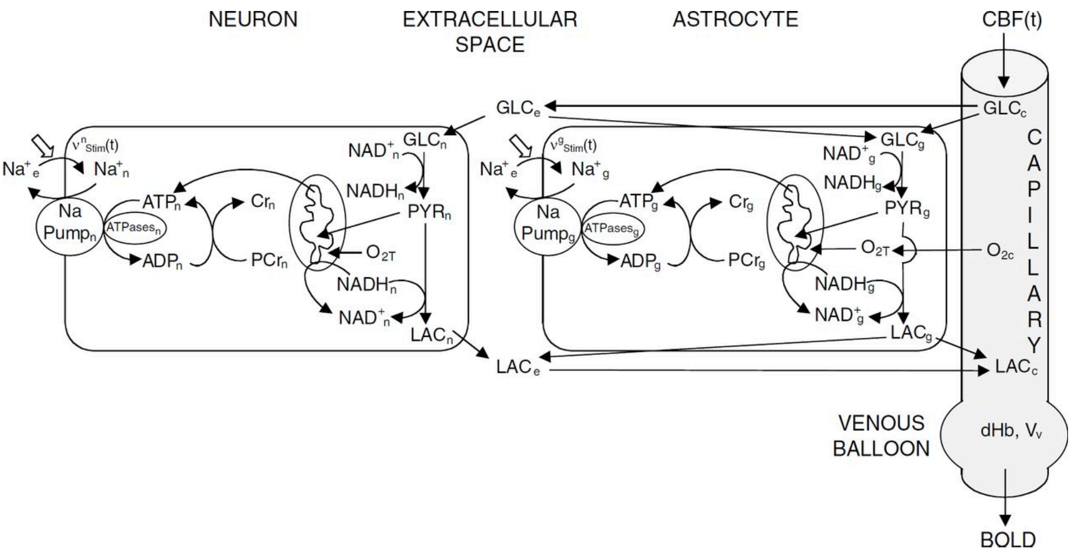

Figure 3.3: Diagram of the compartmental model by Aubert and Costalat [197].

This model includes 4 compartments: astrocyte, neuron, ECS and the capillary. This model is used to understand the importance of the lactate shuttle in the context of metabolic requirements of neurons during stimulation (v^n_{stim}). It considers all the currently known equations of the glycolysis process of cellular respiration. The Krebs cycle is instead simplified to the reduction of Nicotinamide Adenine Dinucleotide (NAD) into $NADH$ required for the production of ATP from Adenosine Diphosphate (ADP). Additionally, there is an assumption made about the hydrolization of ATP into ADP and Adenosine Monosphophate (AMP) as described by Heinrich and Schuster [198]. It states that ADP kinetics depend on ATP, the total concentration of adenine nucleotide concentration A and on the adenylate kinase equilibrium constant q_{AK} as:

$$ADP = \frac{ATP}{2}.\left(-q_{AK} + \sqrt{q_{AK}^2 + 4q_{AK}\left(\frac{A}{ATP} - 1\right)}\right) \tag{3.1}$$

where $A = ATP + ADP + AMP$. Furthermore, there is a relationship between the rate of ATP production and AMP production as follows:

$$\frac{dAMP}{dATP} = -1 + \frac{q_{AK}}{2} - 0.5.u + q_{AK}.\frac{A}{ATP.u} \tag{3.2}$$

where $u = \sqrt{\mathrm{q}_{\mathrm{AK}}^2 + 4q_{AK}\left(\frac{\mathrm{A}}{\mathrm{ATP}} - 1\right)}$. This set of assumptions can be found in a variety of models with different aims as in the work by DiNuzzo *et al.* [199] and Cloutier *et al*. [200]. All of these models aim to describe the metabolic requirements during neuronal stimulation during different conditions. However, none of these models evaluate the cellular metabolic requirements in pathological conditions.

Alternatively, there are works that aim to predict the effects of irregular neurological function. These include the full kinetics of glycolysis and the Krebs cycle as presented in Figure 3.1. Here two models are discussed. The Çakır *et al*. model [201] looks at the neurotransmitters (e.g. dopamine and glutamate) role in cellular metabolism. The model includes 217 reactions and 216 metabolites as it can be seen in Figure 3.4.

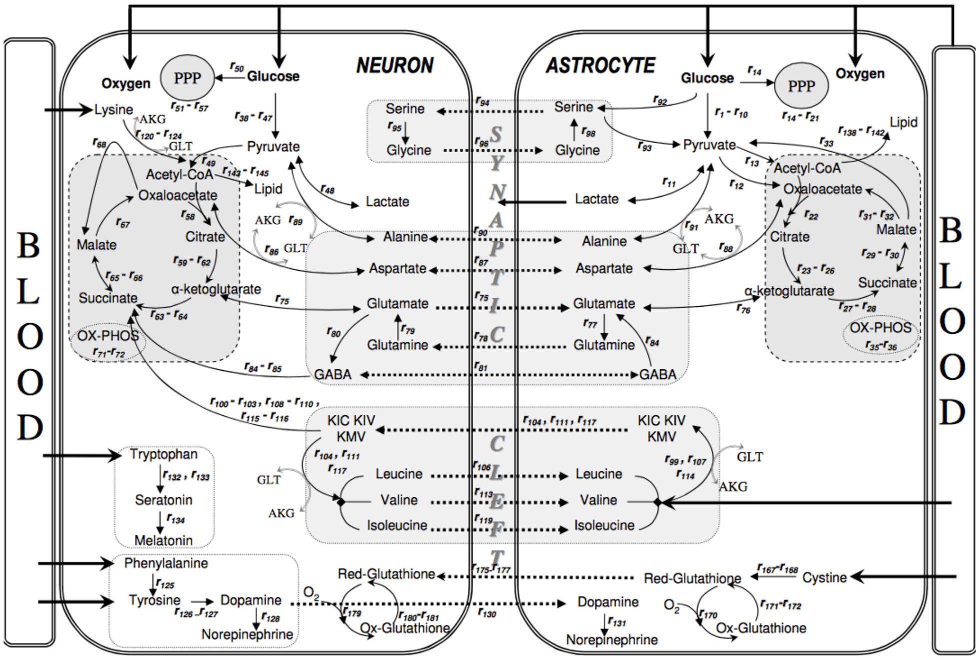

Figure 3.4: The Çakır *et al.* model [201], which combines the flow of metabolites between neurons, astrocytes and the capillary as well as the exchange of neurotransmitters between neurons and astrocytes.

This model was developed to study the effects on the metabolism of lack of access to oxygen. Another model that focuses on the flow of metabolites between neurons and astrocytes was found in Occhippinti *et al*. [202] as seen in Figure 3.5. Additionally, it also includes full metabolic kinetics of the glycolysis process and the Krebs cycle. It includes 5 compartments: the astrocyte, the neuron, the individual mitochondrial compartments and the ECS. Finally, as in the work by Çakır *et al*. [201], the glutamate/glutamine system is included. With this model, the glutaminergic metabolic flows during high and low stimulation are investigated. The model is summarized in Figure 3.5 [202].

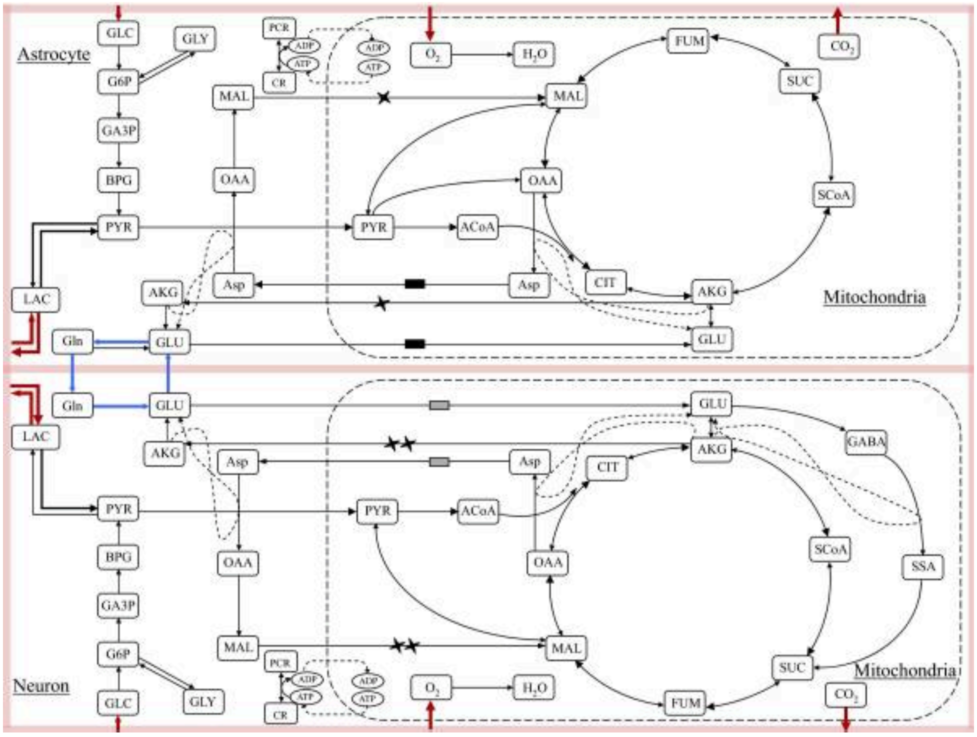

Figure 3.5: Breakdown of all the metabolite flows between neurons and astrocytes. The model has further compartments including the ECS and a capillary [202].

Although both models are validated using experimental data the requirements of the Na^+/K^+ pump are ignored. However, this pump is where 85% of energy requirements are expended and it has been characterized as playing a primary role in ischaemia. Therefore, these models are unsuitable to model ischaemic pathology.

From the available cellular metabolism models in the literature, the Aubert and Costalat [197] model was chosen as a framework. This is because it is the only one that considers the impacts of the Na^+/K^+ pump on cellular metabolism. Furthermore, it has been shown by Orlowski *et al.* [15] to have potential to predict cellular behaviour in the presence of ischemic stroke. All the metabolic models here described are summarized in Table 3.1.

Table 3.1: Comparing the models of brain tissue metabolism found in the literature

Model	Focus	Compartments	# ODE's	# Algebraic equation	# Parameters	Software environment	Conclusions
Aubert and Constalate [2001] [196]	Create a tool to aid the interpretation of fMRI imaging.	Neuron, Capillary	15	18	≅36	Matlab	The model was able to capture interaction between cellular metabolism and haemodynamics.
Aubert and Constalate [2005] [197]	Investigate the interactions between astrocytes and GABAergic neurons	Astrocyte, Neuron, ECS and Capillary	20	42	≅62	Matlab	Verified hypothesis pertaining to the astrocyte-neuron lactate shuttle.
Çakır *et al.* [2007] [203]	Metabolite exchange between neurons and astrocytes	Astrocyte, Neuron and ECS	216	217	Not mentioned	Matlab	The model was able to accurately predict the metabolic flow of the TCA cycle and Glutamate-glutamine cycle.
Cloutier et al. [2008] [200]	Validated model of brain tissue metabolism.	Astrocyte, Neuron, ECS and Capillary	36	64	125	SBML/OpenCell	Following the work Aubert *et al.* it demonstrates the role of the lactate shuttle during neuron stimulation
Occhipinti *et al.* [2010] [202]	Investigate the metabolic needs of inhibition	Astrocyte, Neuron, ECS	≅53	≅80	Not mentioned	Not mentioned	As Aubert and Constalate [2005] the model the model aims at explaining the role of the lactate-shuttle during neuronal stimulation.
Orlowski *et al.* [2010] [14]	Predict pH levels during ischaemic stroke.	Astrocyte, Neuron, ECS and Capillary	58	98	167	OpenCell	The prediction of the model of intracellular pH during stroke match experimental data and it further demonstrates the potential of pH imaging to quantify cell death in stroke.
Orlowski *et al.* [2013] [15]	Predict cellular oedema during ischaemic stroke.	Astrocyte, Neuron, ECS and Capillary	68	117	175	OpenCell	The model simulations matched experimental data and predicted the spread of stroke in a 3D model

3.2.2 Mathematical models of cellular ionic regulation

Throughout the literature, mathematical models have made ionic movement dependent on the transmembrane potential (V_m) and intracellular volume (v_i) [63], [204]–[206]. The potential is commonly defined as the difference between the inner (i) and outer (e) parts of the membrane potential, hence $V_m = V_i - V_e$. Following the work by Malmivuo and Plonsey [207] and Endresen *et al.* [206] the gas model by Goldman and updated by Hodgkin-Huxley [208] is commonly used to describe ionic flow. It states that the current I_S of the ion species S is described as:

$$I_S = \frac{1}{2} z_S P_S F([S]_i e^{z_S c V_m} - [S]_e e^{z_S c V_m}), \tag{3.3}$$

where z_S is the ionic valence, P_S is the membrane permeability to S, $c = \frac{F}{2RT}$, F is the Faraday constant, R the gas constant and T the absolute temperature. From Equation 3.3 the Nernst equilibrium potential V_S can be derived as:

$$V_S = \frac{1}{2cz_S} ln\left(\frac{[S]_e}{[S]_i}\right) \tag{3.4}$$

Additionally, the membrane conductance (g_S) can be described as:

$$g_S = z_S P_S F \sqrt{[S]_e [S]_i} \tag{3.5}$$

From Equations 3.4 and 3.5 Equation 3.3 can be simplified to:

$$I_S = g_S \frac{sinh\,(V_m - V_S)}{cz_S} \tag{3.6}$$

The work by Endresen *et al.* [206] presents this derivation to describe a variety of ionic transport proteins including channels, exchangers and pumps. Such a model of ionic flow has been used by many studies including the ischaemic stroke simulations by Dronne *et al.* [65] and the cytotoxic oedema model by Orlowski *et al.* [15].

However, further simplifications have been made to this model. When $z_S c(V_m - V_S) \ll 1$, Equation 3.6 can be reduced to the linear relationship:

$$I_S = g_S\,(V_m - V_S) \tag{3.7}$$

This simplified model is commonly found in the current state-of-the-art models of ion movement such as those by Dronne *et al* [65]and Østby *et al.* [64].The movement of a particular ion in terms of its osmotic concentration $[S]_i$ can then be derived as:

$$\frac{dn_S^i}{dt} = -\frac{A}{z_S F} I_S \tag{3.8}$$

where $n_S^i = [S]_i . v_i$ is the mass of ion S inside the cell and A is the surface area of the cell. Using the relationship between ion concentration $[S]_i$ and osmotic pressure Π_i that states $\Pi_i = RT[\mathrm{S}]_i$ it is possible to arrive at a relationship between intracellular volume (v_i) and ionic concentration

$$\frac{dv_i}{dt} = R.T.\tau_w.([S]_e - [S]_i) \tag{3.9}$$

where τ_w is the water permeability in s.m^{-1}.

Finally, a relationship between ionic concentration and membrane potential (V_m) can be established. Using Kirchhoff's law the following can be derived:

$$C_m \frac{dV_m}{dt} + \sum I_S = 0 \tag{3.10}$$

Substituting Equation 3.8 it can be shown that

$$C_m \frac{dV_m}{dt} = \frac{v_i}{A}.F.\sum z_S \frac{d[S]_i}{dt} \tag{3.11}$$

Equation 3.9 can then be simplified by approximating the derivatives to the difference between the current value at time t and the value at time $t = 0$.

$$(V_m - V_0) = \frac{v_i}{A.C_m}.F.\sum z_S([S]_i - [S_0]_i) \tag{3.12}$$

where V_0 and $[S_0]_i$ are the initial membrane potential and ion concentration respectively. Hence, $V_0 = \frac{v_i}{A.C_m}.F.\sum z_S([S_0]_i)$ and therefore $V_m = \frac{v_i}{A.C_m}.F.\sum z_S([S]_i)$. Equation 3.10 is derived by assuming that the concentration in the ECS is constant. Removing this assumption and taking the law of conservation of mass that states that $\frac{dn_S^i}{dt} = -\frac{dn_S^e}{dt}$, gives:

$$(V_m - V_0) = \frac{v_i}{A.C_m}.F.\sum z_S.[([S]_i - [S]_e) - ([S]_i^0 - [S]_e^0)] \tag{3.13}$$

From Equation 3.11, as before, the membrane potential can be written as: $V_0 = \frac{v_i}{A.C_m}.F.\sum z_S.[([S]_{\mathrm{i}}^0 - [S]_{\mathrm{e}}^0)]$ and $V_m = \frac{v_i}{A.C_m}.F.\sum z_S.[([S]_{\mathrm{i}} - [S]_{\mathrm{e}})]$.

The derived relationship between membrane potential and cellular volume, based on intracellular and extracellular ionic concentration difference, can be found throughout the literature, e.g. Endresen *et al.* [206], Armstrong *et al.* [204], Orlowski *et al.* 2011 [15] and Østby *et al.* [64]. However, these models consider other forms of ion movement besides diffusive flow due to osmotic pressure. These include ionic pumps (I_{pump}) and exchangers (I_{exch}), which are included in the model by simply adding then to Equation 3.7:

$$I_S = g_S(V_m - V_S) + I_{pump} + I_{exch} \tag{3.14}$$

Additionally, many different assumptions have been made throughout the literature. However, the theoretical basis for all of these studies lies within the framework presented here.

3.2.3 Modelling glutamate kinetics

As shown by the work by Rossi *et al.* [209] four glutamate release mechanisms have been identified: release dependent on extracellular [73] and intracellular Ca^{2+} concentration [210]; release through swelling activated anion channels [211]; an indomethacin –sensitive process in astrocytes [212]–[214] and reverse operation of glutamate transporters [215], [216]. Here, only glutamate release mechanisms dependent on Ca^{2+} kinetics and due to reverse function of the glutamate transporter are presented. These two mechanisms can be split into glutamate release pre and post membrane depolarization.

Starting with the most prominent pre-depolarization mechanism, which is the Ca^{2+} dependent vesicular glutamate release, as explained in Chapter 2, the vesicles are organized into pools. The literature on vesicle pool dynamics is large, due to the variety of vesicle distributions that exist. These depend on the species of animal and the type of neuron considered, as presented by [76]. Additionally, there are several processes involved in the exocytosis and endocytosis of vesicles including: filling up vesicles with neurotransmitters (a pH dependent ATPase pump pushes neurotransmitters inside the vesicle); docking (vesicles move close to the membrane wall depending on Ca^{2+} kinetics); priming (again dependent on Ca^{2+} kinetics vesicles fuse with the membrane becoming ready for release of neurotransmitters) and finally exocytosis and endocytosis.

Due to the complexity of the synaptic vesicular system and the variability of experimental measurements, mathecmatical modelling of these processes varies greatly dependent upon the aim of the model. There are kinetic models for each of the steps of synaptic movement mentioned previously. The work by Hori and Takahashi measured and modelled the process by which vesicles are filled with glutamate. The work by Granseth *et al*. [217] describes and measures the rates of movement between pools and how the process of endocytosis regulates vesicular kinetics. In addition, there is the work by Axmacher *et al*. [218] that describes how vesicular quanta play an integral role in the process of short-term plasticity. As an example, the diagram of the synaptic model by Granseth *et al*. [217] is presented in Figure 3.6.

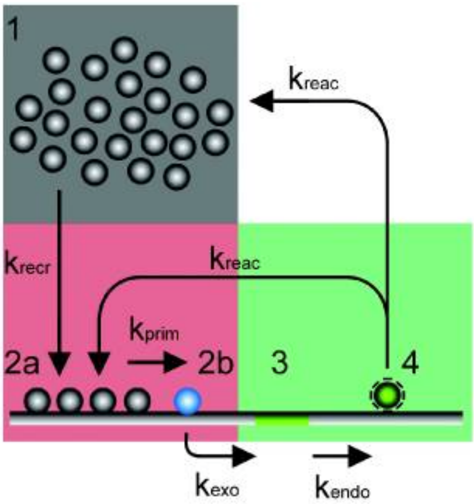

Figure 3.6: A schematic illustration of the model by Granseth *et al*. **[217]**. (1) Vesicles are recruited from the reserve pool to the RRP at the rate k_{recr}. (2) Vesicles at the RRP are made ready for release through the process called priming at the rate k_{prim} and are released at rate k_{exo}. (3) After release vesicles are endocytosis at rate k_{endo}. (4) Finally, the endocytosed vesicles are recycled into the RRP and the reserve pool at rate k_{reac}.

Finally, there are several models that aim to measure and to simulate how Ca^{2+} triggers exocytosis of vesicles. Initial models assumed that it was a sequential process from recruitment until exocytosis and that there was only one mode of vesicle exocytosis triggered by Ca^{2+} [219], [220]. Then it was identified that there were kinetically distinct release phases, including, as stated by Sun *et al* [77]: fast, low frequency triggered synchronous release; slow, high frequency AP train triggered asynchronous release; and spontaneous release. The different forms of release are believed to be due to the enrolment of different populations and pools [221]–[223]. The recruitment of the different pools is dependent on their molecular composition or localization in respect to Ca^{2+} sensors. This theory of varied pools is further verified by the work by [77], [223], [224] that found that eliminating certain Ca^{2+} proteic sensor synaptotagmin (-1 and -2) leads to deletion of fast asynchronous release.

From these discoveries, it was hypothesized that there are multiple sensors controlling either a single pool [77], [225] or different pools [223]. More recently the specific sensors for fast release have been identified as synaptotagmin-1, synaptotagmin-2 and synaptotagmin-9. This hypothesis, where different Ca^{2+} sensors are related to different pools and different modes of release, has been further tested using mathematical modelling [226]. In order to contrast the approaches of Sun *et al.* [77] of assuming only a release pool and of the Walter *et al.* [226] model where there is a parallel release from two different pools a schematic of each strategy is presented in Figure 3.7.

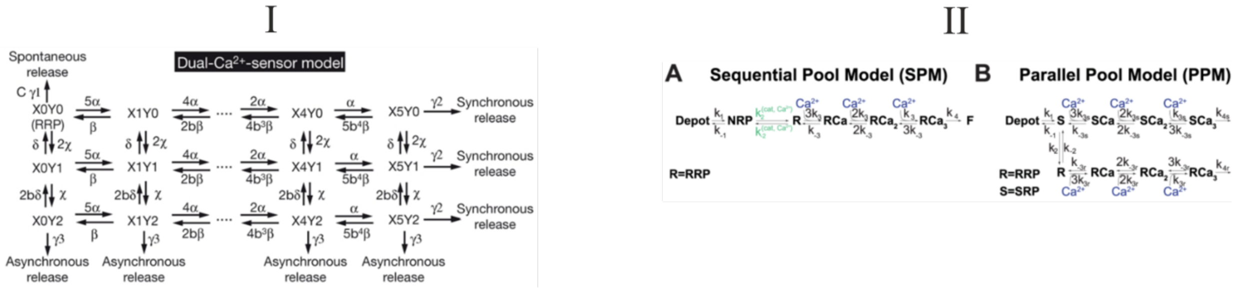

Figure 3.7: I. Schematic of the dual Ca^{2+}sensor model, which includes synchronous asynchronous and spontaneous glutamate release from one pool of vesicles [77]. II. Model by Walter *et al.* [226] where the hypothesis that there are several pools where vesicles are released from is tested.

Post membrane depolarization, as stated by Rossi *et al*. [209], the most prominent glutamate release mechanism is due to the inverse function of the glutamate transporter. The stoichiometry of the transporter is that for each mole of glutamate that enters the cell, 3 moles of Na^+, 1 mole of H^+ and 1 mole of water enter the cell and 1 mole of K^+ leaves the cell. Rossi *et al*. [209] developed a model of the transporter behaviour in terms of membrane potential (V_m) and cellular pH. The model states that the extracellular glutamate equilibrium concentration $[glu]_{o,eq}$ can be calculated using:

$$[glu]_{o,eq} = [glu]_i . \left(\frac{[Na^+]_i}{[Na^+]_o}\right)^3 . \left(\frac{[H^+]_i}{[H^+]_o}\right) \quad . \left(\frac{[K^+]_o}{[K^+]_i}\right) . exp\left(\frac{2.V_m.F}{R.T}\right) \tag{3.15}$$

where $[glu]_i$ is the intracellular concentration of glutamate. Rossi *et al.* [209] assumes that the transporter will aim to ensure that the extracellular concentration $[glu]_o$ approaches equilibrium. This is described as a first order model as:

$$\frac{d[glu]_o}{dt} = \frac{[glu]_{o,eq} - [glu]_o}{\tau_{glu}} \tag{3.16}$$

where τ_{glu} is the glutamate time constant.

As presented here glutamate kinetics are complex and are involved in a variety of mechanisms essential to the health of the cell. Consequently, when developing a mathematical model of the pathological kinetics of glutamate, a combination of all of these mechanisms is required to properly describe its behaviour. An example of such a model is presented in the following section.

3.2.4 Dronne *et al.* model of cytotoxic oedema [65]

In the literature, only the work by Dronne *et al.* [65] has attempted to model glutamate kinetics in an ischemic environment. Its main concern is to capture the swelling of cells after 1 hour of an induced stroke. Although it has validated the concentration of ions after one hour of ischaemic stroke it does not validate the glutamate release simulations.

The model consists of a combination of the state-of-the-art models of membrane ionic channels and transporters of astrocytes and neurons. Besides these two cells, the model has a further compartment: the extracellular space (ECS). The ions here considered were sodium (Na^+), potassium (K^+), calcium (Ca^{2+}) chloride (Cl^-) and the neurotransmitter glutamate (GLU). A diagram of the mathematical model by Dronne *et al.*[65] can be seen in Figure 3.8.

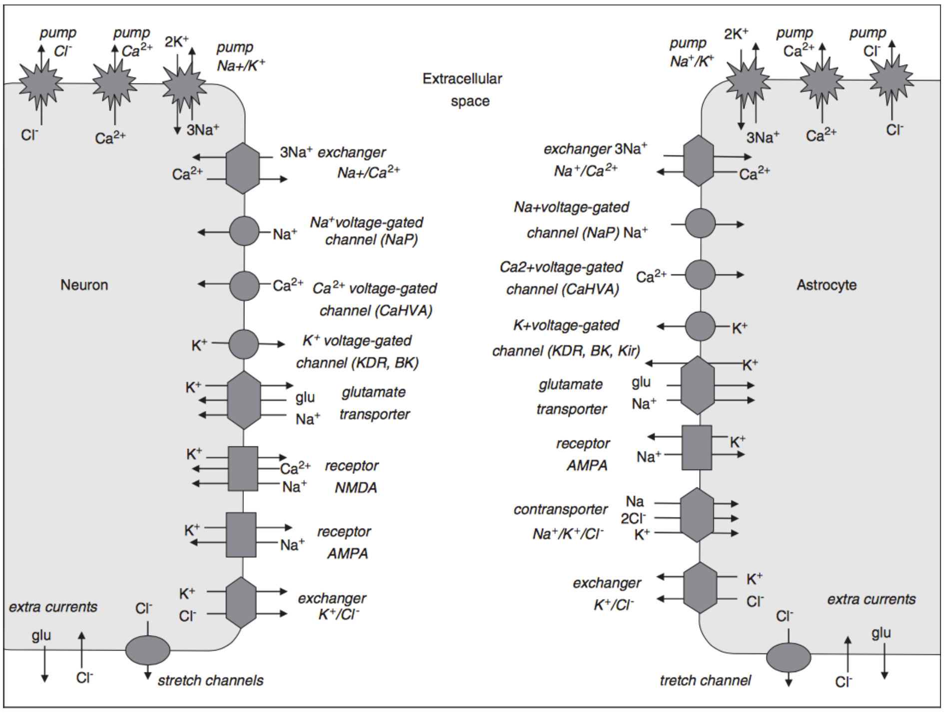

Figure 3.8: Schematic of the mathematical model by Dronne *et al*. [65]

The model considers several types of ionic movement proteins. These include: voltage-gated channels; volume-activated channels; ionic pumps; ionic exchangers and receptor channels. These are described using different types of models, including the Hodgkin-Huxley equations and the Goldman-Hodgkin-Katz formulation. The overall flow of ion (S) is then assumed to be equal to the sum of the currents associated with that particular ion (It_S) as:

$$\frac{d}{dt}.(f.[S]) = \frac{s.It_S}{z_S.F.v} \tag{3.17}$$

where s is the cellular surface area, z_S is the valence for ion S and v is the global volume considered, including neurons, astrocytes and the ECS. The parameter f represents the volume fraction of each compartment, which is assumed to be dependent on osmotic concentration similarly to Equation 3.9.

$$\frac{df}{dt} = \frac{1}{S_0}.\frac{d}{dt}.\left(f\left(\sum_s [S] + [A_0]\right)\right), \tag{3.18}$$

where S_0 is the sum of the extracellular concentrations in physiological conditions and A_0 stands for the concentration of the intracellular impermeant anions. Additionally, the membrane potential is also made dependent on the intracellular ionic concentration as it is assumed that each of the compartments is electrically neutral:

$$\sum_s (z_s[S]) + z_A[A_0] = 0 \tag{3.19}$$

where z_A is the valence of the impermeable ions. It is then assumed that the membrane potential changes as the charged ions move across compartments.

In the particular case of glutamate, two currents are considered. The first is the glutamate transporter ($E_{transporter}$) that is here modelled using the Michaelis-Menten formulation as:

$$I_{K^+} = G_{tra}.\left(V_m - E_{transporter}\right) \tag{3.20}$$

$$I_{Na^+} = -3.I_{K^+} \tag{3.21}$$

$$I_{glu^-} = I_{K^+} \tag{3.22}$$

where, G_{tra} is the permeability of the transporter and $E_{transporter}$ is defined as:

$$E_{transporter} = \frac{RT}{F} log\left(\left(\frac{[Na^+]_e}{[Na^+]_i}\right)^3.\left(\frac{[K^+]_i}{[K^+]_e}\right).\left(\frac{[glu^-]_i}{[glu^-]_e}\right)\right) \tag{3.23}$$

Then a second glutamate current I_{extra} was introduced to ensure that the glutamate kinetics are stable at steady state, defined similarly to Equation 3.20 and 3.23 as:

$$I_{extra} = G_{extra}.\left(V_m - E_{extra}\right), \tag{3.24}$$

$$E_{extra} = \frac{RT}{F} Log\left(\frac{[glu^-]_i}{[glu^-]_e}\right) \tag{3.25}$$

where G_{extra} is the permeability of the extra glutamate channel.

In order to simulate stroke, Dronne *et al.* [65] assumed that the mechanisms being modelled are solely affected by a hindrance to the ionic pumps, due to lack of availability of ATP. The decrease of ATP over time was assumed to follow the fitted model described by Lemieux *et al.* [227]. ATP decreases over time in a severe ischemic environment as:

$$[ATP](t) = [ATP]_{max}(0.35)^{(t/15)} \tag{3.26}$$

This is incorporated into the model by assuming that I_{pump} decreases in a manner proportional to the amount of ATP available as:

$$I_{pump}(t) = (p_{ATP} + [1 - p_{ATP}](0.35)^{\left(\frac{t}{15}\right)}).I_{pump0} \tag{3.27}$$

where p_{ATP} is the proportion of residual ATP production and $\mathrm{I_{pump0}}$ is the current through the pumps at baseline physiological conditions.

The model was validated using two forms of data. The first consists of measured values of intra-neuronal and ECS concentration of ions after severe stroke as measured by [228] and Silver *et al.* [229]. Secondly, it was validated by measurements of the reduced Diffusion Coefficient of water (rADCw), which was shown by Verheul *et al.* [230] to be proportional to a reduction in ECS.

Although Dronne *et al.* [65] have validated its model of ionic kinetics no data was used to validate the predictions of the model in terms of glutamate release during ischaemia. As the concentration of ions and ECS volume fraction are validated it is, instead, assumed that as the concentration of ions that the glutamate concentration is validated as well. This assumption appears to be reasonable, as stated by Rossi *et al.* [209]: that the majority of glutamate is released through the glutamate transporter.

Consequently, as the Na^+ and K^+ concentrations have been validated the glutamate levels are also validated. However, through the work by Rossi *et al.* [209], it has been found that glutamate kinetics involve a variety of mechanisms that have been ignored here. These include intra neuronal glutamate vesicular kinetics. Additionally, metabolic production of ATP involves further mechanisms like the glycine production of glucose and the lactose shunt. Furthermore, pH kinetics have been ignored in the Dronne *et al.* [65] model. However, these have been reported by Rossi *et al* [209] and Orlowski *et al* [15] to play an important role in ionic and glutaminergic kinetics. In the following sections, the literature for models of these systems that were used to overcome the limitations of Dronne *et al*. are presented.

3.3 Mathematical model of Neuromyelitis Optica (NMO)

Only recently has the pathophysiology of NMO been distinguished from that of Multiple Sclerosis (M.S.) [45]. Therefore, there are no models that aim to simulate the pathology of NMO. Consequently, to develop such a model, the kinetics of water transport across the astrocytic membrane and models of the lytic protein cascade had to be combined. In this section those two topics are discussed separately: section 3.3.1 presents the validated models of water kinetics in the presence of AQP4 deletion and section 3.3.2 describes the available models on the different complement pathways.

3.3.1 Models of cellular water kinetics

Glial involvement on synaptic activity has been found to be crucial [79]. One particularity of astrocytes, when compared to neurons is the fact they have water specific channels, termed AQP4 [45]. Besides AQP4 there are other channels that are permeable to water. These include the $Na^+/K^+/Cl^-$ (NKCC1) and the glutamate transporter [81]. The involvement of astrocytic regulation of hydrostatic pressure and ionic regulation has recently been of interest, in particular, its role in the clearance of K^+. The first work to propose such a model was a three compartment model (a neuron, an astrocyte and the ECS) by Østby *et al.* [64] which includes the ions Na^+, K^+, Cl^- and HCO_3^-. The membrane is permeable to each of the ions through individual channels as well as the following transporters: NKCC1, the K^+/Cl^- (KCC1) and Na^+/HCO_3^- (NBC). Finally, the Na^+/K^+ pump is also included (NaKATPase). All these channels are modelled following a similar derivation as was presented in Section 3.2.2. As in Equation 3.9, the volume of the cells (V_i) is made dependent on the difference between the intra and extra osmotic ionic concentration:

$$\frac{dV_i}{dt} = L_p\left([Na^+]_i + [K^+]_i + [Cl^-]_i + [HCO_3^-]_i + \frac{X_i}{V_i} - [Na^+]_o + [K^+]_o + [Cl^-]_o + [HCO_3^-]_o\right), \tag{3.28}$$

where X_i is the concentration of impermeable molecules and L_p is the total membrane water permeability. A summary of the model can be seen in the figure below.

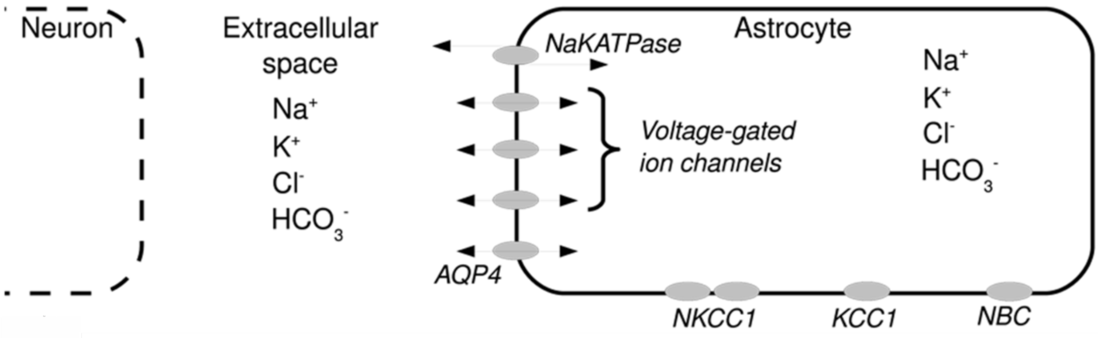

Figure 3.9: Schematic describing the model by Østby *et al.* [64].

Then the model is used to test how deleting NKCC1 and AQP4 affects the ion kinetics. In order to delete AQP4, the model follows the data by Ruiz-Ederra *et al.* [231] that states that the membrane permeability to water is reduced by 80%. Hence, L_p is reduced by 80% and the impact on ion kinetics and consequently cellular volume during neuronal stimulation was tested. With these experiments Østby *et al.* [64] reported that the reduction of water permeability resulted in a 30% reduction of the ECS during stimulation.

The work by Jin *et al.* [82] also investigated the role of AQP4 in K^+ kinetics. However, this model has a narrower approach than that of Østby *et al.* [64] as it only included K^+ kinetics. Water flux across the membrane is again made dependent on osmotic pressure as in Equation 3.9. The simulations performed consisted of varying the values of water permeability and observing how K^+ behave during neuronal stimulation. The results supported that AQP4 water permeability plays a role in the clearance of K^+ during neuro-excitation.

These two studies were the only models found in the literature that explored the effects of AQP4 deletion on neuronal function. However, as proof mounts that astrocytic hydrostatic pressure plays a crucial role in ionic regulation, models that explore other questions related to ionic diffusion and vascular and tissue interface have also included definitions of membrane water permeability. One of these models is the one by Murakami and Kurachi [232] that tries to quantify the importance of K^+ buffering clearance during stimulations. Additionally, the potential of therapies that increase K^+ buffering is tested.

In summary, the discovery of aquaporins as regulators of brain hydrostatic pressure has potential to test hypotheses in a variety of scales from the cellular, as previously demonstrated, to the brain level in the case of hydrocephalus [233]. However, the spatial and temporal scales of the kinetics being studied make it difficult to study them experimentally. Hence, although parameters that describe aquaporins are still being measured experimentally, mathematical models have the potential to test hypotheses effectively and to propose avenues for future experimental work. A summary of all the models here analysed is presented in Table 3.2.

3.3.2 Inflammatory complement lysis models

The full extent of lytic activation, protein cascade and inhibitors behaviour has yet to be fully characterized. Currently, as shown in Fig. 2.20, three pathways have been identified: the classical, the alternative and the lectin. All three pathways result in the formation of membrane attack complex (MAC).

Each of the three pathways has different activation mechanisms. The classical pathway, which is the focus of the work developed here, is triggered by antigen and antibody binding. There are no models that consider the binding of antigen and antibodies and the activation of complement. For the work on NMO, the kinetics of both mechanisms were combined. In terms of antigen-antibody binding, the literature agrees that it can be modelled using the mass action equation as reviewed by Kumagai *et al*. [234].

Then there are models that describe the complement protein cascade. In the literature, three models were found that describe the inflammatory complement system. Firstly there is the work of Hirayama *et al*. [235], which only considers the classical pathway. Additionally, it considers several complement regulating proteins: C1inh (C1 inhibitor), S protein, C4bp (C4 binding protein), decay accelerating factor (DAF), CR_1 (C3b receptor), CR_2 (C3dg receptor), membrane cofactor protein (MCP), Apolipoprotein (clusterin) and CD59 (MAC inhibitor factor). Two strategies are chosen for modelling the reaction between complement proteins and complement regulating proteins. The reactions between proteins are described using mass action equations. In terms of the regulating proteins, these are assumed to be constant throughout the simulations. The conclusions from this model behaviour were found to be limited. Consequently, future models used different approaches.

The model by Korotaevskiy *et al*. [236] models both the classic and the alternative pathways. The activation of the classical pathway is assumed to be through the attachment of protein C1 to the antigen-antibody complex while the alternative pathway is activated through spontaneous hydrolysis of the protein C3. Assuming that the concentration of the antigen-antibody complex is high, the concentration of the antigen-antibody complex is taken to be stationary based on the work by van Dam *et al*. [237]. As in the case of the work by Hirayama *et al*. [235], there is complement regulating proteins: Factor B, Factor D, Factor P, C1inh, Factor H, Factor I, C4bp, S protein and Clusterin.

Comparing the Hirayama *et al*. [235] to the Korotaevskiy *et al.* [236] model it was found that the simulations of the latter resulted in a more accurate representation of the complement system behaviour. This is because it uses Michaelis-Menten kinetics to describe the enzymatic reactions in the different pathways instead of assuming linear relationships. Additionally, the different complement regulating proteins were not taken as constants and instead were defined as model variables and described like other pathway proteins. Most of the values of the different rates were taken from the literature. The remaining rates were found by fitting the model to *in vitro* data of cellular inactivation due to complement. The model has found to accurately predict the formation of MAC formation and consequent cell inactivation.

Finally, there is the complement pathway by Liu *et al.* [238]. These models the classical and lectin pathways. The activation of these two pathways is taken to be due to the recognition of bacterial surface proteins. More specifically, they model the recognition of phosphorylcholine (PC) or N-acetylglucosamine (GlcNac) by C-reactive protein (CRP) and ficolins for the activation of classical and lectin pathways respectively. Additionally, the model takes into account the recent findings by Zhang *et al.* [239], that at particular pH conditions there are interactions between CRP and ficolins, which lead to crosstalk interactions between the classical and lectin pathways. Furthermore, this model does not concern itself with predicting MAC production or cell inactivation; instead, it aims to analyse how the interaction between the lectin and classical pathways impacts the production of C3b.

This is because, as presented in Figure 3.10, this protein is the product of all three pathways and can act as a chemoattractant, trigger phagocytosis and promote the formation of MAC. Therefore, it is assumed by Liu *et al.* [238] that if the production of C3b can be modulated, so can the complement outcomes down the proteic cascade. In addition, the complement inhibitory effects C4bp and H are tested using the model.

The model was developed similarly to the model of Korotaevskiy *et al.* [236], in which the enzymatic reactions are modelled using Michaelis-Menten kinetics, while the remaining reactions are implemented using conservation of mass. These kinetics were fitted to experimental measurements of complement proteins over a variety of conditions including separate activation by PC and GlcNac under inflammatory and non-inflammatory environments.

In conclusion, in both fields of antigen and antibody attachment and inflammatory complement mathematical modelling strategies have to be effective at simulating both mechanisms. However, in terms of complement system models, only the work by Korotaevskiy *et al.* [236] has aimed to capture the proteic cascade from activation to MAC formation. Conversely, only the work by Liu *et al.* [238] have used measurements of individual proteins to validate the model. Therefore, further validated models of the full extent of the complement system are required. Furthermore, a better understanding of the mechanisms that trigger the complement classical pathway after antibody and antigen binding is needed. As Liu *et al.* [238] have shown, the activation of complement is much more complex than the relationship presented by Korotaevskiy *et al.* [236]. All the models analysed in this section are summarised in Table 3.3.

Table 3.2: Models astrocytic water regulation evaluated.

Model	Focus	Compartments	# ODE	# Algebraic equation	# Parameters	Software language	Conclusions
Murakami and Karachi [2015] [68]	Clearance of K^+ by astrocytes to ensure neuronal function.	Synapse, astrocyte, capillary, ECS	14	18	28	Not mentioned	Different strategies to prevent cytotoxic oedema are tested involving the clearance of K^+ by astrocytes.
Østby *et al.* [2009] [64]	Investigate the cause for a 30% shrinkage of the ECS during stimulation.	Neuron, Astrocyte, ECS	34	0	67	CellML	A in silico model to test theories to explained ECS shrinkage was developed.
Jin *et al.* [2013] [82]	Quantifying the importance of different mechanisms responsible for the extraction of K^+ during stimulation.	Neuron, Astrocyte, ECS	5	7	5	Visual Fortram	Supporting evidence that AQP4 deficiency can be responsible for neuroexcitation impairment.

Table 3.3: The inflammatory complement models.

Model	Focus	Pathways	# ODE's	# Algebraic equation	# Parameters	Software language	Conclusions
Hirayama *et al.* [1996] [235]	Theoretical analysis of the complement system.	Classical	26	0	22	Not mentioned	Assuming a linear relationship between the complement proteins
Korotaevkiy et al. [2009] [236]	Develop a model that can reproduce data of MAC production by complement.	Classical, Alternative	34	0	67	Matlab	The first validated with experimental data model complement lysis was developed.
Liu *et al.* [2011] [238]	Test the hypothesis to inhibit the complement system.	Classical, Lectin	42	3	85	SBML	A model is created where modulation of the complement response can be tested for calcium, pH and the protein C4BP.

3.4 Acute inflammation

This form of inflammation acts to kill any invading microorganism, remove any resulting cellular and tissue debris and start the healing processes. This whole process is normally resolved within hours [240]. However, if for some pathological reason the inflammatory event is not terminated, acute inflammation can degenerate into self-perpetuating chronic inflammation, which may last up to years. Although the mechanisms that trigger inflammation and maintain inflammation are known, those that limit and down regulate it are not as well characterized [241]–[243]. Mathematical modelling has been found in this context as a potential tool to test hypotheses of pro-resolving mechanisms.

Acute inflammation is marked by the interaction between two inflammatory species, neutrophils and macrophages [240], [243], [244]. The role of neutrophils is to eliminate any invading pathogen through the release of toxic reagents. Monocytes arrive at the site of inflammation in order to clear dead cells, including neutrophils and debris. It is the interchange between a timely and effective clearance of pathogens and the removal of apoptotic neutrophils that mathematical models try to evaluate. This is because one of the main reasons for the development of chronic inflammation is the necrotic decay of neutrophils and potential release of their intracellular toxins, causing damage to the surrounding tissue [245].

There have been several works that model the acute inflammatory response, starting with the work of Lauffenburger and colleagues [66], [246], [247] that created a generic model of leukocyte response to bacteria. In a series of papers, it shows that cell densities might reach alarming levels if not eliminated.

More recently, there has been increased interest in continuing the modelling approach for acute inflammation initiated by Lauffenburger [66], [246], [247], starting with the work by Kumar *et al.*[248], where a three ODE model was developed. They assumed that the behaviour of all leukocytes acted as one variable. The inclusion of the production of two cytokines aimed to capture the initial arrival of neutrophils followed by monocytes. The model was used to test conditions in which an inflammatory response might degenerate into sepsis.

The Kumar *et al.* [248] model was then extended by Reynolds *et al.* [249] to include anti-inflammatory mediators. The five ODE model includes: pathogens, activated phagocytes, pro and anti-inflammatory mediators and the tissue damage caused. With such a model, the effects of mediators were evaluated. The authors of this work then further developed this model by applying it to a variety of pathological conditions; a review of their work can be seen in Vodovotz *et al.* [250].
In terms of an applied mathematical model of acute inflammation to a pathology, the best example found is in the work by Smith *et al.* [251]. This work demonstrates the importance of inclusion of several species of leukocytes. It presents three models of increasing complexity. The last model described consists of: the pathogen, healthy epithelial cells, infected epithelial cells, pro inflammatory cytokines and the damage to the tissue. It simulates the sequential arrival of neutrophils and monocytes through a delayed differential equation. Taking N to represent neutrophils and M to represent monocytes, the rate of arrival of monocytes (J_M) is made dependent on the concentration of N as:

$$J_M = \xi N(t-\tau)\left(1-\frac{M}{M_{max}}\right) \tag{3.29}$$

where ξ is the rate of monocyte recruitment, τ the delay between neutrophil and monocyte recruitment and M_{max} the maximum number of monocytes that can be recruited. With this model, Smith *et al.* [251] were able accurately to predict the development of pneumococcal lung infection and to test the contribution of each component of the model in the clearance of the pathogen.

Finally, there is the work by Dunster *et al.* [252], which follows the work by Vodovotz *et al.* [250]. Besides considering both pro and anti-inflammatory mediators, which also takes into account different types of leukocytes such as neutrophils and monocytes. Additionally, it considers the apoptotic degradation of neutrophils. With such a model, simulations are made to identify conditions where inflammatory resolution is achieved and the role of anti-inflammatory mediator.

Both Smith *et al.* [251] and Kumar *et al.* [248], considered anti-inflammatory mechanisms. In the case of Kumar *et al.* [248] the anti-inflammatory mediator acted as an inhibitor for the recruitment of leukocytes. Taking P to represent pathogens, N as the leukocytes, D the cellular damage and C as the anti-inflammatory mediators, the relationship between pro and anti-inflammatory events J_N is described in Michaelis-Menten form:

$$J_N = \frac{s_N R}{\mu_N + R}, \qquad R = \frac{k_1 N + k_2 P + k_3 D}{1 + \left(\frac{C}{c_\infty}\right)^2} \tag{3.30}$$

where k_{1-3} are the rates for leukocyte chemotaxis; s_N and μ_N are the Michaelis-Menten parameters and c_∞ is the rate of pro-resolvin by C. The work by Dunster *et al.* [252] implemented a model similar to Equation 3.30 to define the inhibition of neutrophil recruitment by anti-inflammatory mediators. However, it aimed at simplifying the Michalis-Menten kinetics down to an inverse relationship between pro-inflammation events and anti-inflammatory mediators. Taking c and g as the pro- and anti-inflammatory mediators respectively, the neutrophil recruitment rate J_{NS} then became:

$$J_{NS} = \frac{c}{1 + g} \tag{3.31}$$

Additionally, the model by Dunster *et al.* [252] assumed that anti-inflammatory mediators also promote the apoptosis of neutrophils. This is based on the findings that the rate at which neutrophils undergo apoptosis can be modulated by extracellular stimuli [243]. The work of Sehan *et al* [243] showed that this rate is increased in the presence of anti-inflammatory mediators. Conversely, the work by Akgul *et al* [253] showed that the lifespan of a neutrophil increased in inflamed tissue. Furthermore, the work by Rossi and Sawatsky [254] and by Lee *et al.* [255] proved that this effect was due to pro-inflammatory mediators. Dunster *et al.* [252] incorporated these findings into the model by implementing a similar relationship between pro and anti-inflammatory mediators as in Equation 3.30 to define the apoptotic rate J_A:

$$J_A = k_1 N \frac{\left(1 + \frac{g}{k_2}\right)}{\left(1 + \frac{c}{k_3}\right)} \tag{3.32}$$

where k_{1-3} are the rates associated with the apoptotic process.

In summary, acute inflammation is an area of interest in particular to identify the factors that lead it to degenerate into chronic inflammation. The literature presented shows that mathematical modelling has the potential to test hypotheses presented experimentally and to test proposed methods of achieving the resolution of inflammation. The acute inflammatory model literature is summarized in Table 3.4.

3.5 Methods

After selecting the models from the literature these need to be combined and adapted to fit the environment and purpose for which they are intended. Consequently, the novel models created need to go through processes to achieve this. In this section, all the tools used in the development of the models are presented. In section 3.5.1 the languages available to solve the equations are presented. The following section then presents the simplex algorithm that was used to fit the different models. In addition, as the models developed to involve the combination of a variety of models, the resulting models degenerate into models that include a large number of variables and parameters. In cases where it seemed that certain kinetics in models were negligible to the application being considered an effort was made to simplify it. To this effect, a screening algorithm by Campolongo-Morris was implemented as described in Section 3.5.3. In cases where only the input and output of a model was required symbolic regression algorithm was used as described in Section 3.5.4

3.5.1 Mark-up languages for modelling

There are several mark-up languages that can be used to build ODE models. Two have been designed specifically to handle large ODE models, which are CellML [256] and SBML [257]. In the work created both were used depending on the aim. CellML provides an easier interface to develop models. This is because it allows for the visualization of equations and it verifies if units of parameters and equations are consistent throughout the model Additionally, there is a repository with physiological models that was used when developing the work presented here, e.g. Cloutier *et al.* [200]. For CellML a compiler has also been created called OpenCell [256]. This software allows for the graphical visualization of the simulations. Furthermore, it uses the solver from SunDials called CVODE [258] that has been found to be efficient at solving the models developed.

Table 3.4: Models of acute inflammation analysed.

Model	Focus	Cells	Cytokines	# ODE	# Parameters	Software language	Conclusions
Lauffenburger and Keller [1979] [82]	Analyzing the impact of leukocyte motility on bacteria extraction.	Leukocytes	1 pro	3	9	Not mentioned	Agreement was found with peritoneal E.coli inflammatory data that leukocyte motility has a crucial role in inflammatory clearance.
Lauffenburger and Kennedy [1981] [246]	Discussion of how abnormalities in leukocyte recruitment may result in pathological behaviour	Leukocytes	0	2	8	Not mentioned	Using numerical values for parameters measured experimentally to present the predictive nature of the model.
Kumar *et al.* [2004] [248]	Using a simple 3 ODE model to evaluate parameterization choice that simulate acute to chronic degeneration.	Leucocytes	2 pro	3	6	Not mentioned	Several different causes for sepsis were found that require different treatment strategies.
Reynolds *et al.* [2006] [249]	Understand the role of anti-inflammatory cytokines.	Leukocytes	1 pro/ 1 anti	4	21	Not mentioned	Therapeutic strategies are presented by harnessing the potential of anti-inflammatory chemokines.
Smith *et al.* [2011] [251]	The model is used to evaluate therapeutic therapies for Pneumoccocal pneumonia.	Neutrophils/Monocytes	1 pro	7	31	Matlab	The model is able to quantify the contributions of cytotoxicity and immune-mediated damage in pneumococcal pathogenesis.
Durnst *et al.* [2014] [252]	Evaluating the role of pro-resolving chemokines in the treatment of acute inflammation	Neutrophils/Monocytes	1 pro/ 1 anti	5	15	SBML	In order for a treatment to be efficient it need to target monocyte phagocytosis and neutrophils apoptosis.

In addition, OpenCell also provides a tool that translates CellML into more low-level languages as C++ and Matlab, which has been found to very useful as these provide a variety of additional toolboxes.

SBML was created specifically to handle chemical reactions. Hence, a lot of the work developed would be hard to fit into the template required in order to run the models. However, it does provide a series of toolboxes that have been found to be efficient in fitting models to data. Additionally, it also provides tools for sensitivity analysis.

In summary, having a variety of tools aided the work as it consisted of often large and complex models. However, it would be useful to have a tool to translate the code between the two languages, as it would facilitate the development and analysis of the complex models developed. Furthermore, having a translational tool between languages would allow for easier use of the model databases available (OpenCell repository for CellML and Biodatabase for SBML).

3.5.2 Optimization

The models created have a large number of parameters and unfortunately not all their values are available in the literature. Therefore, in order to reproduce data, these parameters had to be estimated using optimization algorithms. For all the fittings performed throughout the chapters the SBML package by Schmidt *et al.* [257] was used as it provides an interface to fit a model to several sets of data. This package provided a series of optimization algorithms. As the parameters have a large uncertainty and the model is non-linear algorithms that do not make use of derivatives; as there might not be a solution for the derivative.

The SBML provides two of the most common algorithms that fit these demands, which include particle swarm algorithm (PSwam) and the simplex algorithm. The former follows a similar procedure as a genetic algorithm: 1. It creates a random number of solutions or particles within a defined parameter space 2. compares each particle to the data using an error function; 3. finds the closest to the optimal solution at that iteration is found and 4. all remaining particles move in the direction of the optimal solution at every iteration. The PSwarm differs from a genetic algorithm as it does not have functions for particle crossing such as mating and mutation and PSwarm has memory. Therefore, it ensures that it does not get stuck in local minima within the range chosen. However, when tested on the models developed it was found to have a large computational cost. As the models developed have a large number of free parameters the simplex method was used, which is a more brute force approach and it had already been tested by Cloutier *et al.* [200] to fit the cellular metabolism model to different sets of data.

As the name implies the simplex algorithm is based on a simplex geometrical shape. Therefore, the algorithm can be explained graphically. The simplex algorithm requires the shape to be a nondegenerative shape, i.e. that it encloses a finite N-dimensional volume. This shape would, therefore, have $N + 1$ vertices. The algorithm then explores the parameter space by considering that each of the $N + 1$ vertices represents one of the parameters of the model and moves them in predefined forms that ensure that the shape of the simplex stays nondegenerate.

In order to initiate the algorithm, an initial point P_0 is required. The remaining N points are defined in terms of P_0 as:

$$P_i = P_0 + \lambda e_i \tag{3.33}$$

where e_i are the N unit vectors and λ defines the characteristic length scale.

From the initial condition, the possible moves fall into four categories. The first is termed reflection and it comprises of taking the highest points of the shape and passing them through the opposite face of the simplex to a lower point. The simplex can also expand in one or more directions in order to take larger steps. In addition, when the simplex reaches a “valley floor” it tries to move down it by contracting in the transverse direction to the valley. Finally, the simplex contracts itself in all directions around its best point when trying to move through “the eye of the needle”.

These steps describe the movement of the simplex downhill through the N-dimensional topography until it meets the termination criteria. The algorithm can be stopped by several user-defined criteria. Typically, the algorithm is terminated when the vector distance moved during a step is smaller in magnitude than a tolerance tol. Alternatively, a tolerance value can be chosen in terms of the function value $ftol$.

Although the algorithm has been found to be efficient it might be fooled by a single large anomalous step and the algorithm does not converge. Therefore, it might be required to restart the model. The re-initialization process is ad hoc and its efficiency unpredictable. However, a commonly implemented strategy is to choose one of the vertices of the previous minimum output simplex as P_0 and to re-start the downhill simplex algorithm. Furthermore, to ensure the solutions found with this algorithm were not local minima several tests were made with different initial conditions.

3.5.3 Sensitivity analysis

The models created have tens of ODE´s and a large number of parameters. Therefore, it is important to evaluate the parameters that have a negligible impact and those parameters that are essential for the predictions of the models. Sensitivity analysis algorithms provide a systematic way of evaluating the relevance of parameters for the output of the models.

There are two main categories for sensitivity analysis (SA) algorithms local (LSA) and Global Sensitivity Analysis (GSA). The former are techniques that investigate the effects of small variations of parameters around a well-defined region. When there are large parameter uncertainties and there the models are nonlinear GSA methods are more appropriate. These methods investigate simultaneous changes of parameter variations and allow to quantify the effects of individual parameters as well as the relationships between parameters.

Another consideration for choosing a SA method is its computational cost. The work by Summer *et al*. [259] has compared different strategies for SA. In particular, the variance based Sobol method and the screening Campolongo-Morris (C-M) method. When applying it to an insulin model with 20 free parameters the Sobol method took more than a day and the C-M method took 15 min to arrive at similar conclusions. As in the fields tackled in this work, there are many parameters that had to be estimated (in some cases approximately 60) it was assumed that a screening strategy would be more sensible.

Besides the C-M method, there have been suggested many screening methodologies. These include iterated fractional factorial design (IFFD), the sequential bifurcation (SB) and the Cotter's design. However, all of these methods in order to have valuable results require that particular assumptions are ensured. The IFFD and SB methods are group-screening methods, which means that parameters need to be grouped before the analysis is performed. The IFFD model only has meaningful results if the model output is only affected by a small number of parameters. The SB requires the user to know the direction of changing each parameter. The Cotter design, in turn, might miss important parameter effects if they cancel each other out. The C-M method does not require any of these assumptions making it the most flexible screening design and it was used to.

The C-M method was implemented based on the work by Saltelli *et al.* [260]. The method consists in varying each parameter (p_i where, $1 \leq i \leq k$) of the model output function $f(p_i)$ individually within a defined parameter space. The function $f(p_i)$ is defined to evaluate any how any model output $M(p_i)$ is affected by varying parameters. In the case of the work here developed a root mean square (RMS) error was used. The error function was used between the model output with the original parameter values p_O and the new parameter values as:

$$f(p) = \sqrt{\sum \frac{(M(p_0)-M(p_i))^2}{T_M}}, \tag{3.34}$$

where T_M is the number of elements in $M(p_i)$.

For each p_i a maximum (p_{max}) and minimum (p_{min}) are chosen. The parameter space is explored by establishing a grid. Each parameter can take *n* uniformly distributed values between the extremities of the space as:

$$p_{i,m} = p_{i,min} + m\frac{p_{i,max} - p_{i,min}}{n-1}, \tag{3.35}$$

where, m is an interger between 0 and $n-1$. A k-dimensional grid with *n* levels is formed with $p_{i,m}$ values as entries. Let $\boldsymbol{p}$ be the current point on the grid corresponding to the complete set of parameters for which the model is tested. Let Δ_i be defined as

$$\Delta_i = m_{\Delta,i}\frac{p_{i,max} - p_{i,min}}{n-1}, \tag{3.36}$$

Then a change of the current point on the grid to a new one can be defined as

$$\boldsymbol{p} = [p_1+\Delta_1, \dots, p_i + \Delta_i, \dots, p_k + \Delta_k] \tag{3.37}$$

with values $m_{\Delta,i}$ defining the number of grid point steps by which the jump occurs for each parameter. In the C-M method only one parameter is varied in turn by Δ_i.For each such change the gradient $d_i(\boldsymbol{p})$ is calculated as:

$$d_i(\boldsymbol{p}) = \frac{f(p_1, \dots, p_i + \Delta_i, \dots, p_k) - f(\boldsymbol{p})}{\Delta_i}, \tag{3.38}$$

Each $d_i(p)$ is called an elementary effect (EE). There are a total of $n^{(k-1)}(n-1)$ EE's.

Starting at a randomly chosen base point $\boldsymbol{p^0}$ a trajectory of $k+1$ values of $\boldsymbol{p}$ are generated by incrementing each parameter p_i by $\pm\Delta_i$ in turn. Each point differs from the precious value in only one parameter. From two points an EE is calculated that pertains to one parameter p_i. Then the process is repeated for r trajectories, requiring a total of $r(k+1)$ function evaluations.

From all the EEs the standard deviation (σ) and the absolute mean (μ^*) are calculated for each p_i. The advantage of computing the absolute mean is that it captures the cumulative effect of varying each parameter in contrast to the mean which would be affected by the signs of EEs. A large μ^* establishes that the parameter has a large effect on the output while those with a small are unimportant. Additionally, the σ can be used to identify those parameters, which have a linear independent effect (small σ) and those with a nonlinear effect and that interact with other parameters (large σ).

The SIMLAB package as presented in [261] was used to apply the algorithm to the models created. In all the cases that it was implemented, the number of levels n was chosen to be even and $m_\Delta = n/2$. The reason for these choices is that, as presented by Morris [69], they guarantee an equal probability sampling from each F_i.

3.5.4 Symbolic regression

In the previous section, a method was introduced that aims at identifying the most relevant kinetics of model in an effort to understand if the model can be simplified. However, in certain cases the intricacies of model kinetics are of no interest. In these cases, an effort was made to reduce the model to a black box that accepts certain inputs and provides the desired outputs.

The cases considered the relationship between inputs and outputs is simple (e.g. second order model). A simple regression algorithm would be sufficient to characterise the model. However, there have been great leaps in the state of the art of symbolic regression that is of great interest. To explore that literature a more complex algorithm was used. In particular, the tools provided by Eureqa [262]. This is a software developed by Nutonian. The software uses symbolic regression to create an initial population of functions based on user specified blocks, which are stored as the operator and the terminal sets [70]. These building blocks consist of a range of operators, e.g. arithmetic, trigonometric, and exponential. Then the genotype is organized as a parse tree where the top and middle of the tree is created from the operator set while the leaves consist of members from the terminal set. The phenotype then results from a function created from this parse tree.

After defining the initial population, the evolutionary algorithm techniques of mutation and crossover are applied to generate offspring. Eureqa implements a single point crossover. This technique consists in swapping a random branch between two individuals, forming two offspring. Mutations consist of selecting a random location in the tree and swapping an operator by another of the same number of arguments. Additionally, the mutation might involve swapping a terminal node with another member of the terminal set. The probabilities for the occurrence of crossing and mutation are commonly defined as $\geq 50\%$ and approximately 1% respectively.

To improve the efficiency of its algorithm, Eureqa implements a method to run genetic algorithms in parallel, entitled the island genetic algorithm [263], [264]. In the context of the EA in Eureqa, the initial population consists of different “islands” that evolve independently. They are allowed to interact with each other at predefined intervals and a percentage of the population is exchanged between random “islands”. By having several “islands” running separately it can explore a larger area of the solution space and the migratory events help to prevent premature convergence.

Furthermore, Eureqa employs another optimizing criterion to prevent premature convergence called age-fitness Pareto [265]. This method consists of considering the age of genetic material besides the error of minimization of an object. The initial population is given an age of one and during crossover, the children inherit the age of the oldest parent. The optimal solution consists of the solution with the highest fitness and minimum age.

The software is used in the work developed here to identify functions to try to simplify the large models to the simplest possible form. As an example, where it is implemented here is in reducing the complement models. In the context of NMO, only the production of MAC is required from all the proteins involved in the complement model. Therefore, a function was created that has as input the triggers for the classical pathway and the output is MAC concentration. As a disclaimer, it is important to note that Eureqa is software under constant update. Therefore, the analysis presented here relates to Eureqa version 8.1.

3.6 Summary

The field of mathematical modelling of neuro degenerative and neuro inflammatory diseases is still relatively novel. However, as presented in this section, there are already several mathematical models of the physiological mechanisms that are targeted by said pathologies. The models developed consist of appropriating the literature by combining the models of the mechanisms believed to play a role in the pathology or that are affected by it. This approach has resulted in large models and consequently, efforts have been made to reduce them.

The models for fitting and sensitivity analysis were the state of the art for large ODE models. The simplex algorithm was equipped to handle the large models created as it explores the parameter space without requiring the model derivatives. However, the termination criteria are ad hoc and therefore the algorithm is prone to get stuck in local minima. The sensitivity analysis implemented using the Campolongo-Morris method clearly demonstrates the parameter and variables that are negligible, however, it does not provide any information on the dependency between parameter/variables. This can result in an ad hoc removal of parameters/variables. The tools available to handle large models still take a brute force approach. Therefore, research is still required that will allow for a more sophisticated development and analysis of large models.

Chapter 4

Mathematical model of glutamate release during ischaemic stroke

4.1 Introduction

Approximately 150,000 people per year in the UK have an ischaemic stroke [266]. A further 1 million patients with ischemic stroke history require care. Direct and indirect costs associated with this condition are estimated at £7-8 billion per year (including informal care and lost productivity) [267].

Ischaemic stroke is characterised by the occlusion of a vessel in the brain. The obstruction diminishes the supply of nutrients to the surrounding neurons, glial cells and, through this shortage, impairs active transport of ions leading to oedema and eventually to cell rupture (necrosis) or programmed cell death (apoptosis) [268].

Current treatments aim to remove the clots from the vasculature through the injection of thrombolytic drugs (tissue plasminogen activator therapy - tPA) [269]. However, according to a study with 2,775 patients [269] this therapy incurs 5.9% risk of intra-cerebral haemorrhage against 1.1% in a control group. Therefore, there is a need to quantify the potential benefits of therapy for an individual patient.

Neuro-protective drugs are being developed that target the agents involved in the pathophysiology of stroke, including inflammation, oxidation, oedema and excitotoxicity, as reviewed by [268]. Efficacy of these drugs is dependent on an adequate dosage and suitable combination determined by the state of the patient. In stroke, this state is dynamically changing and it varies significantly from patient to patient due to the topology of the vasculature, area affected by stroke or genetic factors. This heterogeneity requires a personalised approach to treatment through analysis of patient data. Mathematical modelling has a key role in relating reduced brain perfusion to excitotoxic neuronal death.

Apoptosis in stroke is mainly caused by an ionic imbalance, which triggers the uncontrolled release of glutamate – the most abundant neurotransmitter in the brain responsible for chemically translating an action potential (AP) across the synapse [268]. Excessive glutamate concentration in the extracellular space (ECS) is toxic to the post-synaptic neuron as it can cause cell necrosis and apoptosis as well as triggering genes that initiate post-ischaemic inflammation [268]. Therefore, excitotoxicity has been identified as a prime target for stroke therapy [268].

To understand the behaviour of glutamate release during stroke a mathematical model of glutamate release is introduced and here validated in the context both of neuroexcitation with an AP and of severe ischaemic stroke prior to cell membrane depolarization. In the two environments considered here the most relevant mechanisms of glutamate release are intracellular calcium store triggered glutamate release [77] and the inverse uptake by the glutamate transporter [209]. As both mechanisms are dependent on ion concentrations their metabolic requirements and their impact on cellular volume were also included, based on the work in [15].

In Section 4.2 the developed model is presented. The *in vivo* data used for validation of the model is presented and contrasted against the model simulations in Section 4.3. The potential limitations and extensions of the model are further discussed in Section 4.4.

4.2 Materials and methods

The neurotransmitter glutamate is regulated by interactions between neurons and astrocytes. Additionally, glutamate release is dependent on calcium concentration, pH and the membrane potential [209]. Furthermore, as this work aims at in the case of ischaemic stroke a model of oedema needs to be included, as cell swelling has a significant impact on the concentration of ions inside and outside of the cell [15]. The regulation of these processes requires metabolites. The starting point for this work was to find models that considered these mechanisms.

From the models found in the literature one was chosen to work as the basis to which the glutamate model was built upon. In section 4.2.1 the choice of a metabolic model and the reasons for such a choice are presented. This section is then followed by sections describing how the glutamate model was developed: intra-neuronal glutamate storage (section 4.2.2), the mechanisms of glutamate release considered (section 4.2.3), section 4.2.4 the changes required to consider the glutamates valence are presented and in section 4.2.5 other mechanisms required for validation of the model with AP data and microdialysis measurements are described.

Most of the physiological parameters of the model are based on reports on Calyx of Held neurons for which data are most abundant. Other fundamental assumptions made during the development of the model are summarised in Appendix 4.A.

4.2.1 Brain ischaemic stroke model

There are several integrative models of the metabolic stress caused by ischaemic stroke in the literature, e.g. [15], [65], [268]. From the models found only [15] and [65] are appropriate as they both consider: neuronal, astrocytic and ECS glutaminergic, ionic kinetics and changes of these compartments volume during the ischaemic stroke.

The model by Dronne *et al*. [65] is the only one that considers glutamate release in the presence of stroke. It also successfully reproduces sodium, potassium, calcium and chloride concentrations during a severe stroke. However, it only considers one form of glutamate release (inverse function of the glutamate transporter [209]). Additionally, the rates of ion exchange are several orders of magnitude faster than the microdialysis measurements of ion concentration during severe stroke presented by [270]. Furthermore, glutamate kinetics have not yet been validated with experimental data. The reason for these disparities might be due to neglecting either cellular metabolic reactions or pH kinetics as the availability of ATP and the concentration of H^+ have both been shown to affect ion exchange between compartments [14], [271].

Therefore, the model by Orlowski *et al.* [15] was chosen as it is the only one that has validated cellular metabolism, ionic movement, cellular oedema and pH kinetics in the presence of ischaemic stroke. Additionally, the model by [15] already includes glutamate kinetics, which were validated in the context of a simplified neuro-stimulation trigger in a preceding work by [200]. In [15] brain tissue is divided into four compartments: a neuron, an astrocyte, ECS and vasculature. The model is summarized in Figure 4.1.

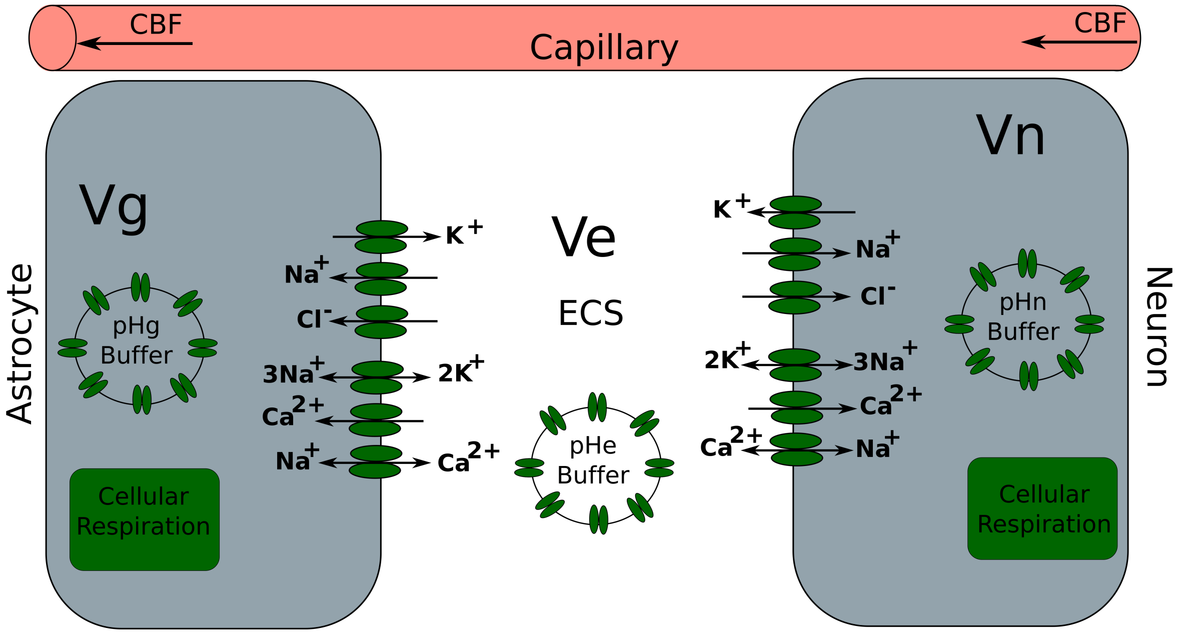

Figure 4.1: Diagram of the Orlowski *et al.* [15] model that includes four compartments: neurons, astrocyte, capillary and the ECS. It models the interactions between these compartments in terms of metabolites, pH and ions. Furthermore, it is able to simulate cytoxic oedema caused by stroke.

However, Orlowski *et al.* [15] did not validate the concentration of individual ions in the presence of ischaemic stroke. Glutamate release is dependent on calcium concentration that permeates the neuron. Therefore, it is necessary to ensure that the Orlowski *et al.* predicts a physiological intaneuronal concentration of calcium during ischaemic stroke. A simulation of a severe stroke using the Orlowski *et al.* model was performed by reducing cerebral blood flow (CBF) following Equation 4.1.

$$CBF = F - \frac{F\alpha}{1 + e^{-30(t-t_1)}} + \frac{F\alpha}{1 + e^{-30(t-(t_1+t_2))}} \tag{4.1}$$

where F is the basal value of CBF [/s]; t is time [s], α is percentage of CBF reduction during stroke [dimensionless], t_1 [s] is the time at which the stroke is initiated and t_2 [s] is the duration of the stroke. The parameter -30 [/s] was chosen to ensure that there is a steep decrease in CBF.

For a severe stroke simulation CBF was reduced by 95% by making α equal to 0.95. The stroke was triggered (t_1) at 900 seconds after the simulation is initiated and reperfusion was not considered ($t_2 \gg t_1$). From the simulation, it was found that as measured by Silver *et al.* calcium increases by 3-4 orders of magnitude from approximately 6×10^{-4} to 0.55 mM, as shown in Figure 4.2. Ensuring such a behaviour it is now possible to build the glutamate model as described in the following sections.

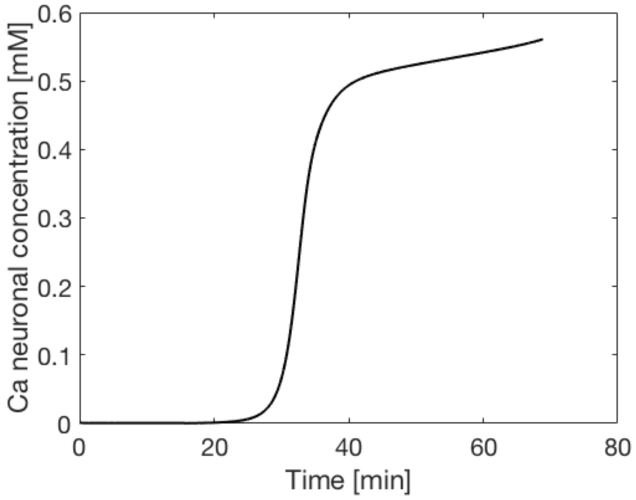

Figure 4.2: Intraneuronal calcium concentration when stroke is simulated using the Orlowski *et al.* [15]. An ischaemic stroke was simulated when CBF is reduced by 95% and it was triggered 15 min after the simulation was initiated.

4.2.2 Intra-neuronal vesicle kinetics

Intra-neuronal glutamate is stored within vesicles of variable diameter. It was assumed here that the diameter is homogeneous between vesicles and set to 40 μm, the mean diameter of Calyx of Held neurons [272]. The vesicles, as described by [76], are distributed between three pools: the reserve pool (RP), the recycling pool (Rc) and the ready releasable pool (RRP). The number of vesicles and the sizes of the pools are dependent on the type of neuron. In the case of the Calyx of Held there are about 190,000 vesicles and the RP, Rc and RRP hold 95, 4 and 1% of them respectively [76].

The RRP consists of vesicles that are fused to the membrane wall in order to ensure immediate release during stimulation. The remaining vesicle pools maintain in a RRP replenished state. The mechanisms of glutamate release are described in Section 4.2.3. After release, vesicles are recycled through one of the three recycling pathways: 1) vesicles are endocytosed after release and join one of the pools ('kiss-and run'); 2) fused vesicles are endocytosed as neurotransmitters are up-taken by the cell ('kiss-and-stay') and 3) after release, vesicles are broken down into an endosome from which new vesicles are formed (endosome recycling) [271]. For fast synapses like the Calyx of Held the theory that best describes vesicle recycling is the 'kiss-and-run' model [273].

The work presented by [274] consists in the most advanced model of a vesicle pool system. This model from [274] includes all rates of vesicle movement between pools for healthy behaviour as well as two additional pools: the fused pool (FP) and the endocytosed pool (ED), which allows for the representation of the 'kiss-and-run' dynamics.

Furthermore, it has been identified that the movement and refill of vesicles are dependent on the frequency of stimulation of the neuron and on the intra-cellular concentration of glutamate [218] through a process called short-term plasticity. This mechanism is characterised by ATP requirements of vesicle neurotransmitter refill and motility. During ischaemic stroke this process is relevant due to the scarcity of ATP. However, the ATP requirements of vesicles have not yet been quantified. Consequently, the approximation presented in [218] is implemented here where the pool refill rate (β_{pool} [/s]) is dependent on: 1) the intra-vesicular glutamate concentration - quantal size (h [dimensionless]); and 2) on the number (n [dimensionless]) of vesicles in the pool:

$$\beta_{pool}(t) = \beta_{max} \times \left(1 - e^{-\frac{h(t)}{h_0}}\right) \times \left(1 - \frac{n(t)}{n_0}\right) \tag{4.2}$$

where β_{max} [/s] is the maximum refill rate, h_0[dimensionless] is the basal vesicular glutamate concentrations and n_0 [dimensionless] is the size of the respective pools.

The quantal, also described by [218], is characterised by constant refill (μ^+ [/s]) and leak (μ^- [/s]) rates of glutamate and is proportional to the intra-neuronal concentration (C [mM]). The quantal size is described by the following:

$$h(t) = \frac{\mu^+}{\mu^-} \times C(t) \tag{4.3}$$

The components of the intra-neuronal vesicle kinetics model are summarised in Figure 4.3. All steady state values and constants for this section of the model can be found in Appendix 4.D.

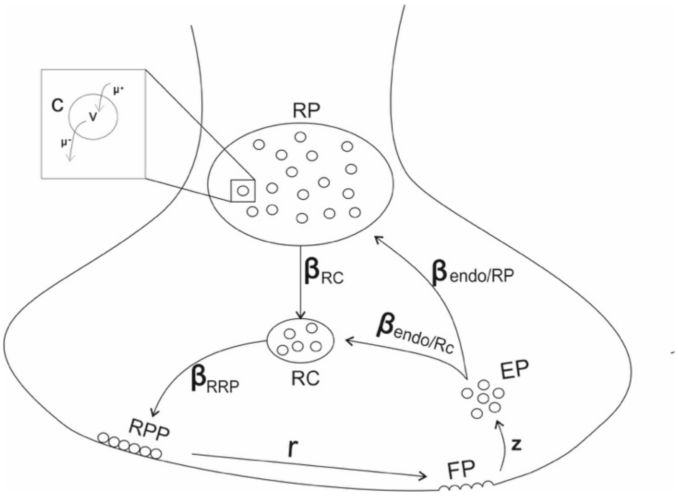

Figure 4.3: Description of the intra-neuronal vesicle pool system which consists in adapting and combining pool refill rates taken from [274], the pool sizes taken from [76] and the short-term plasticity model from [218].

4.2.3 Glutamate release

We are interested in modelling glutamate release in the context of both normal neuro-stimulation with an AP and during ischaemic stroke. Glutamate release differs in these two contexts. AP stimulation is characterised by the depolarisation of the membrane and associated ion movement. Furthermore, it induces glutamate release due to intracellular and extracellular calcium stores (CS). In this case, stimulation drives intracellular calcium $[Ca^{2+}]_i$ to reach a peak, as measured by [275], of 9 μM to 28 μM. This in turn drives glutamate release by vesicle exocytosis. Measured glutamate concentration peak values are between 1 mM and 5 mM [276]. The time frame for an action potential has been measured to be approximately 10 ms and the glutamate current induced has been measured to take from stimulation to steady state a time of between 10 ms to 20 ms [277]

During ischaemic stroke there are several theorised glutamate release triggers: CS; anion channels activated by swelling; the idiomatic-sensitive process in astrocytes; and reverse uptake by the glutamate transporter. As [77] and [209] the release mechanism most relevant in the environments considered are release due to CS and reverse uptake by the glutamate transporter. The release by reverse uptake by the glutamate transporter is done through the glutamate transporter which is voltage and pH dependent and has a stoichiometry of 3:1:1 between sodium, potassium and glutamate, as presented by [209].

Ischaemic stroke physiology includes two stages where these two mechanisms play alternative roles: 1) prior to depolarisation stroke is characterised by changes in osmotic pressure leading to the permeability to calcium which triggers glutamate release by CS, while the glutamate transporter operates in its healthy capacity and uptakes glutamate from the ESC; 2) after depolarisation glutamate release by reverse uptake by the glutamate transporter takes precedence over glutamate release due to intracellular and extracellular calcium stores. The latter mechanism becomes negligible after depolarisation as [209] have shown, glutamate release due to CS only being responsible for 10% of glutamate release during severe ischaemic stroke.

These two mechanisms were implemented according to [77] and [209] respectively. The latter model consists of 18 state equations describing all known forms of CS glutamate release: fast, low frequency triggered synchronous release; slow, high frequency AP train triggered asynchronous release; and spontaneous release. Such a complex model is required for ischaemia since, as [278] has shown, intracellular calcium during stroke increases by 3 to 4 orders of magnitude reaching 1×10^{-1} mM activating all three forms of glutamate release.

The procedure followed by [77] to develop a model that simulates glutamate release due to CS consists in injecting Calyx of Held neurons with marked calcium and measuring the concentration of glutamate released. Therefore, the model presented in [77] only considers glutamate release due to an increase in intracellular glutamate concentration. However, the work presented in [14] states that there is a basal value of intracellular concentration (Ca_0 [mM]). Therefore, in order to combine both models an adaptation to the model from [77] was made ensuring that glutamate does not get released at steady state and that the glutamate release mechanism does not operate due to drops of calcium concentration. The adaptation consisted in making the calcium dependent terms in the model from [77] dependent on the step function α, which is defined as:

$$\alpha = \frac{1}{1 + e^{-\beta \cdot (Ca(t) - Ca_0)}}, \tag{4.4}$$

where β [/mM] is a constant chosen to be 1,000,000 [/mM] in order to ensure there is a rapid activation of glutamate release in response to changes in calcium concentration and $Ca(t)$ [mM] is the intra-neuronal concentration of calcium.

Another adaptation was made to the model from [77] as the spontaneous release is not triggered by CS [209] and the trigger is not known. Additionally, when all modes of release are active spontaneous release is only responsible for approximately 1% of the total release. Hence, it was assumed to be negligible.

4.2.4 Glutamate valence

As glutamate (GLU) has a valence of -1 [76] the membrane potential was made to be dependent on the neurotransmitter kinetics. The model of membrane potential (v $[mV/s]$) by [15] was altered to:

$$\frac{\partial v}{\partial t} = \frac{F \cdot V}{C} \sum \frac{\partial \Delta_{ion}}{\partial t} - \left(\frac{\partial [GLU]_{intra}}{\partial t} - \frac{\partial [GLU]_{extra}}{\partial t} \right) \tag{4.5}$$

where $\frac{\partial \Delta_{ion}}{\partial t}$ $[mM/s]$ is the difference between changes in intra and extra cellular ion, $[GLU]_{intra}$ and $[GLU]_{extra}$ are the intra and extra cellular concentrations of glutamate [mM] respectively, t is time [s], F is Farraday's constant [C/mol], V is the steady state cellular volume [μm^3] and C is the cellular capacity [pF]. The parameter values for Eq.4.5 are provided in Appendix 4.C.

4.2.5 Adaptations for simulations

Three adaptations of the model are necessary to ensure that the physiology is represented with sufficient accuracy: 1) we replace the simple neurostimulation trigger with an altered version of the Huxley and Hodkin model to simulate APs [279]; 2) to ensure that the model captures the rapid evolution of glutamate in the proximity of the synapse, part of the ECS is labelled as a synaptic cleft compartment; and 3) a bi-phasic glutamate extraction mechanism by the astrocyte was included to represent the fact that glutamate is absorbed at different rates during ischaemia and in a normal context.

The Hodkin and Huxley AP model characterises the variance of the membrane potential of the neuron as dependent on the movement of sodium Na^+, potassium K^+ and a non-specific leak current. The parameters that define the model were taken from [279] as they were defined for Calyx of Held neurons. Most importantly the change of the concentration of calcium is captured by the model and hence, as was described previously, this signal can be used as a trigger for the release of glutamate. The addition of the synaptic cleft compartment was necessary as usually glutamate concentration is measured there and not in the ECS. As measured by [37] the cleft has a volume between 0.15×10^{-3} μm^3 and 2.1×10^{-3} μm^3 compared to the ECS volume which is of the order of 1 μm^3 [280]. Hence, the volume of the cleft was assumed to be 10,000 times smaller than that of the ECS.

In [276] it has been identified that the astrocyte has a bi-phasic glutamate extraction depending on how the neuron is stimulated. When glutamate release is induced due to an AP the extraction rate is several orders of magnitude faster than during stroke. Therefore, to reflect this behaviour the Michaelis-Menten extraction kinetics validated by [200] are taken to define astrocytic uptake during stroke simulations while a constant rate four orders of magnitude faster in the case of AP stimulation [279]. All changes made to the Orlowski *et al*. [15] model (in blue) are summarised in Figure 4.4

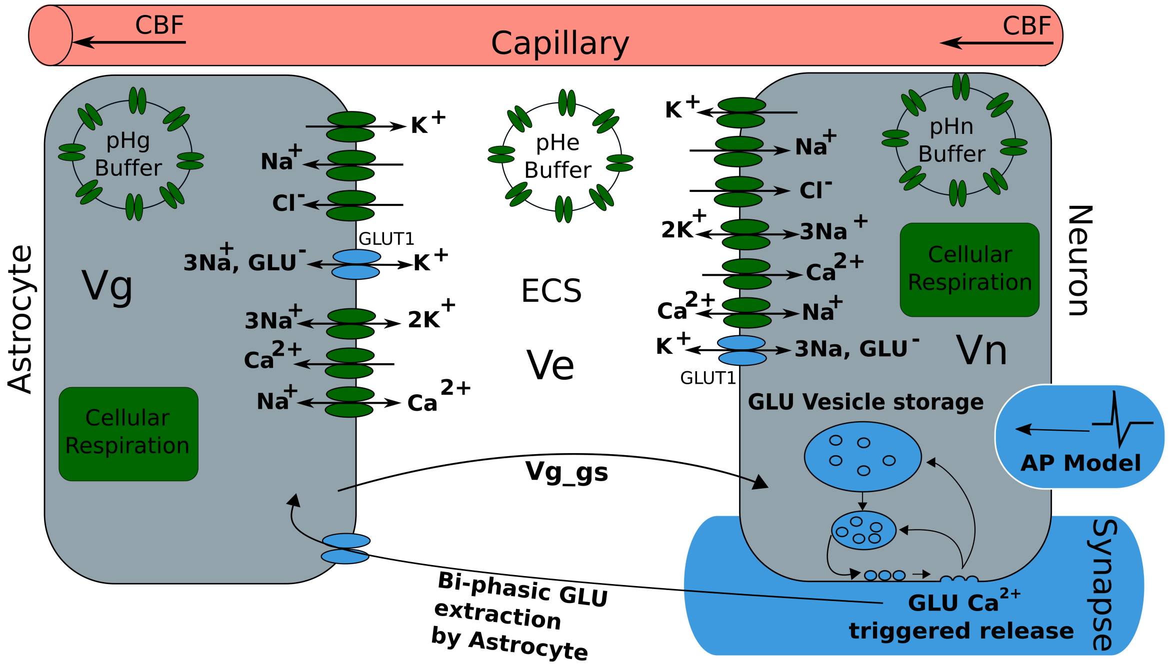

Figure 4.4: Summary of the changes made to the Orlowski *et al.* [15] (in blue) to expand the glutamate kinetics to incorporate glutamate release during stroke that include: intra neuronal glutamate vesicle storage; calcium triggered glutamate release; bi-phasic GLU extraction by astrocytes; an extra compartment to represent the synapse and the Hodgkin and Huxley's AP model.

4.2.6 Experimental data for validation

Different metrics were chosen to validate the model in both a healthy and a diseased context. For the former case it has been found that the peak concentration of glutamate due to an AP is between 1 and 5 mM [276] and that it is extracted back to the basal value within 10 to 20 ms [277].

In order to validate the model, *in vivo* measurements of glutamate concentration before, during and after stroke are required with high temporal resolution. The only type of experimental data found that met these criteria were microdialysis measurements. These experiments consist of inserting a microdialysis probe into rat brains and inducing stroke and re-perfusion by clamping and unclamping all the arteries that feed the brain. During these procedures the probe is used to extract, at a steady rate, samples of the ECF at defined time intervals and the concentration of glutamate is measured in each sample.

Two studies, [88] and [21], have measured glutamate concentration prior to cellular membrane depolarisation after stroke and were chosen to validate our work. The work of [88] consists of simulations of a 5 min stroke where microdialysis samples were collected every 150s at a rate of 0.03

μL/s. There is no mention of how CBF varied throughout the experiment. The animals used were male Mongolian gerbils (total number of rats = 10).

Additionally, [21] simulated stroke for 14min using male Sprague-Dawley rats (total number of rats = 11). The microdialysis samples were extracted every 7 min at a rate of 2.5 μM. CBF during the simulations was measured using a hydrogen clearance method. It is stated that during the induced stroke CBF was reduced by approximately 100% of its basal value.

To produce simulation results in the same format as in these experimental reports the trapezium rule was used to integrate the extracellular glutamate concentration output T according to:

$$T = \frac{r\Delta t}{V_S}\sum_{i}^{N}\frac{[GLU]_e(i\Delta t) + [GLU]_e\big((i+1)\Delta t\big)}{2} \tag{4.6}$$

where i is the number of the current sample, N [dimensionless] is the number of samples, r [mM/s] is the microdialysis extraction rate, Δt [s] is the extraction time for each sample, V_s [L] is the volume of each sample and $[GLU]_e$ [mM] is the extracellular concentration of glutamate output from the model. The different values of Δt were chosen as the ODE solver time step between the two points being calculated therefore ensuring it was small enough so that the error incurred by the numerical integration is minimised.

4.2.7 Implementation

The CellML (University of Auckland, Auckland NZ) code resulting from the work in [67] was used as a base for implementation. Modifications were included and tested using the OpenCell v.0.7 (University of Auckland, Auckland, NZ) software. Additionally, Matlab vR2012a was used to perform the analysis of simulations presented in Section 4.2.6.

4.3 Results

Three sets of simulations were performed: one in a healthy environment (AP) and another two for ischaemic strokes induced for 5 min and 14 min.

4.3.1 Healthy environment

The AP is triggered 0.5 s after the simulation is initiated (Figure 4.5 A). The whole response takes approximately 10 ms. As a result of ionic movement the membrane potential rises to a maximum of +40 mV and subsequently falls to a minimum of -80mV before returning to the basal value of -70mV. These kinetics match the physiological behaviour described in Chapter 2 presented in Figure 2.8.

During the AP simulation $[Ca^{2+}]_i$ (Figure 4.5 B) rises from its basal value of 0.6 μM to 12.67 μM then falling back to 0 μM within 70 ms. The calcium movement drives glutamate to be released into the synaptic cleft as shown in Figure 4.5 C. This reaches a peak of 1.3 mM within 6 ms and then decays to 6 μM within another 6 ms.

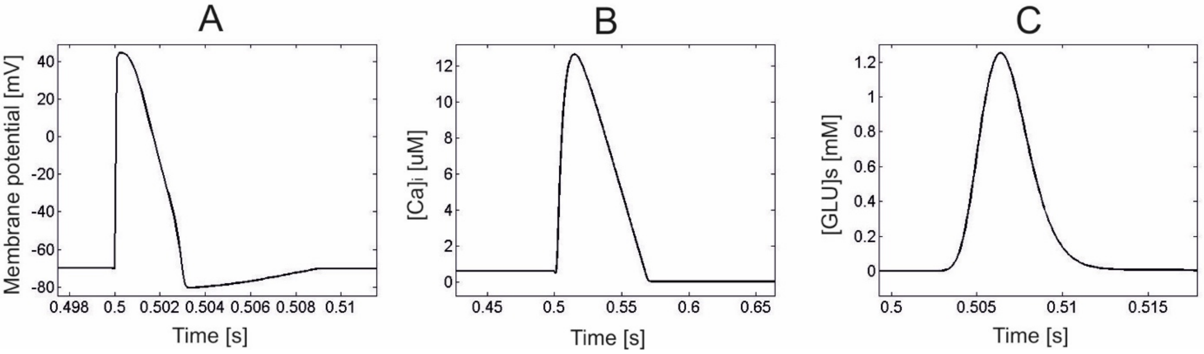

Figure 4.5: Model simulations: A: membrane potential during an AP; B: behaviour of $[Ca]_i$ during an AP; C: Glutamate concentration at the synaptic cleft ($[GLU]_s$) during an action potential.

4.3.2 Stroke Results

For this subset of experiments the data used for validation, taken from [88], are presented in Figure 4.6 A. Here the microdialysis samples were taken every 150 s and each sample had a volume of 4.5 μL. The peak of glutamate concentration at the ECS measured was 3.01 ± 0.34 μM. In order to compare model simulations to the data there are two steps involved: 1) stroke simulations are collected by reducing CBF (parameter α in Equation 4.1) over a range of values; and 2) the trapezium rule is applied to each simulation as in (5), using the parameters taken from the experimental data. The parameter values used are: Δt = 150 s; V_s = 4.5 μL; r = 0.03 μL /s. The concentrations of glutamate 150 s (curve 1) and 300 s (curve 2) after stroke are plotted against the degree of CBF reduction in Figure 4.6 B. Additionally, in Figure 4.6 B the microdialysis measurements presented in Figure 4.6 A as point 1 and 2 with their error margins are included as well as the concentration at which excitotoxicity is initiated.

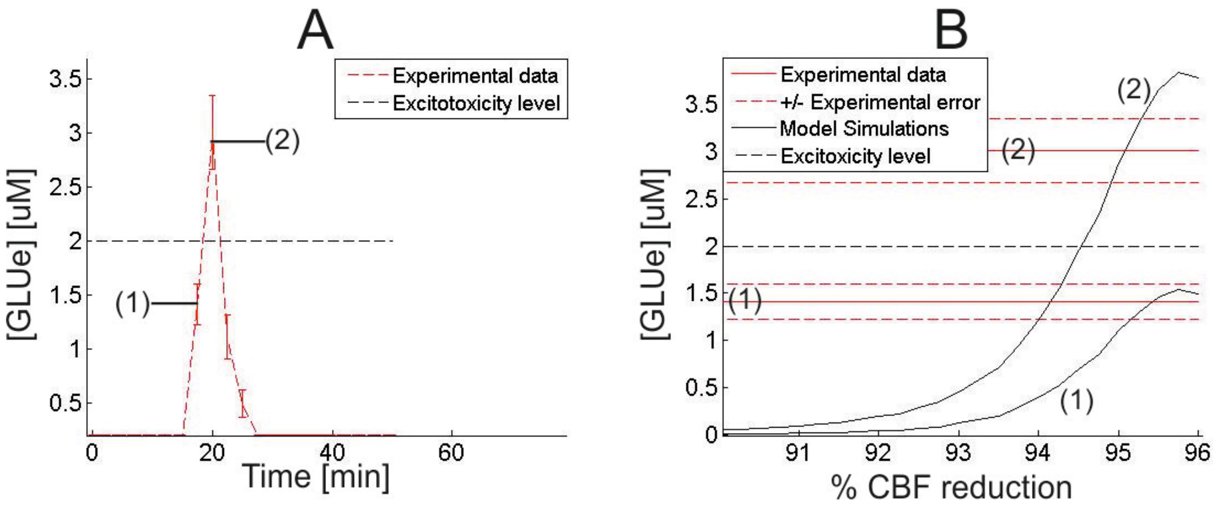

Figure 4.6: A: Data taken from. [88] in which a 5 min stroke is induced to 10 Mongolian gerbils and glutamate concentration is measured using the microdialysis procedure. B: Simulated ECS glutamate concentration as % CBF reduction is varied at 150 s ischaemia (1) and 300 s (2) after ischaemia and compared with the data from Figure 4.6.A at those same points as well as the excitotoxicity threshold.

From Figure 4.6 B it can be seen that for both points the simulations agree with the measured microdialysis range of glutamate concentration when there is a CBF reduction larger than 95%. Furthermore, the curve (2) reaches the glutamate concentration toxic levels, i.e. above 2 μM [281], when CBF is reduced above 94.5%. The data taken from [27] consist of microdialysis samples that are extracted at a rate of 0.0417 μL/s for 420 s and are plotted in Figure 4.7A. The measurements are characterised by a peak glutamate concentration of 8±2.8 µM at a time 630 s after stroke is induced.

Simulations were performed over a range of CBF values. The parameters chosen for Equation 4.6, as presented in [27], were as follows: $\Delta t = 420$s; $V_S = 17.5$ μL; $r = 0.0417$ μL/s. The microdialysis samples are extracted at a time 630 s (point 1 in Figure 4.7 A) after stroke is induced. Therefore, for the simulations the glutamate concentrations 630 s after stroke is initiated is compiled for different CBF levels, as presented in Figure 4.7 B. The latter also includes the concentration measured by [74] presented in Figure 4.7 A as point 1 with its error margin. Additionally, the excitotoxicity concentration threshold is also presented.

It can be observed that a plateau of glutamate concentration is reached for reductions of CBF above 89.5 up to 96%**.** Good correspondence between simulations and the data in [74] is found for CBF reductions above 88.5%. Additionally, neurotoxic levels of glutamate concentration in the synaptic cleft, i.e. 2 µM to 5 µM [26], are reached for CBF reductions of 87.75 % and 88.75 % respectively.

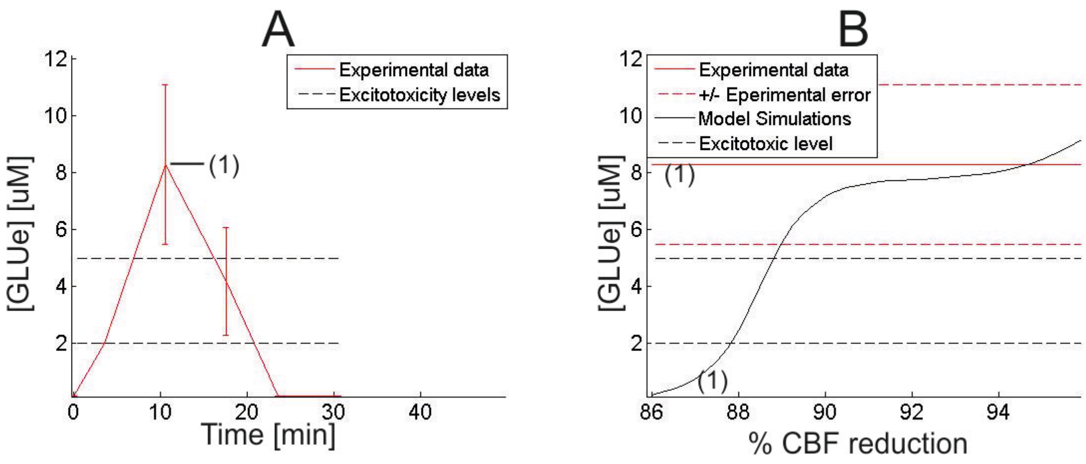

Figure 4.7: A: Data taken from [21] in which a 14 min stroke is induced to 11 Wistar rats and glutamate concentration is measured using the microdialysis procedure. B: Simulated ECS glutamate concentration as % CBF reduction is varied at 7 min after ischaemia (1) and compared with the data from Figure 4.7 A at that same point and the excitotoxicity threshold range is also plotted.

4.4 Discussion

In this section, we discuss both the agreement between the experimental data and the model simulations (Section 4.3); and the key limitations of the model. In particular we focus on potential improvements to the modelling of glutamate extraction rate and of the glutamate transporter and associated ion channels.

´4.4.1 The impact of choosing Calyx of Held kinetics for the model

It should be noted that the Calyx of Held is just one particular type of neuron located in the primary auditory cortex. Although it is not the most common neuron, it is normally used for measurement of intra-neuronal kinetics as its large size facilitates the acquisition. Additionally, Calyx of Held neurons have 1,000 times more vesicles than the average neuron [76] and tend to have a faster release rate for neurotransmitters [76]. However, the model was based on this type of neuron, as there is a lack of data for more common types of neurons. As experimental data as published on more common neurons the model can be updated in the future.

4.4.2 Healthy environment simulations

The results for glutamate release in the presence of an AP are found to be in good agreement with the data. The peak glutamate concentration predicted by the model was 1.25 mM which is within the experimentally measured range of 1–5 mM [277]. Furthermore this peak is reached within 6 ms which also agrees with the experimental measurements [278].

The model predicts that the glutamate current takes 15 ms from its trigger back to its basal concentration of 6 μM. The value reached is within the range of 0.02 μM to 20 μM for basal healthy synaptic concentration stated by [282]. The duration of the current is also within the range stated by [278] of 10 ms to 20 ms.

4.4.3 Stroke simulations

The two sets of stroke simulations have shown agreement with the sets of experimental data. However, in terms of the 5 min stroke simulations, 300s after stroke is induced there is only agreement between the model and the measurements between a CBF drop of 94.75 % to 95.25 %. For larger reductions the maximum concentration reached was 3.8 μM which when compared to the peak concentration measured by [88] of 3.01$\pm$0.34 μM has an error of 26.25 $\pm$ 12.82 %. However, in [88] the CBF levels during the measurements are not stated therefore the magnitude of the error cannot be determined here.

The plateau present in the 14 min simulations as seen in Figure 4.7 B is in agreement with the work of [283]. The later work has shown that for a 30 min stroke and a CBF reduction of between 90% and 96 %, glutamate concentration reaches a plateau. Additionally, there is good agreement between the simulated value 630 s after ischaemia is initiated for a CBF reduction above 88.75% and measured peak glutamate concentration by [21]. For simulation of drops above 96% the cell depolarises and as depolarisation was not modelled a reliable comparison could not be made for these levels.

4.4.4 Astrocyte glutamate clearance rate

Currently, two rates of glutamate clearance by the astrocyte are considered, depending on whether stroke or an AP response is simulated. One hypothesis for this difference might be that glutamate channels are voltage dependent. Hence, when the membrane potential has a fast spike and reaches +40 mV during AP stimulation the rate would be much faster than in the case of stroke where the membrane potential reaches a maximum of -10 mV. This appears to be a promising assumption since the work of [277] has proposed a biphasic clearance rate with decaying times of 100 μsec and 1 ms. However, the reason for such behaviour is not yet known. In order for this work to be verified the interactions between astrocytes and neurons would have to be closely monitored during AP stimulation. However, these measurements might prove to be difficult to acquire due to the very short time scale of these dynamics.

Additionally, in the model presented here it has been assumed that the main mechanism for glutamate removal from the ECS is uptake by the astrocyte. However, [38] have identified that there are other key mechanisms for clearance like diffusion and the binding of glutamate to the post-synaptic glutamate receptors. Due to the lack of experimental data the receptors have not been modelled here.

4.4.5 Glutamate transporter

The work presented in [209] experimentally shows that reverse uptake by the glutamate transporter is responsible for the majority of glutamate release during stroke. However, they also show that the transporter is responsible for release after depolarisation of the membrane. Therefore, although the transporter has been included in our model it does not function as a release mechanism; instead, it is responsible for further uptake of glutamate from the ECS into the neuron.

Modelling cellular behaviour after depolarisation would require more detailed knowledge of apoptotic, necrotic and membrane elasticity properties, which are currently very poorly described. Therefore, this has not been included in this model yet. At the current level of detail and performance the model proposed here is judged to be robust for predicting glutamate release in the moderately hypo-perfused areas of the brain during stroke (the penumbra) or for application to other brain conditions for regions where ischaemia is not so severe.

4.5 Conclusion

A mathematical model which combined a mathematical of cellular metabolic kinetics, cellular ionic regulation and intra and extra cellular glutamate kinetics was created. In terms of intra cellular kinetics the mechanisms modelled were vesicular release triggered by calcium and the inverse reaction of the glutamate transporter following Rossi *et al.* [209]. For the extra-cellular kinetics in order to validate the model in a healthy and diseased environment a bi-phasic rate of astrocytic extraction of glutamate from the ECS was implemented. Additionally, a 5th compartment was included to define synaptic kinetics. With this model, it was possible to validate a model of glutamate release in both healthy and ischaemic stroke conditions. Therefore, being the first mathematical model of glutamate release in a diseased environment. The main assumption of the model is that it only predicts glutamate levels pre-membrane depolarization.

The model is able to associate CBF reduction with glutamate release pre-depolarization, which could be useful when characterizing the penumbra. It could be used to improve the capability of diffusion perfusion mismatch maps at identifying the penumbra. This is because glutamate is the main cause of cell death in stroke and a threshold for neuronal glutamate toxicity has been measured by [21], [88]. Hence it would facilitate identifying tissue at risk in stroke patients and improve the prescription of therapies. Furthermore, the model created could be adapted to test pathological hypothesis of other diseases that are marked by ionic or metabolism deregulation, e.g. Alzheimer's disease where β-amyloid accumulates in the ECS resulting in ionic, metabolic deregulation and it has been reported that toxic levels are present in ECS and responsible for cell death [85].

Appendix 4.A: Summary of assumptions

For convenience, we list the key assumptions made during the model development in Table 4.A1.

Table 4.A.1: Summary of the relevant limits of knowledge on the glutamate cycle and modelling assumptions taken to deal with these challenges.

Knowledge limitations	Modelling assumptions
Unknown ATP requirements for vesicle refill and movement.	Both mechanisms are described as being dependent on intracellular glutamate concentration as presented and validated by [218]
Parameters of glutamate kinetics are known for calyx of held neurons only.	Assume the calyx of held is representative of brain tissue.
The trigger for spontaneous release of glutamate is not known yet.	There is evidence that during stroke and AP stimulation the contribution of spontaneous release is minimal. Hence, discard this mode of release.
Reverse uptake by glutamate transporters is the principle mechanism for glutamate release during severe stroke instead of a calcium trigger.	Since post depolarisation glutamate release is not characterised by the model the glutamate transporter is only responsible for glutamate uptake in the model
The rate of extraction of glutamate is different during stroke and during AP stimulation. Mechanisms responsible for this transition are not known.	Set the extraction rate parameter with either the stroke or AP value depending on the modelled case.

Further omissions were made in the following areas: movement of glutamate from the astrocyte to the neuron and the glutamate and glutamate exchange cycle. These simplifications have been shown by [83] to have a negligible impact on glutamate dynamics and cellular metabolism in both healthy and ischemic conditions.

Appendix 4.B: Metabolic model in [15]

Table 4.B.1: Variables of Cloutier

Variable		Steady-state value	Differential equation
Extracellular states			
GLC_e	Glucose	0.47	$\frac{\partial GLC_e}{\partial t} = v_{GLC}^{ce} - \left(\left(v_{GLC}^{eg}\frac{1}{Reg}\right) + v_{GLC}^{en}\frac{1}{Ren}\right) - y_e GLC_e$
LAC_e	Lactate	0.37	$\frac{\partial LAC_e}{\partial t} = v_{LAC}^{ne}\frac{1}{Ren} + v_{LAC}^{ge}\frac{1}{Reg} - v_{LAC}^{ec} - y_e LAC_e$
Astrocytic and neuronal states			
$O2_n$	Oxygen	0.102	$\frac{\partial O2_n}{\partial t} = R_{en}v_{LAC}^{ne} + R_{eg}v_{LAC}^{ge} - v_{LAC}^{ec} - y_n O2_n$

$O2_g$	Oxygen	0.102	$\frac{\partial O2_g}{\partial t} = R_{en} v_{LAC}^{ne} + R_{eg} v_{LAC}^{ge} - v_{LAC}^{ec} - y_g O2_g$
Capillary			
$O2_c$	Oxygen	7.46	$\frac{\partial O2_c}{\partial t} = v_{O2}^{c} - v_{O2}^{nc} \frac{1}{Rcn} + v_{O2}^{cg} \frac{1}{Rcg}$
$CO2_c$	Carbon dioxide	2.12	$\frac{\partial CO2_c}{\partial t} = kCO2(CO2_{c2} - CO2_c) - 2 \frac{Fin_t}{V_c} (CO2_c - CO2_a)$
GLC_c	Glucose	4.6401	$\frac{\partial GLC_c}{\partial t} = v_{GLC}^{c} - \left(v_{GLC}^{ce} \frac{1}{Rce} + v_{GLC}^{cg} \frac{1}{Rcg} \right)$
LAC_c	Lactate	0.3251	$\frac{\partial LAC_c}{\partial t} = v_{LAC}^{c} + (v_{LAC}^{ec} \times (\frac{1}{Rce}) + v_{LAC}^{gc} \times (\frac{1}{Rcg}))$
Other states			
Vv	Venous volume	0.0237	$\frac{\partial Vv}{\partial t} = F_{int} - F_{out}$
F_{in}	Capillary entering blood flow		$F_{int} = CBF_0 + CBFc\ CBF0 \left(\frac{1}{1 + e^{-30(t - s)}} - \frac{1}{1 + e^{-30\,(time - (s + d))}} \right)$
F_{out}	Capillary leaving blood flow		$F_{out} = \frac{Fin\_t \times \left(\frac{Vv}{Vv0}\right)^{2} + tv \times \left(\frac{Vv}{Vv0}\right)^{-\frac{1}{2}} \times \frac{F_{int}}{Vv0}}{1 + F_{int} \times tv \times \left(\frac{Vv}{Vv0}\right)^{-\frac{1}{2}} \times \frac{1}{Vv0}}$

Table 4.B.2: Kinetic equations for exchange and transport systems

No	Reaction	Differential equation
Transport		
1	GLC exchange between capillary and extracellular fluid	$v_{GLC}^{ce} = vmax_{GLC}^{ce} \left(\frac{GLCc}{GLCc + Km_{ce_{GLC}}} - \frac{GLCe}{GLCe + Km_{ce_{GLC}}} \right)$
2	GLC exchange between extracellular fluid and astrocytes	$v_{GLC}^{cg} = vmax_{GLC}^{cg} \left(\frac{GLCc}{GLCc + Km_{cg_{GLC}}} - \frac{GLCg}{GLCg + Km_{cg_{GLC}}} \right)$
3	GLC exchange between extracellular fluid and neurons	$v_{GLC}^{en} = vmax_{GLC}^{en} \left(\frac{GLCe}{GLCc + Km_{en_{GLC}}} - \frac{GLCn}{GLCn + Km_{en_{GLC}}} \right)$
4	GLC exchange between extracellular fluid and astrocytes	$v_{GLC}^{eg} = vmax_{GLC}^{eg} \left(\frac{GLCe}{GLCc + Km_{eg_{GLC}}} - \frac{GLCg}{GLCg + Km_{eg_{GLC}}} \right)$
5	LAC exchange between extracellular fluid and capillary	$v_{LAC}^{ec} = vmax_{LAC}^{ec} \left(\frac{LACe}{(LACe + Km_{ec_{LAC}})} - \frac{(LACc)}{(LACc + Km_{ec_{LAC}})} \right)$
6	LAC exchange between neurons and extracellular fluid	$v_{LAC}^{ne} = vmax_{LAC}^{ne} \left(\frac{LACn}{(LACn + Km_{ne_{LAC}})} - \frac{(LACe)}{(LACe + Km_{ne_{LAC}})} \right)$
7	LAC exchange between astrocytes and extracellular fluid	$v_{LAC}^{ge} = vmax_{LAC}^{ge} \left(\frac{LACg}{(LACg + Km_{ge_{LAC}})} - \frac{(LACe)}{(LACe + Km_{ge_{LAC}})} \right)$
8	LAC exchange between astrocytes and capillary	$v_{LAC}^{gc} = vmax_{LAC}^{gc} \left(\frac{LACg}{(LACg + Km_{ge_{LAC}})} - \frac{(LACc)}{(LACc + Km_{gc_{LAC}})} \right)$
9	O2 exchange between capillary and neurons	$v_{O2}^{cn} = \frac{PScapn}{Vn} \left(Ko2 \left(\frac{HbOP}{O2c} - 10 \right)^{-\frac{1.0}{nh_{O2}}} - O2n \right)$

10	O2 exchange between capillary and astrocytes	$v_{O2}^{cg} = \frac{PScapg}{Vg}\left(Ko2 \ \left(\frac{HbOP}{O2c} - 1.0\right)^{-\frac{1.0}{nh_{O2}}} - O2g\right)$
11	Blood flow contribution to capillary O2	$vc_{O2} = 2\left(\frac{Fin_t}{Vc}\right)(O2a - O2c)$
12	Blood flow contribution to capillary GLC	$vc_{GLC} = 2\left(\frac{Fin_t}{Vc}\right)(GLCa - GLCc)$
13	Blood flow contribution to capillary LAC	$v_{LAC}^{c} = 2\left(\frac{Fin_t}{Vc}\right).(LACa - LACc)$

Table 4.B.3: Central energy metabolism

Variable		Steady-state value	Differential equation
Neuronal states			
GLC_n	Glucose	0.43	$\frac{\partial GLC_n}{\partial t} = v_{GLC}^{en} - v_{HK}^{n} - y_n GLC_n$
$G6P_n$	Glucose-6-P	0.75	$\frac{\partial G6P_n}{\partial t} = v_{HK}^{n} - v_{PGI}^{n} - v_{C6PDH}^{n} - y_n G6P_n$
$F6Pn$	Fructose-6-P	0.2	$\frac{\partial F6P_n}{\partial t} = v_{PGI}^{n} - v_{PFK}^{n} - v_{PPP}^{n} - y_n F6P_n$
GAP_n	Glyceraldehyde-3-P	0.05	$\frac{\partial GAP_n}{\partial t} = 2.\,v_{PFK}^{n} - v_{PGK}^{n} - v_{mito}^{n} - y_n GAP_n$
PEP_n	Phosphoenolpyruvate	0.025	$\frac{\partial PEP_n}{\partial t} = v_{PGK}^{n} - v_{PK}^{n} - y_n PEP_n$
LAC_n	Lactate	0.28	$\frac{\partial LAC_n}{\partial t} = v_{LDH}^{n} - v_{LAC}^{en} - y_n LAC_n$
ATP_n	Adenosine triphosphate	2.25	$\frac{\partial ATP_n}{\partial t} = \left[-v_{HK}^{n} - v_{PFK}^{n} + v_{PGK}^{n} + v_{PK}^{n} + 15v_{mito}^{n} + v_{CK}^{n} - v_{pump,Na}^{n} - v_{ATPase}^{n}\right]\left[1 - \frac{dAMP_n}{dATP_n}\right]^{-1} - y_n ATPn$
$NADH_n$	Nicotinamide adenine dinucleotide reduced	0.04	$\frac{\partial NADH_n}{\partial t} = v_{PGK}^{n} - v_{LDH}^{n} - v_{mito}^{n} - y_n NADHn \ with \ NADH_n + NAD_n = NADH_{tot}$
PCr_n	Phosphocreatine	4.6401	$\frac{\partial PCr_n}{\partial t} = -v_{CK}^{n} \ with \ PCr_n + Cr_n = PCr_{tot}$
Astrocyte states			
GLC_g	Glucose	0.43	$\frac{\partial GLC_g}{\partial t} = v_{GLC}^{eg} - v_{HK}^{g} - y_g GLC_g$
$G6P_g$	Glucose-6-P	0.75	$\frac{\partial G6P_g}{\partial t} = v_{HK}^{g} - v_{PGI}^{g} - v_{C6PDH}^{g} - y_g G6P_g$
$F6P_g$	Fructose-6-P	0.2	$\frac{\partial F6P_g}{\partial t} = v_{PGI}^{g} - v_{PFK}^{g} - v_{PPP}^{g} - y_g F6P_g$
GAP_g	Glyceraldehyde-3-P	0.05	$\frac{\partial GAP_g}{\partial t} = 2v_{PFK}^{g} - v_{PGK}^{g} - v_{mito}^{g} - y_g GAP_g$
PEP_g	Phosphoenolpyruvate	0.025	$\frac{\partial PEP_g}{\partial t} = v_{PGK}^{g} - v_{PK}^{g} - y_g PEP_g$
LAC_g	Lactate	0.28	$\frac{\partial LAC_g}{\partial t} = v_{LDH}^{g} - v_{LAC}^{eg} - y_g LAC_g$
ATP_g	Adenosine triphosphate	2.25	$\frac{\partial ATP_g}{\partial t} = \left[-v_{HK}^{g} - v_{PFK}^{g} + v_{PGK}^{g} + v_{PK}^{g} + 15.\,v_{mito}^{g} + v_{CK}^{g} - v_{pump,Na}^{g} - v_{ATPase}^{g}\right]\left[1 - \frac{dAMP_g}{dATP_g}\right]^{-1}$
$NADH_g$	Nicotinamide adenine dinucleotide reduced	0.04	$\frac{\partial NADH_g}{\partial t} = v_{PGK}^{g} - v_{LDH}^{g} - v_{mito}^{g} \ with \ NADH_g + NAD_g = NADH_{tot}$
PCr_g	Phosphocreatine	4.6401	$\frac{\partial PCr_g}{\partial t} = -v_{CK}^{g} \ with \ PCr_g + Cr_g = PCr_{tot}$

Table 4.B.4: Kinetic equations for central energy metabolism

No.	Reaction	Differential equation
Neuronal metabolism		
1	Hexokinase	$v_{HK}^{n} = vmax_{HK}^{n} ATP_n \left[\frac{GLCn}{GLCn + Km_{ce_{GLC}}}\right][1 - f(G6P_n, 0.6,20)]$
2	Phosphoglucose isomerase	$v_{PGI}^{n} = vmax_{f,PGI}^{n} \left[\frac{G6Pn}{G6Pn + Km_{G6P}}\right] - vmax_{f,F6P}^{n} \left[\frac{F6Pn}{F6Pn + Km_{F6P-PGI}}\right]$
3	Phosphofructokinase	$v_{PFK}^{n} = k_{PFK}^{n} ATP_n \left[1 + \left(\frac{ATP_n}{KI_{ATP}}\right)^{nH}\right]^{-1} \left[\frac{F6Pn}{F6Pn + Km_{F6P-PFK}}\right]$
4	Phosphoglycerate kinase	$v_{PGK}^{n} = k_{PGK}^{n} GAPnADPn \left[\frac{NADn}{NADHn}\right]$
5	Pyruvate Kinase	$v_{PK}^{n} = k_{PK}^{n}\, PEPnADPn$
6	Mitochondrial oxidation of pyruvate	$v_{mito}^{n} = v_{max,mito}^{n} \left[\frac{PYRn}{PYRn + Km_{PYR}}\right]\left[\frac{ADPn}{ADPn + Km_{ADP}}\right] \left[\frac{O2n}{O2n + Km_{O2n}}\right]\left[1 - f(\frac{ATPn}{ADPn}, 20,5)\right]$
7	Lactate dehydrogenase	$v_{LDH}^{n} = k_{LDH,f}^{n}\, PYR_n NADH_n - k_{LDH,f}^{n}\, LAC_n NAD_n$
8	Creatine kinase	$v_{CK}^{n} = k_{CK,f}^{n}\, PCr_n ADP_n - k_{CK,r}^{n}\, Cr_n ATP_n$
9	ATPase (excluding Na-ATPase)	$v_{ATPase}^{n} = V_{max,ATPase}^{n} \left[\frac{ATP_n}{ATP_n + K_{m,ATP}}\right]$
	Astrocyte metabolism	
10	Hexokinase	$v_{HK}^{g} = k_{HK}^{g}. ATP_g \left[\frac{GLCg}{GLCg + Km_{ce_{GLC}}}\right]\left[1 - f(G6P_g, 0.6,20)\right]$
11	Phosphoglucose isomerase	$v_{PGI}^{g} = vmax_{f,PGI}^{g} \left[\frac{G6Pg}{G6Pg + Km_{G6P}}\right] - vmax_{f,F6P}^{g} \left[\frac{F6Pg}{F6Pg + Km_{F6P}}\right]$
12	Phosphofructokinase	$v_{PFK}^{g} = k_{PFK}^{g} ATP_g \left[1 + \left(\frac{ATP_g}{KI_{ATP}}\right)^{gH}\right]^{-1} \left[\frac{F6Pg}{F6Pg + Km_{F6P}}\right]$
13	Phosphoglycerate kinase	$v_{PGK}^{g} = k_{PGK}^{g} GAPgADPg \left[\frac{NADg}{NADHg}\right]$
14	Pyruvate Kinase	$v_{PK}^{g} = k_{PK}^{g}\, PEPgADPg$
15	Mitochondrial oxidation of pyruvate	$v_{mito}^{g} = v_{max,mito}^{g} \left[\frac{PYRg}{PYRg + Km_{PYR}}\right]\left[\frac{ADPg}{ADPg + Km_{ADP}}\right] \left[\frac{O2g}{O2g + Km_{O2n}}\right]\left[1 - f(\frac{ATPg}{ADPg}, 20,5)\right]$
16	Lactate dehydrogenase	$v_{LDH}^{g} = v_{LDH,f}^{g}\, PYR_g NADH_g - v_{LDH,f}^{g}\, LAC_g NAD_g$
17	Creatine kinase	$v_{CK}^{g} = k_{CK,f}^{g}\, PCr_g ADP_g - k_{CK,r}^{g}\, Cr_g ATP_g$
18	ATPase (excluding Na-ATPase)	$v_{ATPase}^{g} = V_{max,ATPase}^{g} \left[\frac{ATP_g}{ATP_g + K_{m,ATP}}\right]$
	Adenylate kinase (AK) equilibrium (neurons and astrocytes)	
	$ADP = \frac{ATP}{2}\left[-q_{AK} + \sqrt{u}\right]$	
	$\frac{dAMP}{dATP} = -1 + \frac{q_{AK}}{2} - 0.5. \sqrt{u} + q_{AK} \frac{ANP}{ATP\sqrt{u}}$	with $u = q_{AK}^{2} + 4q_{AK}\left(\frac{ANP}{ATP} - 1\right)$

Table 4.B.5: Glycogen storage system

No.	Reaction	Differential equation
Astrocytic state		
GLY_g	Glycogen	$\frac{\partial GLY_g}{\partial t} = v_{GLYS}^{g} - v_{GLYP}^{g}$
Kinetic equations		

1	Glycogen synthase	$v^{g}_{GLYS} = v^{g}_{max,GLYS}\left[\frac{G6Pg}{G6Pg + Km_{G6P}}\right]\left[1 - f(GLY_{g}, 4.2, 20)\right]$
2	Glycogen phosphorylase	$v^{g}_{GLYP} = v^{g}_{max,GLYP}\left[\frac{G6Pg}{G6Pg + Km_{G6P}}\right]\left[1 + f_{GLY}\right]$
3	GLY regulation	$f_{GLY} = \Delta_{GLY}\left[f(t, t_{0,GLY}, 4) - f(t, t_{0,GLY} + t_{end,GLY}, 4)\right]^{*}$

Table 4.B.6: Cloutier *et al.* [200] model parameters

Parameter name	Value	Description	Units
$vmax^{ce}_{GLC}$	0.0489	Maximum transport rate of GLC c to e	mM.s^{-1}
$vmax^{cg}_{GLC}$	0.0098394	Maximum transport rate of GLC c to g	mM.s^{-1}
$vmax^{en}_{GLC}$	0.038089	Maximum transport rate of GLC e to n	mM.s^{-1}
$vmax^{eg}_{GLC}$	0.50417	Maximum transport rate of GLC e to g	mM.s^{-1}
$vmax^{ce}_{LAC}$	0.0325	Maximum transport rate of LAC c to e	mM.s^{-1}
$vmax^{cg}_{LAC}$	0.00021856	Maximum transport rate of LAC c to g	mM.s^{-1}
$vmax^{en}_{LAC}$	0.1978	Maximum transport rate of LAC e to n	mM.s^{-1}
$vmax^{eg}_{LAC}$	0.086124	Maximum transport rate of LAC e to g	mM.s^{-1}
$Km_{ce_{GLC}}$	8.4568	Affinity constant for GLC exchange between c and e	mM
$Km_{cg_{GLC}}$	9.92	Affinity constant for GLC exchange between c and g	mM
$Km_{eg_{GLC}}$	3.53	Affinity constant for GLC exchange between e and g	mM
$Km_{en_{GLC}}$	5.32	Affinity constant for GLC exchange between e and n	mM
$Km_{cg_{GLC}}$	0.129	Affinity constant for LAC exchange between c and g	mM
$Km_{eg_{GLC}}$	0.222	Affinity constant for LAC exchange between e and g	mM
$Km_{en_{GLC}}$	0.09314	Affinity constant for LAC exchange between e and n	mM
$PScap_{n}$	0.2202	O_2 mass exchange constant between c and n	s^{-1}
$PScap_{g}$	0.2457	O_2 mass exchange constant between c and g	s^{-1}
$Ko2$	0.089733	O_2 transport constant	mM
nh_{O_2}	2	O_2 reaction order constant	dimensionless
$vmax^{n}_{HK}$	0.0513	Maximum reaction rate for HK in neurons	mM.s^{-1}
$vmax^{n}_{f,PGI}$	0.5	Maximum forward reaction rate for PGI in neurons	mM.s^{-1}
$vmax^{n}_{r,PGI}$	0.45	Maximum reverse reaction rate for PGI in neurons	mM.s^{-1}
Km_{G6P}	0.5	Affinity for G6P	mM
$Km_{F6P-PGI}$	0.06	Affinity of F6P for PGI	
k^{n}_{PFK}	0.55783	Reaction rate constant for PFK in neurons	mM.s^{-1}
$Km_{F6P-PFK}$	0.18	Affinity of F6P for PFK	mM
k^{n}_{PGK}	0.4287	Reaction rate constant for PGK in neurons	mM.s^{-1}
k^{n}_{PK}	28.6	Reaction rate constant for PK in neurons	mM.s^{-1}
$v^{n}_{max,mito}$	0.05557	Maximum rate of mitochondrial response in neurons	mM.s^{-1}
Km_{PYR}	0.0632	Affinity of PYR for mitochondrial response	mM
Km_{ADP}	0.00107	Affinity of ADP for mitochondrial response	mM
Km_{O2n}	0.0029658	Affinity of O2 for mitochondrial response	mM
$k^{n}_{LDH,f}$	5.30	Maximum forward reaction rate for LDH in neurons	mM.s^{-1}
$k^{n}_{LDH,r}$	0.1046	Maximum reverse reaction rate for LDH in neurons	mM.s^{-1}
$k^{n}_{CK,f}$	0.0524681	Maximum forward reaction rate for CK in neurons	mM.s^{-1}
$k^{n}_{CK,r}$	0.015	Maximum reverse reaction rate for CK in neurons	mM.s^{-1}
$V^{n}_{max,ATPase}$	0.04889	ATPase maximum rate neurons	mM.s^{-1}
$K_{I,ATP}$	0.7595	Inhibition constant for ATP	mM
$vmax^{g}_{HK}$	0.050461	Maximum reaction rate for HK in astrocytes	mM.s^{-1}
$vmax^{g}_{f,PGI}$	0.5	Maximum forward reaction rate for PGI in astrocytes	mM.s^{-1}
$vmax^{g}_{r,PGI}$	0.45	Maximum reverse reaction rate for PGI in astrocytes	mM.s^{-1}
k^{g}_{PFK}	0.403	Reaction rate constant for PFK in neurons	mM.s^{-1}
k^{g}_{PGK}	0.2514	Reaction rate constant for PGK in neurons	mM.s^{-1}
k^{g}_{PK}	2.73	Reaction rate constant for PK in neurons	mM.s^{-1}
$v^{g}_{max,mito}$	0.008454	Maximum rate of mitochondrial response in neurons	mM.s^{-1}
$k^{g}_{LDH,f}$	6.2613	Maximum forward reaction rate for LDH in neurons	mM.s^{-1}
$k^{g}_{LDH,r}$	0.54682	Maximum reverse reaction rate for LDH in neurons	mM.s^{-1}
$k^{g}_{CK,f}$	0.0243	Maximum forward reaction rate for CK in neurons	mM.s^{-1}

$k^{g}_{CK,r}$	0.015	Maximum reverse reaction rate for CK in neurons	mM.s^{-1}
$V^{g}_{max,ATPase}$	0.035657	ATPase maximum rate neurons	mM.s^{-1}
q_{AK}	0.92	Equilibrium constant for AK	dimensionless
$v^{g}_{max,GLYS}$	0.0022	Maximum rate for GLY synthase	mM.s^{-1}
$v^{g}_{max,GLYP}$	0.008	Maximum rate for GLY phosphorilase	mM.s^{-1}
Km_{AMP}	0.016	Affinity of GLY for glycogen synthase	mM

Table 4.B.7: Physical constants and known concentrations

Parameter name	Value	Description	Units
$NADH_{tot}$	0.22	Total NAD+NADH	mM
PCr_{tot}	5.0	Total $PCr + Cr$	mM
O_{2a}	8.34	Arterial O_2 concentration	mM
CO_{2a}	1.2	Arterial CO_2 concentration	mM
GLC_a	4.8	Arterial GLC concentration	mM
LAC_a	0.313	Arterial LAC concentration	mM
k_{pump}	3.17×10^{-7}	Transport rate constant	cm.mM.s^{-1}
CBF_0	0.012	Cerebral blood flow steady state value	s^{-1}
nOP	15	Oxidative phosphorylation ratio	dimensionless
$V_{V,0}$	0.0236	Base venous volume	dimensionless
$HbOP$	8.6	O_2 concentration with haemoglobin	mM
F	96500	Molecular charge	C.mol^{-1}
RT	2577340	Perfect gas constant and temperature	kPa
V_m	-70	Membrane potential	mV
GLY_0	2.5	Steady state value of GLY	mM

Table 4.B.8: States of the ionic species involved in the pH model [14]

Variable		Steady-state value	Differential equation
Neuronal states			
H_n	Hydrogen ions	3.98×10^{-5}	$\frac{\partial H_n}{\partial t} = v^{n}_{buffer} - v^{n}_{CK} - \frac{\partial ATP_n}{\partial t} + \frac{\partial LAC_n}{\partial t} + v^{n}_{NHE} - y_n H_n$
$HCO3_n$	Bicarbonate	15.77	$\frac{\partial HCO3_n}{\partial t} = k_{f2}\, H2CO3_n + k_{b3} CO3_{2n}\, H_n - k_{f3} HCO3_n - k_{b2} H_n HCO3_n - y_n HCO3_n$
$CO3_{2n}$	Carbon trioxide	0.01989	$\frac{\partial CO3_{2n}}{\partial t} = k_{f3}\, HCO3_n - k_{b3} CO3_{2n}\, H_n - y_n CO3_{2n}$
$H2CO3_n$	Carbonic acid	0.0015	$\frac{\partial H2CO3_n}{\partial t} = k_{f1} CO3_{c2} + k_{b2}\, HCO3_n H_n - (k_{f2} + k_{b1}) H2CO3_n - y_n H2CO3_n$
Astrocyte states			
H_g	Hydrogen ions	3.98×10^{-5}	$\frac{\partial H_g}{\partial t} = v^{g}_{buffer} - v^{g}_{CK} - \frac{\partial ATP_g}{\partial t} + \frac{\partial LAC_g}{\partial t} + v^{g}_{NHE} - y_g H_g$
$HCO3_g$	Bicarbonate	15.77	$\frac{\partial HCO3_g}{\partial t} = k_{f2}\, H2CO3_g + k_{b3} CO3_{2g}\, H_g - k_{f3} HCO3_g - k_{b2} H_g HCO3_g - y_g HCO3_g$

$CO3_{2g}$	Carbon trioxide	0.01989	$\frac{\partial CO3_{2g}}{\partial t} = k_{f3}\ HCO3_g - k_{b3}CO3_{2g}\,H_g - y_g CO3_{2g}$
$H2CO3_g$	Carbonic acid	0.0015	$\frac{\partial H2CO3_g}{\partial t} = k_{f1}CO3_{c2} + k_{b2}\ HCO3_g H_g - (k_{f2} + k_{b1})H2CO3_g - y_g H2CO3_g$
ECS states			
H_e	Hydrogen ions	0.0000631	$\frac{\partial H_e}{\partial t} = v_{buffer}^{e} + \frac{1}{R_{eg}}\frac{\partial LAC_g}{\partial t} + \frac{1}{R_{en}}\frac{\partial LAC_n}{\partial t} + \frac{1}{R_{eg}}v_{NHE}^{g} + \frac{1}{R_{en}}v_{NHE}^{n} - y_e H_e$
$HCO3_e$	Bicarbonate	25	$\frac{\partial HCO3_g}{\partial t} = k_{f2}\ H2CO3_e + k_{b3}CO3_{2e}\,H_e - k_{f3}HCO3_e - k_{b2}H_e HCO3_e - y_e HCO3_e$
$CO3_{2e}$	Carbon trioxide	0.05	$\frac{\partial CO3_{2e}}{\partial t} = k_{f3}\ HCO3_e - k_{b3}CO3_{2e}\,H_e - y_e CO3_{2e}$
$H2CO3_e$	Carbonic acid	0.0015	$\frac{\partial H2CO3_e}{\partial t} = k_{f1}CO3_{c2} + k_{b2}\ HCO3_e H_e - (k_{f2} + k_{b1})H2CO3_e - y_n H2CO3_e$
Capillary states			
$CO2_{c2}$	Carbon dioxide	2.5	$\frac{\partial CO2_{c2}}{\partial t} = \frac{\left(\frac{1}{Rcn}v_{c_{CO2}}^{n} + \frac{1}{Rcg}v_{c_{CO2}}^{g} - k_{CO2}\,(CO2_{c2} - CO2_c)\right)}{\left(\frac{1 - V_c}{V_c}\right)}$

Table 4.B.9: Kinetic equations for the pH model

No.	Reaction	Differential equation
Neuron		
1	Cellular buffer solution	$v_{buffer}^{n} = k_{f3}HCO3_n - k_{b3}CO3_{2n}H_n - k_{b2}HCO3_n H_n + k_{f2}\ H2CO3_n$
2	Na^+/H^+ antiporter	$v_{NHE}^{n} = \begin{cases} \frac{-v_{max}^{Na}(Na_e - Na_n)}{VF(K_m^{Na} + Na_e - Na_n)}\frac{1}{1 + e^{\alpha(-6.7+pH_n)}}1000\ when\ pH \leq 7.2 \\ 0\ otherwise \end{cases}$
3	pH calculation from H^+ concentration	$pH_n = -\log\left(\frac{H_n}{1000}\right)$
Astrocyte		
4	Cellular buffer solution	$v_{buffer}^{g} = k_{f3}HCO3_g - k_{b3}CO3_{2g}H_g - k_{b2}HCO3_g H_g + k_{f2}\ H2CO3_g$
5	Na^+/H^+ antiporter	$v_{NHE}^{g} = \begin{cases} \frac{-v_{max}^{Na}(Na_e - Na_g)}{VF(K_m^{Na} + Na_e - Na_g)}\frac{1}{1 + e^{\alpha(-6.7+pH_g)}}1000\ when\ pH \leq 7.2 \\ 0\ otherwise \end{cases}$
6	pH calculation from H^+ concentration	$pH_g = -\log\left(\frac{H_g}{1000}\right)$

Table 4.B.10: Physical constants and known concentrations

Parameter name	Value	Units
k_{f1}	0.11	s^{-1}
k_{f2}	1×10^{4}	s^{-1}
k_{f3}	1.03×10^{4}	s^{-1}
k_{b1}	183.33	s^{-1}
k_{b2}	9508.7	$M\ s^{-1}$
k_{b3}	8.1616×10^{10}	$M\ s^{-1}$
K_m^{Na}	23	mM
v_{max}^{Na}	10	pA

Appendix 4.C: Ionic model [15] plus changes made

Table 4.C.1: Ion Exchange

Variable		Steady-state value	Differential equation
Neuronal states			
Na_n	Sodium	19	$\frac{\partial Na_n}{\partial(t)} = \left(\frac{-iNan - iNaKn\ 3 - iNaCan\ 3}{F\ V} + V_{Namax}\frac{Nae - Nan}{F\ V\ (Km_{Na} + Nae - Nan)}\left(\frac{1}{1 + \mathrm{e}^{-1\times10^{5}\,(-6.7+pHn)}}\right) - \frac{iNa_{act}}{(F\ V)}\right) 1000 - yn\ Nan$
K_n	Potassium	130	$\frac{\partial(Kn)}{\partial(t)} = \frac{2\ iNaKn - iKn - iK_{act}}{F\ V}\ 1000 - yn\ Kn$
Cln	Chloride	9.03609	$\frac{\partial(Cln)}{\partial(t)} = \frac{(iCln + iCl_{act})}{VF} 1000 - yn\ Cln;$
Ca_n	Calcium	0.0006	$\frac{\partial Can}{\partial t} = \frac{2\ iNaCan - iCan}{2\ F\ V}\ 1000 + iCa_{act} - ynCan;$
Astrocyte states			
Na_g	Sodium	19	$\frac{\partial Na_g}{\partial t} = \left(\frac{-iNag - iNaKg\ 3 - iNaCag\ 3}{F\ V} + V_{Namax}\frac{Nae - Nag}{F\ V\ (Km_{Na} + Nae - Nag)}\left(\frac{1}{1 + \mathrm{e}^{-1\times10^{5}\,(-6.7+pHn)}}\right)\right) 1000 - yg\ Nag$
K_g	Potassium	130	$\frac{\partial Kg}{\partial t} = \frac{2\ iNaKg - iKg}{F\ V}\ 1000 - yg\ Kg$
Cl_g	Chloride	9.03609	$\frac{\partial Clg}{\partial t} = \frac{(iClg)}{VF} 1000 - yg\ Clg;$
Ca_g	Calcium	0.0006	$\frac{\partial\ Cag}{\partial t} = \frac{2\ iNaCag - iCag}{2\ F\ V}\ 1000 - ygCag;$
Extra cellular space states			
Na_e	Sodium	140	$\frac{\partial Na_e}{\partial t} = -\frac{1}{Ren}\frac{\partial Na_n}{\partial t} - \frac{1}{Reg}\frac{\partial Na_g}{\partial t} - ye\ Nae$
K_e	Potassium	5	$\frac{\partial K_e}{\partial t} = -\frac{1}{Ren}\frac{\partial K_n}{\partial t} - \frac{1}{Reg}\frac{\partial K_g}{\partial t} - ye\ Ke$
Cl_e	Chloride	1240046	$\frac{\partial Cl_e}{\partial t} = -\frac{1}{Ren}\frac{\partial Cl_n}{\partial t} - \frac{1}{Reg}\frac{\partial Cl_g}{\partial t} - ye\ Cle$
Ca_e	Calcium	2.0023	$\frac{\partial Cl_e}{\partial t} = -\frac{1}{Ren}\frac{\partial Cl_n}{\partial t} - \frac{1}{Reg}\frac{\partial Cl_g}{\partial t} - ye\ Cle$

Table 4.C.2: Ionic Nernst potential potential

No.	Reaction	Equation
Neuronal ionic potentials		
1	Sodium potential	$v_{Na_n} = kT_e \ln\left(\frac{Na_e}{Na_n}\right)$
2	Potassium potential	$v_{K_n} = kT_e\ ln\left(\frac{K_e}{K_n}\right)$
3	Calcium potential	$v_{Ca_n} = \frac{kT_e}{2}\ln\left(\frac{Ca_e}{Ca_n}\right)$

4	Chloride potential	$v_{Cl_n} = kT_e ln\left(\frac{Cl_e}{Cl_n}\right)$
Astrocytic ionic potentials		
5	Sodium potential	$v_{Na_g} = kT_e \ln\left(\frac{Na_e}{Na_g}\right)$
6	Potassium potential	$v_{K_g} = kT_e\, ln\left(\frac{K_e}{K_g}\right)$
7	Calcium potential	$v_{Ca_g} = \frac{kT_e}{2} \ln\left(\frac{Ca_e}{Ca_g}\right)$
8	Chloride potential	$v_{Cl_g} = kT_e ln\left(\frac{Cl_e}{Cl_g}\right)$

Table 4.C.3: Ionic currents

No.	Reaction	Equation
Neuronal potential		
1	Sodium potential	$i_{Na_n} = k_{Na_n} h_n minf_n \sinh\left(\frac{v_n - v_{Na_n}}{2\times kT_e}\right)$ $minf_n = \frac{1}{2}\times(1 + \tanh\left(\frac{v_n - v_{m_n}}{2kT_e}\right)))$
2	Sodium potassium pump	$i_{NaK_n} = k_{NaK_n} ks_n ATP_n \left(1 + \frac{ATP_n}{Km_{pump}}\right)^{-1} \tanh\left(\frac{v_n + 2v_{K_n} - 3v_{Na_n} - v_{ATP_n}}{2\, kT_e}\right) (1 - stim)$
3	Sodium calcium channel	$i_{NaCa_n} = k_{NaCa_n} sinh\left(\frac{v_n - 3v_{Na_n} + 2v_{Ca_n}}{(2\, kT_e)}\right)$
4	Potassium channel	$i_{K_n} = k_{K_n} x_n sinh\left(\frac{(v_n - v_{K_n})}{(2\ kT_e)}\right)$
5	Calcium channel	$i_{Ca_n} = \left(k_{Ca_n}(1 - x_n) dinf_n + k_{bCa_n}\right) sinh\left(\frac{v_n - v_{Ca_n}}{kT_e}\right)$ $dinf_n = \frac{1}{2}\left(1 + \tanh\left(\frac{v_n - vd_n}{\frac{kT_e}{2}}\right)\right)$
6	Chloride channel	$i_{Cl_n} = k_{Cl}\, sinh\left(\frac{v_n - v_{Cl_n}}{kT_e}\right)$
Astrocytic ionic currents		
7	Sodium channel current	$i_{Na_g} = k_{Na_g} h_g minf_g \sinh\left(\frac{v_g - v_{Na_g}}{2\, kT_e}\right)$ $minf_g = \frac{1}{2}\times\left(1 + \tanh\left(\frac{v_g - v_{m_g}}{2kT_e}\right)\right)$
8	Sodium potassium pump	$i_{NaK_g} = k_{NaK_g} ks_g ATP_g \left(1 + \frac{ATP_g}{Km_{pump}}\right)^{-1} \tanh\left(\frac{v_g + 2v_{K_g} - 3v_{Na_g} - v_{ATP_g}}{2\, kT_e}\right)$
9	Sodium calcium channel current	$i_{NaCa_g} = k_{NaCa_g} sinh\left(\frac{v_g - 3v_{Na_g} + 2v_{Ca_g}}{(2\, kT_e)}\right)$
10	Potassium channel current	$i_{K_g} = k_{K_g} x_g sinh\left(\frac{(v_g - v_{K_g})}{(2\ kT_e)}\right)$
11	Calcium channel current	$i_{Ca_g} = \left(k_{Ca_g}(1 - x_g) dinf_g + k_{bCa_g}\right) sinh\left(\frac{v_g - v_{Ca_g}}{kT_e}\right)$ $dinf_g = \frac{1}{2}\left(1 + \tanh\left(\frac{v_g - vd_g}{\frac{kT_e}{2}}\right)\right)$

12	Chloride channel	$i_{Cl_g} = k_{Cl}\, sinh\left(\frac{v_g - v_{Cl_g}}{kT_e}\right)$

Table 4.C.4: Volume model differential kinetics

Variable		Steady-state value	Differential equation
V_n	Neuron volume	0.45	$\frac{\partial V_n}{\partial(t)} = -{V_n}^2 \frac{\sum\ [I_n] - \sum\ [I_e]}{0.45A_{n,0}}$
V_g	Glial volume	0.25	$\frac{\partial V_g}{\partial(t)} = -{V_g}^2 \frac{\sum\ [I_g] - \sum\ [I_e]}{0.25A_{g,0}}$
V_e	ECS volume	0.2	$\frac{\partial V_e}{\partial(t)} = -\frac{\partial V_n}{\partial(t)} - \frac{\partial V_g}{\partial(t)}$

Table 4.C.5: Volume model variables

No.	Reaction	Equation
Neuronal ionic potentials		
1	Volume ratio between e and n	$R_{en} = \frac{V_e}{V_n}$
2	Volume ratio between e and g	$R_{eg} = \frac{V_e}{V_g}$
3	Volume ratio between n and g	$R_{ng} = \frac{V_n}{V_g}$
4	Volume ratio between c and g	$R_{cg} = \frac{V_c}{V_g}$
5	Volume ratio between c and n	$R_{cn} = \frac{V_c}{V_n}$
6	Volume ratio between c and e	$R_{ce} = \frac{V_c}{V_e}$
7	Concentration of insoluble ions in the neuron	$A_n = \frac{0.45A_{n,0}}{V_n}$
8	Concentration of insoluble ions in the astrocytes	$A_g = \frac{0.25A_{g,0}}{V_g}$
9	Intra neuronal concentration correction term	$y_n = \frac{1}{V_n}\frac{\partial V_n}{\partial(t)}$
10	Intra astrocyte concentration correction term	$y_g = \frac{1}{V_g}\frac{\partial V_g}{\partial(t)}$
11	ECS concentration correction term	$y_e = \frac{1}{V_e}\frac{\partial V_e}{\partial(t)}$

Table 4.C.6: Ionic currents of Hodgkin and Huxley model

No.	Reaction	Equation
1	Sodium current	$iNa_{act} = G_{Na}m^3h(v_n - v_{Na})$
2	Potassium current	$iK_{act} = G_K n^4(v_n - v_K)$
3	Chloride current	$iCl_{act} = G_{Cl}(v_n - v_K)$
4	Calcium current	$I_{Ca} = {m_{Ca}}^2 G_{Ca}\,(v_n - v_{Ca})$
5	Calcium channel	$iCa_{act} = -\frac{I_{Ca}A_{btn}}{z_{Ca}FV}1000$

Table 4.C.7: Hodgkin and Huxley model differential kinetics

Variable	Steady-state value	Differential equation
n	0	$\frac{\partial n}{\partial(t)} = A_n(1-n) - B_n n$
m	0	$\frac{\partial m}{\partial(t)} = A_m(1-m) - B_m m$
h	1	$\frac{\partial h}{\partial(t)} = A_h(1-h) - B_h h$
m_{Ca}	0	$\frac{\partial m_{Ca}}{\partial(t)} = \frac{m_{\infty} - m_{Ca}}{t_{m_{Ca}}}$

Table 4.C.8: Hodgkin and Huxley model kinetics

No.	Reaction	Equation
1	Sodium channel activation rate	$A_n = \frac{10(-v_n - 60)}{e^{\left(\frac{(-v_n - 60)}{10}\right)} - 1}$
2	Sodium channel deactivation rate	$B_n = 125\, e^{\frac{-v_n - 70}{80}}$
3	Potassium channel activation rate	$A_m = \frac{100(-v_n - 45)}{e^{\left(\frac{(-v_n - 45)}{10}\right)} - 1}$
4	Potassium channel deactivation rate	$B_m = 4000\, e^{\frac{-v_n - 70}{18}}$
5	Chloride channel activation rate	$A_h = 70\, e^{\frac{-v_n - 70}{20}}$
6	Chloride channel deactivation rate	$B_h = \frac{1000}{e^{\left(\frac{(-v_n - 40)}{10}\right)} + 1}$
7	Calcium channel activation rate	$m_{\infty} = \frac{1}{e^{\left(\frac{(-17 - v_n)}{8.4}\right)} + 1}$

Table 4.C.9: Ionic model parameters

Parameter name	Value	Description	Units
V_{Namax}	10	Maximum Na^+ transport rate of pH channel	pA
Km_{Na}	23	Affinity of Na^+ for the pH sodium channel	mM
kT_e	26.726	Boltzmann constant (k) × temperature (T) × elementary charge (e)	mJ.C^{-1}
k_{Na_n}	5352.3	Sodium channel permeability in neurons	pA
k_{K_n}	48944.1	Potassium channel permeability in neurons	pA
k_{Ca_n}	326.17	Calcium channel permeability in neurons	pA
k_{Cl_n}	1336	Chloride channel permeability in neurons	pA
k_{NaCa_n}	20.19	Sodium calcium channel permeability in neurons	pA
k_{NaK_n}	14.37	Sodium/Potassium pump permeability in neurons	pA
k_{Na_g}	5352.3	Sodium channel permeability in astrocytes	pA
k_{K_g}	48944.1	Potassium channel permeability in astrocytes	pA
k_{Ca_g}	326.17	Calcium channel permeability in astrocytes	pA
k_{Cl_g}	1336	Chloride channel permeability in astrocytes	pA
k_{NaCa_g}	20.19	Sodium calcium channel permeability in astrocytes	pA
k_{NaK_g}	14.37	Sodium/Potassium pump permeability in astrocytes	pA
k_{bCa_n}	0		pA
k_{bCa_g}	0		pA
ks_n	0.089733	O_2 transport constant	mM

ks_g	2	O_2 reaction order constant	Dimensionless
$A_{n,0}$	112.20021	Concentration of insoluble ions in the neuron	mM
$A_{g,0}$	122.20021	Concentration of insoluble ions in the astrocyte	mM
G_{Na}	120×10^3	Permeability of Huxley and Hodgkin's sodium channel	$mS.cm^{-2}$
G_K	36×10^3	Permeability of Huxley and Hodgkin's potassium channel	$mS.cm^{-2}$
G_{Cl}	3×10^2	Permeability of Huxley and Hodgkin's chloride channel	$mS.cm^{-2}$
A_{btn}	1.24	Surface area of neuron	μm^2
z_{Ca}	2	The charge of calcium	Dimensionless
$t_{m_{Ca}}$	10^{-3}	Time variable for the opening of calcium channels during AP	s

Appendix 4.D: Intra-neuronal vesicle kinetics

Table 4.D.1: Equations developed to simulate intra neuronal vesicle kinetics

Description	Equation
RRP pool refill rate	$\beta_{RRP}(t) = \beta_{max/RRP}\times\left(1 - e^{-\frac{h(t)}{h_0}}\right)\times\left(1 - \frac{n(t)}{n_{0/RRP}}\right)$
Vesicle exchange rate RP to RC	$\beta_{Rc}(t) = \beta_{max/Rc}\times\left(1 - e^{-\frac{h(t)}{h_0}}\right)\times\left(1 - \frac{n(t)}{n_{0/Rc}}\right)$
Vesicle endocytosis rate that fills the Rc pool	$\beta_{endo/Rc}(t) = \beta_{endo/Rc}\times\left(1 - e^{-\frac{h(t)}{h_0}}\right)\times\left(1 - \frac{n(t)}{n_{0/Rc}}\right)$
Vesicle endocytosis rate that fills the RRP pool	$\beta_{endo/RRP}(t) = \beta_{endo/RRP}\times\left(1 - e^{-\frac{h(t)}{h_0}}\right)\times\left(1 - \frac{n(t)}{n_{0/RRP}}\right)$
Equation that governs the quantal size of the system	$h(t) = \frac{\mu^+}{\mu^-}\times C(t),$

Table 4.D.2: Constants pertaining to the intra-neuronal vesicle system presented in section 4.2.2 .

Parameter	Value	Units	Reference
$\beta_{max/RRP}$	1.6	/s	[76]
$\beta_{max/Rc}$	0.079	/s	[218]
$\beta_{max/RPi}$	0.8730	/s	[218]
$\beta_{max/RPj}$	0.097	/s	[218]
z	0.097	/s	[218]
$n_{0/RRP}$	3,000	vesicles	[76]
$n_{0/Rc}$	7,000	vesicles	[76]
$n_{0/RP}$	180,000	vesicles	[76]
h_0	100	mM	[218]
μ^+	1	/s	[218]
μ^-	0.1	/s	[218]
C_0	10	mM	[15]

Chapter 5

The role of AQP4 in NMO

5.1 Introduction

Neuromyelitis optica (NMO) is a neuro-inflammatory central nervous system disease characterized by predominant damage to the optic nerve and of the spinal cord. Although rare, with a worldwide incidence of approximately 1 per 100,000, NMO is severe, with a 5-year mortality rate of 32% in patients with a relapsing disease [120].

The IgG1 antibody targeting aquaporin-4 (AQP4) water channels located at the endfeet of astrocytes [45]. The antibody is present in about 60% of NMO patients and is thought to be pathogenic causing the primary astrocytopathy [284]. A mouse model has shown that both AQP4-Ab and human complement in the extracellular space are needed to initiate the pathophysiological process during which astrocytes swell within twelve hours [17]. The swelling has been shown to be due to complement induced membrane lytic holes which facilitate metabolite transport over the membrane and lead to cell growth [17]. In turn, the swelling triggers an inflammatory response marked by granulocyte and macrophage infiltration leading to secondary oligodendrocyte damage, demyelination and neuronal death [45].

There is currently no cure for NMO. Treatment focuses on either the management of the acute phase of the condition or the prevention of relapses using generic immunosuppressive or immunomodulatory treatments [285]. In the former case, the most effective method, out of those trailed, consists of complimentary intravenous injection of methylprednisolone (IVMP) and plasma exchange. The most comprehensive study on the therapeutic effects of plasma exchange is that by [286]. The study consists of the analysis of 59 CNS demyelination patients, where 10 had NMO, who were treated with plasma exchange for acute severe attacks from 1984 to 2000. It found that 44.1% of patients experienced moderate to marked functional improvement.

Current developments focus on inhibiting the breakdown and binding of a range of proteins in the complement cascade. For example, eculizumab binds to C5 and inhibits its cleavage thus preventing further mechanisms leading to membrane lysis. In a pilot study performed by [148], 14 relapsing NMO patients were treated with eculizumab for 12 months. During that period, the average number of relapses fell from 3 to zero. However, these non-controlled data require larger randomized controlled trials to assess true efficacy, which has large resource and cost implications and a greater risk of predictable and unpredictable adverse effects. For example the risk of infection with encapsulated bacteria such as meningococcal infection which is potentially fatal even after vaccination [162].

A promising strategy for complement inhibition is the upregulation of the astrocytic complement inhibitor CD59, which inhibits C5b-9 formation as described by [287]. CD59 is naturally present in astrocytes. However, its concentration has been reported to be smaller in the proximity of the endfeet where the NMO antibody acts. For this reason it is expected that CD59 will have fewer side effects compared to the clinically used therapies above [288].

To evaluate the potential of CD59 there is a need to optimize its dosage and their administration timing. Testing combined effects of novel drugs at different doses at different stages in disease evolution is impossible in patient cohorts, due to both disease rarity and the ethical contraventions in withholding conventional immunosuppression rather than placebo, which is likely to reduce the power to detect a further treatment effect. Furthermore, testing these effects in animal studies or in vitro models is costly, impractical and limited in scope. *In silico* models offer the promise of being able to search for optimal therapeutic regimens and the timing of administration of drugs in simulated environments that can capture the core features of the pathogenic process in disease. However, these methods have been considerably underutilized for studying inflammatory disease.

Hence, we introduce a mathematical model of the swelling of astrocytes during NMO and its modulation by CD59. To capture the pathological cell volume evolution the model extends a state of the art model of metabolism in astrocytes and neurons with a detailed representation of water transport across the cell membrane due to osmotic and hydrostatic pressure. In particular, in addition to representing transport through AQP4 channels and water permeable ionic channels, we model the perforation of the cellular membrane due to NMO specific complement lysis. CD59 acts as a modulator of the complement cascade.

We demonstrate the fidelity of our computational model of the neuroinflammatory environment by demonstrating that the simulation predicts that the primary pathogenic mechanism in NMO is complement induced lysis rather than direct inactivation of AQP4 channels, a fact now experimentally confirmed [17] but originally contentious when the disease was first described. Moreover, we simulate the degree of astrocyte swelling due to complement induced lysis, and map out the time course of this process, and then simulate the impact of a putative therapeutic strategy, CD59 injection on the cellular swelling.

5.2 Materials and methods

As presented by Saadoun *et al.* [17] the process by which antigen antibody binding is responsible for astrocytic oedema is still not fully understood. There are two hypotheses. The first states that the antigen-antibody binding clogs the AQP4 channels. Consequently, astrocytes are unable to regulate hydrostatic pressure leading to the progressive swelling of astrocytes. Alternatively, the other hypothesis is that the astrocytic oedema is caused by complement induced lytic holes. The hypotheses are presented in Figure 5.1.

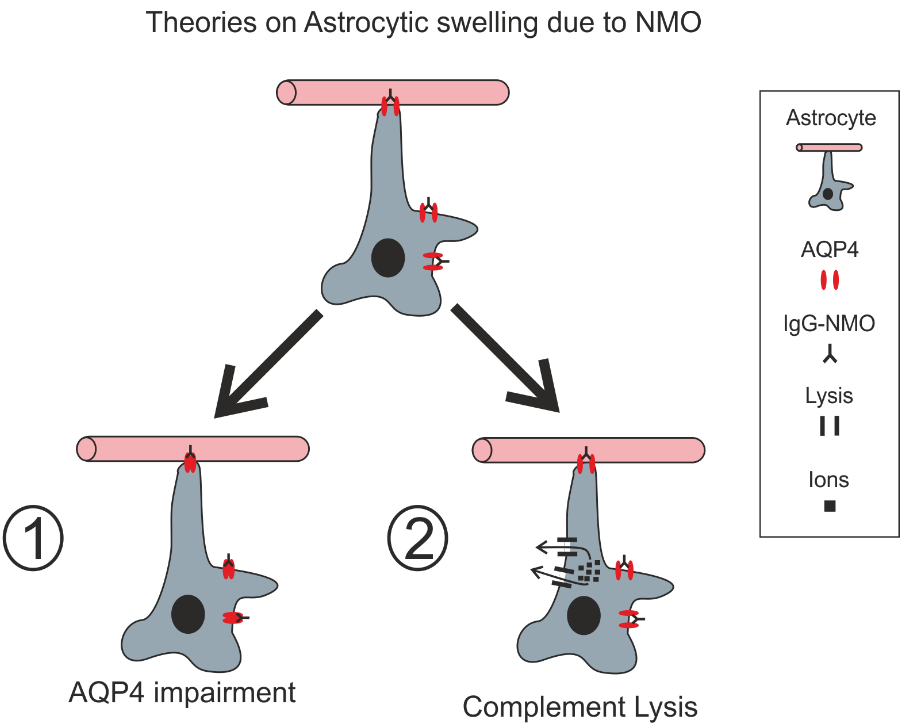

Figure 5.1: A description of the two hypotheses that explain cytotoxic oedema during NMO being tested by this work where the binding of antibody and antigen cause: 1 AQP4 impairment; 2. activation of the inflammatory complement system.

The strategy chosen to test these hypothesis was to take the state of the art model of cytotoxic oedema by Orlowski *et al*. [15] and adapting it to be able to simulate the pathophysiology of NMO. In this section, the changes made to the model by Orlowski *et al*. [15] are presented, starting with changes made to the model to overcome the fact that the Orlowski *et al*. [15] model does not model cellular behaviour past depolarization. The changes made and the revalidation of the model is presented in Section 5.2.1. Then the two hypotheses are tested, the AQP4 occlusion and the complement lysis in Section 5.2.2 and Section 5.2.3 respectively. In section 5.2.4 the potential of up regulating CD59 as a therapeutic procedure for NMO is tested. Section 5.2.5 presents the methodology used to stress test the results achieved. All the software choices used to develop the model are presented in Section 5.2.6. Finally, in section 5.2.7 a summary of the most relevant assumptions made throughout the model are presented.

5.2.1 Adapting Orlowski *et al.* model for post depolarization simulations.

The model adapted consists of a combination of a variety of models in order to develop the first model to accurately predict pH kinetics during an ischaemic stroke. In particular, it utilizes the work by Cloutier *et al.* [200] to model neuronal and astrocytic metabolism. However, the work by Cloutier *et al.* [200] aims at simulating neuronal metabolism during stimulation. Consequently, certain assumptions are not compatible with the simulations where the cerebral blood flow (CBF) is reduced. The particular assumption that was contested is related to the Krebs cycle in the model. It reduces the full cycle into a single equation for $\boldsymbol{v_{mito}}$. This rate aims to capture the production of ATP from pyruvate (PYR) dependent on adenosine triphosphate (ADP) and oxygen (O2) concentrations. The relationship between all these components is assumed to be governed by Michaelis-Menten kinetics. Additionally, in the particular case of metabolism stimulation it considers a step function that is dependent on the ratio between ATP and ADP. The rate is summarized in Equation 5.1.

$$v_{mito}^{i} = v_{max,mito}^{i}\left[\frac{PYR_i}{PYR_i + K_{m,PYR}}\right]\left[\frac{ADP_i}{ADP_i + K_{m,ADP}}\right]\left[\frac{O2_i}{O2_i + K_{m,O2}}\right] \tag{5.1}$$

where i stands for the astrocyte or the neuron, $v_{max,mito}^{i}$ is the maximum rate of ATP production and $K_{m,PYR}$, $K_{m,ADP}$, $K_{m,O2}$ are the Michaelis-Menten rates for PYR, ADP and O2 respectively.

This assumption for the representation of the metabolic rate has been made in many models in the field of neurological metabolism aimed at studying neural stimulation, starting with the work by [196]. However, as the NMO model is aimed at stimulating a stress scenario, further refinement is required here. Following [200] Eq. 5.1 was extended with the bi-directional reaction (reduction/oxidation) of nicotinamide adenine dinucleotide (NAD) between NAD^{+} and NADH. NAD and NADH were also assumed to reduce/oxidize with Michaelis-Menten kinetics. The new Krebs cycle equation ($v_{mito,new}^{i}$) is then defined as:

$$v_{mito,new}^{i} = v_{mito}^{i}\left[\frac{[NAD]_i}{[NAD]_i + K_{m,NAD}}\right]\left[\frac{[NADH]_i}{[NADH]_i + K_{m,NADH}}\right] \tag{5.2}$$

where $K_{m,NAD}$ and $K_{m,NADH}$ are the Michaelis Menten parameters for NAD and NADH respectively.

Similarly, it was found that the family of models that the [200] work is part of assumes that the metabolic reactions of hexokinase (v_{hk}^{i}) and phosphofructokinase (v_{pfk}^{i}) have a linear relationship with $[ATP_i\ ]$. This assumption was found to result in the inability of the model to converge when simulating metabolic stress during an ischaemic stroke. Therefore, to overcome this limitation, as in the case of v_{mito}^{i}, these rates were assumed to have a Michaelis-Menten relationship with $[ATP]$ as:

$$v_{hk,new}^{i} = k_{HK}^{i}\left[\frac{[ATP]_i}{[ATP]_i + K_{mHK,ATP}}\right]\left[\frac{[GLC]_i}{[GLC]_i + K_{m,GLC}}\right]\left[\frac{1}{1 + e^{-20(G6P_n - 0.6)}}\right] \tag{5.3}$$

$$v_{pfk,new}^{i} = k_{PFK}^{i}\left[\frac{[ATP]_i}{[ATP]_i + K_{mPFK,ATP}}\right]\left[1 + \left(\frac{[ATP]_i}{K_{I,ATP}}\right)^{nH}\right]^{-1}\left[\frac{[F6P]_i}{[F6P]_i + K_{m,F6P}}\right] \tag{5.4}$$

where k_{HK}^{i} and k_{PFK}^{i} are the reaction rate constants, $[GLC]_i$, $[F6P]_i$ and $[F6P]_i$ are glucose, fructose-6-p and glucose-6-p respectively, $K_{mHK,ATP}$ and $K_{m,GLC}$ are the HK Michaelis-Menten affinity constants $K_{m,F6P}$ and $K_{mPFK,ATP}$ are the PFK Michaelis-Menten affinity constants for fructose-6-p and ATP respectively and $K_{I,ATP}$ and nH are the Hill constants for ATP.

To ensure that the behaviour of the initial model is only minimally changed by the modification, the [200] model was refitted. As in [200] the simplex method from the SBML package by [257] was used for fitting. Two conditions were established to refit the model. The first consisted in ensuring the steady state behaviour of the model is comparable to that of the original work by Cloutier *et al.* [200]. The states of interest for the work here presented are the metabolites glucose and ATP. Comparing the two models it was found that steady state simulations of these metabolites vary by less than 1%, as it can be seen in Figure 5.2.

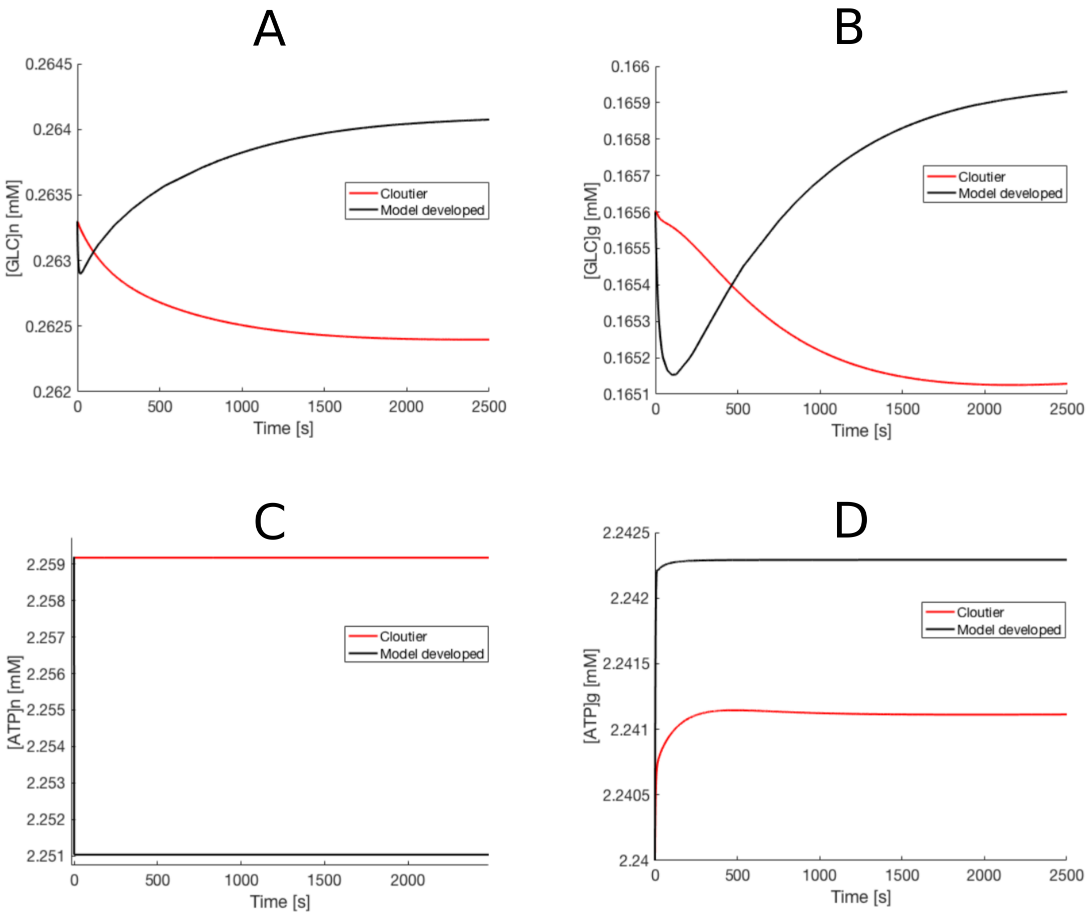

Figure 5.2: Comparing the steady state simulations of the Cloutier *et al.* [200] model (red) and the model developed (black) for intracellular Glucose and ATP for the neuron (A and C) and the astrocyte (B and D).

The Cloutier *et al.* work [200] aims at capturing neuronal and glial metabolism during brain stimulation. The data used to validate the model consist of measurements of glucose and lactate in the ECS during brain stimulation. The second condition defined for the refit was to ensure the behaviour of the model during stimulations was maintained. The fit was found to be satisfactory, as shown in Figure 5.3. The values of parameters found can be seen in Appendix 5.A.

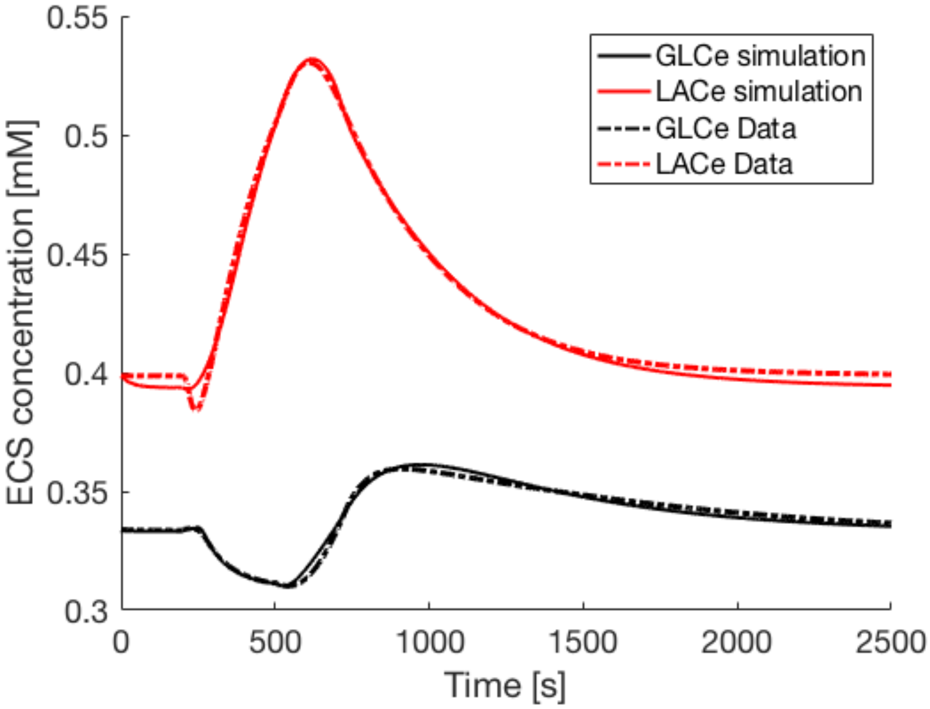

Figure 5.3: Revalidation of the metabolic model by [200] after the changes presented. The data consists of lactate and glucose in the ECS measurements during brain stimulation by an action potential. The simulation of the model of ECS glucose and lactate concentration during action potential stimulation as in [200] is here presented.

5.2.2 Cellular water kinetics

The water kinetics model developed here was added to the validated compartmental model of cellular metabolism and cytotoxic oedema proposed by Orlowski *et al.* [14], [15]. Four compartments are considered: neuron, astrocyte, extracellular space (ECS) and capillary. The model developed consists of making the compartments' volume kinetics to be described by the Starling equation [289]. This equation states that, assuming water is an incompressible fluid, that the volume of the cell is dependent on the movement of water. Water flow (Q) is dependent on osmotic ($\Delta\pi$) and hydrostatic (ΔH) pressure gradient between intracellular and extracellular compartments as:

$$Q = \frac{AM}{RT} k[\Delta H - \Delta\pi] \tag{5.5}$$

where, A is the cells surface area, M is the molecular weight of water at 310.15K [290], R is the gas constant and T is temperature. In section 5.2.2.1 Equation 5.5 is adapted to include the impact of AQP4 blocking is presented.

According to a recent review by [81], there are two known types of channels transporting water: water specific aquaporin channels and ionic channels permeable to water. Further water flows through non-specific pathways. Hence, the net membrane flux can be expressed as:

$$Q = Q_{AQP4} + Q_{ic} + Q_{ns}, \tag{5.6}$$

where the indices *AQP4*, ic and ns stand for the AQP4, ionic channel and non-specific channels respectively.

5.2.2.1 Flux through AQP4 channels

AQP4 is the aquaporin subtype expressed in astrocytes. AQP4 can be oriented towards the vasculature at the astrocytic endfeet and towards the extracellular space (ECS). In the model created here, these two orientations were considered by defining the flux through AQP4 channels as:

$$Q_{AQP4} = \frac{AM}{RT}\Big[\big(\gamma k_{AQP4}\big)\big[\Delta H_{cg} - \Delta\pi_{cg}\big] - \big((1-\gamma)k_{AQP4}\big)\big[\Delta H_{ge} - \Delta\pi_{ge}\big]\Big], \tag{5.7}$$

where the indices c, e and g stand for the capillary, the ECS and the astrocyte respectively, γ stands for the proportion of AQP4 channels at the perivascular interface and k_{AQP4} is the permeability of AQP4 channels. The parameter γ was assumed to be equal to 0.8 based on the work by [81] that states that the majority of AQP4s are oriented towards the perivascular space. The value of k_{AQP4} was defined from the work by [291], which measured astrocytic membrane permeability when astrocytes are grown both with AQP4 and without. It was found that there is a 7-fold reduction of membrane permeability when AQP4 is eliminated. Finally, hydrostatic pressures in capillaries and the ECS is defined based on the work by [292], stating average pressures of 15 mmHg and 7.5 mmHg respectively.

5.2.2.2 Water flux through ionic channels

According to [81] the two ionic channels currently known to be permeable to water in astrocytes are the glutamate transporter ($GTR1$) and the sodium-potassium-chloride co-transporter ($NKCC1$).

Several studies have considered the kinetics of the NKCC1 channels and their involvement in the clearance of potassium after neuronal stimulation [64], [65], [82]. However, only the [65] model considered both the glutamate transporter (GLT1) and the NKCC1 channel during swelling caused by cytotoxic oedema. Hence, their model is adopted here. Based on their work, ionic currents through the channels are modelled with the Goldman equation. Accounting for the stoichiometry of the transport, the Nernst potentials are defined as

$$E_{GTR1} = \frac{RT}{F} ln\left(\frac{[GLU^-]_e}{[GLU^-]_i}\frac{[K^+]_i}{[K^+]_e}\left(\frac{[Na^+]_e}{[Na^+]_i}\right)^3\right), \tag{5.8}$$

$$E_{NKCC} = \frac{RT}{F} ln\left(\frac{[Na^+]_e}{[Na^+]_i}\frac{[K^+]_e}{[K^+]_i}\left(\frac{[Cl]_e}{[Cl^-]_i}\right)^2\right), \tag{5.9}$$

where $[GLU^-]$, $[K^+]$, $[Na^+]$ and $[Cl^-]$ are the concentrations of glutamate and potassium, sodium and chloride ions respectively in the extra and intra cellular space as indicated by indices e and i. The ionic currents through the cell membrane are then defined as:

$$i_{GTR1} = -S_g k_{GTR}(v_g - E_{GTR}) \tag{5.10}$$

$$i_{NKCC} = -S_g k_{NKCC} E_{NKCC} \tag{5.11}$$

where S_g is the surface area of the astrocyte, v_g is the astrocyte membrane potential and k_{GTR} and k_{NKCC} are permeabilities of the two channels. According to [81] the transport of one mole of each ion through their respective channels is accompanied with the transport of one mole of water. Hence, water flux Q_{ic} is proportional to these ionic currents as

$$Q_{ic} = M\frac{i_{GTR}+i_{NKCC}}{VF}, \tag{5.12}$$

where V is the total volume considered in [200] model and F is the faraday constant.

5.2.2.3 Water flux through non-specific pathways

The flux through non-specific pathways has been assumed to be proportional to the hydrostatic and osmotic pressure gradients across the membrane with the same permeability k_0 across the perivascular and ECS interfaces as

$$Q_{ns} = k_0 \frac{AM}{RT}\left[\left[\Delta H_{cg} - \Delta\pi_{cg}\right] - \left[\Delta H_{ge} - \Delta\pi_{ge}\right]\right]. \qquad (5.13)$$

The osmotic pressure of the compartments was defined as being equal in all the compartments as previously presented in Orlowski *et al.* [15] and validated by the work by Kimelberg *et al.* [292]. Following Orlowski *et al.* [15] the intracellular osmotic pressure is defined as the sum of the ionic concentrations in each compartment as:

$$\pi \;= iRT([Na^+] + [K^+] + [GLU^-] + [Ca^{2+}] + [HCO_3^-] + [A^-]), \qquad (5.14)$$

where i is the van't Hoff factor, $[K^+]$, $[Na^+]$, $[HCO_3^-]$, $[Ca^{2+}]$ and $[GLU^-]$ are the potassium, sodium, carbonate, calcium and glutamate ionic concentrations respectively. Additionally, an assumption is made that there are impermeable anions $[A^-]$ inside the cells. The initial concentrations of these anions, following the work by [15] and [64], are calculated to ensure that the net pressure across the cells membranes is zero at the steady initial state. This procedure is explained in the Appendix 5.B. All changes made to the Orlowski *et al.* [15] model can be seen in Figure 5.4.

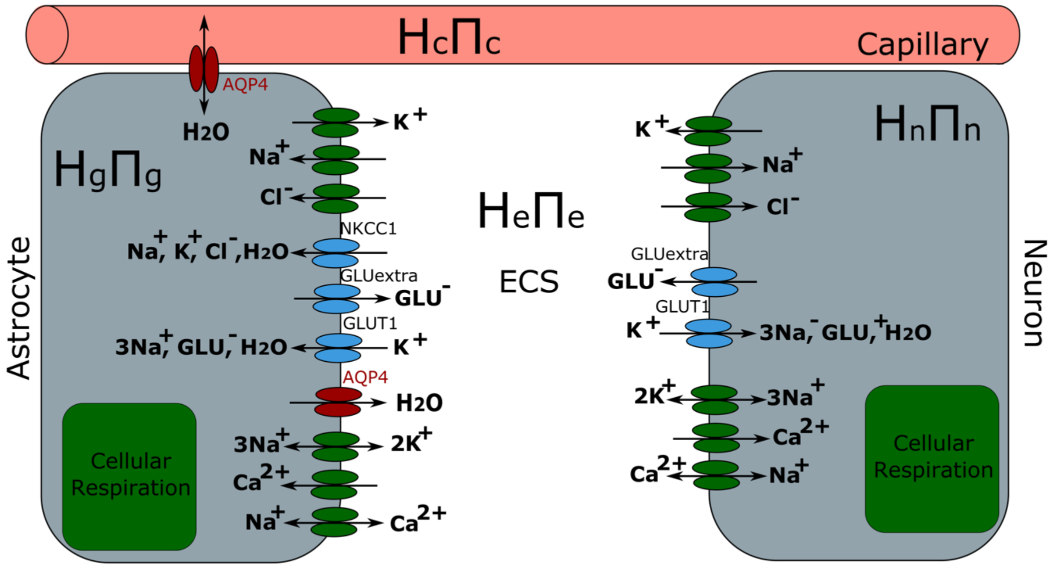

Figure 5.4: Diagram summarizing the astrocyte swelling model, which consists in the combination of three models: 1. The [15] model of cytotoxic oedema (green) 2. Ionic channels responsible for water movement (blue) was based on the work by [65] and 3. Water kinetics through AQP4 channels (red) based on the work by[292].

With this new model of astrocytic water permeability, it is important to quantify which of the three mechanisms ($Q_{AQP4}, Q_{ic}\ or\ Q_{ns},$) is responsible for the largest amount of water flow across the astrocytic membrane. To this effect, a steady state simulation was performed where the flow of the three mechanisms is evaluated for 12 hours, as seen in Figure 5.5. It is possible to see that Q_{ic} water transport is a rate 10^4 s^{-1} orders of magnitude smaller than the remaining two. Additionally, AQP4 water transport is the most significant mechanisms of hydrostatic pressure maintenance by the astrocyte. Therefore, demonstrating its importance in astrocytic volume regulation. The new cellular volume kinetics model is summarised in Appendix 5.C.

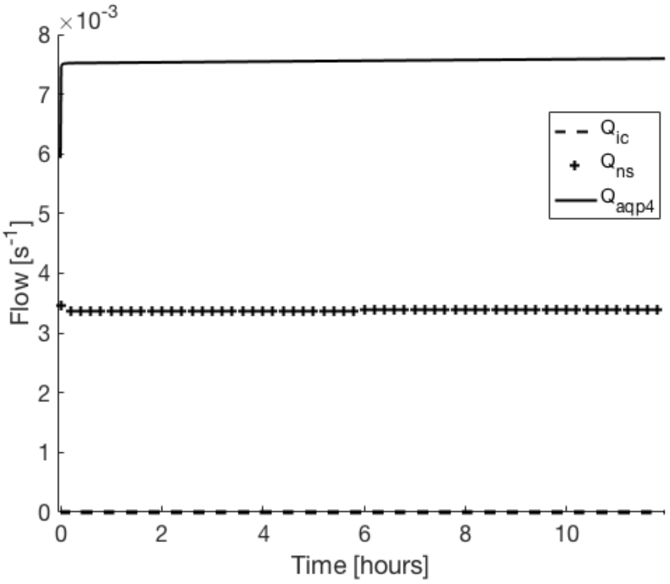

Figure 5.5: Steady state simulation of the water flow across the three mechanisms considered by the model: (Q_{ic}) flow through ionic channels permeable to water, (Q_{ns}) flow through water non-specific pathways and (Q_{AQP4}) flow through aquaporin 4 channels

5.2.3 NMO complement lysis

The work developed on complement lysis due to NMO aims at mimicking the experimental procedure implemented by [17]. Here, the human complement and human AQP4-Ab are injected into the brain of rats. After 12 hours the animals are sacrificed and the NMO lesions generated are analysed.

The model of NMO complement holes developed was added to the model presented in Figure 5.4 and consists of combining three concepts: 1) the binding of AQP4-Ab antibodies to AQP4 antigens (Section 5.2.3.1), 2) the complement protein cascade leading to the production of the Membrane Attack Complex (MAC) forming holes in the membrane (Section 5.2.3.2); and 3) the ionic and water currents through the forming membrane holes (5.2.3.3). The pathology captured by the model developed here is summarized in Figure 5.6.

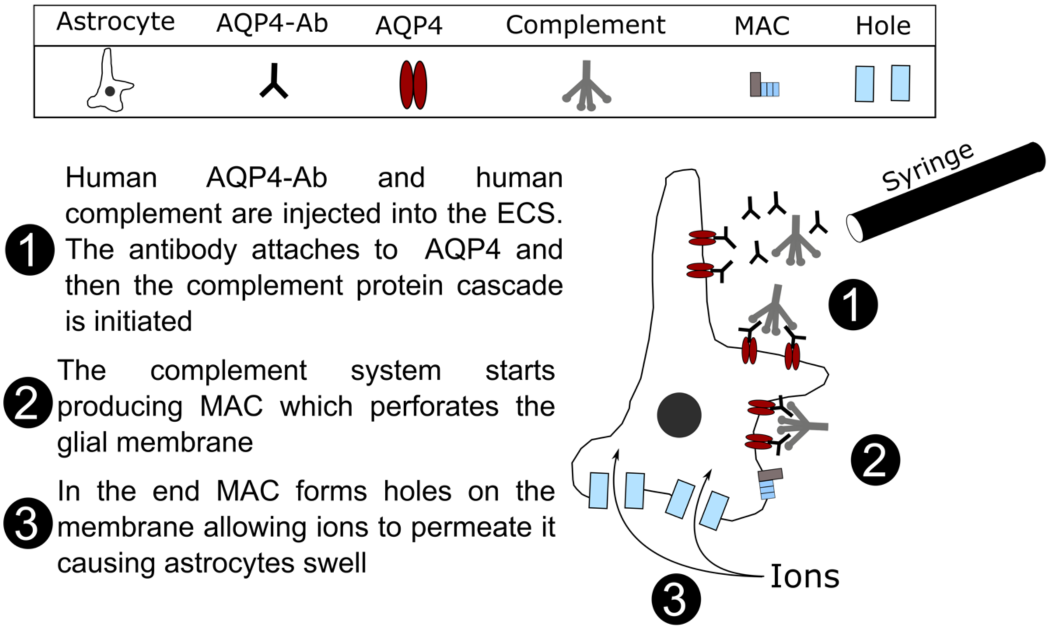

1 Human AQP4-Ab and human complement are injected into the ECS. The antibody attaches to AQP4 and then the complement protein cascade is initiated

2 The complement system starts producing MAC which perforates the glial membrane

3 In the end MAC forms holes on the membrane allowing ions to permeate it causing astrocytes swell

Figure 5.6: Description of the hypothesized NMO pathology presented by [17]

5.2.3.1 Antigen antibody binding

The production of the AQP4-Ab and AQP4 complex was modelled using the generic model of antibody antigen binding developed by Kumagai *et al.* [234] and represented by the following biochemical equation:

$$AQP4_{IgG} + AQP4 \overset{k_d}{\underset{k_b}{\leftrightarrows}} Complex. \tag{5.15}$$

The binding (k_b) and detachment (k_d) rates were taken from the IgG antibody-antigen binding measurements by Kumagai *et al.* [234]. The later work found that k_b has an order of magnitude between 10^2-10^3 mM^{-1}s^{-1} and k_d has an order of magnitude between 10^{-4}-10^{-3} s^{-1}. In the model, the rates were taken to be the average value within those ranges.

The concentration of AQP4-Ab was set to follow the injection pattern in the *in vivo* experiments by [17]. As the cells membrane concentration of AQP4 ($[AQP4]_g$) has yet to be measured it was based on the literature. It was estimated using Equation 5.16:

$$[AQP4]_g = \frac{n_{AQP4}}{N_A V_m}, \tag{5.16}$$

where n_{AQP4} is the number of AQP4 channels found in the membrane of the astrocyte, N_A is the Avogadro number and V_m is the volume of the astrocyte membrane. V_m was calculated based on measurements of the average astrocyte surface area in [65] (2.09241×10^{-7} dm^2) and measurements of membrane thickness in [293] (8 nm). Hence, $[AQP4]_g$ was set to 3.97×10^{-3} mM.

5.2.3.2 MAC production

After inflammation is activated by the interaction between antigens and antibodies one of the anti-bacterial mechanisms triggered is the inflammatory complement system [56]. It has many anti-bacterial effects including chemoattractant production. Here the main focus is another product of the complement system, which results in the formation of holes in the membrane of bacteria. These holes are formed by piercing proteins entitled membrane attack complex (MAC). This process is believed to be the reason behind astrocytic oedema during NMO pathology [17].

Here, only the classical pathway is considered, as it is the only one known to be activated during NMO [45]. The classical pathway consists of the breakdown and binding of a cascade of proteins in the following steps [56]: 1) the protein C1 binds to the antibody-antigen complex which in turn activates the cleavage of C4 and C2 into C4b and C4a, and C2a and C2b respectively; 2) C4b and C2a form a complex and bind to the astrocytic surface, which initiates the breakdown of C3, C3a being released into the ECS and acting as an inflammatory chemoattractant while the protein C3b binds to the C4b2a complex; 3) the binding leads to the cleavage of C5, C5a is released into the ECS also behaving as chemoattractant and the protein C5b instead binds to the astrocytic membrane enrolling the proteins C6, C7 and C8 resulting in the formation of C5bC6C7C8 complex (C5b-8); 4) the final step consists of the activation C9 proteins these binding to the C5b-8 complex or MAC and perforate the astrocytic membrane. The steps of MAC formation are summarized in Figure 5.7.

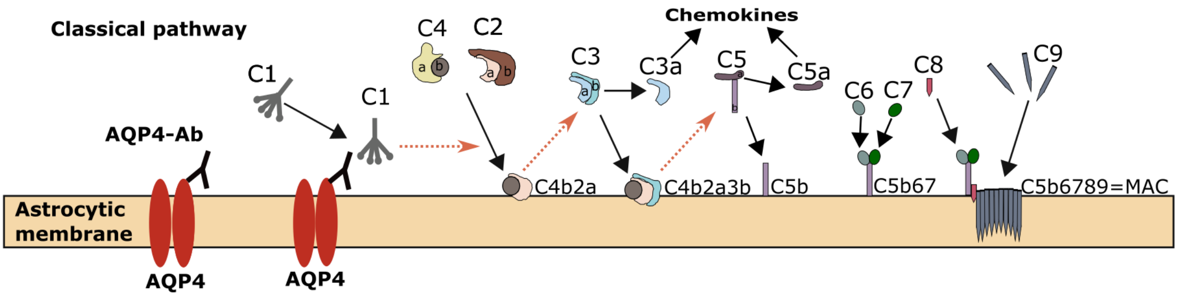

Figure 5.7: Breakdown of the classical complement pathway protein cascade leading to the formation of the membrane attack complex.

In the literature, there are three models that capture the protein cascade of the complement system [235], [236], [238]. In Korotaevskiy *et al*. [236] and Liu *et al*. [238], it was found that the model of Hirayama *et al.* cannot reproduce experimental data. Alternatively, the work of [238], although it has validated its model with experimental data, does not model the full pathway from complement activation to the formation of MAC. Hence the model of Korotaevskiy *et al*. [236] was chosen.

Two adaptations were made to the model of Korotaevskiy *et al.* [236]. As they considers both the classical and alternative pathways the latter was deactivated by making the plasma concentration of proteins involved in this pathway equal to zero. Secondly, the antigen-antibody complex was assumed to follow the kinetics shown in Eq. 5.15.

The complement model by Korotaevskiy *et al*. [236] involves 37 biochemical equations. In an effort to reduce the complexity of the model two strategies were implemented to reduce its size to its most relevant mechanisms to model complement lysis in NMO. The first, as presented in Section 5.2.3.2.1, the screening method as described by Campolongo-Morris [294] is presented. Secondly, in Section 5.2.3.2.2 the model is aimed to fit a second order model to the MAC production kinetics from [236].

5.2.3.2.1 Sensitivity analysis

The model of cytotoxic oedema by Orlowski *et al*. [15] consists of approximately a hundred variables. Adding the full complement would increase the complexity of the model substantially. Additionally, in order to test astrocytic oedema during NMO only the production of MAC is relevant.

A screening procedure was chosen to identify the proteins that mostly effect MAC kinetics. From the literature the better equipped to handle large models was found to be the Campolongo -Morris (C-M) method [260].

The algorithm was implemented as described in Section 3.5.3. The Campolongo-Morris algorithm will generate different results depending on the range of values considered. Additionally, the model is designed to be able to handle different concentrations of complement injected. Therefore, the range of concentration for each protein is calculated over ±100% of the value states in Korotaevskiy *et al*. [236].

The standard deviation (σ) and the absolute mean (μ^*) of the elementary effects for each protein in the complement model of [236] were calculated at every 100 seconds between 100 and 1000 seconds in the simulations. The mean of σ and μ^* for all time points was calculated for each protein. Within the time range MAC goes from zero to a steady state of 2.4×10^{-4} mM. The different parameters that define the grid used by the Campolongo-Morris method to explore the parameter space were chosen through an ad hoc process to identify the parameters that better cluster the parameters with larger impact and lowest impact. The result of this analysis is presented in Figure 5.8.

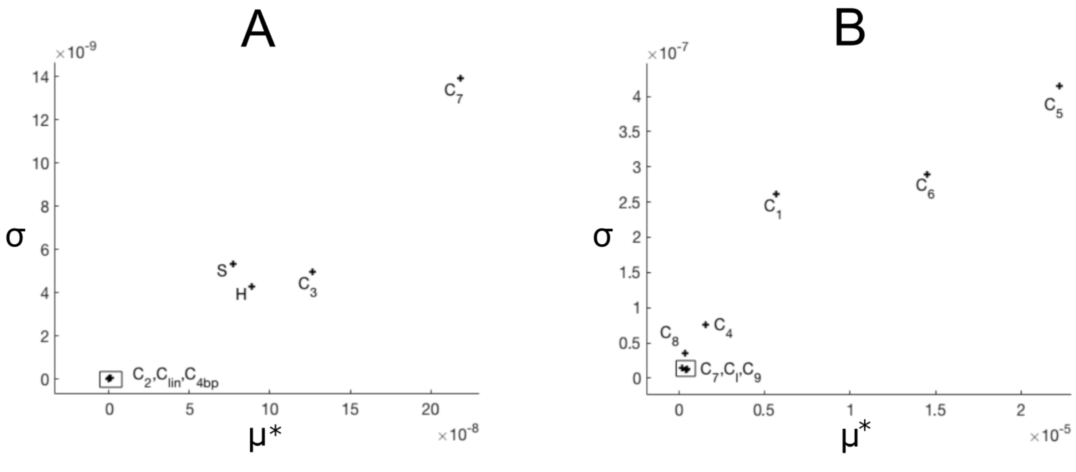

Figure 5.8: Results from applying the Campolongo-Morris method to the Korotaevskiy *et al*. [236] MAC production model. The EE's were defined as being the difference between the MAC production at each interaction and the Korotaevskiy *et al*. [236] model.

From this analysis, it was possible to identify that, even when the concentration of each protein is varied by 100% several proteins have little impact on the production of MAC. These proteins were removed from the model thereby reducing the number of inputs from 13 down to 9. In Figure 5.9 the production of MAC by the original model and the simplified model is presented. The root mean square between the original and the simplified model is of approximately 5.35×10^{-2} and therefore negligible.

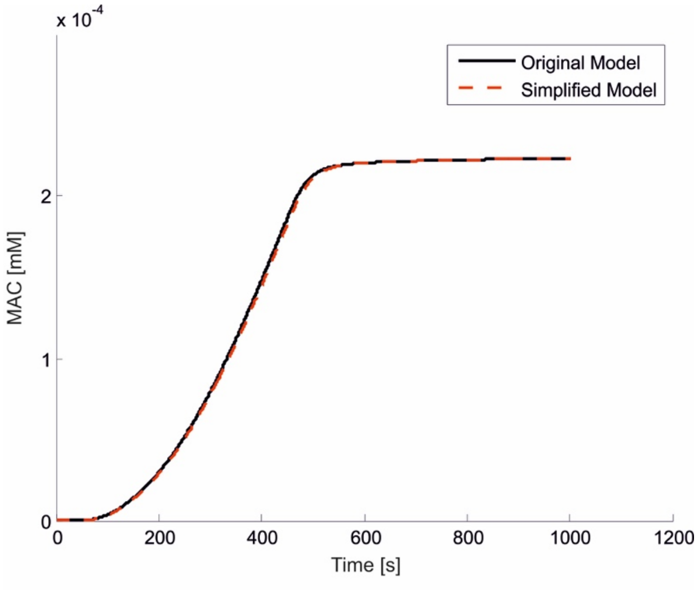

Figure 5.9: The result of removing the proteins that were found to be negligible through the Campolongo- Morris method.

5.2.3.2.2 2nd order approximation of the complement system

As described in Figure 5.6, the experimental procedure in [17] consists of injecting human complement and human AQP4-Ab into mice brain tissue. The simplified model would therefore have the concentration of these two agents as its inputs. A first analysis of the system consists of observing how the system behaves in response to these two inputs. Simulations were performed over a range of values of these two inputs. IgG in [17] was injected with a concentration of 1.375×10^{-1} mM and therefore the concentration was chosen to vary between 100 times smaller and larger than that concentration. In terms of complement the concentration was taken from [236] and it was varied between ±100 times the concentration injected. Figure 5.10 A and B shows how the system varies when the complement and IgG are varied respectively over the ranges described.

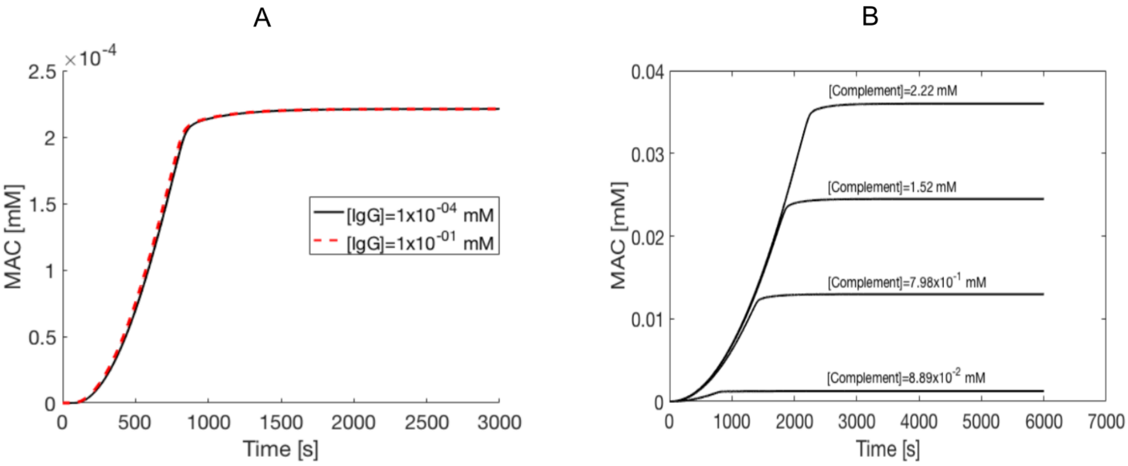

Figure 5.10: The simulations of the complement model developed by varying the inputs AQP4-Ab (A) and complement (B) over the ranges described.

From Figure 5.10 A it can be concluded that varying the concentration of AQP4-Ab within the range defined had little impact on the speed of MAC formation and no impact on the concentration. This behaviour is expected, as the concentration of AQP4-Ab injected is six to ten orders of magnitude higher than the concentration of AQP4. Consequently, the effect of AQP4-Ab was ignored in the simplified model of complement lysis developed here. From this analysis, it was concluded that the parameters of the model developed should only be dependent on MAC concentration.

As it can be seen in Figure 5.10 the behaviour of complement MAC production resembles a step function. It was therefore assumed that a differential equation model would be a good approximation. An analysis was made to identify the order of the model that would have the least RMS. This experiment consisted in fitting increasing order models to one of the curves shown in Figure 5.10.B. In order to facilitate this analysis, the curves in Figure 5.10 B were all normalized. The result of fitting differential equation models with increasing order can be seen in Figure 5.11 A.

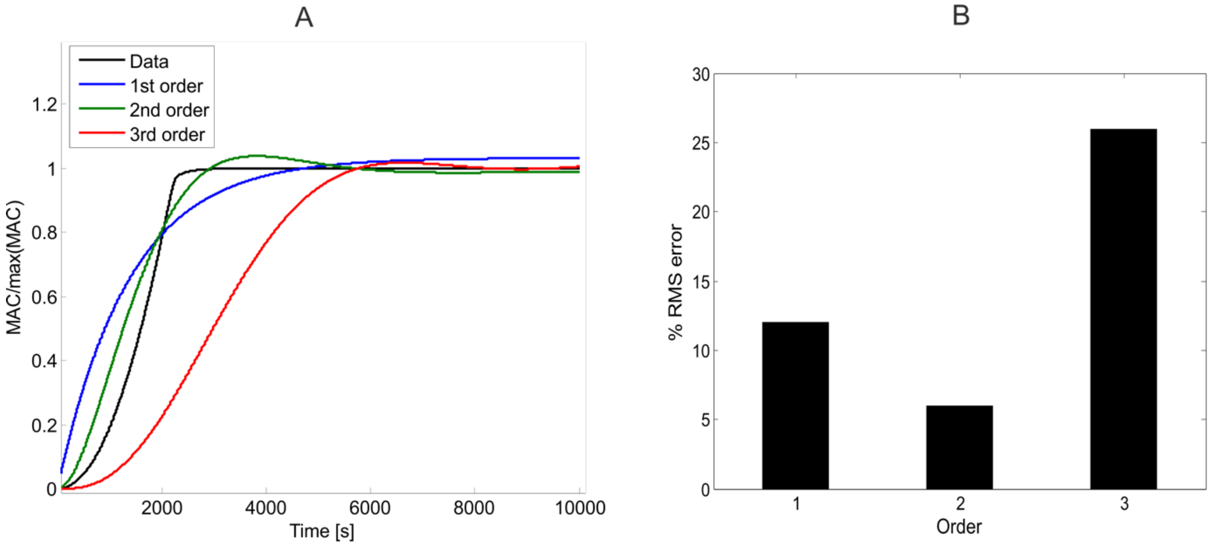

Figure 5.11: A. Comparing the fits to the complement model [236] by different order models; B. RMS error between the different order models and the complement model from [236].

As can be seen in Figure 5.11 B the second order model is the best fit for the model. Then the parameters were fitted to complement model by [236] simulations for the range of complement concentration (C) described. The resulting model is of the form:

$$a(C).y'' + b(C).y' + c(C).y = m(C) \tag{5.17}$$

The four functions $a(C), b(C), c(C)$ and $m(C)$ were then fitted using the symbolic regression software Eureqa [262]. The plot of each function and the equation fitted can be found in detail in Appendix 5.D.

When comparing the curves to the model it is possible to see that as complement concentration increases the performance of the model worsens. This can be seen in Figure 5.12.B where the RMS error was calculated for the curves. However, when considering the curve when complement concentration is taken from [236], as shown in Figure 5.12 A, the RMS error is approximately 3.5%. Additionally, as the simulations were required to last 12 hours the behaviour of the model in the first 30 min is relatively negligible. The resulting equations can be seen in Appendix 5.D.

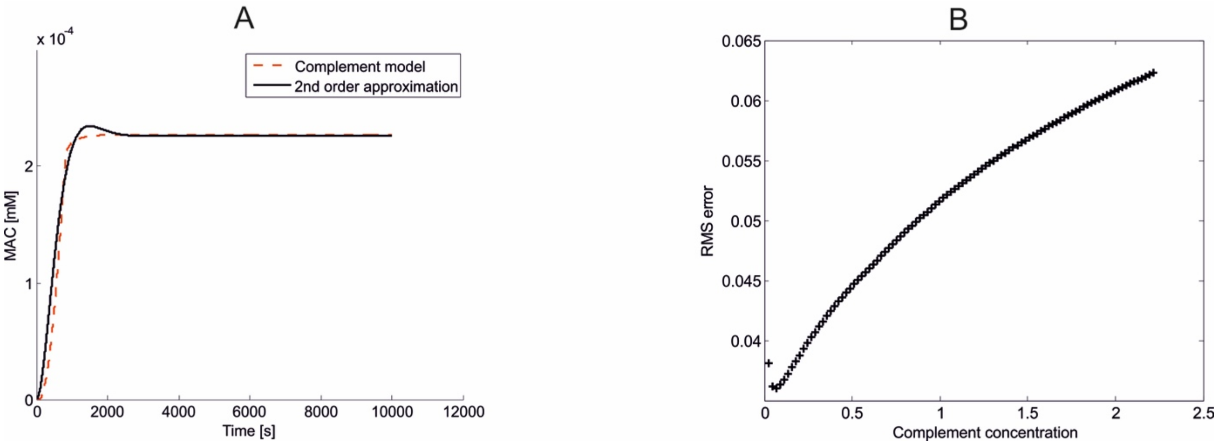

Figure 5.12: A. Comparing the 2nd order model approximation to the complement model when complement concentration is equal to the one in [236]; B. The RMS error between the 2nd order model predictions and the curves in Figure 5.11 A.

5.2.3.3 Hole formation

In the literature, the work of Wiese *et al*. [295] has measured the current of stained interstitial fluid across the membrane induced by lytic holes dependent on the number of C9 attached to the C5b678 complex. However, the current of ions has been ignored. Therefore, a novel model was developed here. Wiese *et al*. [295] found that the formation of one hole required α molecules of C9, α being in the range 12 to 18. Hence, the number of holes formed was set to:

$$h = V_e M \frac{N_A}{\alpha}, \tag{5.18}$$

where V_e is the volume of the ECS, M is the concentration of MAC and N_A is the Avogadro number. When holes are formed in the astrocytic membrane, ions are able to move freely across. Ionic currents through the lytic holes (i_h) were assumed to be proportional to the Nernst potential as for models of standard ion channels by [206], as:

$$i_h = h k_{h,P} \sinh\left(\frac{v_{cell} - E_P}{v_t}\right), \tag{5.19}$$

where, $k_{h,i}$ is the permeability of one hole for ion P $v_t = \frac{RT}{F}$, R is the gas constant, T is temperature and F is the Faraday constant. k_C is defined as being proportional to the concentration of the P channel with scaling factor of the ratio of the area of the hole to that of the channel leading to:

$$k_{h,P} = \frac{k_P}{n_P}\left(\frac{r_h}{r_P}\right)^2, \tag{5.20}$$

where k_P is the permeability of all ion channels of type P, r_h is the radius of the hole, r_P is the radius of the channel of type P and n_P is the number of channels of type P in the membrane.

Similarly, holes are also assumed to be permeable to water. As holes are small, water flowing through the hole cannot be assumed to be a continuum. Hence, as in Eq. 5.20 the permeability has been assumed to be proportional to an AQP4 channel permeability with a constant equal to the ratio of the area of the hole to that of the channel (r_{AQP4}), leading to:

$$k_{h,w} = \frac{k_{AQP4}}{n_{AQP4}}\left(\frac{r_h}{r_{AQP4}}\right)^2. \tag{5.21}$$

The flow of the water through holes is defined as:

$$Q_{h,cg} = hk_{h,w}\gamma\left[\Delta H_{cg} - \Delta\pi_{cg}\right], \tag{5.22}$$

$$Q_{h,ge} = hk_{h,w}(1-\gamma)\left[\Delta H_{ge} - \Delta\pi_{ge}\right], \tag{5.23}$$

where, $Q_{h,cg}$ and $Q_{h,ge}$ is the water flow through the AQP4 perivascular and ECS interfaces respectively. The equations and parameters concerning channels in the model can be found in the supplementary material. The equations and parameters for all the channels can be found in Appendix 5.E.

5.2.4 CD59 kinetics

CD59 is a complement inhibitor that is naturally found on the surfaces of cells including astrocytes. Many pathologies are associated with a lack of expression of this protein e.g. hemolytic anaemia [296] and breast cancer [297]. Additionally, it is hypothesized by [18] that a down regulation of this protein at the astrocytic endfeet processes is the reason why these are targeted during NMO. The CD59 inhibits MAC formation by binding to C5b-8 and to C5b-9, stopping further C9 from attaching to the complex as presented in Figure 5.13.

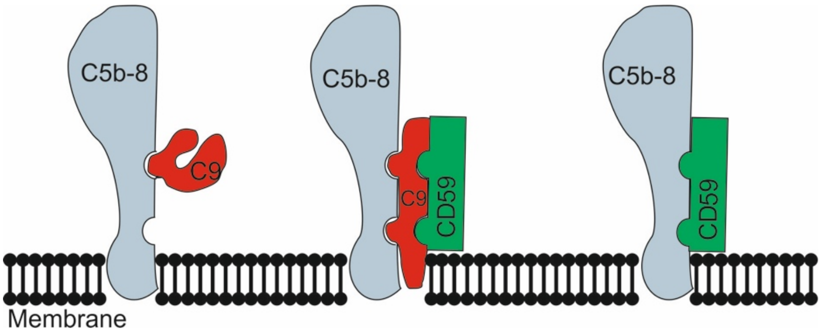

Figure 5.13: The protein CD59 inhibits the formation of MAC by blocking the binding of the perforating C9 proteins. CD59 is able to prevent the formation or during hole formation by binding to C5b-9 complex. Additionally, it can bin to C5b-8 and inhibits MAC formation alltogether.

The model of CD59 inhibition was developed here based on the work of Rollins *et al.* [165]. This work consists of *in vivo* experiments where the proteins C5b6, C7, C8 and C9 are introduced into a cell suspension. Then a range of CD59 concentrations are added and the level of lysis inflicted on the cells is measured using radiolabeling.

In order to simulate the kinetics of MAC formation from C5b6 to C5b6789, model equations are taken from [236]. The concentrations of the different proteins are taken from [236] (in Appendix 5.F the concentrations of the different proteins and the data used are both given). Then to simulate the effect of CD59, following the models of complement inhibitors from [236], [238], two assumptions were made: 1. the reduction of lysis from [236] is taken to be linearly proportional to the reduction of MAC concentration; and 2. the bindings between CD59 and C5b678 and C5b6789 were defined using mass action kinetics as follows:

$$Cb5678 + CD59 \underset{k_2}{\overset{k_1}{\leftrightarrows}} Cb5678\_CD59 \tag{5.24}$$

$$MAC + CD59 \underset{k_4}{\overset{k_3}{\leftrightarrows}} MAC\_CD59 \tag{5.25}$$

where, $k_{1,2,3,4}$ were fitted to the data from [165] using the simplex method present in the SBML package [257] (more details can be found in Appendix 5.F). In Figure 5.14 the result of the fitting is presented. The smallest error found was approximately 10%.

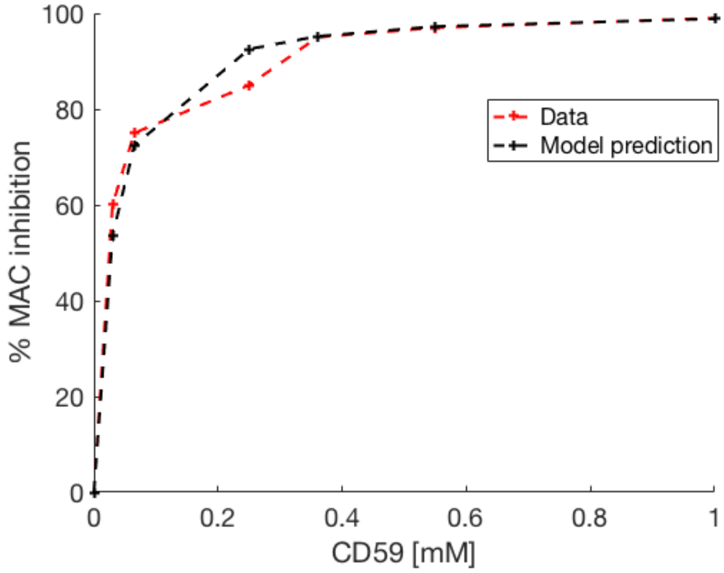

Figure 5.14: The result from fitting the kinetics presented in Equation 5.24 and 5.25 to the data from [165].

5.2.5 Implementation

The cellular model was developed using the OpenCell platform v.0.7 developed by [67]. The model was also implemented in Matlab and solved using the CVODE package from Sundials [258]. The Campolongo-Morris method was implemented using the package provided by [260]. Finally, the CD59 model was fitted to data using the simplex method provided by SBML from [257].

5.2.6 Summary of assumptions

As this is the first work that aims to use mathematical modelling to test these pathological hypotheses of NMO several assumptions were required. In this section, all of them are summarized in Table 5.1 to facilitate future research and improvements to this study. The assumptions presented are further explored and justified in Section 5.4.

Table 5.1: List of assumptions made throughout the development of the model

Section	Assumptions
5.2.2.1 Water flow	• In order to ensure the net hydrostatic for each compartment is stable, the intracellular hydrostatic pressure was calculated. For the net osmotic pressure, it was assumed that there are impermeable intracellular anions $[A^{-}]$ and its concentration was calculated to ensure that the osmotic pressure is stable across compartments.
5.2.2.2 Ionic channels permeable to water	• The water permeable channels $iNKCC$ and the glutamate transporter $(iGTR)$ were implemented. • A further channel $iGLU$ was created to ensure that the model is stable at

	steady state.
5.2.3.1 Antigen antibody binding	• The number of AQP4 channels in an astrocytic membrane was estimated to be equal to 40,000 channels.
5.2.3.2 MAC production	• Only the complement protein cascade model by [236] was taken into account, as it is the only one that comprises the full system from antibody-antigen binding to MAC production.
5.2.3.3 Sensitivity analysis	• The method implemented was the Campolongo-Morris screening method as it was the only one suited for ODE models with more than 5 ODE.
5.2.3.4 2nd order approximation of the complement system	• The model has two inputs: the concentrations of AQP4-Ab and complement; • The concentration of AQP4-Ab was found to have a negligible effect on the production of MAC.
5.2.3.5 Hole formation	• The number of holes was made proportional to MAC concentration by considering that 14 moles of C9 are consumed per hole. • The ionic currents created are proportional to their ionic channels taking into consideration the ratio between their radii.
5.2.4 CD59 kinetics	• CD59 binds to both C5b678 and Cb56789. • The concentration of the complement proteins in [165] were taken from [236] . • The model was made to behave according to mass action kinetics.

5.3 Results

Several experiments were made to test the hypothesis of the pathophysiology of NMO and to evaluate the therapeutic potential of CD59 to treat NMO. Before presenting the summary of results related to NMO, the process to revalidate the cytotoxic oedema model is presented in Section 5.3.1. Following the validation of the model the NMO pathology tests are organized as follows: in Section 5.3.2 is the impact on glial volume due to AQP4; the simulations of cellular oedema due to complement lysis are presented in Section 5.3.3 and finally, the inhibitory effect of CD59 is presented in Section 5.3.4.

5.3.1 Validating oedema model

The model by Orlowski *et* al. [15] was validated using *in vivo* data by Lundbaek *et al.* [298] and by Syková *et al.* [299] that have found that the ECS volume fraction falls between 0.1-0.04 30 min after a severe ischaemic stroke. The simulation of ischemic stroke consisted in reducing cerebral blood flow (CBF) by 98%. It was found that 30 min after stroke is induced the volume fraction of the ECS is approximately 0.04. The result of the stroke validation can be seen in Figure 5.15 A.

Additionally, it is shown in Figure 5.15 B that with the changes made to Cloutier *et al.* [200] introduced in Section 5.2.1 it is now possible to simulate cytotoxic oedema for 12 hours.

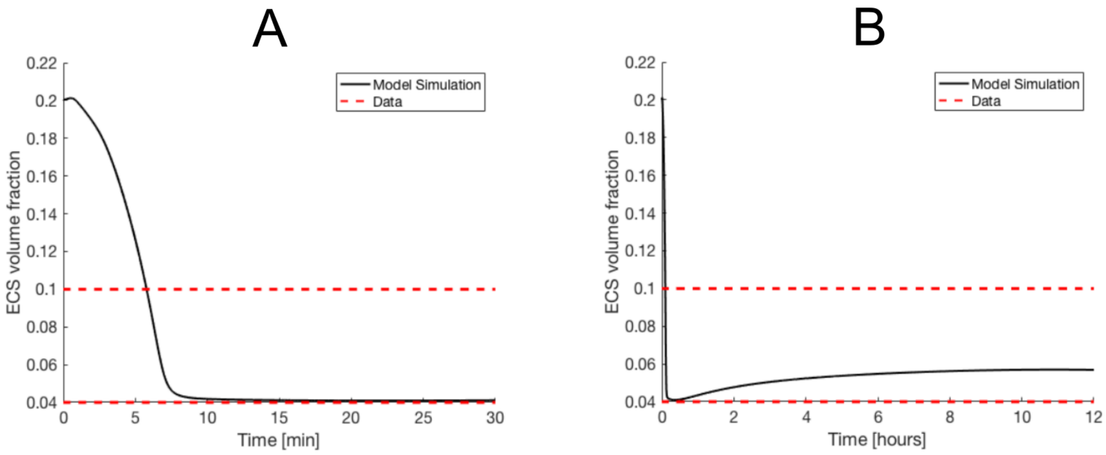

Figure 5.15: Ischaemic stroke simulations using the combined water dynamics model in Section 5.2.1 and metabolism and cell swelling model in Section 5.2.2. A. presents ECS volume fraction after a simulation of cytotoxic oedema for 30 min following the experimental procedure described by [298] and [299]. B. serves to demonstrate that the model is able to simulate ischaemic stroke for the required 12 hours.

5.3.2 AQP4 impairment

The distribution of AQP4 across the astrocytic membrane is not currently known across its two interfaces. In order to fully test the impact of AQP4 permeability impairment two experiments were made. The first consists of deactivation of the perivascular ($nAQP_c$) and ECS ($nAQP_e$) oriented AQP4 in turn. In both cases, simulations were made where the percentage AQP4 (parameter γ in Eq. 5.23) oriented towards each interface is varied over a range. Each simulation was performed for 12 hours following the procedure [17]. Figure 5.16 presents the percentage of astrocytic volume change is presented for each distribution 12 hours after the AQP4 is deactivated.

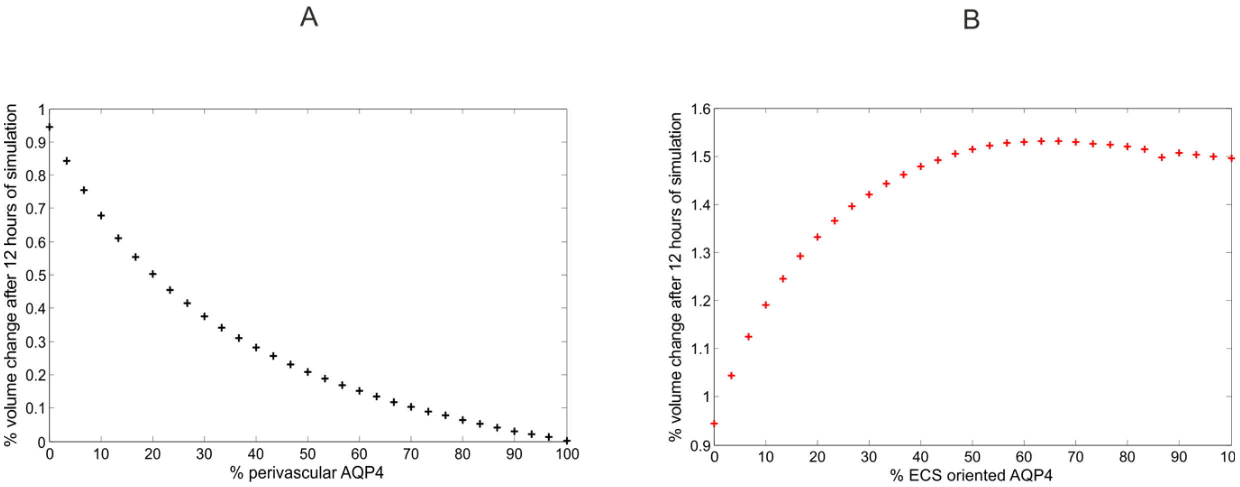

Figure 5.16: A. Percentage of volume change due to deactivation of perisynaptic AQP4 for different percentages of perivascular AQP4; B. percentage of volume change at different deactivation of perivascular AQP4

Figure 5.16 shows that a decrease in AQP4 percentage at the perivascular orientation leads to an increase in volume. Alternatively, an increase in the percentage of AQP4 oriented towards the ECS resulted in an increase in volume change. From all the simulations, it was found that the larger increase in volume was found to occur when the distribution of AQP4 was when there is no perivascular AQP4 and there a larger than 60% AQP4 oriented towards the ECS.

The maximum volume change found is further confirmed by the second experiment where the total membrane permeability due to AQP4 is deactivated. This simulation is presented in Figure 5.17. The maximum amount of volume change registered here was approximately 1%.

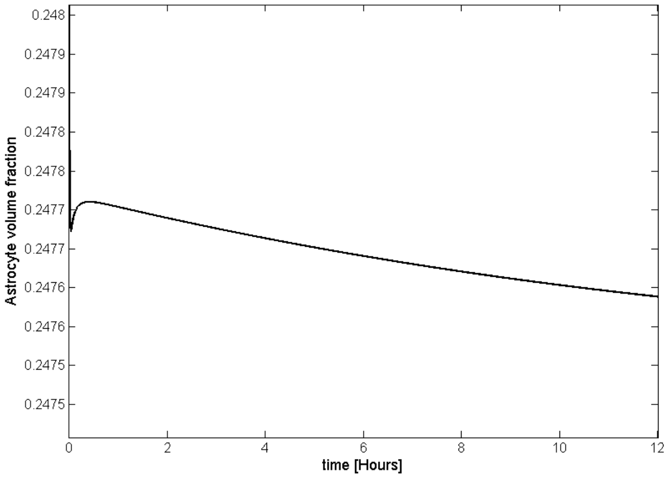

Figure 5.17: Simulations of the changes in astrocytic volume due to AQP4 impairment.

5.3.3 Simulating complement lysis

Saadoun *et al.* [17] found that only when both AQP4-Ab (16.8 μl solution) and human complement (11.2 μl solution) are injected to NMO lesions develop. To simulate this experiment AQP4-Ab and human complement were set as input to the model. Their respective initial concentrations at the injection site were calculated based on solution preparation details in [17] and the molar masses of AQP4-Ab (150 kDa) and human complement reported by [300]) and [236] respectively. From these assumptions, the initial concentration of AQP4-Ab was calculated to be $8.82\times10^{-5}\ mM/L$. Calculated concentrations of protein cascade proteins can be found in Appendix 5.F.

Model simulations span 12 hours to mimic the experimental work by [17] who analysed histological data of the brain of mice models sacrificed after this time from an injection. As shown in Figure 5.18, the model predicts that after approximately one and half hours the volume reaches a steady state at 20% above its initial value. A maximum increase in the volume of 26% occurs after about 50 min.

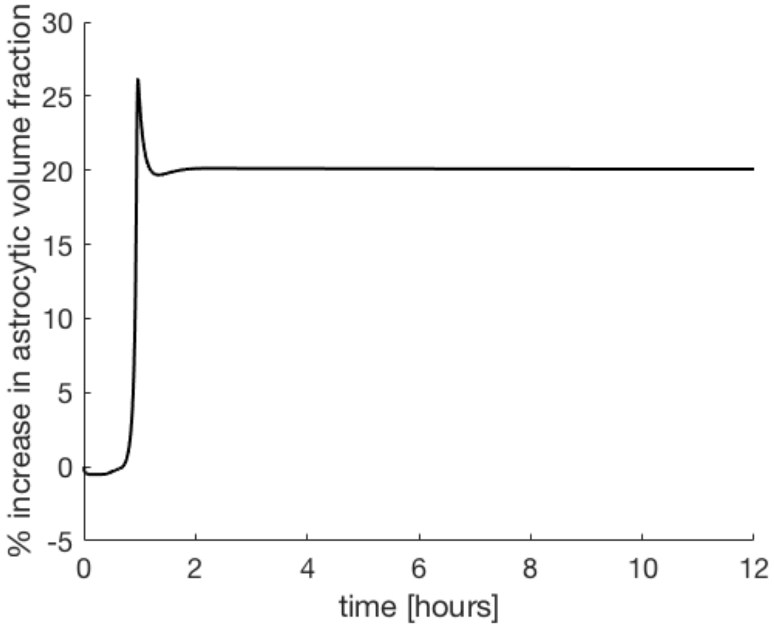

Figure 5.18: A simulation of astrocytic volume fraction when complement lysis is induced and no CD59 is injected.

5.3.4 CD59 therapeutic potential

The potential of CD59 as an astrocyte swelling inhibitor was tested by varying the ECS CD59 concentration and simulating the astrocyte volume change. Increasing the initial CD59 concentration resulted in a progressive increase of time after which the cell volume change plateau is reached (from 30 min to 3 hours for an increase in CD59 concentration from 0 to 1.5 mM) and a reduction of its value (from a 20% to a 17% volume increase plateau for an increase in CD59 concentration from 0 to 1.5 mM). Furthermore, the peak of the volume change is reduced (from an approximately 25% to a 20% peak increase in astrocytic volume for a CD59 concentration of 0 mM and 1.5 mM respectively) as illustrated in Figure 5.19. The cell volume does not change within 12 hours of complement cascade onset for CD59 concentrations above 2.5 mM.

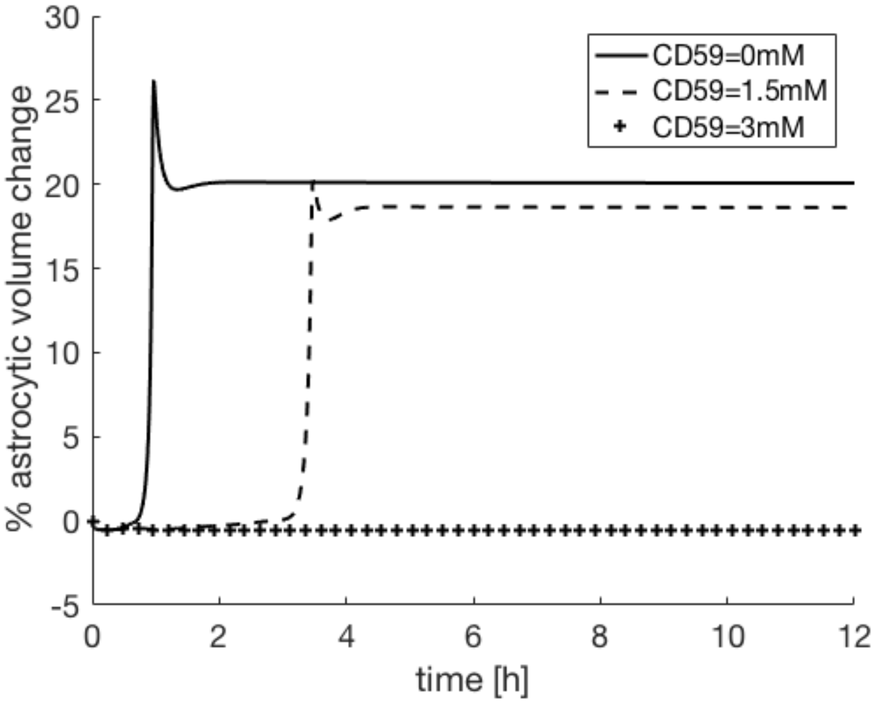

Figure 5.19: A range of CD59 concentrations were injected and a threshold for astrocytic swelling was found: below 2.5 mM the membrane astrocytic membrane depolarizes inevitably leading to 20% volume increase while above 2.5 mM astrocytic cytotoxic oedema is completely inhibited resulting in a negligible 0.1% volume increase.

5.3.5 Screening results

The method described in Section 3.5 was implemented to evaluate the sensitivity of the model predictions to the fitted parameters. It was applied to the validation of the cytotoxic oedema predictions with ischaemic stroke data by varying parameters by ±5%. The *in vivo* experimental work used for validation [298], [299] found that the ECS volume fraction is between 0.04 and 0.1 after 30 of ischaemic stroke. For each iteration of the C-M algorithm, stroke was simulated by reducing CBF by 98%. In this case, the EE was assumed to be the difference between the volume fraction of ECS after 30 min of stroke and the prediction with fitted parameters, as seen in Figure 5.15 A. From this analysis, it was found that the maximum change was of ±2.5 percentage points resulting in the ECS volume fraction being between 4.49×10^{-2} and 4.72×10^{-2}.

Additionally, the method was applied to the predicted CD59 complement lysis inhibition potential identified, as seen in Figure 5.19. The parameters fitted when developing the metabolic model (Section 3.2) as well as the parameters fitted to create the CD59 inhibition model (Section 3.3) were varied by ±5%. For each iteration, it was evaluated if 2.5 mM of CD59 prevented lysis within 12 hours of triggering the inflammatory complement cascade. The EE, at each iteration, is the difference between the volume fraction of astrocyte 12 hours after complement lysis is induced and the prediction presented in Figure 5.19. This analysis performed is summarised in Figure 5.20.

By analysing the results of the sensitivity analysis, it was possible to divide the parameters into two categories: those that with a change of 5% result in the depolarisation of the astrocytic membrane even with the injection of 2.5 mM of CD59 (Figure 5.20 A) and those that have a negligible impact on the threshold for CD59 inhibition of complement lysis (Figure 5.20 B).

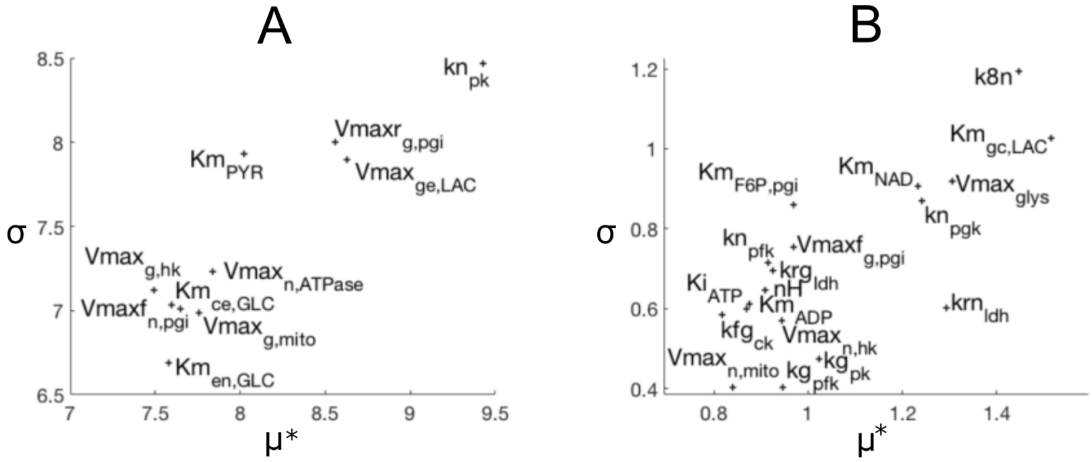

Figure 5.20: Outcome of applying the C-M sensitive analysis method to CD59 inhibitory predictions to the model where parameters are varied by 5%. At each iteration of the C-M method, complement lysis was simulated for 12 hours when 2.5 mM of CD59 are injected. The EE for was chosen to be the difference between the astrocytic volume fraction at 12 hours for each iteration parameter choice and the result presented in Figure 5.19. Two groups were found. A and B present the parameters that severely and negligible impact the model predictions respectively.

5.4 Discussion

The model developed here was the first to capture cytotoxic oedema caused by complement lysis. As such, assumptions were required to overcome the limitations in the literature. In this section, those assumptions are explained and the experimental measurements require to test them are suggested. This section starts by commenting on the procedure and validation of the cytotoxic oedema model created in (section 5.4.1). The following sections can be clustered into the two NMO pathology theories tested. In section 5.4.2 the assumptions made to arrive at the results of AQP4 impairment on astrocytic volume are commented. Then sections 5.4.3, 5.4.4 and 5.5.5 all examine the complement lysis model created. More specifically these sections cover: the assumptions made when adapting for purpose the complement protein cascade model (5.4.3); the antibody-antigen binding model (5.4.4) and the results and limitations of the MAC formation and the resulting ionic currents. This analysis is preceded by an examination of the CD59 experiments performed. Finally, in section 5.4.7 the sensitivity analysis method used, its limitations and its assumptions are explained.

5.4.1 Revalidating the model

In the literature, there is a lack of data on the effects of pathologies on cellular metabolism. Recently, there have been studies on the effects of certain pathologies on neuronal metabolism, e.g. the work by Poliquin *et al.* [301] presents a single neuron metabolism model validated with measurements of lactate and ATP consumption in mice models of Parkinson's disease. Similar to Poloquin *et al*. [301] the literature on the impacts of neuropathologies on metabolism focus on single neuron kinetics. In the work developed there is a need to consider the interactions between neurons, astrocytes and capillaries.

The literature on mathematical models of cellular metabolism that takes the interaction between those three components focuses on tissue kinetics during stimulation. The state of the art model found in the literature is the Cloutier *et* al. [200] model. Understandably, however, the model is not fit for pathological conditions. The models that focus on metabolism in a pathological environment take into account the full set of biochemical equations involved in the Krebs cycle. A decision was made that this limitation would be overcome without having to include all the Krebs cycle equations in the model as it would substantially increase the number of variables in the model and there is a lack of data to validate such a complex model. The middle ground found was to make changes to Cloutier *et al.* [200] and to revalidate it with the same neuronal stimulation data. It was found that the result would greatly improve if the steady state stability were ignored. It is proposed that in order to improve the validation of the model in different conditions further data in terms of metabolites are required, especially intracellular metabolite kinetics.

To this metabolism model, the Endresen *et al*. [206] model was added. An assumption was made that both species of cells have firstly the same intracellular ion concentration as well as membrane potential. As presented by other mathematical models such as Dronne *et al*. [65] and Østby *et al*. [64] such an assumption is contested. However, with such an assumption the work of Orlowski *et al*. [15] has shown that the model developed is able to validate cellular kinetics in pathological environments. Following Orlowski *et* al. [15] model the model developed was validated in an ischaemic stroke environment. As it can be seen in Figure 5.15 A, after 30 min of an induced stroke at

CBF reduction of 98% the model predicts that the ECS volume fraction falls between 0.04 and 0.1 of the total brain volume. Therefore, the model is in agreement with the data from [298], [299]. Additionally, the model reaches a steady state within this boundary, where the ECS volume stays at a level of approximately 0.05.

Additionally, this result was stress tested by again applying the C-M method. The parameters fitted for the developed metabolic model (Section 5.2.1) were varied by ±5%. It was found that for all simulations the ECS volume fraction after 30 min of full ischemia was between the boundaries experimentally measured. Therefore, ensuring confidence in the model predictions.

However, no model of cytotoxic oedema in the literature has validated metabolite kinetics. In order to improve the literature, a study is required to simultaneously track metabolites and cellular volume. It is here suggested that the metabolite measurements could be performed *in vivo* using CEST following the work of Kogan *et al.* [302]. Then following the work of Syková *et al.* [299] ion concentrations could be measured and ECS volume fraction estimated *in vivo* using ion selective microelectrodes.

5.4.2 The impact of AQP4 impairment on astrocytic volume

The mechanisms of water regulation by the astrocyte have been of interest lately. Most research in this field focuses on trying to prove the hypothesis that water flow to the astrocyte is responsible for the 30% decrease in ECS volume during action potential stimulation [64], [82]. Currently, the NKCC, the glutamate transporter and AQP4 are the only channels identified as being permeable to water. Previous mathematical models have been successful at incorporating these channels into models of cellular ionic exchange regulation.

When AQP4 impairment is simulated, as captured in Figure 5.16 and Figure 5.17, it can be seen that decreasing the permeability of water has a little impact independent of what species of AQP4 is disabled. The maximum change of approximately 1.5% was found when it is assumed that there are only perisynaptic AQP4 channels. However, as the work by [81] has shown, there is a larger concentration of AQP4 located at the astrocytic endfoot processes. Therefore, by including all the current understanding of astrocytic kinetics AQP4 impairment cannot be the main mechanism responsible for the astrocytic cytotoxic oedema reported by [17].

5.4.3 Complement protein models

In the literature, there are only 3 models of the complement protein cascade. The work by Hirayama *et al.* [235] assumes that all mass exchange equations are linear which as discussed by [236], [238] is unsuitable to capture the complexity of this mechanism.

When considering the work by Liu *et al.* [238], the model was found to be incomplete for the needs of the work here presented. The model in [238] focuses on the impact of C4bp as an inhibitor of C3b formation, which as it was shown is a powerful chemokine. Consequently, it does not consider the reactions from C3b to the formation of MAC. In order to test the feasibility of implementing this model the missing equations were taken from [236] and added to the model by Liu *et al.* [238]. However, as presented in the sensitivity analysis in Section 5.2.3.3 the equations prior to C3b formation have little impact on MAC formation. Therefore, the model by Liu *et al.* [238] was not considered further.

Taking all these points into consideration, the model by Korotaevskiy *et al.* [236] was chosen. However, there were certain concerns as some parameters were omitted in the paper [236]. To overcome this the missing parameters were related to the complement inhibitors C_{1est} and S protein. These parameters were fitted to ensure that $\frac{\partial C_{1est}}{\partial t}$ and $\frac{\partial S}{\partial t}$ were equal to zero at time equal to zero. With these parameters, the model was found to still behave the same as described in Figure 4 in [236]. Furthermore, when looking at the Campolongo-Morris analysis of the model these two proteins have little impact on MAC formation. Therefore, the impact of the parameters fitted is negligible in terms of the needs of the model here presented.

Furthermore, complement cascade section of the model has its kinetics defined based on data gathered from exposure of bacteria to human complement. The astrocyte is a bigger cell for which kinetics might be different. A dedicated experiment following the procedure described in the work of

[236] should be performed on astrocytes to make the complement cascade model more representative of the NMO scenario.

5.4.4 AQP4 and AQP4-Ab binding

There are several models that capture the binding of antibodies to antigens. Therefore, average rates have been measured. The main assumption made in this work is that, as in [236], [238], there is a mass action relationship between antibody antigen binding and complement activation. As Liu *et al*. [238] have presented, besides the binding of C1 and antibody-antigen complex the classical complement pathway activation mechanism involves surface membrane proteins. However, the work by Green and Golberg [303] showed that cells treated with antibody and complement suffer swelling within 2 minutes. Since the simulations required run for 12 hours it is assumed that the inclusion of more complex complement activation mechanisms would have a negligible impact on the final results found.

Additionally, due to gaps in the literature, the number of AQP4 at the astrocytic membrane has yet to be estimated. Researchers have identified many characteristics of the AQP4 channels: the dimensions, permeability and location have been defined by Höfinger *et al*. [304]. However, the density of AQP4 on the membrane of astrocytes has yet to be measured. There has been research where the channels were stained with golden particles [305], which were used to estimate the number of AQP4 channels. A more accurate estimate of the number of AQP4 channels would be important to better predict cellular oedema due to lysis. However, as shown in Figure 5.10 A, considering the previous assumptions, the binding of antibodies to antigens can only affect the speed of MAC formation.

5.4.5 Astrocytic oedema due to complement lysis

The work developed here has led to the first model of astrocyte swelling during NMO. The swelling is initiated by the injection of the NMO antibody and human complement into the ECS with respective concentrations replicating an experiment on a mouse model. The simulation predicts that the swelling occurs in one hour and leads to a volume increase of 25%. The concentration of the injected human complement is 60% [306] of that in the human plasma. Hence, the swelling process can potentially be faster depending on the mechanism of complement transport into the ECS during the condition. To appreciate the sensitivity of the evolution of the cell volume to a different initial complement concentration and to estimate the maximum rate of change of the cell volume during NMO, the model, with no CD59 added, was re-simulated with an ECS complement concentration equal to that of the plasma. i.e. a tentative estimate of the uppermost value that a cell can experience during an episode of NMO. The complement concentration change resulted in the plateau volume being reached 5 minutes earlier compared to the 60% dilution simulation. This result suggests that dynamic change of cell volume during NMO will not take less than 1 hour. Hence, any experiment planning to characterize these dynamics would have to be designed with a matching temporal resolution.

From simulating complement cytotoxic oedema, it was found that the astrocyte volume experiences an exponential swelling as seen in Fig. 5.16. This behaviour is in line with the exponential production of MAC occurring in the complement cascade, as explained in [236]. This behaviour is further confirmed by the experimental microscopy work by [307], who have shown that cellular conductance increases in steps of exponentially increasing magnitude every time a MAC hole is formed. Additionally, [307] fitted a model to the conductance curve measured where the membrane conductance (i) is defined as:

$$i(n) = i_0(N_0 + N)^2, \tag{5.26}$$

where i_0 is the initial conductance, $N_0 = 1$ and N is the number of holes formed. However, this analysis did not take into account the changes in the membrane permeability to each ion as was done in the model developed here.

The slow change of volume at the beginning of the simulation can be attributed to the sodium potassium pump managing to counterbalance the additional ionic flux occurring through membrane holes. This hyperactivity leads to a rapid depletion of ATP reserves and an inability of the pump to restore ionic balance with increasing currents due to more holes being created. As complement proteins are consumed the number of holes reaches a maximum of approximately 350 holes. This stabilizes the permeability of the membrane. Hence, after the exponential swelling, the astrocyte volume reaches a peak of 25% increase. However, the peak is then followed by a decrease of 5% and the volume of the astrocyte stabilizes. This behaviour can be explained by the swelling of the neuron responding to changes in the osmotic pressure of the ECS. The evolution of the volume fraction occupied by each cell compartment is shown in Figure 5.20.

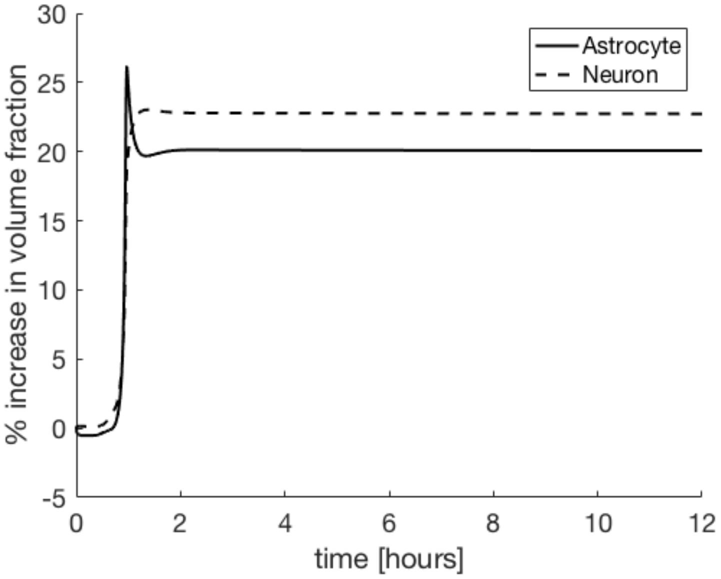

Figure 5.20: Comparison between the behaviour of astrocytic and neuron volume in the presence of astrocytic complement lysis.

The dynamic change of volume in both stroke and NMO simulations is rapid and occurs within a few hours. To improve validation, the model should be compared to data with multiple samples taken during that timeframe. Unfortunately, available data with such resolution are limited. To improve validation a study could simultaneously track metabolites and cellular volume during ischaemia and NMO. Examples of existing tools for these measurements include the use of CEST as in the work of [302] or ion selective electrodes as in the work of [299].

Such new data could challenge some of the assumptions of the current model. For example, it may lead to changes being required in its metabolic section. A new model capturing neuronal metabolic function in the presence of Parkinson’s disease by [301] found that implementing kinetics of the full Krebs cycle was indispensable in order to achieve a satisfactory fit to data. A similar refinement may be needed here.

Finally, the permeability of holes to water and ions has been defined in the model to be proportional to the permeability of AQP4 channels and that of ion channels respectively with a scaling factor defined as the ratio of the cross-section area of the hole to that of the respective channel. An experiment is needed to define these permeabilities. [303] presented experimental work on complement effects on mammalian erythrocytes. It reported that within 5 minutes after complement activation with a large concentration of complement, 90% of erythrocyte intracellular potassium egressed while extracellular sodium and water entered the cytoplasm. It is here proposed that a similar experimental procedure should be implemented in order to measure ionic fluxes during astrocytic complement lysis.

5.4.6 CD59 kinetics

The data available to create this model were limited because, as shown by [165], the inhibition of MAC formation by CD59 is species dependent. In the literature, only one study was found that performs measurements on humans [165]. However, the concentration of all the proteins is not clearly stated, which is required to reproduce their experimental procedure, in particular, the concentration of C8 and C9. As these concentrations were taken from human plasma it was assumed here that they were similar to the ones in, which also extracted complement proteins from human plasma.

In order to further improve this work a more detailed analysis of CD59 mechanisms is required. The experimental procedure presented by [165] is efficient at measuring the inhibition of MAC by CD59. However, this study aimed to quantify the efficacy of CD59 inhibition of MAC for different species. Therefore, in order to be able to further test the therapeutic potential of CD59 for NMO, a similar study is here suggested where it would aim to at measure the CD59 mechanism using astrocytes.

With the present assumptions, the simulation of the injection of the CD59 MAC production inhibitor with AQP4-Ab and human complement shows that there is a CD59 concentration threshold of 2.5 mM beyond which swelling can be completely prevented. This level of inhibition allows for only 30 holes to be created. As in this case, the permeability of the cell is about 10 times lower than in the case where no CD59 is injected, the sodium potassium pump is able to maintain ionic balance for at least 12 hours and no volume increase is observed. Furthermore, this conclusion is in line with the theory by [18] that NMO targets the astrocytic endfoot processes due to a smaller concentration of CD59 in that area.

When the initial CD59 concentration is below the 2.5 mM threshold it inhibits the number of holes formed in the membrane compared to the no CD59 case. However, it cannot stop the sodium-potassium pump failure. The astrocyte volume peak is reduced as fewer holes formed means that the added membrane permeability is lower than in the no CD59 case. For the same reason, the steady cell volume is also lower. These differences can be observed in Figure 5.19.

Furthermore, sensitivity analysis showed that the CD59 concentration threshold for complement lysis inhibition is sensitive to certain parameters such as kn_{pk} and $Vmax_{ge,LAC}$ from the metabolic model have a determinant impact on the predictions of the model. These parameters define the production of ATP by the cell. Therefore, slight changes might result in the inability of the sodium potassium pump to maintain osmotic equilibrium when there is a slight increase in astrocytic membrane permeability due to lytic holes. Consequently, the membrane of the astrocyte depolarises and cell swells. Therefore, measuring the parameters and kinetics of cellular metabolism is crucial to evaluate oedema in this and other pathological contexts. The importance of these parameters is further confirmed by the sensitivity analysis performed on the adapted metabolic model, as presented in Appendix A.

Additionally, the parameters fitted for the CD59 inhibition model (Section 5.2.4) were found to result in maximum μ^* of ±1% when varied by ±5%. The astrocytic membrane within this range of parameter values did not depolarise. Therefore, the bi-phasic nature (polarized vs depolarized) of the results demonstrate that the predictive nature of the model relies on ensuring that the model is able to simulate a biologically relevant amount cellular ATP.

5.4.7 Reducing the model

As described in the work by [260] there are many procedures to discover redundant variables and therefore to reduce the size and computational time of a mathematical model. However, due to the size of the model (approximately 13 ODE's) many common procedures, e.g. non-dimensionalization, become obsolete.

From the tools available the one initially chosen was the process of screening the model presented by Campolongo and Braddock [294]. This method, as shown in Figure 5.6, provided a metric to identify the variables that had the least impact on MAC formation. However, it only presented the relative impact of variable compared to all the others. Therefore, it required further trial and error to see which ones, in fact, could be removed. From this analysis, it was only possible to reduce 4 variables down to constants. Additionally, this method is dependent on the range of values considered, as described by [260]. Therefore, a better understanding of how complement varies in human plasma could render better simplifications of the model.

In an attempt to overcome the limitations of the reduction tools provided, a brute force method was used where a second order model was simply fitted to the complement protein cascade. The results presented in Section 5.2.3.4 show that such a simplification is successful within the range considered, also when considering the duration of the simulations. However, when testing therapies for NMO the 2^{nd} order model becomes limited.

With this analysis, it is shown that the current tools available to simplify models are still ill-equipped to handle very large models. Additionally, although mathematical modelling is able to capture a larger number of mechanisms, an effort needs to be made to ensure that those irrelevant variables are not carried through, making large models impractical to handle.

5.5 Summary of findings

The current model of astrocyte swelling during NMO showed good qualitative agreement with existing data measuring water transport during complement lysis. The model was also in agreement with an experimental study showing that AQP4 impairment is not the primary cause of swelling during NMO. Furthermore, the metabolic and water transport sections of the model showed robustness to tests with available data characterizing swelling during ischaemia.

The model was used to test the inhibitory effect of CD59 on NMO induced astrocytic oedema. Simulations predicted that, to be effective, CD59 needs to be injected with a concentration beyond a potential threshold. Thus, the model shows potential for use in further predictive *in silico* studies applied to NMO. The complement cascade and complement lysis are pathological mechanisms generic to many brain conditions including ischaemia [308] neurodegenerative diseases such as Alzheimer's [46] and multiple sclerosis [309]. Hence, this fundamental model can be repurposed for similar *in silico* studies in these new contexts.

Appendix 5.A: New metabolic parameter values

All the values found for the parameters when refitting the Cloutier *et al.* [200] model are presented in Table A.1.

Table 5.A.1: Refitting the parameters from Cloutier *et al*. model [200] with the new Krebs cycle 5uation.

Parameter	Value	Units	Description
$Km_{en,GLC}$	9.4722	mM	Affinity constant for GLC uptake by the neuron from the ECS
$Vm_{en,GLC}$	0.90332	mM/s	Maximum uptake rate of GLC in astrocytes
$V_{max,n,hk}$	0.099625	mM/s	Maximum reaction for HK in the neuron
$V_{\mathrm{maxf,n,pgi}}$	0.47657	mM/s	Maximum forward reaction rate for PGI in neurons
$V_{maxr,n,pgi}$	0.44408	mM/s	Maximum reverse reaction rate for PGI in neurons
$k_{n,\mathrm{pfk}}$	0.71693	$\mathrm{mM^{-1}s^{-1}}$	Reaction rate constant for PFK in the neuron
$k_{n,pgk}$	0.45454	$\mathrm{mM^{-1}s^{-1}}$	Reaction rate constant for PGK in the neuron
$k_{\mathrm{n,pk}}$	30.486	$\mathrm{mM^{-1}s^{-1}}$	Reaction rate constant for PK in the neuron
$k_{\mathrm{fn,ldh}}$	0.00063581	$\mathrm{mM^{-1}s^{-1}}$	Forward reaction rate constant for LDH in the neuron
$k_{\mathrm{rn,ldh}}$	$5.2952\mathrm{x}10^{-5}$	$\mathrm{mM^{-1}s^{-1}}$	Reverse reaction rate constant for LDH in the neuron
$V_{\mathrm{max,n,mito}}$	0.0421	mM/s	Maximum reaction rate for the mitochondrial response for the neuron
Km_{NADH}	0.011621	mM	Affinity constant of mitochondria for NADH
Km_{NAD}	0.021631	mM	Affinity constant of mitochondria for NAD
$V_{max,ne,LAC}$	0.29499	mM/s	Maximum reaction rate for LAC exchange between ECS and neurons
$Km_{\mathrm{ne,LAC}}$	$2.26\mathrm{x}10^{-5}$	mM	Affinity constant for LAC exchange between ECS and neurons
$V_{\mathrm{max,n,ATPase}}$	0.047727	mM/s	Maximum rate of ATP consumption for cellular processes in the neuron
$k_{\mathrm{rn,ck}}$	0.023917	$\mathrm{mM^{-1}s^{-1}}$	Reverse reaction rate constant for CK in the neuron
$k_{\mathrm{fn,ck}}$	0.077236	$\mathrm{mM^{-1}s^{-1}}$	Forward reaction rate constant for CK in the neuron
nh_{O2}	1.3652	dimensionless	O^2 reaction order constant
PScap_n	0.19173	s^{-1}	O^2 mass transfer constant between capillary and neurons
$K_{\mathrm{m,eg,GLC}}$	3.5745	mM	Affinity constant for GLC exchange between ECS and astrocytes

$V_{\mathrm{m,eg,GLC}}$	0.038856	mM/s	Maximum rate of ATP consumption for cellular processes in the neuron
$K_{\mathrm{m,cg,GLC}}$	16.959	mM	Affinity constant for GLC exchange between capillary and astrocytes
$V_{\mathrm{m,cg,GLC}}$	0.0072884	mM/s	Maximum rate of GLC exchange between capillaries and astrocytes
$V_{\mathrm{max,g,hk}}$	0.085572	mM/s	Maximum reaction rate for HK in the astrocyte
$V_{\mathrm{maxf,g,pgi}}$	0.49349	mM/s	Forward reaction rate for PGI in the neuron
$V_{\mathrm{maxr,g,pgi}}$	0.46734	mM/s	Reverse reaction rate for PGI in the neuron
$k_{\mathrm{g,pfk}}$	0.34282	$mM^{-1}s^{-1}$	Reaction rate constant for PFK in the astrocyte
$k_{\mathrm{g,pgk}}$	0.19204	$mM^{-1}s^{-1}$	Reaction rate constant for PGK in the astrocyte
$k_{\mathrm{g,pk}}$	2.1073	$mM^{-1}s^{-1}$	Reaction rate constant for PK in the astrocyte
$k_{\mathrm{f,g,ldh}}$	10.447	$mM^{-1}s^{-1}$	Forward rate constant for LDH in the astrocyte
$k_{\mathrm{r,g,ldh}}$	0.96618	$mM^{-1}s^{-1}$	Reverse rate constant for LDH in the astrocyte
$V_{\mathrm{max,g,mito}}$	0.0092873	mM/s	Forward rate constant for LDH in the astrocyte
$V_{\mathrm{max,ge,LAC}}$	0.023223	mM/s	Maximum reaction rate for the mitochondrial response for the astrocyte
$K_{\mathrm{m,ge,LAC}}$	0.37539	mM	Reaction rate constant for LAC exchange between astrocytes and ECS
$V_{\mathrm{max,gc,LAC}}$	0.00012605	mM/s	Maximum rate for LAC exchange between astrocytes and capillary
$K_{\mathrm{m,gc,LAC}}$	0.16258	mM	Reaction constant for LAC exchange between astrocytes and capillary
$V_{\mathrm{max,g,ATPase}}$	0.02335	mM/s	Maximum rate of ATP consumption for cellular processes in the astrocyte
$k_{\mathrm{r,g,ck}}$	0.038754	$mM^{-1}s^{-1}$	Reverse reaction rate constant for CK in the astrocyte
$k_{\mathrm{f,g,ck}}$	0.047902	$mM^{-1}s^{-1}$	Forward reaction rate constant for CK in the astrocyte
$PScap_g$	0.13413	s^{-1}	O^2 mass transfer constant between capillary and astrocytes
$K_{m,\mathrm{ce,GLC}}$	6.8233	mM	Reaction constant for GLC exchange between the capillary and the ECS
$V_{\mathrm{m,ce,GLC}}$	0.046212	mM/s	Reaction rate for GLC exchange between the capillary and the ECS
$K_{\mathrm{m,ec,LAC}}$	0.03698	mM	Reaction constant for LAC exchange between the capillary and the ECS
$V_{\mathrm{m,ec,LAC}}$	1.0652	mM/s	Reaction rate for LAC exchange between the capillary and the ECS
$V_{\mathrm{max,g,gs}}$	0.0038215	mM/s	Maximum exchange rate for GLU exchange between the neuron and astrocyte
$V_{\mathrm{max,eg,GLU}}$	0.01081	mM/s	Maximum rate for GLU exchange between the ECS and the astrocyte
$V_{\mathrm{max,gys}}$	5.6488×10^{-5}	mM/s	Maximum rate for GLY synthase at the astrocyte
Km_{gys}	0.49488	mM	Rate constant for GLY synthase at the astrocyte
$V_{\mathrm{max,glyp}}$	2.5664×10^{-5}	mM/s	Maximum rate for GLY phosphorylase at the astrocyte
Km_{GLY}	0.00045247	mM	Rate for GLY phosphorylase at the astrocyte
Km_{PYR}	0.036199	mM	Affinity constant of mitochondria for PYR
Km_{ATP}	0.010436	mM	Affinity constant of mitochondria for ATP
Ki_{ATP}	0.78806	mM	Affinity constant of PFK for ATP
Km_{ADP}	8.4212×10^{-6}	mM	Affinity constant of ADP
Km_{O2}	0.00014805	mM	Affinity constant of O_2
Km_{GLC}	0.11182	mM	Affinity constant of GLC
Km_{GLU}	0.072481	mM	Affinity constant of GLC
Km_{G6P}	0.53149	mM	Affinity constant of G6P
$Km_{\mathrm{F6P,pgi}}$	0.072171	mM	Affinity constant of PGI for F6P
$Km_{\mathrm{F6P,pfk}}$	0.20247	mM	Affinity constant of PGI for PFK
Km_{pump}	0.32452	mM	Affinity constant of ATP for NaK-pump
Ko2	0.048077	mM	O_2 transport constant
qak	0.42136	dimensionless	Equilibrium constant for AK
nH	3.4637	dimensionless	Hill coefficient for ATP inhibition
$Km_{\mathrm{hk,ATP}}$	5.9857×10^{-5}	mM	Affinity constant of HK for ATP
$Km_{\mathrm{pfk,ATP}}$	0.0048526	mM	Affinity constant of PFK for ATP

This solution was stress tested by applying the Campolongo-Morris method [294] as described in Section 3.5 in the manuscript. The test aims at evaluating how sensitive the fitting of the model is to individual changes to parameters. For this test, each parameter was varied by ±5% of the fitted value. The elementary-effect (EE) for each iteration was calculated to be the difference in RMS error between every simulation and the solution of the fit presented in Figure 5.3. Table 5.A.2 presents the $\boldsymbol{\mu}^* \pm \boldsymbol{\sigma}$ of the 10 most and least impactful parameters to the result.

This analysis demonstrated that changing the parameters by 5% led to an increase in error by 10^{-1} to 10^{4}%. This demonstrates that this model and the models of the family of Cloutier *et al.* [200] are dependent in the parameter choices. Therefore, identifying biological relevant ranges for these parameters would be crucial to ensure the reliability and predictability of the models.

Table 5.A.2: Results of applying the C-M method to the model after the changes to Cloutier *et al.* [200] after changes were made.

	C-M Output [%]			C-M Output [%]	
Parameters	$\boldsymbol{\mu}^*$	$\boldsymbol{\sigma}$	Parameters	$\boldsymbol{\mu}^*$	$\boldsymbol{\sigma}$
Km_{ATP}	0.16978	0.12068	Km_{G6P}	296.14	118.02
$Km_{gc,LAC}$	0.17347	0.084518	$Km_{ce,GLC}$	300.39	119.95
$Vmax_{ne,LAC}$	0.19708	0.094874	$Vmaxr_{g,pgi}$	317.2	115.32
Km_{ADP}	0.34005	0.13037	kn_{pfk}	335.82	98.966
Km_{GLY}	0.35788	0.18736	$Vmax_{g,mito}$	408.64	156.03
krn_{ldh}	0.38015	0.14628	$Vm_{ce,GLC}$	411.09	107.94
$Vmax_{gc,LAC}$	0.38367	0.18414	$Vmaxr_{n,pgi}$	481.68	205.4
$Km_{pfk,ATP}$	0.47836	0.21098	$Vmaxf_{n,pgi}$	684.22	265.09
kn_{pk}	0.56531	0.2563	nH	1841.3	460.98
$Km_{hk,ATP}$	0.57865	0.26216	Ki_{ATP}	2132.4	566.93

Appendix 5.B: Fitting water co-transporters to the ionic model

Adding the new channels to the ionic model in Orlowski *et al.* [15] resulted in the following kinetics:

$$\frac{d[Na]_g}{dt} = \frac{-iNa_g - iNaK_g - iNaCa_g + iNKCC - 3\times iGTR1_g}{V\times F} - \gamma_g . [Na]_g \tag{5.B.1}$$

$$\frac{d[Na]_n}{dt} = \frac{-iNa_n - iNaK_n - iNaCa_n - 3\times iGTR1_n}{V\times F} - \gamma_n . [Na]_n \tag{5.B.2}$$

$$\frac{d[K]_g}{dt}=\frac{iK_g+iNaK_g+iNKCC+iGTR1_g}{V\times F}-\gamma_g.[K]_g \tag{5.B.3}$$

$$\frac{d[K]_n}{dt}=\frac{iK_n+iNaK_n+iGTR1_n}{V\times F}-\gamma_n.[K]_n \tag{5.B.4}$$

$$\frac{d[Ca]_g}{dt}=\frac{iCa_g+iNaCa_g}{V\times F}-\gamma_g.[Ca]_g \tag{5.B.5}$$

$$\frac{d[Ca]_n}{dt}=\frac{iCa_n+iNaCa_n}{V\times F}-\gamma_n.[Ca]_n \tag{5.B.6}$$

$$\frac{d[Cl]_g}{dt}=\frac{iCl_g-2\times iNKCC}{V\times F}-\gamma_g.[Cl]_g \tag{5.B.7}$$

$$\frac{d[Cl]_n}{dt}=\frac{iCl_n}{V\times F}-\gamma_n.[Cl]_n \tag{5.B.8}$$

$$\frac{d[GLU]_g}{dt}=\frac{-iGLU_g+iGTR1_g}{V\times F}-\gamma_g.[GLU]_g \tag{5.B.9}$$

$$\frac{d[GLU]_n}{dt}=\frac{-iGLU_n+iGTR1_n}{V\times F}-\gamma_n.[GLU]_n \tag{5.B.10}$$

where the currents iNa_c, iK_c, iCl_c, iCa_c are the currents through the ion specific channels for sodium, potassium, chloride and calcium respectively; $iNaK_c$ stands for the sodium potassium pump; $iNaCa_c$ is the sodium-calcium co-transporter and γ_g and γ_n are the rate of change to the concentration of the ion due to volume change.

Before refitting the model, further alterations to the Orlowski *et al.* [15] model were required due to the implementation of glutamate Nernst potential. This is because the potential depends on the quotient between the intra and extra cellular glutamate concentrations. Orlowski *et al.* [15] assumes that both the astrocyte and the ECS have no glutamate at steady state, which would result on indeterminate Nernst potential. To overcome this limitation of the model the concentrations of glutamate for the astrocyte and ECS were replaced with the concentrations in Dronne *et al.* [65].

These new concentrations of glutamate alter the osmotic pressure in these compartments. Therefore the model required recalibration. The steps presented in Section 2.1 in the work by Orlowski *et al.* [15] were followed:

1. The concentration of chloride at the ECS is calculated to ensure the compartment is electrically neutral which means:

$$[Na^{+}]_{e}+[K^{+}]_{e}+2\times[Ca^{2+}]_{e}-[HCO_{3}^{-}]_{e}-[Cl^{-}]_{e}-[GLU^{-}]_{e}=0 \tag{5.B.11}$$

2. The intracellular concentration of chloride is calculated to make the Nernst potential equal to -70 mV.

3. Then it is assumed that there are impermeable anions (A_i) inside the cell that ensure that the net osmotic pressure across the membrane is zero:

$$\begin{aligned}&([Na^{+}]_{i}+[K^{+}]_{i}+[Ca^{2+}]_{i}+[HCO_{3}^{-}]_{i}+[Cl^{-}]_{i}+[GLU^{-}]_{i}+[A^{-}]_{i})-([Na^{+}]_{e}+[K^{+}]_{e}\\&\quad+[Ca^{2+}]_{e}+[HCO_{3}^{-}]_{e}+[Cl^{-}]_{e}+[GLU^{-}]_{e})=0\end{aligned} \tag{5.B.12}$$

4. Finally, the A_i charge (z_{A_i}) is calculated to ensure the intra-cellular space is neutrally charged; which means:

$$[Na^{+}]_{i}+[K^{+}]_{i}+2\times[Ca^{2+}]_{i}-[HCO_{3}^{-}]_{i}-[Cl^{-}]_{i}-[GLU^{-}]_{i}-z_{A_i}[A^{-}]_{i}=0 \tag{5.B.13}$$

In the following Table 5.B.1 all the initial conditions found in the literature and the ones calculated are presented.

Table 5.B.1: Initial conditions and parameters for the ionic model.

Parameter	Value	Units	Reference
$[Na^{+}]_{n,g}$	19	mM	[15]
$[Na^{+}]_{e}$	140	mM	[15]
$[K^{+}]_{n,g}$	5	mM	[15]
$[K^{+}]_{e}$	130	mM	[15]
$[Ca^{2+}]_{n,g}$	0.0006	mM	[15]
$[Ca^{2+}]_{e}$	2.0023	mM	[15]
$[Cl^{-}]_{n,g}$	9.0360	mM	Calculated
$[Cl^{-}]_{e}$	124.0036	mM	Calculated
$[HCO_{3}^{-}]_{n,g}$	15.77	mM	[14]
$[HCO_{3}^{-}]_{e}$	25	mM	[14]
$[GLU^{-}]_{n,g}$	3	mM	[65]
$[GLU^{-}]_{e}$	0.001	mM	[65]
$[A^{-}]_{n,g}$	119.2003	mM	Calculated
z_{A_g}	1.0168	dimensionless	Calculated

Table 5.B.2: Fitted ionic channel permeabilities.

Parameter	Value	Units	Description
kK_n	168140	pA	Permeability of the of the neuronal potassium channel.
kNa_n	29104.3	pA	Permeability of the sodium channel at the neuron.
kCa_n	810.679	pA	Calcium channel permeability at the neuron.
kCl_n	2532.07	pA	Chloride channel permeability at the neuron.
$kNaK_n$	41.1898	pA	Sodium potassium pump permeability for the neuron.
$kNaCa_n$	49.3498	pA	Sodium calcium co-transporter neuronal permeability
$kGTR1_n$	0.0475551	pS/μm^2	Neuronal glutamate transporter permeability.
$kGLU_n$	0.0336054	pS/μm^2	Glutamate channels permeability at the neuron.
kNa_g	164871	pA	The glial sodium channel permeability
kK_g	164871	pA	Potassium channel permeability at the astrocyte.
kCa_g	819.409	pA	Glial calcium channel permeability.
kCl_g	2319.28	pA	Permeability of the glial chloride channel.
$kNaK_g$	39.9515	pA	Glial sodium and potassium pump permeability
$kNaCa_g$	50.0884	pA	Calcium and sodium glial co-transporter permeability
$kNKCC_g$	0.0167471	pS/μm^2	Sodium-potassium and chloride glial permeability
$kGTR1_g$	0.0464557	pS/μm^2	Glial glutamate transporter permeability
$kGLU_g$	0.0328149	pS/μm^2	Glutamate glial channel permeability

With these new ionic concentrations the permeability of the channels in Orlowski *et al.* [15] model and the new channels are fitted to ensure the ionic currents are stable at steady state. The resulting permeabilities can be seen in Table 5.B.2.

Appendix 5.C: Parameters and kinetics of the new volume model

Table 5.C.1: Initial conditions and parameters of the compartmental volume kinetics.

	Value	Units	Description	Reference
Initial conditions				
V_g	0.25	dimensionless	Volume fraction of astrocyte	[15]
V_n	0.45	dimensionless	Volume fraction of the neuron	[15]
V_{ECS}	0.20	dimensionless	Volume fraction of the ECS	[15]
Parameters and Constants				
H_g	12.3930	kPa	Net intra-glial hydrostatic pressure	calculated
H_n	-4.99	kPa	Net intra-neuronal hydrostatic pressure	[292]
H_{ECS}	-5	kPa	Net Hydrostatic pressure at the ECS	[292]
H_c	15	kPa	Capillary net hydrostatic pressure	[292]
π_c	762.9104	kPa	Net osmotic pressure at the capillary	calculated
V_v	-2.88	/s	Rate of fluid extraction from the ECS by the ventricles	calculated
k_0	7×10^{-5}	m/s	Astrocytic membrane permeability not due to AQP4	[291]
k_{aqp}	4.3×10^{-4}	m/s	Astrocytic membrane permeability due to AQP4	[291]
k_n	3×10^{-4}	m/s	Neuronal membrane permeability	[310]
k_c	3.2×10^{-15}	m^3/(kPa.s)	Capillary rate of plasma filtration	[311]
M	1.807×10^{-7}	L/mmole	Water molar volume at 310.15 K	[290]
V	25,000	μm^3	Total volume of space considered	[65]
S_g	2,092.41	μm^2	Astrocytic surface area	[65]
S_n	2,244.66	μm^2	Neuronal surface area	[65]
F	96,485.309	C/mole	Faraday constant	[15]
R	8,309.97904	mVC/(molK)	Gas constant	[15]
T	310.15	K	Temperature	[15]

Adding all the components described in Section 5.2.2 the astrocytic, neuronal and ECS volume kinetics can be summarized in Equation 5.C.1, 5.C.2 and 5.C.3 respectively:

$$\frac{dV_g}{dt} = M\frac{iNKCC + iGTR1_g}{V \times F} + MV_w + \frac{S_g M}{RTV}\left[\left(k_0 + nk_{aqp}\right)\left[\Delta H_{cg} - \Delta\pi_{cg}\right] - \left(k_0 + (100-n)k_{aqp}\right)\left[\Delta H_{ge} - \Delta\pi_{ge}\right]\right] \quad (5.C.1)$$

$$\frac{dV_n}{dt} = M\frac{iGTR1_n}{V \times F} + MV_w + \frac{S_n M}{RTV}k_n\left[\Delta H_{ne} - \Delta\pi_{ne}\right] \quad (5.C.2)$$

$$\frac{dV_e}{dt} = -\frac{dV_n}{dt} - M\frac{iNKCC + iGTR1_g}{V \times F} - MV_w + \frac{S_g M}{RTV}\left(k_0 + (100-n)k_{aqp}\right)\left[\Delta H_{ge} - \Delta\pi_{ge}\right] + k_c\left[\Delta H_{ce} - \Delta\pi_{ce}\right] - V_{gli} \quad (5.C.3)$$

The volume of the capillary is assumed to stay constant throughout the simulations.

The list of initial conditions and constants can be found in Table 5.C.1.

Appendix 5.D: The full 2nd order approximation model

The analysis in Section 5.2.3.2.2 presented a second order model as:

$$a(C).y'' + b(C).y' + c(C).y = m(C), \quad (5.D.1)$$

where, C is the complement concentration in mM.

After each curve in Figure 5.8 was fitted, the relationship between each parameter and complement concentration were derived. Using the software Eureqa an equation was fitted to each curve. From the equations proposed by Eureqa one was chosen taking into consideration the best fit with least number of terms. The equations chosen were as follows:

$$a(C) = 9.949\times10^4 + 3.65\times10^5 C - 8.597\times10^4\sqrt{C} \quad (5.D.2)$$

$$b(C) = 163.2 + 52.5C + 621.7\sqrt{C} + 33.64\frac{\sqrt{C}}{C} \quad (5.D.3)$$

$$c(C) = 1.002 + 0.004522C + 1.423\times10^{-5C} + 0.0001617C^3 - 5.632\times10^{-4}C^2 \quad (5.D.4)$$

$$m(C) = 0.01632C - 0.0001132 \quad (5.D.5)$$

The results of the fit can be seen in Figure 5.D.1.

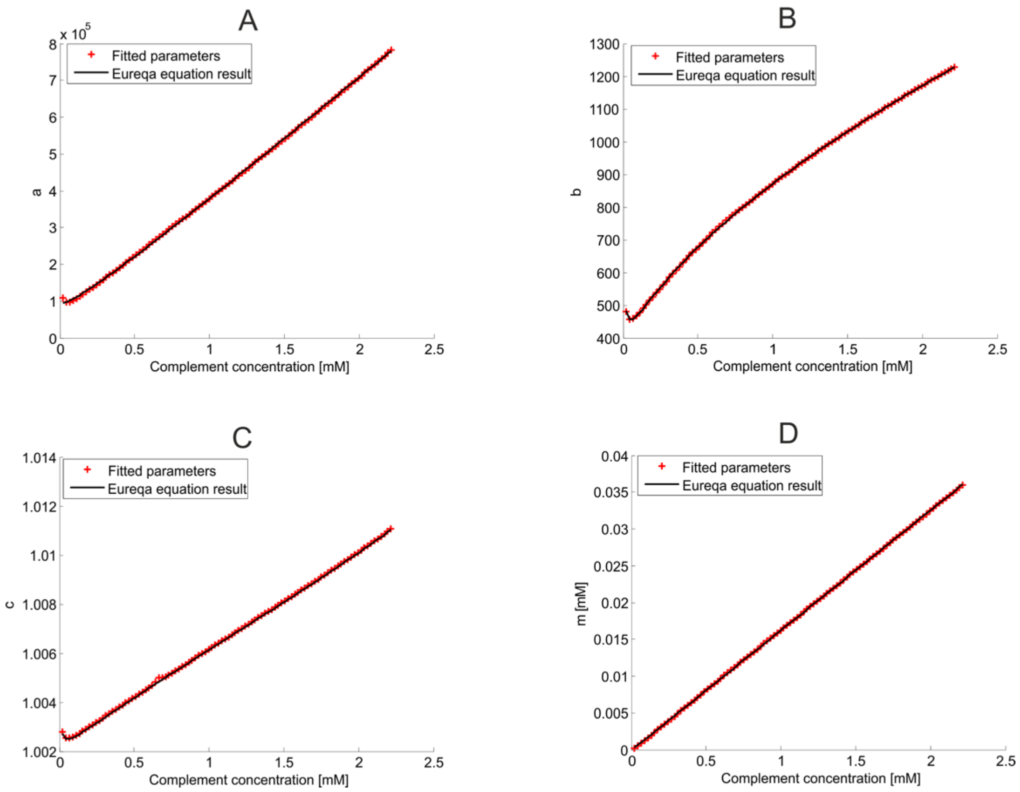

Fig 5.D.1: Comparing the resulting equations derived by Eureqa to the second order ode model parameters fitted.

Appendix 5.E: Ion movement through lytic holes

In order to calculate the permeability k_i of the hole to each ion, two constants need to be calculated. Firstly, there is the average number of channels n of a particular in a cellular membrane with surface area of 2,092.41 μm^2:

Table 5.E.1: Cellular membrane channel density.

Ions	Density [/um2]	Reference	n_i
Na+	5	[312]	10,462
Ca2+	0.5	[313]	1,046.2
K+	5000	[314]	10,462,000
Cl-	62	[315]	129,729

Secondly the ratio of diameter r between the channels (r_c) and the holes ($r_h = 8\ nm$) using the Poiseuille's equation:

Table 5.E.2: Ionic channel radii.

Ions	Diameter r_c [A]	Reference	r_i
Na+	120	[316]	1.235×10^{-2}
Ca2+	6.2	[317]	1.732×10^{3}
K+	12	[318]	1.23×10^{2}
Cl-	5	[319]	4.096×10^{3}

Then the permeability of each ion channel from [15] (k_{0i}) can be adapted to take into consideration the parameters n_i and r_i as:

$$k_i = r_i.\left(\frac{k_{0i}}{n_i}\right) \tag{5.E.1}$$

Then the ionic channel equations presented in [14] are adapted to include the formation of holes and the individual k_i.

Table 5.E.3: Kinetics of the ionic currents through the lytic holes.

Ions	Equation	
Na^+	$iNa = H.k_{Na}.sinh\left(\frac{v - vNa}{2.Vt}\right)$	(5.E.2)
Ca^{2+}	$iCa = H.k_{ca}.sinh\left(\frac{v - vCa}{Vt}\right)$	(5.E.3)
K^+	$iK = H.k_k.sinh\left(\frac{v - vK}{2.Vt}\right)$	(5.E.4)
Cl^-	$iCl = H.k_{cl}.sinh\left(\frac{v + vCl}{Vt}\right)$	(5.E.5)

where v is the membrane potential; vCl, vK, vNa and vCa are the Nernst potentials of chloride, potassium, sodium and calcium respectively and $Vt = \frac{RT}{F}$, where R is the gas constant, T is temperature and F is the Faraday constant.

Appendix 5.F: Model created to fit the CD59 data.

In order to create the CD59 inhibition model the experimental procedure from [17] was mimicked. The aim of the work was to quantify the sensitivity of complement from different species to CD59. The procedure consists of injecting human complement into a culture of chicken erythrocytes. The proteins injected are C7, C8, C9 and protein complex C5b6. The work by [44] only mentions the mass of C7, C8 and C5b6. These need to be converted to mM by considering the molar mass values of the proteins [236] and the volume presented in [165] of 1 mL. These conversions are shown in the table below. In the case of the proteins C8 and C9 they were taken from [236].

Table 5.F.1: Complement proteins concentration.

Protein	Mass [g]	Molar mass [Da]	Moles	Concentration [mM]	Reference
C5b6	2.70×10^{-7}	3.28×10^{5}	1.04×10^{10}	1.04×10^{-4}	[165]
C7	1.50×10^{-8}	1.10×10^{5}	3.64×10^{11}	3.64×10^{-5}	[165]
C8		1.52×10^{5}		3.6×10^{-4}	[236]
C9		6.90×10^{4}		9×10^{-4}	[236]

Then different concentrations of CD59 are injected into the medium where again the mass in g is presented and it has to be converted to concentration in mM. The molar mass was found to be 2×10^4 Da, also taken from [165].

Table 5.F.2: Calculation of CD59 concentration

Mass [g]	Moles	Concentration [mM]
5.00×10^{-08}	2.50×10^{-12}	2.50×10^{-6}
1.00×10^{-07}	5.00×10^{-12}	5.00×10^{-6}
1.50×10^{-07}	7.50×10^{-12}	7.50×10^{-6}
2.50×10^{-07}	1.25×10^{-11}	1.25×10^{-5}
5.00×10^{-07}	2.50×10^{-11}	2.50×10^{-5}
1.00×10^{-06}	5.00×10^{-11}	5.00×10^{-5}

The inhibition of MAC formation is measured by [165] by considering the % of lysis inhibited when compared to complement lysis when there is no CD59 present. The results in humans were extracted from Figure 5.1 from [165].

Table 5.F.3: Data taken from [165] of lysis inhibition by increasing concentrations of CD59.

CD59 [ug]	0	0.03	0.065	0.25	0.36	0.55	1
% Lysis	100	40	25	15	5	3	1

Then a mathematical model based on the work of [236] was created.

$$\frac{d(C7)}{d(t)} = -K_1.C5b6.C7 + K_2.C5b67 \tag{5.F.1}$$

$$\frac{d(C8)}{d(t)} = -K_3.C5b67.C8 + K_4.C5b678 \tag{5.F.2}$$

$$\frac{d(C9)}{d(t)} = -K_5.C5b678.C9 + K_6.C5b6789 \tag{5.F.3}$$

$$\frac{d(C5b6)}{d(t)} = K_2.C5b67 - K_1.C5b6.C7 \tag{5.F.4}$$

$$\frac{d(C5b67)}{d(t)} = K_1.C5b6.C7 - K_2.C5b67 - K_3.C5b67.C8 + K_4.C5b678 \tag{5.F.5}$$

$$\frac{d(C5b678)}{d(t)} = K_3.C5b67.C8 - K_4.C5b678 - K_5.C5b678.C9 + K_6.C5b6789 - K_7.CD59.C5b678 + K_8.CD59Cb8 \tag{5.F.6}$$

$$\frac{d(C5b6789)}{d(t)} = K_5.C5b678.C9 - K_6.C5b6789 - K_9.CD59.C5b6789 + K_{10}.CD59MAC \tag{5.F.7}$$

$$\frac{d(CD59)}{d(t)} = -K_7.CD59.C5b678 + K_8.CD59Cb8 - K_9.CD59.C5b6789 + K_{10}.CD59MAC \tag{5.F.8}$$

$$\frac{d(CD59Cb8)}{d(t)} = K_7.CD59.C5b678 \; - \; K_8.CD59Cb8\,; \tag{5.F.9}$$

$$\frac{d(CD59MAC)}{d(t)} \; = \; K_9.CD59.C5b6789 \; - K_{10}.CD59MAC; \tag{5.F.10}$$

The parameters values are as follows:

Table 5.F.4: Kinetics of the model created to fit to CD59 inhibition data.

Parameter	Value	Units	Reference	Parameter	Value	Units	Reference
K_1	733.3	$mM^{-1}s^{-1}$	[236]	K_6	0	s^{-1}	[236]
K_2	0	s^{-1}	[236]	K_7	0.0157	s^{-1}	Fitted
K_3	1100	$mM^{-1}s^{-1}$	[236]	K_8	0.0019	$mM^{-1}s^{-1}$	Fitted
K_4	0	s^{-1}	[236]	K_9	0.0437	s^{-1}	Fitted
K_5	2833.3	$mM^{-1}s^{-1}$	[236]	K_{10}	0.1501	$mM^{-1}s^{-1}$	Fitted

Chapter 6

A model for the optimization of anti-inflammatory treatment with Chemerin

6.1 Introduction

Chronic pain, a key feature of inflammation, is a leading cause of morbidity worldwide with an estimated prevalence as high as 50% in Europe [320]. Based on a survey of over 46000 respondents, chronic pain is reported to affect 19% of Europeans [3]. 7 out of 28 prevalence studies included in a recent report on pain in the EU showed a strong link between chronic pain and ageing [321]. Hence, the prevalence of pain is expected to increase in ageing populations.

Typical treatment of mild to moderate pain involves the use of non-steroidal anti-inflammatory drugs (NSAIDs) and paracetamol [320]. However, the use of NSAIDs may lead to complications including gastrointestinal (GI) symptoms (especially for patients with a high cardiovascular risk) which can result in fatal peptic ulceration and bleeding – about 2,500 people die in the UK each year due to NSAID related GI [322]. Hence, there is a need for new and safe drugs.

To achieve this goal, there has been interest in characterizing the role of mediators in the successful termination of the inflammatory response. In particular, the role of resolvins and chemerin-derived peptides, which mediate their effects through the ChemR23 G protein-coupled receptors (GPCRs) has been examined [323].

Accepted for publication at Interface focus

To test the potential of injecting extra chemerin into the inflammatory site a reliable and reproducible experimental inflammatory model is required. To this effect a zymosan induced peritonitis mouse model of inflammation was used as presented in [324] (detailed in the Materials and Methods section). No similar model was found for the CNS. There are marked differences between the acute inflammatory response between in the CNS and other regions [325]. The differences are mainly due to the existence of BBB that makes this environment less porous. Therefore, leukocytes find it harder to permeate into the ECS. However, as described in [325], in diseases where the BBB is compromised such as stroke and NMO [17] the acute inflammatory response is akin to that reported in non-neuronal tissue.

Using the peritonitis animal model, it was found that the recruitment of inflammatory cells is indeed reduced when chemerin with a concentration of 500 μg ml^{-1} is injected in the peritoneum two hours after inflammation onset. There is a need now to characterize both the drug concentration and timing of injection that optimizes inflammation inhibition to evaluate therapeutic potential of chemerin. As assessing the time course of just one treatment approach requires the sacrifice of approximately 50 mice for statistical significance it would be time consuming and ethically questionable to do an exhaustive experimental search for the optimum. Hence, a mathematical model was introduced of zymosan-induced peritonitis and its modulation by chemerin to identify chemerin delivery optimization hypotheses for further experimental validation.

The model here developed breaks from the family of models developed in Chapters 4 and 5. This is because there is no data on the specifics of CNS acute inflammatory response. Therefore, this modelling study constitutes a step towards developing generic methods for following inflammation kinetics in pre-clinical models prior to any translational studies in human volunteers.

6.2 Materials and Methods

In this section, the experimental work performed and the mathematical model developed are presented. The experimental work was performed by the lab lead by Professor Greaves from the William Dunn Department of Pathology at Oxford. In Section 6.2.1 the methodology to measure cytokine levels and cellular numbers in response to injecting chemerin in a peritonitis mouse model induced by zymosan injection is presented.

This is followed by the development of the mathematical model that aims at optimizing the effects of chemerin. The model is broken down into three sections. In Section 6.2.2 a description is made of the current understanding of the chemerin/ChemR23 pro-resolving pathway. Finally, in section 6.2.3 the model developed and how all the inflammatory mechanisms were defined e.g. chemotaxis and phagocytosis are presented.

6.2.1 Measurement of Chemerin inhibition using a zymosan induced peritonitis model

For acquiring pilot data the experimental procedure described by Cash *et al.* [324] has been used. The method consists in inducing peritonitis by injecting zymosan into a mouse peritoneum. At regular intervals from the onset, the animals are sacrificed by exposing them to increasing concentrations of CO_2 and with death confirmed with cervical dislocation. The peritoneum of the sacrificed mice is lavaged to count inflammatory cells and measure the concentration of inflammatory mediators.

Cash *et al.* [324] have that this procedure has several advantages compared to other models of inflammation: 1. it allows to modulate the severity of the inflammatory insult dependent on the concentration of zymosan injected; 2. it allows for the collection of reasonable quantity of exudate for the analysis of multiple inflammatory mediators; 3. compared to artificial cavities the peritoneum provides a more realistic experimental environment as it has lymphatic clearance of inflammatory cells and 4. it is a simple procedure and it is reproducible.

This procedure was used to measure the concentration of inflammatory chemokines such as CXCL1, CCL2 and chemerin as well as the number of neutrophils and monocytes. The steps consisted on inducing peritonitis and killing a variable number of animals at intervals up to 96 hours after onset

To evaluate the inhibitory effect of chemerin the procedure was modified by injecting 500 μg ml^{-1} of recombinant murine chemerin (R&D systems; aa17-156) chemerin 2 hours after inflammation was induced. At 4 and 16 hours post onset, the animals were sacrificed and the number of inflammatory cells were measured. Through this procedure, it was found that the number of neutrophils and monocytes is reduced by up to 7% 2 hours after onset. At 16 hours the numbers are reduced by 12% and 20% for neutrophils and monocytes respectively. Therefore, a significant inhibitory effect was identified. The remainder of the paper details the design of a mathematical model of the progress of inflammation in the zymosan mouse model to identify likely optimal chemerin injection parameters and hence reduce the extent of experimental work required to find this result. All collected data is provided in the supplementary material.

6.2.2 Overview of the mechanisms of acute inflammation modulation by chemerin

Chemerin is a plasmacytoid dendritic cell, a natural killer cell, and a macrophage chemoattractant naturally found in circulation [171]. Chemerin is present in the circulation and is secreted as an inactive precursor. It needs to undergo C-terminal proteolytic cleavage by neutrophil proteases to become active (Fig. 6.1 A). An increased concentration of neutrophils, aimed at killing infectious agents, is characteristic for inflamed tissue and hence chemerin becomes active as inflammation develops. Activated chemerin becomes a monocyte chemoattractant. Diffusing through the tissue and into blood vessels it binds to ChemR23 receptors of monocytes and recruits them, from the circulation into the tissue and towards the inflammation site, where their role is to clear apoptotic neutrophils and inflammation by-products (Fig. 6.1 B/C). At the site of inflammation, macrophages produced from monocytes release proteases (Fig. 6.1 D), which break down chemerin into peptides (Fig. 6.1 E). In particular, the resulting peptide C15 binds to the receptor ChemR23 of macrophages, which has pro-resolving effects i.e. it inhibits the release of pro-inflammatory chemokines (Fig. 6.1 F) and it promotes apoptotic neutrophil phagocytosis (Fig. 6.1 G). The full Chem/ChemR23 system is summarized in Fig. 6.1 [171].

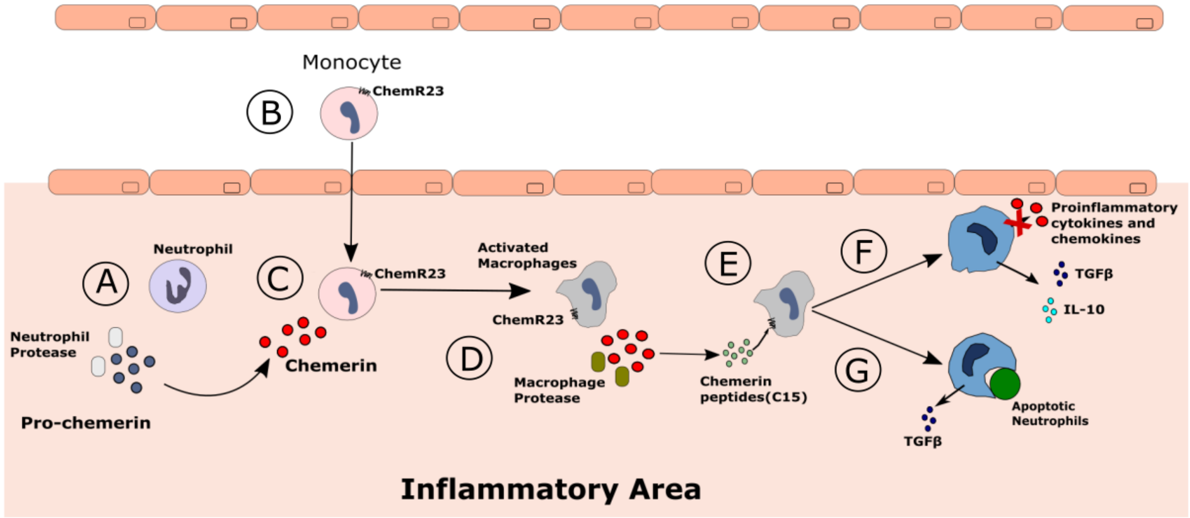

Figure 6.1: Schematic representation of the key seven stages of the modulation of inflammation by chemerin. A: neutrophils are recruited to the inflammation site and secrete pro-chemerin proteases. B and C: proteases activate chemerin precursors. The activated chemerin is a chemoattractant for monocytes, which are recruited to the inflammation site from blood vessels and are transported through chemotaxis. D: once at the inflammation site monocytes differentiate into macrophages, which clear apoptotic neutrophils and inflammation debris. This activity leads to the release of macrophage proteases which break down chemerin into peptides, including the C15 peptide. E: the C15 peptide binds to the macrophages, which (F) inhibits their release of pro- inflammatory cytokines and chemokines and (G) promotes phagocytosis of apoptotic neutrophils [171].

Therefore, the key characteristic affecting the resolution of the inflammatory response that needs to be modelled is the competing action of pro- and anti-inflammatory mediators that affect the recruitment of neutrophils and monocytes after their sequential arrival to the inflammatory site.

6.2.3 Model of the modulation of zymosan induced peritonitis by chemerin

Several authors have developed models that capture acute inflammatory response. Early works, e.g. Lauffenburger and Kennedy [246], [247] developed a generic model of leukocyte recruitment to bacterial infection. Since then developments have been made where the effects of cytokines [248] as well as anti-inflammatory mediators [249] are considered.

From the experimental measurements of inflammatory cells and cytokines from the peritoneum presented in Section 6.2.1 three inflammatory mechanisms are required to be considered. The first is that two types of leukocytes are present in the experiments: neutrophils and monocytes. The second consist in the fact that neutrophils and monocytes arrive at the inflammation cite sequentially. This is confirmed by the production of neutrophil and monocyte cytokines CCL2 and CXCL1 respectively. In acute inflammation, David et al found that when CCL2 reaches its peak concentration CXCL1 starts being produced followed an initial reduction CCL2 production and consequent CXCL1 production. This is in line with the known inflammatory physiology that neutrophils firstly arrive at the site of inflammation to kill the invading bacteria and that monocytes are then recruited to clear apoptotic neutrophils and debris. Thirdly, the conflict between pro- and aniti- inflammatory mediators should be considered in the model in order to investigate the chemerin/ChemR23 pro-resolving mechanism.

In the literature, the only two models that take into account different species of leukocytes are the Smith *et al*. [251] and the Dunster *et al*. [252] models. Additionally, the former is the only model that model that considers the sequential recruitment of inflammatory cells. Additionally, it includes two forms of macrophages: first, alveolar macrophages (M_A) and monocyte derived macrophages (M). The sequence of events is as follows: first the alveolar macrophages target the pneumococci (P) and release cytokines (C) that recruit neutrophils (N); then, the monocytes (M) are recruited dependent on the concentration of neutrophils. Furthermore, the pneumococci target healthy pulmonary epithelial cells (E_U) and infects them (E_A). These infected cells and apoptotic neutrophils can then become inflammatory debris (D), which is then removed by M_A. The model is summarised in Figure 6.2.

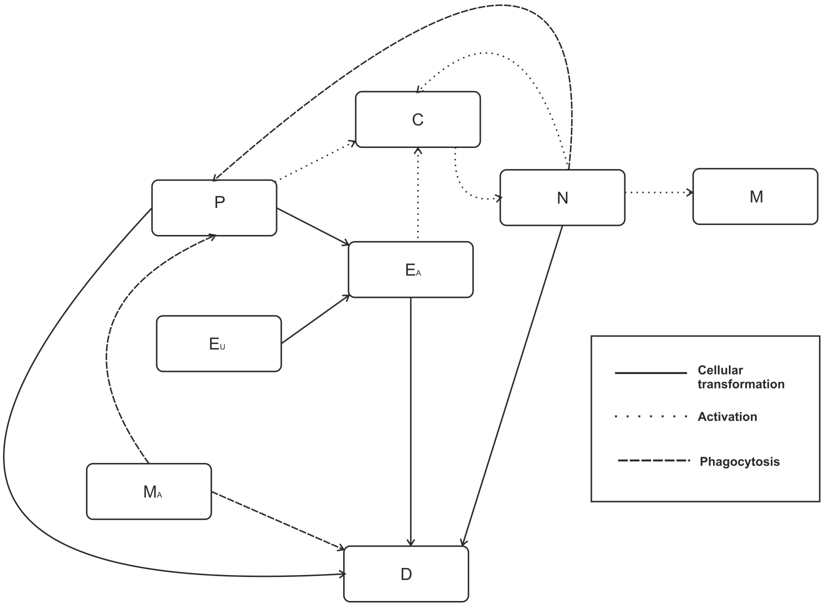

Figure 6.2: Network diagram for the model developed by Smith *et al*. [251].

The Dunster *et al.* [252] besides taken into account neutrophils (N) and monocytes (M) it combines: pro (C) and anti (G) inflammatory mediator production and it analyses the decay of neutrophils into apoptotic neutrophils (A). Additionally, the rate of neutrophil apoptosis is dependent on anti-inflammatory mediators. In turn, apoptotic neutrophils further aggravate the inflammatory process by producing cytokines. Finally, the model incorporates the clearance of apoptotic neutrophils by monocytes. A diagram of the model is shown in Figure 6.3.

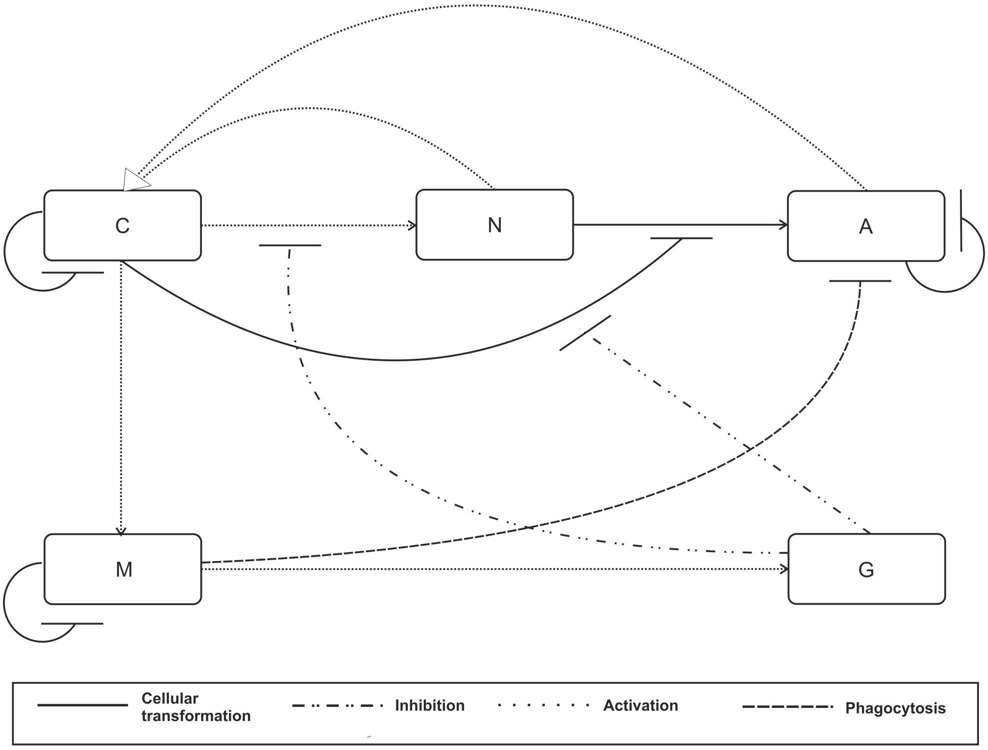

Figure 6.3: Network diagram for the model developed by [252]. Definition of the different variables (C, N, A, M and G) can be found in the text.

The model here developed combines aspects of these state of the art models. It is composed of nine time dependent variables, including: the irritant zymosan (Z), inflammatory cells neutrophils (N), apoptotic neutrophils (A) and monocytes (M) cytokines CCL2 (C_2), CXL1 (C_1) and chemerin (C_h) and the general effect of anti-inflammatory mediators (G).

The work here developed aims at mimicking the experimental procedure presented in Section 6.2.1. It starts by injecting Z is injected into the peritoneum and triggers the production of C_l and C_h (rate J_1 and J_{11}). C_l then acts as a chemoattractant for N (rate J_4). At the inflammatory site neutrophils start to degenerate and to become A (rate J_2). Both N and A promote the production of C_l that recruit

N further(rate J_{10}). Additionally, N and A promote M chemokines such as C_2 and C_h (rate J_3). C_2 and C_h recruit M (rate J_5). Both N and M phagocytose Z (rate J_6). Enzymes produced by monocytes break down chemerin, which leads to the production of anti-inflammatory peptides such as C_{15} (rate $J9$). M also performs the phagocytosis of A which is promoted by C_{15} (rate J_7). As A is being phagocytosed the production of other anti-inflammatory chemokines G is promoted (rate J_8). Both G and C_{15} inhibit the recruitment of further neutrophils. Finally, through diffusion, all the inflammatory intervenient considered are extracted to the circulation (rate J_{12}). The full model is encapsulated in Figure 6.4.

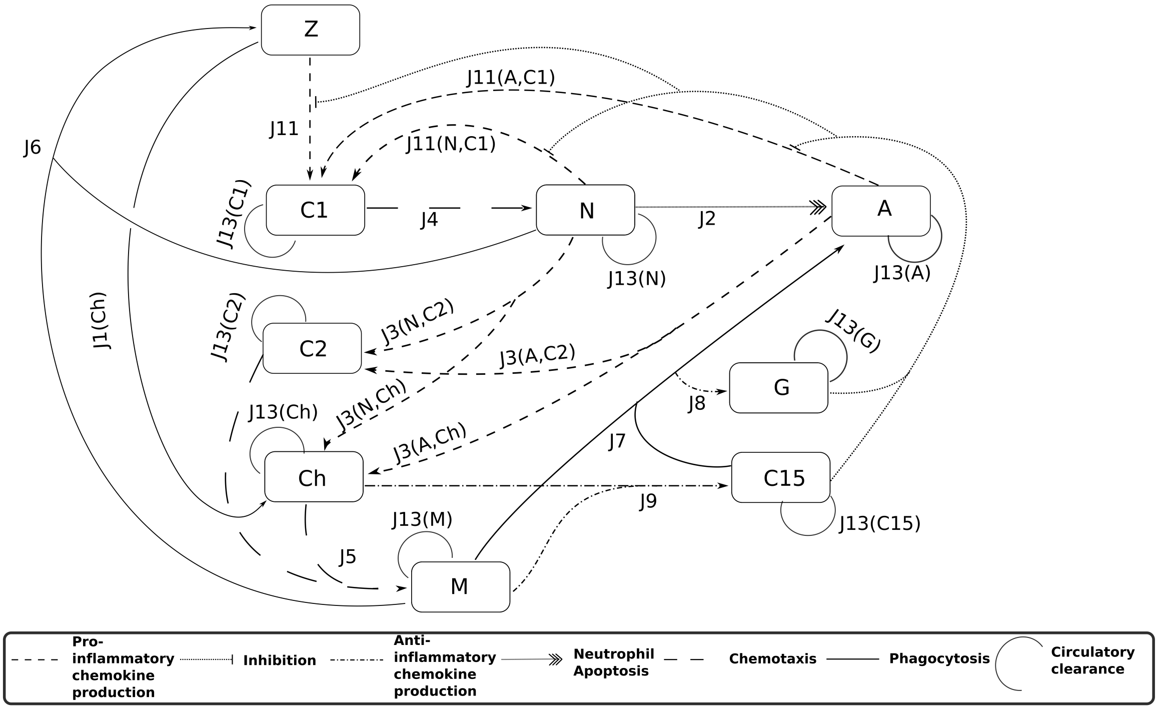

Figure 6.4: Schematic representation of the model developed of acute inflammation with the chemerin/ChemR23 pathway.

In the following sub sections, the definition how the different rates were described is presented. Section 6.2.3.1 focuses on the activation of cytokine production and zymosan phagocytosis. This is followed by a description of neutrophil and monocyte chemotaxis in section 6.2.3.2. Then in section 6.2.3.3 the rate of neutrophil apoptosis is explained as well as how these cells are phagocytized by monocytes. In section 6.2.3.4 it is presented how the anti-inflammatory chemokines are produced and how what they impact acute inflammatory mechanisms. The model of chemerin injection is described in section 6.2.3.5. Section 6.2.3.6 the model of diffusion from the inflammatory site to the circulation is explained. Finally, in section 6.2.3.7 the full inflammatory model is presented.

6.2.3.1 Pro and anti-inflammatory chemokine production

Attractants for inflammatory cells expressed in the zymosan peritonitis model include IL-6, CCL4, CXCL10, CXCL1 and CCL2. Here, only CXCL1 and CCL2 chemokines have been considered as they are the main chemokines for the recruitment of neutrophils and monocytes respectively.

Following Smith *et al.* [251] the recruitment of the neutrophils and monocytes is sequential. However, the authors assumed a constant delay between the arrival of the two species, which would not be appropriate here, as the model is intended to capture the injection of chemerin at different times during inflammation. Instead, neutrophil and monocyte specific chemokines were defined.

As neutrophils are the first recruited cells, it was assumed that the tissue cells produce C_1 as zymosan is injected. Additionally, the data shows that chemerin starts being produced by the tissue as soon as zymosan is injected. Therefore, chemerin production was assumed to be triggered by the injection of zymosan. The mechanisms responsible for the production of cytokines involve enzymatic reactions [252]. Therefore, the production of C_1 and C_h in response to Z is assumed to have Michaelis-Menten kinetics, as:

$$J_1(\mu_Z) = V_{\mu_Z}\left(\frac{Z}{k_{\mu_Z} + Z}\right), \tag{6.1}$$

where μ_Z stands for C_1 or C_h and k_{μ_Z} and V_{μ_Z} are the Michaelis-Menten parameters related to each chemokine.

At the inflammation site, the neutrophils that are not cleared by the circulation become apoptotic. As described in Smith *et al.* [251], the rate of apoptosis, k_{an}, is proportional to the number of neutrophils as:

$$J_2 = k_{an}N, \tag{6.2}$$

Both neutrophils and apoptotic neutrophils contribute to the promotion of inflammation by stimulating the production of CXCL1. Additionally, neutrophils intervene in mechanisms that result in the recruitment of monocytes [326]. It is assumed that all those mechanisms can be captured by making the production of CCL2 and chemerin dependent on N and A. Neutrophil production of chemokines was modelled based on the work by Dunster *et al.* [252] as:

$$J_3(I,\mu) = V_{I,\mu}\left(\frac{I^2}{k_{I,\mu}^2 + I^2}\right), \tag{6.3}$$

where I stands for either N or A, μ for the type of cytokine produced (C_1, C_2 or C_h) and $k_{I,\mu}^2$ is a parameter specific to each cytokine and cell pair.

6.2.3.2 Neutrophil and monocyte chemotaxis

Neutrophil and monocyte chemotaxis was modelled based on the work by Smith *et al.* [251]. Neutrophils are recruited at a rate, k_{c_1n}, proportional to CXCL1 concentration. Additionally, according to Smith *et al.* [251], a maximum number of neutrophils, N_{max}, is set to account for the saturation of space available for these cells as inflammation progresses. The resulting flow of neutrophils is represented by

$$J_4 = k_{c_1n}[C_1]\left(1 - \frac{N}{N_{max}}\right). \tag{6.4}$$

Similarly, monocyte chemotaxis is modelled by setting the rate of recruitment to be proportional to chemerin and CCL2 concentrations and imposing a maximum number of monocytes, M_{max}, to account for the saturation of space as inflammation progresses. Hence, monocyte recruitment is modelled as

$$J_5 = \left(k_{c_2m}[\mathrm{C2}] + k_{hm}[\mathrm{C}_h]\right)\left(1 - \frac{M}{M_{max}}\right), \tag{6.5}$$

where k_{cm} and k_{hm} are the rate constants for monocyte recruitment due to CCL2 and chemerin respectively.

6.2.3.3 Zymosan and apoptotic neutrophil phagocytosis

Following the work of Dunster *et al.* [252] the phagocytosis rate of zymosan is performed by both neutrophils and monocytes at rates k_{pn} and k_{pm} proportional to their number respectively

$$J_6 = k_{pn}N + k_{pm}M. \tag{6.6}$$

The apoptotic neutrophils are phagocytosed by monocytes as in Dunster *et al.* [252] at a rate k_{pa} as:

$$J_7 = k_{pa}AM. \tag{6.7}$$

6.2.3.4 Anti-inflammatory chemokine production and role in neutrophil recruitment and phagocytosis action

Two anti-inflammatory cytokines are considered: a generic chemokine G, as in Durnster *et al.* [252], and the chemerin peptide C_{15}. The former is produced proportionally (k_g) to the phagocytosis of apoptotic neutrophils by monocytes as:

$$J_8 = k_g J_6. \tag{6.8}$$

C_{15} is formed by the breakdown of chemerin by macrophage proteases (Fig.6.1 F). As it is an enzymatic reaction it is modelled with Michaelis-Menten kinetics with parameters V_{H15} and $K_{m,C_{15}}$ as:

$$J_9 = V_{C_{15}} \frac{[\mathrm{C}_h]}{K_{m,C15}+[\mathrm{C}_h]} \mathrm{M}. \tag{6.9}$$

Following Durnster *et al.* [252] the anti-inflammatory chemokines inhibit neutrophil recruitment. Here, the recruitment of neutrophils is performed by CXCL1. It was then assumed that the anti-inflammatory chemokines inhibit the production of CXCL1. This was done by modifying Eq. 6.1 and Eq. 6.3 by adding the chemokine inhibition term defined by Anderson *et al.* [327] leading to

$$J_{10} = V_{C_1,Z}\left(\frac{Z}{k_{C_1,Z} + Z}\right)\left(\frac{1}{\left(1 + \left(\frac{[C_{15}]}{k_{Z,C_{15}}}\right)^{w_{Z,C_{15}}}\right)\left(1 + \left(\frac{[G]}{k_{Z,G}}\right)^{w_{Z,G}}\right)}\right), \tag{6.10}$$

$$J_{11}(I, C_1) = V_{I,C_1}\left(\frac{I^2}{k_{I,C_1}^2 + I^2}\right)\left(\frac{1}{\left(1 + \left(\frac{[C_{15}]}{k_{I,C_{15}}}\right)^{w_{I,C_{15}}}\right)\left(1 + \left(\frac{[G]}{k_{I,G}}\right)^{w_{I,G}}\right)}\right), \tag{6.11}$$

where I stands for N and A and $k_{Z,C_{15}}$, $k_{I,C_{15}}, w_{Z,C_{15}}, w_{I,C_{15}}$ and $k_{Z,G}$, $k_{I,G}$, $w_{Z,G}$, $w_{I,G}$ are the parameters for C_{15} and G inhibition respectively.

Additionally, C_{15} promotes phagocytosis [182]. To account for this promotion the rate of phagocytosis defined in Eq. 6.7 was adapted by including C_{15} dependence based on the chemokine promotion model by Dunster *et al.* [252] leading to:

$$J_7{}' = k_{pa}AM\left(1 + \frac{[C_{15}]}{k_{c15}}\right). \tag{6.12}$$

6.2.3.5 Injection of additional chemerin model

The rate of injection of extra chemerin $[\mathrm{C}_h]_i$ was modeled as the derivative of a step function as:

$$J_{12}([\mathrm{C}_h]_i, \tau) = [\mathrm{C}_h]_i \frac{\delta e^{-\delta(t-\tau)}}{1 + e^{-\delta(t-\tau)}}, \tag{6.13}$$

where δ and τ are the parameters that define the speed of the step function and the time when the step occurs respectively. τ was chosen to match the experimental procedure performed where extra chemerin is injected 2 hours after inflammation is induced. The remaining parameter δ was defined by trying to ensure that it would make the step function as fast as possible and to ensure solution stability. Taking these two aspects into consideration the maximum speed for the injection was found to be 10 min. This is unrealistic as an injection is on the time scale of a few seconds. However, as seen in Fig. 6.5, since the experiments take up to 96 hours it is here assumed that the difference between the injection taking seconds or a few minutes is negligible.

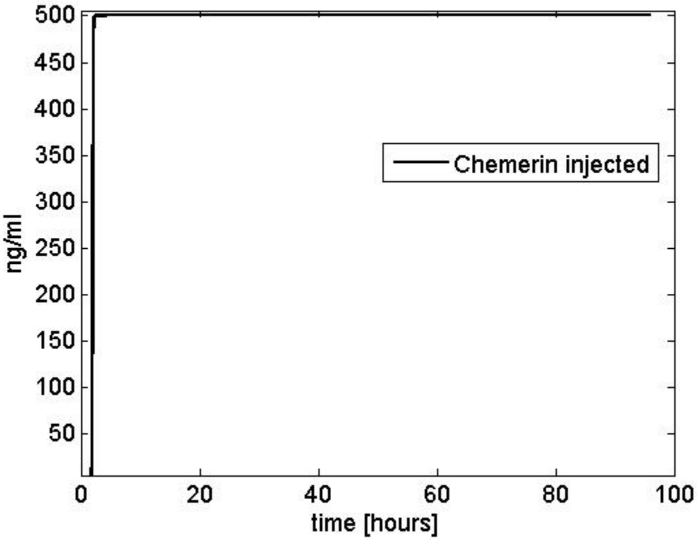

Figure 6.5: Step size representing the injection of extra chemerin.

6.2.3.6 Clearance model

The rate of clearance of free inflammatory agents by the vasculature is assumed to be proportional to their concentration as

$$J_{13}(U) = \gamma_U U, \tag{6.14}$$

where γ_U is the rate of vascular clearance of species U (N, M, A, $[\mathrm{C}_1]$, $[\mathrm{C}_2]$, $[\mathrm{C}_h]$, $[\mathrm{C}_{15}]$ or $[\mathrm{G}]$).

6.2.3.7 Conservation of mass equations

Assuming conservation of mass within the modelled systems the rate of change of the different species can be expressed by equations 6.15 to 6.22 in Table 6.1.

Table 6.1: Summary of the conservation of mass equations of the chemerin inflammation modulation model

Equation	#	Initial conditions	Units
$\frac{d[\mathrm{C}_1]}{dt} = J_{10} + J_{11}(N,[\mathrm{C}_1]) + J_{11}(A,[\mathrm{C}_1]) - J_{12}([\mathrm{C}_1])$	(6.15)	0	ng ml^{-1}
$\frac{d[\mathrm{Z}]}{dt} = -J_6$	(6.16)	100	ng ml^{-1}
$\frac{d[\mathrm{C}_2]}{dt} = J_3(N,[\mathrm{C}_2]) + J_3(A,[\mathrm{C}_2]) - J_{13}([\mathrm{C}_2])$	(6.17)	5.17×10^{-3}	ng ml^{-1}
$\frac{dN}{dt} = J_4 - J_7' - J_{13}(N)$	(6.18)	1.71×10^{-1}	cell×10^{6}
$\frac{d[\mathrm{C}_h]}{dt} = J_1(\mathrm{C}_h) + J_3(N,[\mathrm{C}_h]) + J_3(A,[\mathrm{C}_h]) + J_{11} - J_{13}([\mathrm{C}_h])$	(6.19)	1.92	ng ml^{-1}
$\frac{dM}{dt} = J_5 - J_7' - J_{13}(M)$	(6.20)	7.72×10^{-2}	cell×10^{6}
$\frac{dA}{dt} = J_7' - J_8 - J_{13}(A)$	(6.21)	0	cell×10^{6}

$\frac{d[C_{15}]}{dt} = J_9 - J_{13}([C_{15}])$	(6.22)	0	ng ml^{-1}
$\frac{d[G]}{dt} = J_8 - J_{13}(G)$	(6.23)	0	ng ml^{-1}

6.3 Results

6.3.1 Model fitting

Wherever possible model parameters were defined based on values reported in the literature or directly available from data. Malech [328] reported the rate constant of neutrophil clearance (γ_N). The clearance rate of all cytokines ($\gamma_{C1}, \gamma_{C2,}\gamma_H$ and γ_{C15}) was set to the measured generic value [329]. All set parameters are summarized in Table 6.2. Experimentally, it was possible to define the saturation levels N_{max} and M_{max} as 4×10^6 and 9×10^6 cells respectively based on the measurements performed when 500 µg/ml of zymosan is injected into the peritoneum.

Table 6.2: List of model parameters for which values are reported in the literature.

Parameter	Units	Value	Reference
γ_N	h^{-1}	6.3×10^{-2}	[328]
γ_{C1}	h^{-1}	8.3×10^{-1}	[329]
γ_{C2}	h^{-1}	8.3×10^{-1}	[329]
γ_H	h^{-1}	8.3×10^{-1}	[329]
γ_{C15}	h^{-1}	8.3×10^{-1}	[329]
γ_G	h^{-1}	8.3×10^{-1}	[329]

The remaining parameters were fitted numerically. The allowed range for all fitted parameters was set empirically so that to reflect the rate at which different variables evolve during the experimental study. Two sets of data were used for the fitting: 1) N, M, $[\mathrm{C}_1]$, $[\mathrm{C}_2]$ and $[\mathrm{C}_h]$ in control data and; 2) N, M at 2 and 14 hours after 500 ng ml^{-1} of chemerin are injected.

The model has 45 parameters with a wide parameter space and needs to be fitted to 40 data points spanning 5 variables of which 2 are measured in two experiments. For this reason, since it is hard to envisage how the fit varies as the parameter space is sampled, methods designed to avoid local minima were considered to perform the fit.

The initial selection of the fitting method was performed by running all global optimization methods from the SBML toolbox the method that produced the best fit in a reasonable time was the simplex method [68]. The result of the fit is shown in Fig. 6.6 and the full list of fitted parameters is provided in Appendix 6.B.

Fitting errors were normalized with respect to the maximum value measured for each variable to ensure equal weighting of each one in the final fit. This was achieved by setting the root mean square (RMS) value to

$$RMS(x) = \sqrt{\sum_{x=1}^{7} \frac{\left(\frac{S_x - D_x}{\max(D_x)}\right)^2}{n_x}}, \tag{6.24}$$

where S_x is the simulated value, D_x is the data point, the index x stands for the different variables being fitted and $\max(D_x)$ stands for the maximum of the data set.

As shown in Fig. 6.6 the fit exhibits all key characteristics observed in measurements: the sequential arrival of neutrophils and monocytes (Fig. 6.6 C); the removal of neutrophils and monocytes from the inflammatory site (Fig. 6.6 C); as well as sharp peaks of numbers and concentrations of inflammatory cells and chemokines respectively. Achieved RMS values are predominantly low and approximately 0.05, 0.1, 0.1 and 0.12 for neutrophils (Fig. 6.6 C), monocytes (Fig. 6.6 C), chemerin (Fig. 6.6 B) and CXCL1 (Fig. 6.6 A) respectively. The RMS value for CCL2 (Fig. 6.6 A) is 0.47 and is due to a rapidly varying function where a small time delay between the fitted and measured curves leads to a large RMS error.

RMS values for chemerin injection experiments were also low with 0.001 and 0.006 for neutrophils and monocytes respectively (Fig. 6.6 D).

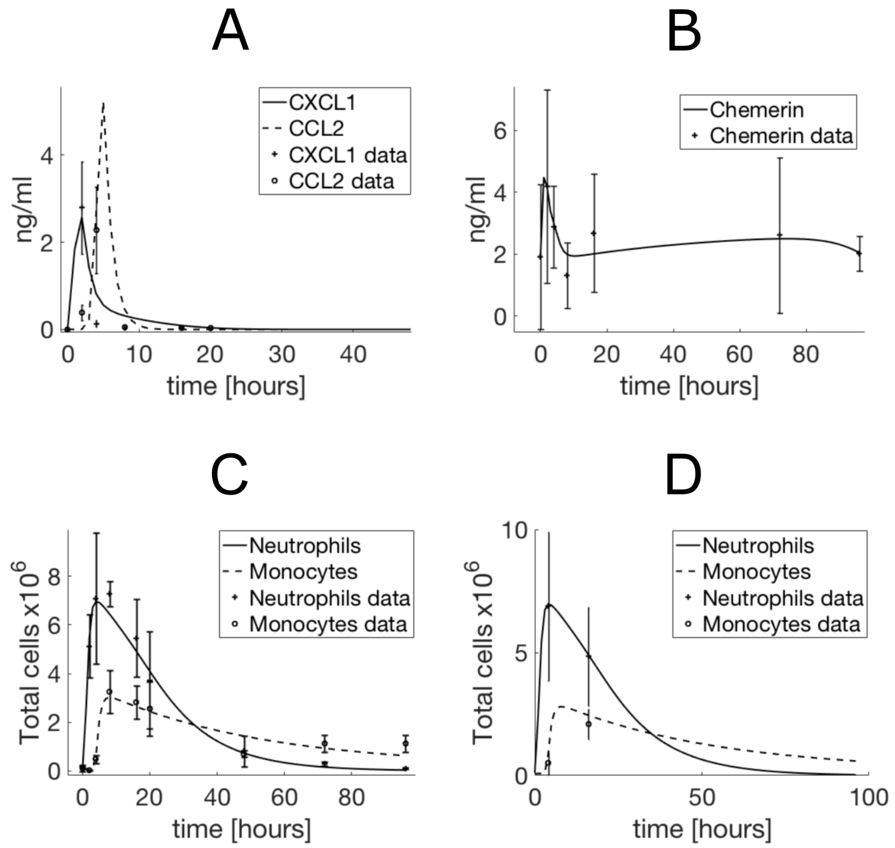

Figure 6.6: Results from the fitting of the model to the data: (A) control cytokines CCL2 and CXCL1; (B) control chemerin; (C) control neutrophils and monocytes and; (D) neutrophils and monocyte when extra chemerin is injected after 2 hours from peritonitis onset.

6.3.2 Optimizing the therapeutic potential of chemerin

The aim of this work is to identify the optimal concentration and time of injection of chemerin to inhibit inflammation. These two parameters, $[\mathrm{C}_h]_i$ and τ respectively, are the inputs to Eq. 6.11. The extent of the inhibitory effect W of chemerin is evaluated by comparing the average number of all inflammatory cells over the course of the experiment, i.e. 96 hours, with and without chemerin injected. This can be expressed as

$$W([\mathrm{C}_h]_i,\tau) = \frac{\sum S_{x,O} - \sum S_{x,Ch}([\mathrm{C}_h]_i,\tau)}{\sum S_{x,O}} \times 100. \tag{6.25}$$

where x stands for the type of cell being compared. To optimize Eq. 6.25 the simplex method [257] was implemented.

With this protocol two conditions were tested. The first consists in optimizing the percentage of chemerin inhibition over a range of $[\mathrm{C}_h]_i$ so that the total number of cells ($x = N, M, A$) is minimized, as shown in Fig. 6.7 A. It was found that for the whole range of $[\mathrm{C}_h]_i$ the optimal time for injecting chemerin was as soon as possible after inflammation onset. Hence, to simulate immediate chemerin injection the initial concentration of chemerin was set to $[\mathrm{C}_h]$=$[\mathrm{C}_h]_0$+$[\mathrm{C}_h]_i$ in Eq. 6.19 (Table 1). The maximum inhibition is approximately 27% when 2×10^3 ng ml^{-1} of chemerin are injected. The maximum inhibitory effect is reduced by 1% when the injection is delayed by 5 minutes.

After the maximum inhibitory effect is reached, injection of further chemerin will increase the total number of cells. This effect can be explained by the dual role that chemerin exhibits in the inflammatory pathway. On one hand, it attracts monocytes and on the other hand it leads to further production of C15 that inhibits neutrophil recruitment and promotes apoptotic neutrophil phagocytosis. The maximum inhibition found is more than double of the effect observed in the pilot experimental study.

When breaking down the 27% reduction of the total of inflammatory cells into the three types of inflammatory cells considered there was an inhibition of approximately 53% and 6% in the number of monocytes and neutrophils respectively. However, there was an increase of apoptotic neutrophils by approximately 160%.

As apoptotic neutrophils have been found to play a crucial role in the degeneration of acute inflammation into chronic inflammation [249] a second set of optimizing tests were made to identify the optimal conditions for injecting chemerin to reduce the number of neutrophils and apoptotic neutrophils $(x = N, A)$. It was found that the maximum inhibition was also experienced when chemerin is injected minutes after inflammation onset. Furthermore, as seen in Fig. 6.7 B, a maximum inhibition was found of approximately 35% and 88% in neutrophils and apoptotic neutrophils respectively. However, as chemerin concentration increases so does the number of monocytes by approximately 74%.

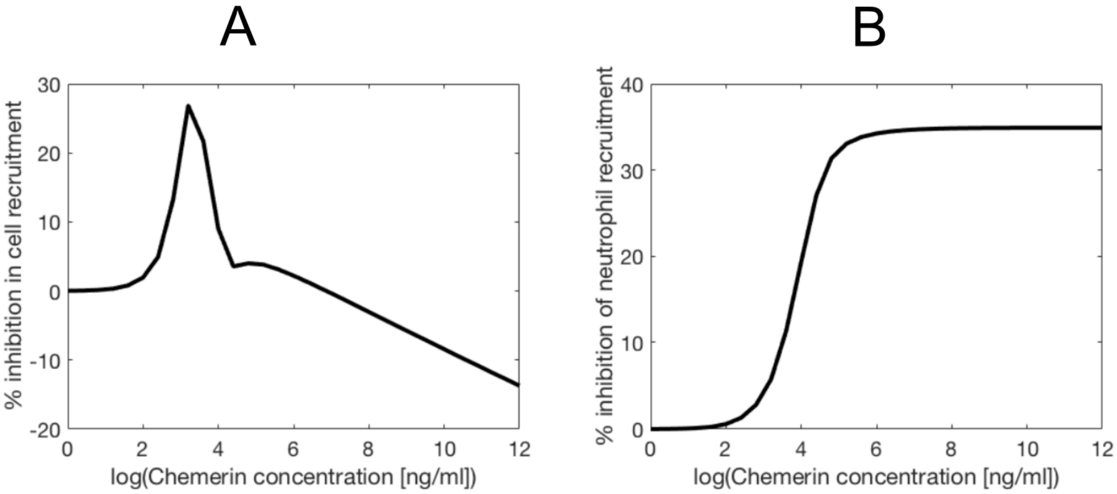

Figure 6.7: Simulations made to minimize Eq. 6.25 for chemerin injections over a range of chemerin concentrations. (A) Eq. 6.25 was minimized when $\boldsymbol{x} = \boldsymbol{N}, \boldsymbol{M}, \boldsymbol{A}$. It resulted in a maximum reduction of 6% and 53% in $\boldsymbol{N}$ and $\boldsymbol{M}$ respectively and a 160% increase in apoptotic neutrophils when 2×10^3 ng ml^{-1} of chemerin are injected. (B) The number of neutrophils and apoptotic neutrophils was minimized ($\boldsymbol{x} = \boldsymbol{N}, \boldsymbol{A}$ in Eq. 6.25) resulting in a 35% reduction in neutrophils, an 88% reduction in apoptotic neutrophils and an increase of monocyte recruitment of 70% when $\geq 1\times10^5$ ng ml^{-1} of chemerin are injected.

6.3.3 Sensitivity analysis

To assess the risk of overfitting, a screening algorithm was performed on the fitted model. The model consists of 8 ODE equations (Equations 6.15-6.23) with 45 parameters. Due to its large size and the number of parameters, it was decided to use a global rather than local method. As it is anticipated that this complex model will not be stable over the whole parameter space the global Campolongo-Morris (C-M) method, as described in Chapter 3, was chosen. Furthermore, to assess the risk of sensitivity to data, a Remove-One Bootstrap [330] analysis was performed. Both studies are reported below.

6.3.3.1 Campolongo-Morris screening analysis

This algorithm consists, as described in Section 3.5.3, in exploring the parameter space by varying each parameter from the model (including the parameters in fitted in Section 6.3.1 and Table 6.2 and the data derived parameters N_{max} and M_{max}) in turn over a pre-defined range [331]. As the range found for parameter definitions in the literature, as in Smith *et al.* [251], is large, the range was chosen to be $\pm 80\%$ of the value fitted.

Each time a parameter is varied its impact on the output of the model is evaluated, which is termed elementary effect (EE). In the particular case of the model developed the EEs were defined as the sum between: 1. the RMS between the model with the new parameter definitions and the data using Eq. 6.24 and 2. the RMS between the fitted model simulations when extra chemerin is injected and the model with the new parameter values, again using Eq. 6.24. The inclusion of this sum ensures that the analysis takes into consideration the behaviour of the model with and without extra chemerin injected.

In Fig. 6.8 the results are plotted for all the parameters. EE statistics are plotted in Fig. 6.8. Fig. 6.8 B shows that the model is most sensitive to the parameters pertaining to the production of the chemokines CXCL1 and CCL2. Additionally, the rate of apoptotic neutrophils by monocytes (k_{pa}) has a marked impact on the behaviour of the model. The data derived parameters that describe the maximum number of neutrophils (N_{max}) have also been found to impact the fit and the predictions of the model. Related to cellular number kinetics the rate of monocyte extraction rate (γ_m) was also found to substantially impact model behaviour.

To quantify how the most sensitive parameters (Fig 6.8 B) impact model predictions in more detail, the Campolongo-Morris method was reapplied. The remaining parameters of the model were kept constant while the sensitive parameters were varied by ± 5%. EEs were redefined to assess the change in predicted maximum inhibition, the optimal time of injection and optimal chemerin concentration as in Eq. 6.24. It was found that the optimal concentration was constant for all simulations, the percentage of total cell inhibition was found to vary between 20% and 34% and the maximum neutrophil inhibitory effect varied between 30% and 40%.

Fig. 6.8 A presents the parameters found to perturb the summed RMS by less than 1%. These parameters are related to the production of cytokines by apoptotic neutrophils and to the inhibitory effect of the generic pro-resolving cytokine (G). As the parameters presented in Fig. 6.8 A ($k_{A,G}$, $k_{A,C_{15}}$, k_{N,C_2},V_{N,C_2}, V_{A,C_2}, V_{A,C_1}, k_{A,C_1}, w_{A,C_1} , k_{A,C_h}, $w_{A,G}$, V_{N,C_h} $k_{C_h,Z}$, $k_{Z,G}$, $k_{m,C_{15}}$, w_{A,C_2}) have a negligible effect on the output of the model they were removed. Starting with the parameters V_{A,C_h} and k_{A,C_h}their removal leads to

$$J_3(A, C_h) = 0. \tag{6.26}$$

Second, as $k_{Z,G}$ has negligible effect on the model response, it was assumed that $w_{Z,G}$ also has minimal impact on the model output and therefore they were removed leading to

$$J_{10}(C_1) = V_{N,C_1}\left(\frac{Z}{k_{Z,G}+Z}\right)\left(\frac{1}{\left(1+\left(\frac{[C_{15}]}{k_{Z,C_{15}}}\right)^{w_{Z,C_{15}}}\right)}\right). \tag{6.27}$$

Similarly for apoptotic neutrophils the parameters V_{A,C_1}, k_{A,C_1}, , $w_{A,G}$, $k_{A,G}$ were removed, leading to

$$J_{11}(A, C_1) = 0. \tag{6.28}$$

Simulations were performed to test the impact of removing the remaining parameters on the model fit and predictions. These simulations illustrate the limitations of the Campolongo-Morris which does not take into account the non-linear relationship between parameters. From these simplifications, it was possible to reduce the free parameters from 47 down to 35 and an increase of summed RMS by less than 1×10^{-3}%.

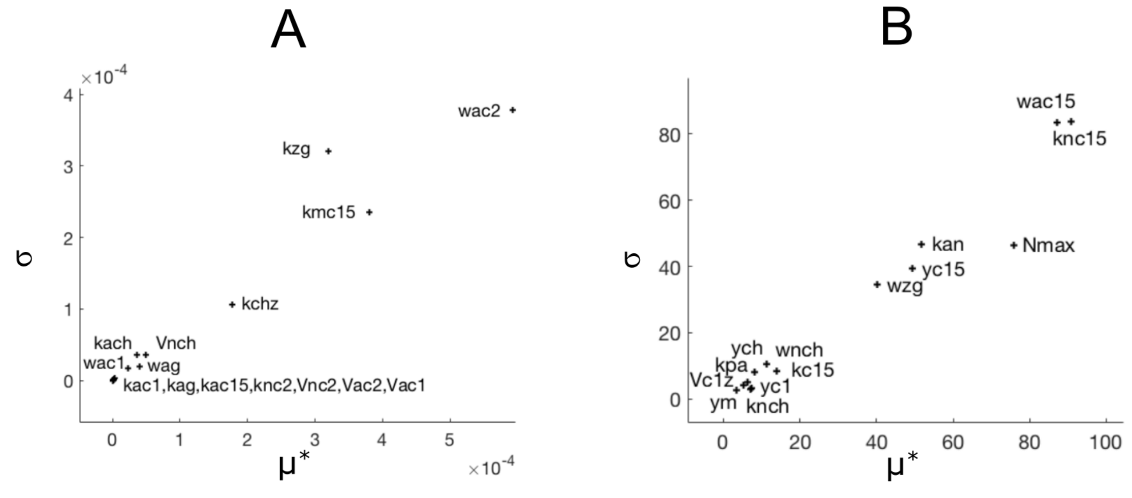

Figure. 6.8: Resulting Campolongo-Morris parameter standard deviation (**σ**) and absolute mean (**μ^***) [331]. (A) the parameters that influence the output the least and (B) the parameters that lead to the largest increase of RMS difference between the data and the model.

6.3.3.2 Remove-One Bootstrap analysis

In the fitting process, 7 variables tracked during the zymosan induced peritonitis experiment were used. To check how the fit and key predictions are affected by measurements, 1 data point from each 7 datasets before fitting was removed at random i.e. it was possible to have up to 7 data points removed at the same time for a simulation instance. The experiment was performed 100 times and changes in predicted optimal chemerin dosing and maximal expected inhibition were recorded. A histogram presenting the distribution of results can be seen in Figure 6.9.

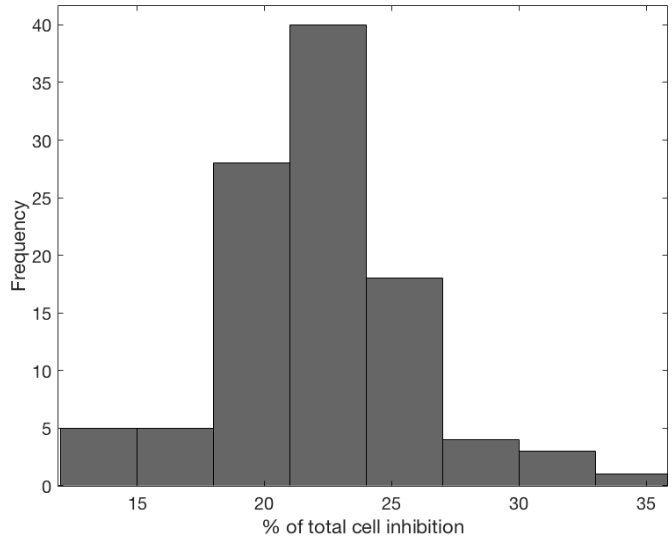

Figure 6.9: Histogram presenting the results from applying the Remove-One bootstrap method to the fitting of the model to the data. Resulting in a mean % of inhibition of 22% and standard deviation 3.7%.

Inflammation inhibition varied between 10-35% (mean of 22% and standard deviation of 3.7%) of the control value (i.e. no chemerin injected). The optimal injection time and the optimal chemerin concentration did not change.

A further set of experiments was performed where only one data point at a time was removed per simulation instance. For measurements with a low standard derivation, the removal of a single data point did not affect inhibition significantly. In case, of high standard deviation measurements i.e. in the dynamic range of the curves presented inhibition varied between 10% and 60%.

6.4 Discussion

This work has led to the development of the first mathematical model of chemokine mediated leukocyte recruitment and clearance during zymosan induced peritonitis. As evidenced by results in Section 6.3.1, it was possible to fit the model to achieve good agreement with data from a pilot experimental study. RMS values were predominantly low, however, for more confidence in the quality of the fit more data points should be acquired in the future to sample the studied functions with more frequency as they vary rapidly. Furthermore, individual point estimates in the dynamic range are based on measurements with a high standard deviation. More measurements per point or more precise timing for data collection will be necessary in the future to improve fit quality. Indeed, a Remove-One bootstrap analysis showed that removing a single measurement from a signal point estimate in this dynamic range could lead to the inhibition changing by up to 25 percentage points (i.e. from 10% to 35% with mean 22% and standard deviation 3.7%).

Sensitivity analysis identified 6 out of 45 parameters that had little impact on the results of the model simulation. Furthermore, the analysis highlighted those parameters with high impact on the output of the model pointing to model assumptions that should be verified experimentally.

The fitted model was used to maximize theoretically the degree of inflammation inhibition by chemerin. In brief, a maximum inhibition of 18% of the average of total number of inflammatory cells over the course of the experiment was predicted for an immediate chemerin injection with a concentration of about $2x10^3$ ng ml^{-1}. Optimization aimed at minimizing neutrophil recruitment found an optimal chemerin concentration of 10^5 ng ml^{-1} to be injected immediately after inflammation onset. These results are discussed in more detail below. For a table of all the assumptions made throughout this work please refer to Appendix 6.C.

Furthermore, individual point estimates in the dynamic range are based on measurements with a high standard deviation. More measurements per point or more precise timing for data collection will be necessary in the future to improve fit quality. Indeed, a Remove-One bootstrap analysis showed that removing a single measurement from a signal point estimate in this dynamic range could lead to the inhibition changing by up to 50 percentage points (i.e. from 10% to 60%).

6.4.1 Sensitivity analysis

In the model here presented the production of CXCL1 depends on zymosan concentration while the production of CCL2 depends on the number of neutrophils and apoptotic neutrophils attracted by

CXCL1. Hence, the output of the model is sensitive to any variation of the rate of production of these chemokines as was correctly identified by sensitivity analysis. As the range set for these parameters during the fitting process was set somewhat arbitrarily, future experimental work is needed to confirm the values found and to provide more theoretical insight into the mechanisms behind the observed delay in recruitment of leukocytes.

The parameters that define apoptotic neutrophil phagocytosis (rate of monocyte phagocytosis and the rate of C15 promotion of phagocytosis) exert a noticeable effect on the output of the model. This is due to the assumption that the inflammatory process can only be resolved after total clearance of apoptotic neutrophils. In addition, the rate of circulatory monocyte clearance is also relevant for the behaviour of the model for the same reasons.

Finally, the parameter that defines the maximum recruitment number of neutrophils has a large impact on the solution. It was derived from the data. As shown from the simulations performed where data points are removed at random one data point might lead the prediction to vary by 25% points. Additionally, the Campolongo-Morris method showed that varying these parameters as little as 5% might lead to large changes in the predictions of the model. Hence, future experimental work to refine the definition of these parameters is required. These measurements could be obtained using the methodology developed as part of this pilot study [324].

Conversely, the C-M method also identified the parameters that least affect the output. These are related to chemerin production by apoptotic neutrophils and to the inhibitory effect of G on chemokine production. In both cases, this lack of importance might be explained by a lack of data to inform the fitting.

The fitting process led to a solution where the number of apoptotic neutrophils is much lower than that of neutrophils (order of magnitude of 10^7 cells). Checking whether this is a realistic distribution should form part of future validation and development of the model.

The model assumed that there is a generic chemokine G inhibiting neutrophil recruitment further experimental work would be needed to identify prominent individual chemokines involved in this process.

6.4.2 Treatment perspectives involving Chemerin/ChemR23 pro-resolving pathway

Chemerin has been associated with a variety of conditions that have as one of its pathological mechanisms chronic inflammation. These include, obesity, metabolic syndrome and diabetes [332]. Additionally, chemerin has been proposed as a biomarker for chronic inflammation, as its increased expression is found to be unique to the inflammatory region [333].

Assuming two therapeutic strategies consisting in either the reduction of the total number of inflammatory cells during the course of inflammation or focus on the reduction of the number of apoptotic neutrophils the model predicted theoretical optimal solutions for both. In the first case, the model predicts that injecting chemerin up to 7 min after injecting zymosan at a concentration of 2×10^{3} ng ml^{-1} will have the maximum overall inhibitory effect of 27%. Individual cell recruitment, in that case, was reduced by 35% for monocytes and by 6% for neutrophils with a 160% increase in the number of apoptotic neutrophils.

This result suggests that it is impossible to reduce the number of apoptotic neutrophils and monocytes simultaneously. This is a concern since, as suggested by Kumar *et al.* [56], both types of cells are involved in the pathological mechanisms that lead to the degeneration of acute inflammation into chronic inflammation. This behaviour can be explained by the fact that the model assumes that inflammation can only be resolved if apoptotic neutrophils are cleared. Additionally, it is assumed that the mechanisms responsible for the clearance of these cells are diffusion of apoptotic cells into the circulation and monocyte phagocytosis. Therefore, a reduction in the number of monocytes will result in a larger presence of apoptotic neutrophils. Therefore, it should be investigated if there are other mechanisms of removal of apoptotic neutrophils. If a more dominant mechanism exists besides monocyte phagocytosis, perhaps there could be a strategy by which the injection of chemerin could reduce the number of monocytes and apoptotic neutrophils simultaneously.

In the second case, the model predicts that a large concentration of chemerin (1×10^{5} ng ml^{-1}) needs to be injected approximately 10 min after zymosan injection. Such a treatment would lead to approximately a 35% reduction of neutrophils as well as a 88% reduction is the number of apoptotic neutrophils. However, it also leads to a 70% increase in the number of monocytes. Above 1×10^5 ng ml^{-1} there is no increase in neutrophil inhibition and there is a linear increase in the number of monocytes.

The steady state observed in Fig 6.7. B is explained by the assumption that there is a maximum number of neutrophils and monocytes that can be recruited to the site of inflammation [251]. These parameters were defined from zymosan induced peritonitis experiments when 500 μg ml^{-1} of zymosan were injected. In order to test the impact of these parameters on the model output, a further experiment was performed where the values of N_{max} and M_{max} were increased by 30%. The change of the RMS value with the new parameters was negligible (<0.01%). However, the new parameter values reduce the maximum level of inhibition of the total number of cells recruited by 20% and the plateau observed in Fig. 6.7 B is increased by 50%. Hence, in future work, it will be critical to further refine the definition of these parameters.

The inhibitory potential of chemerin identified by the model is informed by the efficiency of the fit. The model captures well the behaviour of variables in the control environment and when chemerin is injected until 16 hours after peritonitis onset. Although, there are data for longer periods of time in the control environment there are no measurements when chemerin is injected. Consequently, when fitting the model to both types of datasets the fitting algorithm assumes that the profile of neutrophil and monocyte behaviour resembles that of the control data. When computing the inhibitory effect of chemerin using Eq. 6.25 the full 96 hours of the simulation are used. Therefore, although the results show that chemerin is able to inhibit the number of cells recruited it does not show if injecting chemerin aids in a faster resolution of inflammation. To overcome this limitation it is proposed that using the zymosan induced peritonitis procedure [324] measurements of cellular species should be made at around 40 hours after zymosan is injected. With the new data, it would be possible to confirm if the clearance of neutrophils and monocytes is faster in the presence of extra chemerin.

The results of this study contribute to the ongoing debate on whether chemerin has a generic anti-inflammatory function or whether it applies only to specific conditions [332]. Animal models have demonstrated a requirement of chemerin signalling in the development of inflammation and leukocyte infiltration [334]. Conversely, animal studies have shown that inhibition of endogenous chemerin activity exacerbates inflammation [332]. Additionally, the chemerin inhibitory pathway might require the involvement of other mediators e.g. Resolvin E1, which shares some of the receptors to which chemerin attaches [335].

Using the models referred in this work it was possible to capture the broad dynamics of the inhibitory role of chemerin during zymosan-induced peritonitis and to identify a high potential for inhibition with a specific selection of chemerin concentration and time of injection. These results encourage further experimental work to confirm simulation outcomes and allow for a detailed planning of future experimental work. The Chemerin/ChemR23 pro-resolving pathway could be involved in many conditions and it is hoped that this model will serve as a basis for the study of the role of chemerin in pathophysiology.

Appendix 6.A: Data used for fitting

Table 6.A.1: Measurement of the mean and standard deviation of the concentration of CCL2 CXXL1 and chemerin concentrations at different times during the zymosan induced peritonitis experiment.

Time [hours]	CCL2 [ng ml^{-1}]	CXCL1 [ng ml^{-1}]	Chemerin [ng ml^{-1}]
0	$5.17\times10^{-3} \pm 6.7\times10^{-4}$	0 ± 0	1.21 ± 2.34
2	$3.89\times10^{-1} \pm 1.81\times10^{-1}$	2.791 ± 1.62	3.58 ± 3.13
4	$2.75\pm9.93\times10^{-1}$	$1.37\times10^{-1}\pm7.\times10^{-2}$	2.54 ± 1.32
8	$5.32\times10^{-2}\pm6.16\times10^{-2}$	$2.72\times10^{-2}\pm0$	1.31 ± 1.06
16	$5.36\times10^{-2}\pm1.88\times10^{-2}$	$4.17\times10^{-2}\pm3.4\times10^{-3}$	2.68 ± 1.91
20	$4.09\times10^{-2}\pm5.26\times10^{-3}$	N/A	N/A
72	N/A	N/A	2.61 ± 2.51
96	N/A	N/A	$2.02\pm5.67\times10^{-1}$

Table 6.A.2: Measurement of the mean and standard deviation of the number of neutrophils and monocytes at different times during the zymosan induced peritonitis experiment.

Time [hours]	Neutrophil [cell×10^{6}]	Monocytes [cell×10^{6}]
0	$1.08\times10^{-1}\pm1.35\times10^{-1}$	$7.73\times10^{-2}\pm9.39\times10^{-2}$
2	5.13 ± 1.3	$2.5\times10^{-2}\pm7.92\times10^{-3}$
4	7.09 ± 2.68	$4.91\times10^{-1}\pm1.66\times10^{-1}$
8	$7.28\pm5.27\times10^{-1}$	$3.26\pm8.86\times10^{-1}$
16	5.51 ± 1.59	$2.81\pm6.8\times10^{-3}$
20	3.73 ± 1.99	2.56 ± 1.12
48	$8.12\times10^{-1}\pm6.29\times10^{-1}$	$7.06\times10^{-1}\pm1.46\times10^{-1}$
72	$1.06\times10^{-1}\pm8.56\times10^{-2}$	$1.13\pm3.56\times10^{-1}$
96	$2.29\times10^{-1}\pm4.06\times10^{-2}$	$1.13\pm3.46\times10^{-1}$

Table 6.A.3: Measurement of the mean and standard deviation of the number of neutrophils and monocytes at different times during the zymosan-induced peritonitis with extra chemerin injected two hours after inflammation onset.

Time [hours]	Neutrophil [cell×10^6]	Monocytes [cell×10^6]
4	6.88 ± 3.039	$4.99\times10^{-1} \pm 4.53\times10^{-1}$
16	4.84 ± 2.01	$2.09 \pm 5.97\times10^{-1}$

Appendix 6.B: Result of fitting model

Table 6.B.1: Summary of fitted parameter values of the chemerin inflammation modulation model

Parameter	Description	Units	Value
k_{pN}	Rate of zymosan phagocytosis by neutrophils	h^{-1}	2.013
k_{pM}	Rate of zymosan phagocytosis by monocytes	h^{-1}	1.285
V_{C_1Z}	Rate of CXCL1 production in response to zymosan injection	ng ml^{-1} h^{-1}	2.86
k_{C_1Z}	Rate of CXCL1 production in response to zymosan injection	ng ml^{-1}	1×10^{-3}
k_{AN}	Rate of neutrophil apoptosis	h^{-1}	1.152×10^{-3}
k_{NG}	G rate of inhibition of CXCL1 production by neutrophils	ng ml^{-1}	6.259×10^{-3}
k_{ZG}	G rate of inhibition of CXCL1 production by zymosan	ng ml^{-1}	1.218×10^{-3}
V_{NC_1}	Rate of CXCL1 production by neutrophils	ng ml^{-1} h^{-1}	4.46
k_{NC_1}	Rate of CXCL1 production by neutrophils	cell×10^6	10.273
$k_{NC_{15}}$	C_{15} rate of inhibition of CXCL1 production by neutrophils	ng ml^{-1}	1.632×10^{-1}
V_{AC_1}	Rate of CXCL1 production by apoptotic neutrophils	ng ml^{-1} h^{-1}	1.307×10^{-3}
k_{AC_1}	Rate of CXCL1 production by apoptotic neutrophils	cell×10^6	3.553×10^{-1}
$k_{AC_{15}}$	C_{15} rate of inhibition of CXCL1 production by apoptotic neutrophils	ng ml^{-1}	2.631×10^{-3}
k_{AG}	G rate of inhibition of CXCL1 production by apoptotic neutrophils	ng ml^{-1}	2.819×10^{-2}
V_{C_1N}	Rate of neutrophil chemotaxis by CXCL1	cell×10^6 h^{-1}	2.65
k_{pA}	Rate of apoptotic neutrophil phagocytosis by monocytes	h^{-1}	3.412×10^{-3}
$k_{C_{15}}$	C_{15} rate of apoptotic neutrophil phagocytosis by monocytes	ng ml^{-1}	1.2×10^{-3}
k_{C_2M}	Chemoattractant rate of monocytes by C_2	h^{-1}	5.182×10^{-1}
k_{C_hM}	Chemoattractant rate of monocytes by C_h	h^{-1}	1×10^{-3}
y_M	Monocyte clearance rate by the capillary	h^{-1}	1.986×10^{-2}
$V_{C_{15}}$	Maximum velocity for the enzymatic reaction that produces C_{15}.	ng ml^{-1} h^{-1}	2.687×10^{-1}
w_{NC_h}	Parameter of chemerin production function by neutrophils	dimensionless	2.12
w_{AC_h}	Parameter of chemerin production function by apoptotic neutrophils	dimensionless	2.769×10^{-1}
w_{NC_2}	Parameter of CCL2 production function by neutrophils	dimensionless	1.621×10^{-3}
w_{AC_2}	Parameter of CCL2 production function by apoptotic neutrophils	dimensionless	5
w_{NC_1}	Parameter of CXCL1 production function by neutrophils	dimensionless	5
w_{AC_1}	Parameter of CXCL1 production function by apoptotic neutrophils	dimensionless	2.321
w_{NG}	Parameter of G inhibition of CXCL1 production function by neutrophils	dimensionless	3.431
w_{AG}	Parameter of G inhibition of CXCL1 production function by apoptotic neutrophils	dimensionless	1.736
$w_{AC_{15}}$	Parameter of C_{15} inhibition of CXCL1 production function by neutrophils	dimensionless	1.819×10^{-2}
$w_{NC_{15}}$	Parameter of C_{15} inhibition of CXCL1 production function by apoptotic neutrophils	dimensionless	4.395×10^{-3}
w_{ZG}	Parameter of G inhibition of CXCL1 production function in response to zymosan injection	dimensionless	1.048
$w_{ZC_{15}}$	Parameter of C_{15} inhibition of CXCL1 production function in response to zymosan injection	dimensionless	3.802×10^{-1}
$K_{mC_{15}}$	Michaelis-Menten constant of C_{15} production from monocyte proteases cleavage of chemerin	ng ml^{-1}	1.695×10^{-1}

k_g	Rate of G production in response to apoptotic neutrophil phagocytosis by monocytes	ng ml^{-1} h^{-1}	3.553×10^{-3}
V_{NC_h}	Maximum rate of chemerin production by neutrophils	ng ml^{-1} h^{-1}	2.33
k_{NC_h}	Michaelis-Menten constant for the chemerin production by neutrophils	cell$\times10^6$	1.932×10^{-2}
V_{AC_h}	Maximum rate of chemerin production by apoptotic neutrophils	ng ml^{-1} h^{-1}	5.887×10^{-3}
k_{AC_h}	Michaelis-Menten constant for the chemerin production by apoptotic neutrophils	cell$\times10^6$	5.736×10^{-2}
V_{NC_2}	Maximum rate of CCL2 production by neutrophils	ng ml^{-1} h^{-1}	1.899×10^{-3}
k_{NC_2}	Michaelis-Menten constant for the CCL2 production by neutrophils	cell$\times10^6$	1.073
V_{AC_2}	Maximum rate of CCL2 production by apoptotic neutrophils	ng ml^{-1} h^{-1}	26.749
$k_{ZC_{15}}$	C_{15} inhibition rate of CXCL1 production in response to zymosan injection	ng ml^{-1}	1.061×10^{-2}
k_{AC_2}	Michaelis-Menten constant for the CCL2 production by apoptotic neutrophils	cell$\times10^6$	2.5×10^{-2}
y_A	Apoptotic neutrophil clearance rate by the capillary	h^{-1}	1.75×10^{-3}
k_{C_hZ}	Rate of chemerin production in response to zymosan injection	ng ml^{-1}	1.099
V_{C_hZ}	Rate of chemerin production in response to zymosan injection	ng ml^{-1} h^{-1}	3.15

Appendix 6.C: Summary of assumptions

Table 6.C.1: List of assumptions

Section	Assumption
6.2 Materials and methods	• From the literature the models by Smith *et al.* [251] and Dunster *et al.* [252] were adapted to create the chemerin pro resolving model as they take into accountdifferent types of leukocytes (neutrophils and monocytes) and pro resolving chemokines.
6.2.3.1 Pro and anti-inflammatory chemokine production	• It is assumed that the injection of zymosan only leads to the production of CXCL1. • CCL2 and chemerin are produced in response to the arrival of neutrophils and monocytes.
6.2.3.2 Neutrophil and monocyte chemotaxis	• Based on the work by Smith *et al.* [251] and the peritonitis model measurements show that there is a maximum number of neutrophils and monocytes recruited.
6.2.3.4 Anti-inflammatory chemokine production and role in neutrophil recruitment and phagocytosis action	• Two pro-resolving effects of C15 were considered as proposed by [171]: - promotes phagocytosis of apoptotic neutrophils; - inhibits production of pro inflammatory cytokines. • The arrival of neutrophils and monocytes is assumed to be pro-inflammatory and anti-inflammatory respectively. Therefore, anti-inflammatory cytokines only influence the arrival of neutrophils.
6.2.3.5 Injection of additional chemerin model	• It was found to be tasking for the ode solver to simulate a chemerin injection. This is because the injection has a timescale of seconds and the timescale of the model is hours making the injection close to instantaneous. In order to overcome the solver errors that occur by this contrast the injection was assumed to take approximately 10 min.
6.3.1 Model fitting	• From the work by Smith *et al.* [251] the rate of cytokine decay and neutrophil vasculature extraction were found. • The rate of cytokine decay was assumed to be the same for all cytokines. • The rate of apoptotic neutrophil extraction rate was considered separately to the neutrophil one. • The model is fitted using the simplex method, which was chosen due to its ability to handle large models.

	• The range chosen for the fit was set empirically to reflect the rate at which different variables evolve during the experimental study.
6.3.2 Optimizing the therapeutic potential of chemerin	• The optimal point for chemerin injection was identified using as criteria: - zymosan cleared as efficiently as model fitted to control data. - maximum reduction of number of neutrophils, monocytes and apoptotic neutrophils.
6.3.3 Sensitivity analysis	• Due to the size of the model and number of parameters the best way to tackle sensitivity analysis of the model was found to be the Campolongo-Morris method. • The RMS error function was defined to take into the behaviour of the model compared to the control data; the data when 500 μg ml^{-1} and when the time and concentration of chemerin injection is optimized. • The parameters for which perturbations exerted the least an RMS error increase of approximately 1% were removed.

Chapter 7

Conclusion and Future work

In this thesis, three models were developed, which aimed at capturing pathological mechanism common to many CNS diseases. Three mechanisms were focused on: glutamate excitotoxicity, cytotoxic oedema and acute inflammation. Each model is placed in different contexts and answers individual questions provided by experimental labs. Through this process, it was possible to narrow down the exact experiments required to test the hypothesis ensuring more ethical and cost effective experimental work.

To investigate glutamate excitotoxicity a four-compartmental model was developed that includes the exchange of this neurotransmitter between neurons and astrocytes in an ischaemic stroke environment. With it was possible to create the firs model of glutamate release validated in stroke. To achieve such a model a novel approach to glutamate kinetics was used where the literature of intra neuronal/astrocytic kinetics of glutamate, the relationships between glutamate release and ionic regulation and the metabolic requirements of the glutamate cycle. By combining these models with values identified as biologically sound values it was possible to predict the release of glutamate in the presence of a severe ischaemic stroke.

Cytotoxic oedema was studied in the context of NMO. The aim of the work was to test two hypotheses for the observed astrocytic oedema present in NMO lesions. The hypotheses consisted in understanding if the swelling was due to the impairment of the cells water regulation through AQP4 channels or if it was due to holes formed by inflammatory complement. The model developed was the first to investigate astrocytic water regulation in a pathological environment. From simulations, it was found that impairing AQP4 had negligible impact on the cell volume and that it could not be the reason for registered oedema.

In order to investigate the second hypothesis, the first model of the ionic flow through lytic holes formed by complement MAC was created. Furthermore, the complement inhibitor CD59 was tested as a potential preventative therapy. To this effect, the first model of the effects of this protein was created. With this model, a threshold for the efficiency of therapies was found below which therapies have a negligible effect on the development of NMO lesions.

For the inflammatory study, a model was developed for the acute inflammatory response to evaluate the pro-resolving pathway of chemerin. This was the first model that tested the effects of an intervention on acute inflammation. With the model, it was possible to identify an optimal time and concentration to inject chemerin in order to inhibit the recruitment of inflammatory cells. Such a study would have been proven to be costly and unethical if it was done experimentally. From the optimal injection found it is now expected to plan a new experimental study that will evaluate the veracity of the findings and if the model needs to be further updated.

The approach taken to develop these models consisted in adapting models found in the literature that have evolved over the past 50 years. The mechanisms that they capture are well understood and assumptions made are widely accepted. Two areas of research were considered. The first involved expanding the work developed on cytotoxic oedema in ischaemic stroke by Orlowski and colleagues [14], [15]. This model already had implemented this strategy by combining the metabolic model of Cloutier *et al.* [200] and the cellular ionic regulation of Endresen *et al.* [206]. This model was then repurposed to create a model of glutamate release in stroke and astrocytic oedema in NMO. The second involved appropriating the models of acute inflammation by Lauffenburger and colleagues [66], [246], [247]. This appears to be a common approach in this field as it was followed by the state of the art models of acute inflammation by Dunster *et al.* [252] and Smith *et al.* [251].

The work done has shown that by combining established models it is possible to define complex pathologic mechanisms. However, as presented in Chapter 3 this approach has certain limitations. As these models are being applied to new contexts where there is, in some cases, little data available not all parameters for the kinetics implemented here have been experimentally measured. Therefore, certain parameters had to be fitted. Due to the size of the models created the number of algorithms that are both efficient and able to arrive at solutions is restricted. The algorithm chosen was selected based on the criteria established by the work by Cloutier *et al.* [200] that established that for models of these dimensions the fitting has to be done without requiring the derivative of the model. This is because in these large models it is not guaranteed that a solution for the derivative of the model exists. Hence, as in Cloutier *et al.* [200], the simplex algorithm was chosen [68].

The limitations of this method are that it is dependent on the range chosen for the parameter space and that it has an ad hoc stopping criteria. For all fittings made, the parameter space was then chosen based, when possible, on data available or similar parameters. In terms of the stopping criteria, the best approach found was to develop an assisted way of evaluating individual iterations of the method. Only in this way was it possible to identify when the algorithm got stuck on local minima. This work showed that there are tools available to handle the models of this size. In the field of neuronal tissue modelling, a more sophisticated fitting method is required as there are many barriers to measuring parameters.

Furthermore, when trying to develop models of these complex diseases the result tends to be a large model with tens of equations. To overcome this, sensitivity analysis algorithms were implemented. Through this process, it is possible to identify the parameters and kinetics that are negligible to the behaviour of the model. As described by Saltelli *et al.* [260] there are several strategies to evaluate models. One such strategy suitable for large models was developed by Campolongo *et al.* [294]. This method involves exploring the parameter space over a defined range and comparing the output of the model to the one desired. This tool is also useful to inform future experimental work in order to improve the models created and to uncover pathological mechanisms. Throughout the work, this method was implemented and it was found to be useful. However, the output of the method relies on the definition of the range chosen. In the field of mathematical modelling of brain tissue, the range of the parameters is not known for a number of parameters.

Therefore, the choice of range for some parameters was ad hoc. To allow for a more refined analysis of models of this kind, a better understanding of all the parameters involved in these models is required.

Using this method, it was only possible to reduce the complexity by one order of magnitude in the case of the complement model. In the case where only the output and inputs are of relevance, an effort was made to reduce the model into a black box. The success of these simplified models is evaluated, as explained by Cladwell *et al.* [336], by ensuring the novel model is able to replicate the original predictions of the model over a range of inputs. This was implemented when trying to reduce the complement model to just a MAC production model in response to antibody-antigen binding. Due to the shape of the output, a second order model was chosen to fit the complement model. Additionally, a symbolic genetic algorithm was used to fit how the parameters of the second order model vary with the inputs of the model. Through this process, a model of approximately 30 ODEs was reduced to two. To ensure the versatility of the model the ranges chosen for inputs were large (four orders of magnitude). However, the model is only valid within that range.

As the field of mathematical modelling of degenerative diseases is novel there are many limitations in the literature. Additionally, to develop models of these diseases models with a large number of equations were combined. As discussed in Chapter 3 these are the main characteristics of "sloppy" models. To avoid or mitigate the effects of such models strategies were employed that follow the principle presented by Gutenkunst *et al.* [193]. These include that a model should aim at accurately predict a variety of physiological behaviour and not be concerned with the values of individual parameters.

In Chapter 4 the glutamate model was developed by not fitting the kinetics to data but instead taking the different models from the shelf combining them and evaluating how the model behaves compared to 3 sets of data. It was found that it accurately predicts the release of glutamate in response to an action potential. Additionally, in the case of ischaemic stroke, it was shown that for certain levels of CBF the model accurately predicts glutamate concentration at the ECS for a 5 min and a 14 min stroke.

For the NMO work presented in Chapter 5 it was harder to mitigate the “sloppiness” of the model as there is very little data and the understanding in the literature is limited. The model involved adapting combining models from different contexts. An effort was made to ensure that when models were adapted to new contexts that they were validated with the data used to validate the model in its original context. Additionally, the predictions of the model were stress tested using the C-M method. Furthermore, the experimental procedure to test and improve the model simulations is presented.

Finally, the chemerin pro-resolving model was also stress tested using two algorithms. The first consisted in using the C-M method again to investigate the parameters to which the model is more sensitive. Additionally, a remove-one bootstrap approach was used to identify how dependent the model was to individual data points. From this analysis, it is clearly demonstrated how sensitive the predictions of the model are and experimental procedures are proposed to overcome these limitations.

Managing the pathological mechanisms considered, the assumptions made and the size of the models required many discussions with supervisors and collaborators. The present models were achieved after many iterations and after hearing all the inputs of all the involved parties. In the remainder of this chapter, the main assumptions made in each chapter are discussed, and experimental measurements are proposed that could aid future iterations of the models developed.

7.1 Glutamate excitotoxicity

The main assumption made in this work is that only the pre-membrane depolarization glutamate release is characterized as post depolarisation the cells are defined as dead. This fact informed how the work was organized. Following the work by Rossi *et al.* [209] the mechanisms for glutamate release modelled were the release by vesicular exocytosis triggered by calcium and by the reverse function of glutamate transporters. The model was defined to be used to predict glutamate levels at the penumbra.

After the changes made in Chapter 5 by refitting the Cloutier *et al.* [200], it is able to simulate cellular behaviour post depolarisation. In order to characterize glutamate release post-depolarisation, further adaptions would be required. To describe the exchange of glutamate between vesicles and the cytoplasm the kinetics are not fully understood seeing that the only mathematical model that considers the filling of vesicles was the one by Axmacher *et al*. [218]. Additionally, the filling of vesicles requires ATP as reported by Albers and Siegel [337]. The metabolic requirements and kinetics of this pump have yet to be measured.

Furthermore, the best data that evaluated the levels of glutamate during stroke consisted in *in vivo* microdialysis measurements where an ischaemic stroke is induced over a period of time followed by reperfusion [73], [88]. As is in these experiments stroke was induced for a relatively small amount of time (in the order of tens of minutes) it was assumed that tissue was able to return to its basal state without severe damage. However, as described by Nour *et al*. [338] reperfusion might trigger pathological mechanisms that may lead to cell death. No mathematical model has yet attempted to model ionic and metabolic cellular behaviour after reperfusion.

In order to overcome these limitations, further data on glutamate kinetics during a stroke are required. It is here proposed that using CEST to image glutamate levels [339] during a simulated stroke as in the microdialysis studies [73], [88] could provide more accurate data with better time resolution. With such data, it would be possible to understand if the mechanisms considered suffice to model glutamate kinetics or if further complexity is required such as anion activated glutamate release channels, as described by Rossi *et al*. [209].

7.2 NMO pathophysiology

The work developed in this chapter can be divided into three sections: 1. The fits performed of the Cloutier *et al*. [200] and of the Endresen *et al*. [206] models; 2. Adapting Orlowski *et al.* [15] model of cytotoxic oedema to consider hydrostatic pressure and the dependence of the astrocytic membrane on AQP4 and 3. Testing the effects of complement lysis on astrocytic volume. In each of these topics, assumptions were made that can affect the outcome of the model. When refitting the model, the biggest concern involved the choice for the parameter range of the parameters being fitted. In the work by Cloutier *et al*. [200] and Endresen *et al*. [206] the range chosen to fit the parameters was not mentioned. Therefore, it was chosen *ad hoc*. Additionally, the toolbox used by Schmidt and

Jirstrand [257] allows for user supervision while the algorithm is running. This way it was possible to steer the algorithm away from local minima. For a more informed fitting measurements of parameters, made from human subjects, are required.

After having a metabolic model that is able to simulate kinetics post depolarisation and stable glutamate kinetics the effects of removing AQP4 permeability on astrocytic volume. This section of the work was based on Starlings equation [289]. The biggest concern is this section resulted from missing parameters values available in the literature. To overcome these limitations the parameters were calculated to ensure the model was stable at steady state conditions.

Additionally, the distribution of perivascular and presynaptic AQP4 along the astrocytic membrane is not known. For this reason, a test was made to see how the distribution affected the results of removing the two types of AQP4 orientations separately and all together. The work by Nagelhus *et al*. [305] was able to stain AQP4 channels of Müller cells in the optic nerve with gold particles. Using this method, the average concentration of AQP4 in astrocytes could be measured. The distribution of these channels would be more complicated to integrate into the model as the work by Østby *et al*. [64] states that the AQP4 channel expression and location varies depends on the function of the astrocyte.

The third section of the NMO project involved modelling cytotoxic oedema triggered by inflammatory complement. This work can be divided into three sections: 1. Choosing and adapting inflammatory complement model; 2. Creating a MAC hole model and 3. CD59 kinetics. As explained in Chapter 5, the Korotaevkiy *et al*. [236] model of the complement cascade was implemented as it was the only validated model that considers the full proteic cascade from activation to MAC formation. However, parameters had to be fitted in order to overcome mistakes in the publication. As there is interest for inflammatory complement kinetics in many pathological contexts it would be of interest to have a fully validated model of these kinetics introduced into a recognised model database such as the CellML repository [256] or the Biomodel database [340]. Additionally, the Korotaevkiy *et al*. model [236] was validated using Borrelia burgdorferi bacteria *in vitro* data. For the case of NMO, it would be pertinent to perform similar experiments with astrocytes, as the size of the cells is different.

The creation of the MAC hole model involved a series of assumptions as there is no current model of how individual ions flow through lytic holes. It was then assumed that the flow through a MAC hole was proportional to the flow across a membrane channel, as described by Endresen *et al.* [206]. The work by Schröder *et al.* [307] measured and fitted kinetics to the flow through lytic holes. However, it does not take into consideration the different ions. This would be of great interest as these values could be used to identify the flow of the ions as biomarkers for cell death [341].

In this thesis, a mathematical modelling was used to test the potential of CD59, a MAC inhibitor, as a preventative therapy for relapsing NMO. From this work, a concentration threshold bellow which the effects of CD59 are negligible. However, in order to arrive at this, result, the CD59 kinetics had to be developed, as no mathematical model was found. The work by Rollins and collaborators [165], [342] have characterised CD59 as an inhibitor of inflammatory complement using erythrocytes from different species. Although its impact has been evaluated they have not measured CD59 kinetics. Therefore, a model was fitted to the data in [165] that presents data with human erythrocytes. The model was developed by making it similar to the kinetics from Korotaevkiy *et al.* [236] for complement inhibitors. In order to better understand the effects of CD59, a similar experimental procedure as in Rollins *et al.* [342] could be used using an *in vitro* culture of astrocytes.

This project was the first mathematical model that aims at tackling the pathophysiology of NMO. Therefore, some kinetics of the model had to be developed using a brute force approach. In order to refine the model, the experiments proposed would be required. Despite, its limitations this work showed that pathological hypothesis of a complex disease, such as NMO, could be tested using mathematical modelling. Furthermore, a model of cytotoxic oedema due to complement lysis was developed, a mechanism common to many pathologies. It could then be adapted to many other contexts to test the hypothesis surrounding the complement lysis component in other pathologies.

7.3. Chemerin/ChemR23 pro-resolving pathway

This work was developed based on a pilot study by our collaborators the Professor Greaves group of the Sir William Dunn Physiology Department at Oxford. As this is a pilot study the number of data points is limited, which informed many of the assumptions made. Additionally, the full chemerin pro-resolving pathway as described by Cash *et al*. [171] has not been fully characterised. This section is organized into three topics, the assumptions made to overcome the limitations in terms of (1) the data, (2) the literature into chemerin pro-resolving kinetics and (3) the effects of pro-resolving mechanisms.

The data available consisted of measurements of neutrophils and monocytes cell numbers and several inflammatory mediators. From the mediators measured, besides chemerin, only CCL2 and CXCL1 were considered. The reason for this was that these were found to be the ones that best correlated with the arrival of neutrophils (CXCL1) and monocytes (CCL2). Furthermore, only these two cells kinetics were modelled. This was done because, as described in [56], these two cells mark the difference in behaviour between acute and chronic inflammation.

In order to develop a model of the Chemerin/ChemR23, there was the need to overcome the limitations in the literature on the mechanism behind this pathway and the limited number of models that exist on acute inflammation. In terms of the latter only the models by Smith *et al*. [251] and Dunster *et al*. [252] that considered the behaviour of both types of leukocytes and the pro-resolving mechanisms. These models consider the processes of chemokine production, cell recruitment, leukocyte phagocytosis, neutrophil apoptosis and cell clearance. Additionally, the work by Dunster *et al*. [252] uses the model of chemokine inhibition by Anderson *et al.* [327]. All these concepts were introduced in the model. However, as described by Cash *et al*. [171] the Chemerin/ChemR23 pathway is complex mechanisms that involved a variety of reactions. As there are neither measurements nor models of these reactions assumptions were made to overcome these limitations. As shown in Fig. 6.1 A chemerin is inactive at steady and only acts as a chemoattractant after the arrival of neutrophils. These cells release enzymes that trigger the chemoattractive nature of chemerin. Due to the lack of data on this reaction, it was assumed that including it would add an extra level of complexity and therefore it was assumed that chemerin does not require activation. Similarly, when monocytes arrive at the site of inflammation (Fig. 6.1 E) they release enzymes that are hypothesised to break down chemerin into peptides, such as C15, that exert a variety of function. Here, a Michaelis-Menten equation was used and its parameters were fitted to the data. In order to overcome these assumptions, a study would be required to measure these different rates. Additionally, the production of C15 from chemerin still needs to be confirmed as the work by Bondue *et al.* [343] contradicts the findings by Cash *et al.* [171].

In terms of building an inhibition model, as the literature is limited assumptions were required. From the data, there were no measurements of pro-resolving chemokines. Therefore, following Dunster *et al.* [252], a generic pro-resolving chemokine was implemented titled G. Then in terms of the effects of anti-inflammatory chemokines G and C_{15} the model created was also based on the model Dunster *et al.* [252], which assumed that pro-resolving chemokines only act on pro-inflammatory mechanisms. Additionally, the arrival of monocytes was seen as a pro-resolving mechanism. Therefore, the inhibitory action of pro-resolving chemokines only targeted the recruitment of neutrophils. As the concept of these chemokines is new a better understanding of their behaviour is needed to make the model more sophisticated.

In addition, as the field of complex models of inflammation is relatively a large number of parameters were fitted (45 in total). To refine the model development measurements of average values for acute inflammation are required. The work by Reynolds *et al.* [249] has attempted to identify a variety of parameters values throughout the literature for a model that includes anti-inflammatory mechanisms. However, due to its simplicity, many of the parameters found are not applicable to the more complex case of the Chmerin/ChemR23 context. It is, therefore, suggested that many of the parameters related to cell recruitment could be measured using the peritonitis animal model implemented to collect the data used.

The work developed arrived at the conclusion that there is maximum to the anti-inflammatory effect of chemerin. Additionally, a trade-off was identified between inhibiting the recruitment of neutrophils and monocytes. Through this work, it is hoped to inform future experimental work in the field of acute inflammation and through the partnership between mathematical modelling and experimental measurements arrive at a standard for testing treatments and hypothesis to prevent the degeneration of this mechanism into acute inflammation.

Bibliography:

[1] J. Hardy and H. Orr, "The genetics of neurodegenerative diseases," *J. Neurochem.*, vol. 97, no. 6, pp. 1690–1699, Jun. 2006.

[2] U. Nations, "World population ageing 2013," *Dep. Econ. Soc. Aff. PD*, 2013.

[3] H. Breivik, B. Collett, V. Ventafridda, R. Cohen, and D. Gallacher, "Survey of chronic pain in Europe: prevalence, impact on daily life, and treatment," *Eur. J. Pain*, vol. 10, no. 4, pp. 287–287, 2006.

[4] C. Spuch, O. Saida, and C. Navarro, "Advances in the treatment of neurodegenerative disorders employing nanoparticles," *Recent Pat. Drug Deliv. Formul.*, vol. 6, no. 1, pp. 2–18, Apr. 2012.

[5] B. V. Zlokovic, "Neurovascular mechanisms of Alzheimer's neurodegeneration," *Trends Neurosci.*, vol. 28, no. 4, pp. 202–208, Apr. 2005.

[6] I. K. Puri and L. Li, "Mathematical Modeling for the Pathogenesis of Alzheimer's Disease," *PLOS ONE*, vol. 5, no. 12, p. e15176, Dec. 2010.

[7] L. Edelstein-Keshet, *Mathematical models in biology*. SIAM, 2005.

[8] R. Ganguly and I. K. Puri, "Mathematical model for the cancer stem cell hypothesis," *Cell Prolif.*, vol. 39, no. 1, pp. 3–14, Feb. 2006.

[9] A. Lomakin, D. B. Teplow, D. A. Kirschner, and G. B. Benedek, "Kinetic theory of fibrillogenesis of amyloid β-protein," *Proc. Natl. Acad. Sci.*, vol. 94, no. 15, pp. 7942–7947, Jul. 1997.

[10]M. M. Pallitto and R. M. Murphy, "A mathematical model of the kinetics of β-amyloid fibril growth from the denatured state," *Biophys. J.*, vol. 81, no. 3, pp. 1805–1822, 2001.

[11]L. Edelstein-Keshet and A. Spiros, "Exploring the formation of Alzheimer's disease senile plaques in silico," *J. Theor. Biol.*, vol. 216, no. 3, pp. 301–326, 2002.

[12]M. Luca, A. Chavez-Ross, L. Edelstein-Keshet, and A. Mogilner, "Chemotactic signaling, microglia, and Alzheimer's disease senile plaques: Is there a connection?," *Bull. Math. Biol.*, vol. 65, no. 4, pp. 693–730, 2003.

[13]A. Kolodkin, E. Simeonidis, R. Balling, and H. V. Westerhoff, "Understanding complexity in neurodegenerative diseases: in silico reconstruction of emergence," *Front. Physiol.*, vol. 3, Jul. 2012.

[14]P. Orlowski, M. Chappell, C. S. Park, V. Grau, and S. Payne, "Modelling of pH dynamics in brain cells after stroke," *Interface Focus*, vol. 1, no. 3, pp. 408–416, Jun. 2011.

[15]P. Orlowski, D. O'Neill, V. Grau, Y. Ventikos, and S. Payne, "Modelling of the physiological response of the brain to ischaemic stroke," *Interface Focus*, vol. 3, no. 2, p. 20120079, 2013.

[16]M. Szatkowski and D. Attwell, "Triggering and execution of neuronal death in brain ischaemia: two phases of glutamate release by different mechanisms," *Trends Neurosci.*, vol. 17, no. 9, pp. 359–365, Sep. 1994.

[17]S. Saadoun, P. Waters, B. A. Bell, A. Vincent, A. Verkman, and M. C. Papadopoulos, "Intra-cerebral injection of neuromyelitis optica immunoglobulin G and human complement produces neuromyelitis optica lesions in mice," *Brain*, vol. 133, no. 2, pp. 349–361, 2010.

[18]S. Saadoun and M. C. Papadopoulos, "Role of membrane complement regulators in neuromyelitis optica," *Mult. Scler. J.*, vol. 21, no. 13, pp. 1644–1654, 2015.

[19]N. R. Carlson, *Physiology of Behavior, with Neuroscience Animations and Student Study Guide CD-ROM*. Pearson a&b, 2003.

[20]T. J. Drake, S. Jezzini, P. Lovell, L. L. Moroz, and W. Tan, "Single cell glutamate analysis in Aplysia sensory neurons," *J. Neurosci. Methods*, vol. 144, no. 1, pp. 73–77, May 2005.

[21]K. Nanri, S. Takizawa, H. Fujita, S. Ogawa, and Y. Shinohara, "Modulation of extracellular glutamate concentration by nitric oxide synthase inhibitor in rat transient forebrain ischemia," *Brain Res.*, vol. 738, no. 2, pp. 243–248, 1996.

[22]J. W. Olney, "Inciting excitotoxic cytocide among central neurons," *Adv. Exp. Med. Biol.*, vol. 203, pp. 631–645, 1986.

[23]B. Meldrum and J. Garthwaite, "Excitatory amino acid neurotoxicity and neurodegenerative disease," *Trends Pharmacol. Sci.*, vol. 11, no. 9, pp. 379–387, 1990.

[24]B. S. Meldrum, "The role of glutamate in epilepsy and other CNS disorders.," *Neurology*, 1994.

[25]K. Takeda, A. Ishida, K. Takahashi, and T. Ueda, "Synaptic vesicles are capable of synthesizing the VGLUT substrate glutamate from α-ketoglutarate for vesicular loading," *J. Neurochem.*, vol. 121, no. 2, pp. 184–196, Apr. 2012.

[26]G. Palaiologos, L. Hertz, and A. Schousboe, "Evidence that aspartate aminotransferase activity and ketodicarboxylate carrier function are essential for biosynthesis of transmitter glutamate," *J. Neurochem.*, vol. 51, no. 1, pp. 317–320, Jul. 1988.

[27]V. T. Karamyan and R. C. Speth, "Animal models of BMAA neurotoxicity: A critical review," *Life Sci.*, vol. 82, no. 5, pp. 233–246, Jan. 2008.

[28]K. S. Grant, T. M. Burbacher, E. M. Faustman, and L. Gratttan, "Domoic acid: neurobehavioral consequences of exposure to a prevalent marine biotoxin," *Neurotoxicol. Teratol.*, vol. 32, no. 2, pp. 132–141, Apr. 2010.

[29]C. Bendotti *et al.*, "Transgenic SOD1 G93A mice develop reduced GLT-1 in spinal cord without alterations in cerebrospinal fluid glutamate levels," *J. Neurochem.*, vol. 79, no. 4, pp. 737–746, Nov. 2001.

[30]P. Mesci *et al.*, "System xC- is a mediator of microglial function and its deletion slows symptoms in amyotrophic lateral sclerosis mice," *Brain J. Neurol.*, vol. 138, no. Pt 1, pp. 53–68, Jan. 2015.

[31]J. Sasabe *et al.*, "D-serine is a key determinant of glutamate toxicity in amyotrophic lateral sclerosis," *EMBO J.*, vol. 26, no. 18, pp. 4149–4159, Sep. 2007.

[32]M. M. Zeron *et al.*, "Increased sensitivity to N-methyl-D-aspartate receptor-mediated excitotoxicity in a mouse model of Huntington's disease," *Neuron*, vol. 33, no. 6, pp. 849–860, Mar. 2002.

[33]A. Scimemi, J. S. Meabon, R. L. Woltjer, J. M. Sullivan, J. S. Diamond, and D. G. Cook, "Amyloid-β1-42 slows clearance of synaptically released glutamate by mislocalizing astrocytic GLT-1," *J. Neurosci. Off. J. Soc. Neurosci.*, vol. 33, no. 12, pp. 5312–5318, Mar. 2013.

[34]A. Schallier *et al.*, "Region- and age-specific changes in glutamate transport in the AβPP23 mouse model for Alzheimer's disease," *J. Alzheimers Dis. JAD*, vol. 24, no. 2, pp. 287–300, 2011.

[35]J. Fan *et al.*, "P38 MAPK is involved in enhanced NMDA receptor-dependent excitotoxicity in YAC transgenic mouse model of Huntington disease," *Neurobiol. Dis.*, vol. 45, no. 3, pp. 999–1009, Mar. 2012.

[36]E. Foglio and L. F. Rodella, "Aquaporins and Neurodegenerative Diseases," *Curr. Neuropharmacol.*, vol. 8, no. 2, pp. 112–121, Jun. 2010.

[37]R. Ventura and K. M. Harris, "Three-dimensional relationships between hippocampal synapses and astrocytes," *J. Neurosci.*, vol. 19, no. 16, pp. 6897–6906, 1999.

[38]D. E. Bergles, J. S. Diamond, and C. E. Jahr, "Clearance of glutamate inside the synapse and beyond," *Curr. Opin. Neurobiol.*, vol. 9, no. 3, pp. 293–298, Jun. 1999.

[39]E. A. Nagelhus *et al.*, "Immunogold evidence suggests that coupling of K+ siphoning and water transport in rat retinal Müller cells is mediated by a coenrichment of Kir4.1 and AQP4 in specific membrane domains," *Glia*, vol. 26, no. 1, pp. 47–54, Mar. 1999.

[40]J. J. Iliff *et al.*, "A paravascular pathway facilitates CSF flow through the brain parenchyma and the clearance of interstitial solutes, including amyloid β," *Sci. Transl. Med.*, vol. 4, no. 147, p. 147ra111–147ra111, 2012.

[41]J. J. Iliff and M. Nedergaard, "Is there a cerebral lymphatic system?," *Stroke J. Cereb. Circ.*, vol. 44, no. 6 0 1, pp. S93–S95, Jun. 2013.

[42]E. Küppers *et al.*, "AQP4 expression in striatal primary cultures is regulated by dopamine–implications for proliferation of astrocytes," *Eur. J. Neurosci.*, vol. 28, no. 11, pp. 2173–2182, 2008.

[43]T. Jimi *et al.*, “Aquaporin 4: lack of mRNA expression in the rat regenerating muscle fiber under denervation,” *Neurosci. Lett.*, vol. 291, no. 2, pp. 93–96, 2000.

[44]M. E. Gurney, R. Liu, J. S. Althaus, E. D. Hall, and D. A. Becker, “Mutant CuZn superoxide dismutase in motor neuron disease,” *J. Inherit. Metab. Dis.*, vol. 21, no. 5, pp. 587–597, 1998.

[45]M. C. Papadopoulos, J. L. Bennett, and A. S. Verkman, “Treatment of neuromyelitis optica: state-of-the-art and emerging therapies,” *Nat. Rev. Neurol.*, vol. 10, no. 9, pp. 493–506, 2014.

[46]Y. Shen, L. Yang, and R. Li, “What does complement do in Alzheimer’s disease? Old molecules with new insights,” *Transl. Neurodegener.*, vol. 2, no. 1, p. 21, 2013.

[47]R. L. Mosley, J. A. Hutter-Saunders, D. K. Stone, and H. E. Gendelman, “Inflammation and adaptive immunity in Parkinson’s disease,” *Cold Spring Harb. Perspect. Med.*, vol. 2, no. 1, p. a009381, 2012.

[48]P. Eikelenboom and F. C. Stam, “Immunoglobulins and complement factors in senile plaques,” *Acta Neuropathol. (Berl.)*, vol. 57, no. 2, pp. 239–242, 1982.

[49]P. Eikelenboom, E. Van Exel, R. Veerhuis, A. J. Rozemuller, W. A. Van Gool, and J. J. Hoozemans, “Innate immunity and the etiology of late-onset Alzheimer’s disease,” *Neurodegener. Dis.*, vol. 10, no. 1–4, pp. 271–273, 2012.

[50]P. L. McGeer, H. Akiyama, S. Itagaki, and E. G. McGeer, “Activation of the classical complement pathway in brain tissue of Alzheimer patients,” *Neurosci. Lett.*, vol. 107, no. 1, pp. 341–346, 1989.

[51]K. W. Boyett *et al.*, “Increased fibrillar β-amyloid in response to human C1q injections into hippocampus and cortex of APP+ PS1 transgenic mice,” *Neurochem. Res.*, vol. 28, no. 1, pp. 83–93, 2003.

[52]L.-B. Yang, R. Li, S. Meri, J. Rogers, and Y. Shen, “Deficiency of complement defense protein CD59 may contribute to neurodegeneration in Alzheimer’s disease,” *J. Neurosci.*, vol. 20, no. 20, pp. 7505–7509, 2000.

[53]D. A. Loeffler, D. M. Camp, and S. B. Conant, “Complement activation in the Parkinson’s disease substantia nigra: an immunocytochemical study,” *J. Neuroinflammation*, vol. 3, no. 1, p. 29, 2006.

[54]F. M. LaFerla and K. N. Green, “Animal models of Alzheimer disease,” *Cold Spring Harb. Perspect. Med.*, vol. 2, no. 11, p. a006320, 2012.

[55]J. L. Watson, L. Ryan, N. Silverberg, V. Cahan, and M. A. Bernard, “Obstacles And Opportunities In Alzheimer’s Clinical Trial Recruitment,” *Health Aff. Proj. Hope*, vol. 33, no. 4, pp. 574–579, Apr. 2014.

[56]V. Kumar, A. K. Abbas, and J. C. Aster, *Robbins basic pathology*. Philadelphia, USA: Elsevier Health Sciences, 2012.

[57]S. Amor *et al.*, “Inflammation in neurodegenerative diseases--an update,” *Immunology*, vol. 142, no. 2, pp. 151–166, Jun. 2014.

[58]M. Letiembre *et al.*, “Screening of innate immune receptors in neurodegenerative diseases: a similar pattern,” *Neurobiol. Aging*, vol. 30, no. 5, pp. 759–768, 2009.

[59]E. Okun, K. J. Griffioen, J. D. Lathia, S.-C. Tang, M. P. Mattson, and T. V. Arumugam, “Toll-like receptors in neurodegeneration,” *Brain Res. Rev.*, vol. 59, no. 2, pp. 278–292, 2009.

[60]X. Wang *et al.*, “Resolution of inflammation is altered in Alzheimer’s disease,” *Alzheimers Dement.*, vol. 11, no. 1, pp. 40–50, 2015.

[61]M. Zhu *et al.*, “Pro-Resolving Lipid Mediators Improve Neuronal Survival and Increase Aβ42 Phagocytosis,” *Mol. Neurobiol.*, vol. 53, no. 4, pp. 2733–2749, May 2016.

[62]A. Aubert, R. Costalat, and R. Valabrègue, “Modelling of the coupling between brain electrical activity and metabolism,” *Acta Biotheor.*, vol. 49, no. 4, pp. 301–326, 2001.

[63]A. L. Hodgkin and A. F. Huxley, “A quantitative description of membrane current and its application to conduction and excitation in nerve,” *J. Physiol.*, vol. 117, no. 4, pp. 500–544, Aug. 1952.

[64]I. Østby *et al.*, “Astrocytic mechanisms explaining neural-activity-induced shrinkage of extraneuronal space,” *PLoS Comput Biol*, vol. 5, no. 1, p. e1000272, 2009.

[65]M.-A. Dronne, J.-P. Boissel, and E. Grenier, “A mathematical model of ion movements in grey matter during a stroke,” *J. Theor. Biol.*, vol. 240, no. 4, pp. 599–615, 2006.

[66]D. Lauffenburger and K. H. Keller, “Effects of leukocyte random motility and chemotaxis in tissue inflammatory response,” *J. Theor. Biol.*, vol. 81, no. 3, pp. 475–503, Dec. 1979.

[67]A. A. Cuellar, C. M. Lloyd, P. F. Nielsen, D. P. Bullivant, D. P. Nickerson, and P. J. Hunter, “An Overview of CellML 1.1, a Biological Model Description Language,” *SIMULATION*, vol. 79, no. 12, pp. 740–747, Dec. 2003.

[68]B. P. Flannery, W. H. Press, S. A. Teukolsky, and W. Vetterling, “Numerical recipes in C,” *Press Synd. Univ. Camb. N. Y.*, vol. 24, 1992.

[69]M. D. Morris, “Factorial sampling plans for preliminary computational experiments,” *Technometrics*, vol. 33, no. 2, pp. 161–174, 1991.

[70]N. Allgaier and R. McDevitt, *Reverse Engineering the Brain with Eureqa*. UVM, 2011.

[71]J. L. Cash *et al.*, “Synthetic chemerin-derived peptides suppress inflammation through ChemR23,” *J. Exp. Med.*, vol. 205, no. 4, pp. 767–775, 2008.

[72]B. Karaszewski *et al.*, “Measurement of brain temperature with magnetic resonance spectroscopy in acute ischemic stroke,” *Ann. Neurol.*, vol. 60, no. 4, pp. 438–446, Oct. 2006.

[73]H. Benveniste, J. Drejer, A. Schousboe, and N. H. Diemer, “Elevation of the extracellular concentrations of glutamate and aspartate in rat hippocampus during transient cerebral ischemia monitored by intracerebral microdialysis,” *J. Neurochem.*, vol. 43, no. 5, pp. 1369–1374, 1984.

[74]J. Zhang, H. Benveniste, B. Klitzman, and C. A. Piantadosi, “Nitric oxide synthase inhibition and extracellular glutamate concentration after cerebral ischemia/reperfusion,” *Stroke*, vol. 26, no. 2, pp. 298–304, 1995.

[75]D. Purves *et al.*, *Cognitive Neuroscience*. Sunderland: Sinauer Associates, Inc, 2008.

[76]S. O. Rizzoli and W. J. Betz, “Synaptic vesicle pools,” *Nat. Rev. Neurosci.*, vol. 6, no. 1, pp. 57–69, 2005.

[77]J. Sun, Z. P. Pang, D. Qin, A. T. Fahim, R. Adachi, and T. C. Südhof, “A dual-Ca2+-sensor model for neurotransmitter release in a central synapse,” *Nature*, vol. 450, no. 7170, pp. 676–682, 2007.

[78]M. P. Mattson, F. M. LaFerla, S. L. Chan, M. A. Leissring, P. N. Shepel, and J. D. Geiger, “Calcium signaling in the ER: its role in neuronal plasticity and neurodegenerative disorders,” *Trends Neurosci.*, vol. 23, no. 5, pp. 222–229, 2000.

[79]X. Wang, T. Takano, and M. Nedergaard, “Astrocytic calcium signaling: mechanism and implications for functional brain imaging,” in *Dynamic Brain Imaging*, Springer, 2009, pp. 93–109.

[80]L. Venance, N. Stella, J. Glowinski, and C. Giaume, “Mechanism involved in initiation and propagation of receptor-induced intercellular calcium signaling in cultured rat astrocytes,” *J. Neurosci.*, vol. 17, no. 6, pp. 1981–1992, 1997.

[81]E. A. Nagelhus and O. P. Ottersen, “Physiological roles of aquaporin-4 in brain,” *Physiol. Rev.*, vol. 93, no. 4, pp. 1543–1562, 2013.

[82]B.-J. Jin, H. Zhang, D. K. Binder, and A. Verkman, “Aquaporin-4–dependent K+ and water transport modeled in brain extracellular space following neuroexcitation,” *J. Gen. Physiol.*, vol. 141, no. 1, pp. 119–132, 2013.

[83]R. G. Shulman and D. L. Rothman, *Brain energetics and neuronal activity: applications to fMRI and medicine*. John Wiley & Sons, 2005.

[84]A. Lau and M. Tymianski, “Glutamate receptors, neurotoxicity and neurodegeneration,” *Pflüg. Arch.-Eur. J. Physiol.*, vol. 460, no. 2, pp. 525–542, 2010.

[85]J. L. Crimins, A. Pooler, M. Polydoro, J. I. Luebke, and T. L. Spires-Jones, “The intersection of amyloid beta and tau in glutamatergic synaptic dysfunction and collapse in Alzheimer’s disease,” *Ageing Res. Rev.*, vol. 12, no. 3, pp. 757–763, 2013.

[86]J. A. Kemp, A. C. Foster, and E. H. Wong, “Non-competitive antagonists of excitatory amino acid receptors,” *Trends Neurosci.*, vol. 10, no. 7, pp. 294–298, 1987.

[87]P. Werner, D. Pitt, and C. S. Raine, “Multiple sclerosis: altered glutamate homeostasis in lesions correlates with oligodendrocyte and axonal damage,” *Ann. Neurol.*, vol. 50, no. 2, pp. 169–180, 2001.

[88]A. Mitani, Y. Andou, and K. Kataoka, “Selective vulnerability of hippocampal CA1 neurons cannot be explained in terms of an increase in glutamate concentration during ischemia in the gerbil: brain microdialysis study,” *Neuroscience*, vol. 48, no. 2, pp. 307–313, 1992.

[89]V. J. Majo, J. Prabhakaran, J. J. Mann, and J. D. Kumar, “PET and SPECT tracers for glutamate receptors,” *Drug Discov. Today*, vol. 18, no. 3, pp. 173–184, 2013.

[90]K. Cai *et al.*, “Magnetic resonance imaging of glutamate,” *Nat. Med.*, vol. 18, no. 2, pp. 302–306, 2012.

[91]R. Bartha *et al.*, “Measurement of Glutamate and Glutamine in the Medial Prefrontal Cortex of Never-Treated Schizophrenic Patients and Healthy Controls by Proton Magnetic Resonance Spectroscopy,” *Arch. Gen. Psychiatry*, vol. 54, no. 10, pp. 959–965, Oct. 1997.

[92]R. Crescenzi *et al.*, “In vivo measurement of glutamate loss is associated with synapse loss in a mouse model of tauopathy,” *Neuroimage*, vol. 101, pp. 185–192, 2014.

[93]R. G. González, J. A. Hirsch, W. Koroshetz, M. H. Lev, and P. W. Schaefer, *Acute ischemic stroke*. Springer, 2011.

[94]W. Smith and others, “Safety of mechanical thrombectomy and intravenous tissue plasminogen activator in acute ischemic stroke. Results of the multi Mechanical Embolus Removal in Cerebral Ischemia (MERCI) trial, part I,” *Am. J. Neuroradiol.*, vol. 27, no. 6, pp. 1177–1182, 2006.

[95]P. B. Gorelick and S. M. Weisman, “Risk of hemorrhagic stroke with aspirin use an update,” *Stroke*, vol. 36, no. 8, pp. 1801–1807, 2005.

[96]F. Chen and Y.-C. Ni, “Magnetic resonance diffusion-perfusion mismatch in acute ischemic stroke: An update,” *World J. Radiol.*, vol. 4, no. 3, p. 63, 2012.

[97]A. G. Sorensen *et al.*, “Hyperacute stroke: evaluation with combined multisection diffusion-weighted and hemodynamically weighted echo-planar MR imaging.,” *Radiology*, vol. 199, no. 2, pp. 391–401, 1996.

[98]S. Lee, D. Kim, E. Jeong, P. Yoon, S. Cha, and J. Lee, “Temporal changes in reversible cerebral ischemia on perfusion-and diffusion-weighted magnetic resonance imaging: the value of relative cerebral blood volume maps,” *Neuroradiology*, vol. 44, no. 2, pp. 103–108, 2002.

[99]C. Z. Simonsen, L. Røhl, P. Vestergaard-Poulsen, C. Gyldensted, G. Andersen, and L. Østergaard, “Final Infarct Size after Acute Stroke: Prediction with Flow Heterogeneity 1,” *Radiology*, vol. 225, no. 1, pp. 269–275, 2002.

[100]L. M. Hamberg *et al.*, “Functional CT perfusion imaging in predicting the extent of cerebral infarction from a 3-hour middle cerebral arterial occlusion in a primate stroke model,” *Am. J. Neuroradiol.*, vol. 23, no. 6, pp. 1013–1021, 2002.

[101]J. Fiehler *et al.*, “Cerebral Blood Flow Predicts Lesion Growth in Acute Stroke Patients,” *Stroke*, vol. 33, no. 10, pp. 2421–2425, Oct. 2002.

[102]M. Luby *et al.*, “Visual perfusion–diffusion mismatch is equivalent to quantitative mismatch,” *Stroke*, vol. 42, no. 4, pp. 1010–1014, 2011.

[103]B. C. Campbell *et al.*, “Visual assessment of perfusion-diffusion mismatch is inadequate to select patients for thrombolysis,” *Cerebrovasc. Dis.*, vol. 29, no. 6, pp. 592–596, 2010.

[104]N. Canal, L. Frattola, and S. Smirne, “The metabolism of cyclic-3 -5 -adenosine monophosphate (cAMP) in diseased muscle,” *J. Neurol.*, vol. 208, no. 4, pp. 259–265, 1975.

[105]P. Z. Sun, T. Benner, W. A. Copen, and A. G. Sorensen, “Early experience of translating pH-weighted MRI to image human subjects at 3 Tesla,” *Stroke*, vol. 41, no. 10 suppl 1, pp. S147–S151, 2010.

[106]R. Corbett, A. Laptook, and P. Weatherall, “Noninvasive measurements of human brain temperature using volume-localized proton magnetic resonance spectroscopy,” *J. Cereb. Blood Flow Metab.*, vol. 17, no. 4, pp. 363–369, 1997.

[107]S. Schwab, M. Spranger, A. Aschoff, T. Steiner, and W. Hacke, “Brain temperature monitoring and modulation in patients with severe MCA infarction,” *Neurology*, vol. 48, no. 3, pp. 762–767, 1997.

[108]B. Karaszewski *et al.*, “Early brain temperature elevation and anaerobic metabolism in human acute ischaemic stroke,” *Brain*, vol. 132, no. 4, pp. 955–964, 2009.

[109]W.-D. Heiss, “Ischemic Penumbra: Evidence From Functional Imaging in Man,” *J. Cereb. Blood Flow Metab.*, vol. 20, no. 9, pp. 1276–1293, 2000.

[110]J. V. Guadagno *et al.*, “The diffusion-weighted lesion in acute stroke: heterogeneous patterns of flow/metabolism uncoupling as assessed by quantitative positron emission tomography,” *Cerebrovasc. Dis.*, vol. 19, no. 4, pp. 239–246, 2005.

[111]W.-D. Heiss, R. Graf, and K. Wienhard, “Relevance of experimental ischemia in cats for stroke management: a comparative reevaluation,” *Cerebrovasc. Dis.*, vol. 11, no. 2, pp. 73–81, 2001.

[112] K. R. Lees *et al.*, “NXY-059 for acute ischemic stroke,” *N. Engl. J. Med.*, vol. 354, no. 6, pp. 588–600, 2006.

[113] H. Ehrenreich *et al.*, “Recombinant human erythropoietin in the treatment of acute ischemic stroke,” *Stroke*, vol. 40, no. 12, pp. e647–e656, 2009.

[114] S. M. Davis *et al.*, “Selfotel in acute ischemic stroke possible neurotoxic effects of an NMDA antagonist,” *Stroke*, vol. 31, no. 2, pp. 347–354, 2000.

[115] G. W. Albers, L. B. Goldstein, D. Hall, L. M. Lesko, A. A. S. Investigators, and others, “Aptiganel hydrochloride in acute ischemic stroke: a randomized controlled trial,” *Jama*, vol. 286, no. 21, pp. 2673–2682, 2001.

[116] R. L. Sacco *et al.*, “Glycine antagonist in neuroprotection for patients with acute stroke: GAIN Americas: a randomized controlled trial,” *JAMA*, vol. 285, no. 13, pp. 1719–1728, Apr. 2001.

[117] M. Jd and M. Jh, “The relationship among canine brain temperature, metabolism, and function during hypothermia.,” *Anesthesiology*, vol. 75, no. 1, pp. 130–136, 1991.

[118] J. V. Sarma and P. A. Ward, “The complement system,” *Cell Tissue Res.*, vol. 343, no. 1, pp. 227–235, Sep. 2010.

[119] J. Palace, I. Leite, and A. Jacob, “A practical guide to the treatment of neuromyelitis optica,” *Pract. Neurol.*, vol. 12, no. 4, pp. 209–214, Aug. 2012.

[120] M. A. Lana-Peixoto, “Devic’s neuromyelitis optica: a critical review,” *Arq. Neuropsiquiatr.*, vol. 66, no. 1, pp. 120–138, 2008.

[121] D. M. Wingerchuk, V. A. Lennon, S. J. Pittock, C. F. Lucchinetti, and B. G. Weinshenker, “Revised diagnostic criteria for neuromyelitis optica,” *Neurology*, vol. 66, no. 10, pp. 1485–1489, 2006.

[122] S.-H. Kim, W. Kim, X. F. Li, I.-J. Jung, and H. J. Kim, “Repeated treatment with rituximab based on the assessment of peripheral circulating memory B cells in patients with relapsing neuromyelitis optica over 2 years,” *Arch. Neurol.*, vol. 68, no. 11, pp. 1412–1420, Nov. 2011.

[123] R. C. Axtell, C. Raman, and L. Steinman, “Type I interferons: beneficial in Th1 and detrimental in Th17 autoimmunity,” *Clin. Rev. Allergy Immunol.*, vol. 44, no. 2, pp. 114–120, Apr. 2013.

[124] S. Saadoun, L. R. Bridges, A. S. Verkman, and M. C. Papadopoulos, “Paucity of natural killer and cytotoxic T cells in human neuromyelitis optica lesions,” *Neuroreport*, vol. 23, no. 18, pp. 1044–1047, Dec. 2012.

[125] S. Jarius *et al.*, “Mechanisms of disease: aquaporin-4 antibodies in neuromyelitis optica,” *Nat. Clin. Pract. Neurol.*, vol. 4, no. 4, pp. 202–214, Apr. 2008.

[126] S. Jarius *et al.*, “Cerebrospinal fluid antibodies to aquaporin-4 in neuromyelitis optica and related disorders: frequency, origin, and diagnostic relevance,” *J. Neuroinflammation*, vol. 7, p. 52, 2010.

[127] M. Varrin-Doyer *et al.*, “Aquaporin 4-specific T cells in neuromyelitis optica exhibit a Th17 bias and recognize Clostridium ABC transporter,” *Ann. Neurol.*, vol. 72, no. 1, pp. 53–64, Jul. 2012.

[128] M. Koga, T. Takahashi, M. Kawai, K. Fujihara, and T. Kanda, “A serological analysis of viral and bacterial infections associated with neuromyelitis optica,” *J. Neurol. Sci.*, vol. 300, no. 1–2, pp. 19–22, Jan. 2011.

[129] S. Nishiyama *et al.*, “A case of NMO seropositive for aquaporin-4 antibody more than 10 years before onset,” *Neurology*, vol. 72, no. 22, pp. 1960–1961, Jun. 2009.

[130] S. Mader *et al.*, “Complement activating antibodies to myelin oligodendrocyte glycoprotein in neuromyelitis optica and related disorders,” *J. Neuroinflammation*, vol. 8, p. 184, Dec. 2011.

[131] J. M. Crane, C. Lam, A. Rossi, T. Gupta, J. L. Bennett, and A. S. Verkman, “Binding affinity and specificity of neuromyelitis optica autoantibodies to aquaporin-4 M1/M23 isoforms and orthogonal arrays,” *J. Biol. Chem.*, vol. 286, no. 18, pp. 16516–16524, May 2011.

[132] G. P. Nicchia *et al.*, “Aquaporin-4 orthogonal arrays of particles are the target for neuromyelitis optica autoantibodies,” *Glia*, vol. 57, no. 13, pp. 1363–1373, Oct. 2009.

[133] S. R. Hinson *et al.*, “Molecular outcomes of neuromyelitis optica (NMO)-IgG binding to aquaporin-4 in astrocytes,” *Proc. Natl. Acad. Sci.*, vol. 109, no. 4, pp. 1245–1250, Jan. 2012.

[134] P. J. Waters *et al.*, “Serologic diagnosis of NMO,” *Neurology*, vol. 78, no. 9, pp. 665–671, Feb. 2012.

[135] C. Trebst *et al.*, “Update on the diagnosis and treatment of neuromyelitis optica: recommendations of the Neuromyelitis Optica Study Group (NEMOS),” *J. Neurol.*, vol. 261, no. 1, pp. 1–16, Jan. 2014.

[136] D. J. Kimbrough *et al.*, “Treatment of Neuromyelitis Optica: Review and Recommendations,” *Mult. Scler. Relat. Disord.*, vol. 1, no. 4, pp. 180–187, Oct. 2012.

[137] P. J. Barnes, “Corticosteroids: the drugs to beat,” *Eur. J. Pharmacol.*, vol. 533, no. 1–3, pp. 2–14, Mar. 2006.

[138] N. Muls *et al.*, “Upregulation of IL-17, but not of IL-9, in circulating cells of CIS and relapsing MS patients. Impact of corticosteroid therapy on the cytokine network,” *J. Neuroimmunol.*, vol. 243, no. 1–2, pp. 73–80, Feb. 2012.

[139] H. M. Reeves and J. L. Winters, “The mechanisms of action of plasma exchange,” *Br. J. Haematol.*, vol. 164, no. 3, pp. 342–351, Feb. 2014.

[140] M. Bonnan and P. Cabre, “Plasma Exchange in Severe Attacks of Neuromyelitis Optica,” *Mult. Scler. Int.*, vol. 2012, p. e787630, Feb. 2012.

[141] M. Bonnan, R. Valentino, S. Olindo, H. Mehdaoui, D. Smadja, and P. Cabre, “Plasma exchange in severe spinal attacks associated with neuromyelitis optica spectrum disorder,” *Mult. Scler. Houndmills Basingstoke Engl.*, vol. 15, no. 4, pp. 487–492, Apr. 2009.

[142] C. Costanzi *et al.*, “Azathioprine: tolerability, efficacy, and predictors of benefit in neuromyelitis optica,” *Neurology*, vol. 77, no. 7, pp. 659–666, Aug. 2011.

[143] A. Jacob *et al.*, “Treatment of Neuromyelitis Optica With Mycophenolate Mofetil: Retrospective Analysis of 24 Patients,” *Arch. Neurol.*, vol. 66, no. 9, pp. 1128–1133, Sep. 2009.

[144] G. S. Bedi, A. D. Brown, S. R. Delgado, N. Usmani, B. L. Lam, and W. A. Sheremata, “Impact of rituximab on relapse rate and disability in neuromyelitis optica,” *Mult. Scler. Houndmills Basingstoke Engl.*, vol. 17, no. 10, pp. 1225–1230, Oct. 2011.

[145] J. Kitley *et al.*, “Prognostic factors and disease course in aquaporin-4 antibody-positive patients with neuromyelitis optica spectrum disorder from the United Kingdom and Japan,” *Brain J. Neurol.*, vol. 135, no. Pt 6, pp. 1834–1849, Jun. 2012.

[146] S.-H. Kim, W. Kim, M. S. Park, E. H. Sohn, X. F. Li, and H. J. Kim, “Efficacy and safety of mitoxantrone in patients with highly relapsing neuromyelitis optica,” *Arch. Neurol.*, vol. 68, no. 4, pp. 473–479, Apr. 2011.

[147] D. B. Bichuetti, E. M. Lobato de Oliveira, D. M. Oliveira, N. Amorin de Souza, and A. A. Gabbai, “Neuromyelitis optica treatment: analysis of 36 patients,” *Arch. Neurol.*, vol. 67, no. 9, pp. 1131–1136, Sep. 2010.

[148] S. J. Pittock *et al.*, “Eculizumab in AQP4-IgG-positive relapsing neuromyelitis optica spectrum disorders: an open-label pilot study,” *Lancet Neurol.*, vol. 12, no. 6, pp. 554–562, Jun. 2013.

[149] M. Araki *et al.*, “Efficacy of the anti–IL-6 receptor antibody tocilizumab in neuromyelitis optica,” *Neurology*, vol. 82, no. 15, pp. 1302–1306, Apr. 2014.

[150] I. Ayzenberg *et al.*, “Interleukin 6 receptor blockade in patients with neuromyelitis optica nonresponsive to anti-CD20 therapy,” *JAMA Neurol.*, vol. 70, no. 3, pp. 394–397, Mar. 2013.

[151] B. C. Kieseier *et al.*, “Disease amelioration with tocilizumab in a treatment-resistant patient with neuromyelitis optica: implication for cellular immune responses,” *JAMA Neurol.*, vol. 70, no. 3, pp. 390–393, Mar. 2013.

[152] K. Iwata *et al.*, “Effect of neutrophil elastase inhibitor (sivelestat sodium) in the treatment of acute lung injury (ALI) and acute respiratory distress syndrome (ARDS): a systematic review and meta-analysis,” *Intern. Med. Tokyo Jpn.*, vol. 49, no. 22, pp. 2423–2432, 2010.

[153] R. E. Young *et al.*, “Neutrophil elastase (NE)-deficient mice demonstrate a nonredundant role for NE in neutrophil migration, generation of proinflammatory mediators, and phagocytosis in response to zymosan particles in vivo,” *J. Immunol. Baltim. Md 1950*, vol. 172, no. 7, pp. 4493–4502, Apr. 2004.

[154] V. Papayannopoulos, K. D. Metzler, A. Hakkim, and A. Zychlinsky, “Neutrophil elastase and myeloperoxidase regulate the formation of neutrophil extracellular traps,” *J. Cell Biol.*, vol. 191, no. 3, pp. 677–691, Nov. 2010.

[155] H. Zhang and A. S. Verkman, “Eosinophil pathogenicity mechanisms and therapeutics in neuromyelitis optica,” *J. Clin. Invest.*, vol. 123, no. 5, pp. 2306–2316, May 2013.

[156] P. Imbach *et al.*, "High-dose intravenous gammaglobulin for idiopathic thrombocytopenic purpura in childhood," *Lancet Lond. Engl.*, vol. 1, no. 8232, pp. 1228–1231, Jun. 1981.

[157] M. J. Magraner, F. Coret, and B. Casanova, "The effect of intravenous immunoglobulin on neuromyelitis optica," *Neurol. Barc. Spain*, vol. 28, no. 2, pp. 65–72, Mar. 2013.

[158] L. Tradtrantip *et al.*, "Anti-aquaporin-4 monoclonal antibody blocker therapy for neuromyelitis optica," *Ann. Neurol.*, vol. 71, no. 3, pp. 314–322, Mar. 2012.

[159] L. Tradtrantip *et al.*, "Small-molecule inhibitors of NMO-IgG binding to aquaporin-4 reduce astrocyte cytotoxicity in neuromyelitis optica," *FASEB J. Off. Publ. Fed. Am. Soc. Exp. Biol.*, vol. 26, no. 5, pp. 2197–2208, May 2012.

[160] P.-W. Phuan *et al.*, "C1q-targeted monoclonal antibody prevents complement-dependent cytotoxicity and neuropathology in in vitro and mouse models of neuromyelitis optica," *Acta Neuropathol. (Berl.)*, vol. 125, no. 6, pp. 829–840, Jun. 2013.

[161] L. Tradtrantip, N. Asavapanumas, and A. S. Verkman, "Therapeutic Cleavage of Anti–Aquaporin-4 Autoantibody in Neuromyelitis Optica by an IgG-Selective Proteinase," *Mol. Pharmacol.*, vol. 83, no. 6, pp. 1268–1275, Jun. 2013.

[162] L. A. Lewis and S. Ram, "Meningococcal disease and the complement system," *Virulence*, vol. 5, no. 1, pp. 98–126, Jan. 2014.

[163] N. Asavapanumas, J. Ratelade, M. C. Papadopoulos, J. L. Bennett, M. H. Levin, and A. S. Verkman, "Experimental mouse model of optic neuritis with inflammatory demyelination produced by passive transfer of neuromyelitis optica-immunoglobulin G," *J. Neuroinflammation*, vol. 11, p. 16, 2014.

[164] H. Zhang and A. S. Verkman, "Longitudinally extensive NMO spinal cord pathology produced by passive transfer of NMO-IgG in mice lacking complement inhibitor CD59," *J. Autoimmun.*, vol. 53, pp. 67–77, Sep. 2014.

[165] S. A. Rollins, J. Zhao, H. Ninomiya, and P. J. Sims, "Inhibition of homologous complement by CD59 is mediated by a species-selective recognition conferred through binding to C8 within C5b-8 or C9 within C5b-9," *J. Immunol. Baltim. Md 1950*, vol. 146, no. 7, pp. 2345–2351, Apr. 1991.

[166] J. Ratelade, H. Zhang, S. Saadoun, J. L. Bennett, M. C. Papadopoulos, and A. S. Verkman, "Neuromyelitis optica IgG and natural killer cells produce NMO lesions in mice without myelin loss," *Acta Neuropathol. (Berl.)*, vol. 123, no. 6, pp. 861–872, Jun. 2012.

[167] J. Ratelade, N. Asavapanumas, A. M. Ritchie, S. Wemlinger, J. L. Bennett, and A. S. Verkman, "Involvement of antibody-dependent cell-mediated cytotoxicity in inflammatory demyelination in a mouse model of neuromyelitis optica," *Acta Neuropathol. (Berl.)*, vol. 126, no. 5, pp. 699–709, Nov. 2013.

[168] T. Hosokawa *et al.*, "Increased serum matrix metalloproteinase-9 in neuromyelitis optica: implication of disruption of blood-brain barrier," *J. Neuroimmunol.*, vol. 236, no. 1–2, pp. 81–86, Jul. 2011.

[169] M. M. Bakhuraysah, C. Siatskas, and S. Petratos, "Hematopoietic stem cell transplantation for multiple sclerosis: is it a clinical reality?," *Stem Cell Res. Ther.*, vol. 7, no. 1, Dec. 2016.

[170] G. G. Illei *et al.*, "Current state and future directions of autologous hematopoietic stem cell transplantation in systemic lupus erythematosus," *Ann. Rheum. Dis.*, vol. 70, no. 12, pp. 2071–2074, Dec. 2011.

[171] J. L. Cash, L. V. Norling, and M. Perretti, "Resolution of inflammation: targeting GPCRs that interact with lipids and peptides," *Drug Discov. Today*, vol. 19, no. 8, pp. 1186–1192, Aug. 2014.

[172] V. Wittamer, B. Bondue, A. Guillabert, G. Vassart, M. Parmentier, and D. Communi, "Neutrophil-mediated maturation of chemerin: a link between innate and adaptive immunity," *J. Immunol. Baltim. Md 1950*, vol. 175, no. 1, pp. 487–493, Jul. 2005.

[173] B. A. Zabel *et al.*, "Chemerin activation by serine proteases of the coagulation, fibrinolytic, and inflammatory cascades," *J. Biol. Chem.*, vol. 280, no. 41, pp. 34661–34666, Oct. 2005.

[174] B. A. Zabel, A. M. Silverio, and E. C. Butcher, "Chemokine-like receptor 1 expression and chemerin-directed chemotaxis distinguish plasmacytoid from myeloid dendritic cells in human blood," *J. Immunol. Baltim. Md 1950*, vol. 174, no. 1, pp. 244–251, Jan. 2005.

[175] C. Odaka, T. Mizuochi, J. Yang, and A. Ding, "Murine macrophages produce secretory leukocyte protease inhibitor during clearance of apoptotic cells: implications for resolution of the inflammatory response," *J. Immunol. Baltim. Md 1950*, vol. 171, no. 3, pp. 1507–1514, Aug. 2003.

[176] C. Bandeira-Melo *et al.*, “Cyclooxygenase-2-derived prostaglandin E2 and lipoxin A4 accelerate resolution of allergic edema in Angiostrongylus costaricensis-infected rats: relationship with concurrent eosinophilia,” *J. Immunol. Baltim. Md 1950*, vol. 164, no. 2, pp. 1029–1036, Jan. 2000.

[177] S. F. Oh, M. Dona, G. Fredman, S. Krishnamoorthy, D. Irimia, and C. N. Serhan, “Resolvin E2 formation and impact in inflammation resolution,” *J. Immunol. Baltim. Md 1950*, vol. 188, no. 9, pp. 4527–4534, May 2012.

[178] J. M. Schwab, N. Chiang, M. Arita, and C. N. Serhan, “Resolvin E1 and protectin D1 activate inflammation-resolution programmes,” *Nature*, vol. 447, no. 7146, pp. 869–874, Jun. 2007.

[179] M. Spite *et al.*, “Resolvin D2 is a potent regulator of leukocytes and controls microbial sepsis,” *Nature*, vol. 461, no. 7268, pp. 1287–1291, Oct. 2009.

[180] H. Seki *et al.*, “The anti-inflammatory and proresolving mediator resolvin E1 protects mice from bacterial pneumonia and acute lung injury,” *J. Immunol. Baltim. Md 1950*, vol. 184, no. 2, pp. 836–843, Jan. 2010.

[181] C. D. Palmer, C. J. Mancuso, J. P. Weiss, C. N. Serhan, E. C. Guinan, and O. Levy, “17(R)-Resolvin D1 differentially regulates TLR4-mediated responses of primary human macrophages to purified LPS and live E. coli,” *J. Leukoc. Biol.*, vol. 90, no. 3, pp. 459–470, Sep. 2011.

[182] J. L. Cash, A. R. Christian, and D. R. Greaves, “Chemerin peptides promote phagocytosis in a ChemR23- and Syk-dependent manner,” *J. Immunol. Baltim. Md 1950*, vol. 184, no. 9, pp. 5315–5324, May 2010.

[183] V. Wittamer *et al.*, “Specific recruitment of antigen-presenting cells by chemerin, a novel processed ligand from human inflammatory fluids,” *J. Exp. Med.*, vol. 198, no. 7, pp. 977–985, Oct. 2003.

[184] M. Arita, T. Ohira, Y.-P. Sun, S. Elangovan, N. Chiang, and C. N. Serhan, “Resolvin E1 selectively interacts with leukotriene B4 receptor BLT1 and ChemR23 to regulate inflammation,” *J. Immunol. Baltim. Md 1950*, vol. 178, no. 6, pp. 3912–3917, Mar. 2007.

[185] J. Hardy and D. J. Selkoe, “The Amyloid Hypothesis of Alzheimer9s Disease: Progress and Problems on the Road to Therapeutics,” *Science*, vol. 297, no. 5580, pp. 353–356, Jul. 2002.

[186] F. G. Miller and H. Brody, “What Makes Placebo-Controlled Trials Unethical?,” *Am. J. Bioeth.*, vol. 2, no. 2, pp. 3–9, Mar. 2002.

[187] C. F. Craver, “Physical law and mechanistic explanation in the Hodgkin and Huxley model of the action potential,” *Philos. Sci.*, vol. 75, no. 5, pp. 1022–1033, 2008.

[188] J. Bogen, “Regularities and causality; generalizations and causal explanations,” *Stud. Hist. Philos. Sci. Part C Stud. Hist. Philos. Biol. Biomed. Sci.*, vol. 36, no. 2, pp. 397–420, Jun. 2005.

[189] J. Gunawardena, “Models in biology: ‘accurate descriptions of our pathetic thinking,’” *BMC Biol.*, vol. 12, p. 29, Apr. 2014.

[190] V. Chelliah *et al.*, “BioModels: ten-year anniversary,” *Nucleic Acids Res.*, vol. 43, no. D1, pp. D542–D548, Jan. 2015.

[191] P. Hunter *et al.*, “A vision and strategy for the virtual physiological human: 2012 update,” *Interface Focus*, vol. 3, no. 2, p. 20130004, Apr. 2013.

[192] K. S. Brown and J. P. Sethna, “Statistical mechanical approaches to models with many poorly known parameters,” *Phys. Rev. E*, vol. 68, no. 2, p. 21904, 2003.

[193] R. N. Gutenkunst, J. J. Waterfall, F. P. Casey, K. S. Brown, C. R. Myers, and J. P. Sethna, “Universally Sloppy Parameter Sensitivities in Systems Biology Models,” *PLOS Comput. Biol.*, vol. 3, no. 10, p. e189, Oct. 2007.

[194] J. F. Apgar, D. K. Witmer, F. M. White, and B. Tidor, “Sloppy models, parameter uncertainty, and the role of experimental design,” *Mol. Biosyst.*, vol. 6, no. 10, pp. 1890–1900, Oct. 2010.

[195] J. L. Stobart and C. M. Anderson, “Multifunctional role of astrocytes as gatekeepers of neuronal energy supply,” *Front. Cell. Neurosci.*, vol. 7, 2013.

[196] A. Aubert and R. Costalat, “A model of the coupling between brain electrical activity, metabolism, and hemodynamics: application to the interpretation of functional neuroimaging,” *Neuroimage*, vol. 17, no. 3, pp. 1162–1181, 2002.

[197] A. Aubert and R. Costalat, “Interaction between Astrocytes and Neurons Studied using a Mathematical Model of Compartmentalized Energy Metabolism,” *J. Cereb. Blood Flow Metab.*, vol. 25, no. 11, pp. 1476–1490, Nov. 2005.

[198] R. Heinrich and S. Schuster, *The Regulation of Cellular Systems*. Springer Science & Business Media, 2012.

[199] M. DiNuzzo, S. Mangia, B. Maraviglia, and F. Giove, "Changes in Glucose Uptake Rather than Lactate Shuttle Take Center Stage in Subserving Neuroenergetics: Evidence from Mathematical Modeling," *J. Cereb. Blood Flow Metab.*, vol. 30, no. 3, pp. 586–602, Mar. 2010.

[200] M. Cloutier, F. B. Bolger, J. P. Lowry, and P. Wellstead, "An integrative dynamic model of brain energy metabolism using in vivo neurochemical measurements," *J. Comput. Neurosci.*, vol. 27, no. 3, pp. 391–414, 2009.

[201] T. Çakır, S. Alsan, H. Saybaşılı, A. Akın, and K. Ö. Ülgen, "Reconstruction and flux analysis of coupling between metabolic pathways of astrocytes and neurons: application to cerebral hypoxia," *Theor. Biol. Med. Model.*, vol. 4, p. 48, 2007.

[202] R. Occhipinti, E. Somersalo, and D. Calvetti, "Energetics of inhibition: insights with a computational model of the human GABAergic neuron–astrocyte cellular complex," *J. Cereb. Blood Flow Metab.*, vol. 30, no. 11, pp. 1834–1846, Nov. 2010.

[203] T. Cakir, S. Alsan, H. Saybaşili, A. Akin, and K. O. Ulgen, "Reconstruction and flux analysis of coupling between metabolic pathways of astrocytes and neurons: application to cerebral hypoxia," *Theor. Biol. Med. Model.*, vol. 4, p. 48, Dec. 2007.

[204] C. M. Armstrong, "The Na/K pump, Cl ion, and osmotic stabilization of cells," *Proc. Natl. Acad. Sci.*, vol. 100, no. 10, pp. 6257–6262, May 2003.

[205] K. A. DeBruin and W. Krassowska, "Modeling electroporation in a single cell. I. Effects Of field strength and rest potential," *Biophys. J.*, vol. 77, no. 3, pp. 1213–1224, Sep. 1999.

[206] L. Endresen, K. Hall, J. Høye, and J. Myrheim, "A theory for the membrane potential of living cells," *Eur. Biophys. J.*, vol. 29, no. 2, pp. 90–103, 2000.

[207] J. Malmivuo and R. Plonsey, *Bioelectromagnetism: Principles and Applications of Bioelectric and Biomagnetic Fields*. Oxford University Press, 1995.

[208] D. C. Sterratt, "Goldman-Hodgkin-Katz Equations," in *Encyclopedia of Computational Neuroscience*, D. Jaeger and R. Jung, Eds. Springer New York, 2015, pp. 1300–1302.

[209] D. J. Rossi, T. Oshima, and D. Attwell, "Glutamate release in severe brain ischaemia is mainly by reversed uptake," *Nature*, vol. 403, no. 6767, pp. 316–321, 2000.

[210] A. N. Katchman and N. Hershkowitz, "Early anoxia-induced vesicular glutamate release results from mobilization of calcium from intracellular stores," *J. Neurophysiol.*, vol. 70, no. 1, pp. 1–7, Jul. 1993.

[211] C. E. Gross, M. M. Bednar, D. B. Howard, and M. B. Sporn, "Transforming growth factor-beta 1 reduces infarct size after experimental cerebral ischemia in a rabbit model.," *Stroke*, vol. 24, no. 4, pp. 558–562, Apr. 1993.

[212] V. Parpura, T. A. Basarsky, F. Liu, K. Jeftinija, S. Jeftinija, and P. G. Haydon, "Glutamate-mediated astrocyte-neuron signalling," *Nature*, vol. 369, no. 6483, pp. 744–747, Jun. 1994.

[213] T. D. Hassinger *et al.*, "Evidence for glutamate-mediated activation of hippocampal neurons by glial calcium waves," *J. Neurobiol.*, vol. 28, no. 2, pp. 159–170, Oct. 1995.

[214] P. Bezzi *et al.*, "Prostaglandins stimulate calcium-dependent glutamate release in astrocytes," *Nature*, vol. 391, no. 6664, pp. 281–285, Jan. 1998.

[215] M. Szatkowski, B. Barbour, and D. Attwell, "Non-vesicular release of glutamate from glial cells by reversed electrogenic glutamate uptake," *Nature*, vol. 348, no. 6300, pp. 443–446, Nov. 1990.

[216] M. Szatkowski, B. Barbour, and D. Attwell, "The potassium-dependence of excitatory amino acid transport: resolution of a paradox," *Brain Res.*, vol. 555, no. 2, pp. 343–345, Aug. 1991.

[217] B. Granseth, B. Odermatt, S. J. Royle, and L. Lagnado, "Clathrin-Mediated Endocytosis Is the Dominant Mechanism of Vesicle Retrieval at Hippocampal Synapses," *Neuron*, vol. 51, no. 6, pp. 773–786, Sep. 2006.

[218] N. Axmacher, M. Stemmler, D. Engel, A. Draguhn, and R. Ritz, "Transmitter Metabolism as a Mechanism of Synaptic Plasticity: A Modeling Study," *J. Neurophysiol.*, vol. 91, no. 1, pp. 25–39, Jan. 2004.

[219] C. Heinemann, L. von Rüden, R. H. Chow, and E. Neher, "A two-step model of secretion control in neuroendocrine cells," *Pflüg. Arch.*, vol. 424, no. 2, pp. 105–112, Jul. 1993.

[220] S. Weis, R. Schneggenburger, and E. Neher, “Properties of a Model of Ca++-Dependent Vesicle Pool Dynamics and Short Term Synaptic Depression,” *Biophys. J.*, vol. 77, no. 5, pp. 2418–2429, Nov. 1999.

[221] J. Trommershäuser, R. Schneggenburger, A. Zippelius, and E. Neher, “Heterogeneous Presynaptic Release Probabilities: Functional Relevance for Short-Term Plasticity,” *Biophys. J.*, vol. 84, no. 3, pp. 1563–1579, Mar. 2003.

[222] D. R. Stevens, C. Schirra, U. Becherer, and J. Rettig, “Vesicle pools: lessons from adrenal chromaffin cells,” *Front. Synaptic Neurosci.*, vol. 3, p. 2, 2011.

[223] T. Voets, “Dissection of three Ca2+-dependent steps leading to secretion in chromaffin cells from mouse adrenal slices,” *Neuron*, vol. 28, no. 2, pp. 537–545, Nov. 2000.

[224] M. Geppert *et al.*, “Synaptotagmin I: a major Ca2+ sensor for transmitter release at a central synapse,” *Cell*, vol. 79, no. 4, pp. 717–727, Nov. 1994.

[225] S. Nadkarni, T. M. Bartol, T. J. Sejnowski, and H. Levine, “Modelling Vesicular Release at Hippocampal Synapses,” *PLOS Comput. Biol.*, vol. 6, no. 11, p. e1000983, Nov. 2010.

[226] A. M. Walter, P. S. Pinheiro, M. Verhage, and J. B. Sørensen, “A Sequential Vesicle Pool Model with a Single Release Sensor and a Ca2+-Dependent Priming Catalyst Effectively Explains Ca2+-Dependent Properties of Neurosecretion,” *PLoS Comput. Biol.*, vol. 9, no. 12, Dec. 2013.

[227] D. R. Lemieux, J. Beaumont, and F. A. Roberge, “A mechanistic action potential model of the guinea-pig cardiac myocyte,” *J. Mol. Cell. Cardiol.*, vol. 23, p. S100, 1991.

[228] P. K. Stys and R. M. LoPachin, “Mechanisms of calcium and sodium fluxes in anoxic myelinated central nervous system axons,” *Neuroscience*, vol. 82, no. 1, pp. 21–32, Sep. 1997.

[229] I. A. Silver, J. Deas, and M. Erecińska, “Ion homeostasis in brain cells: differences in intracellular ion responses to energy limitation between cultured neurons and glial cells,” *Neuroscience*, vol. 78, no. 2, pp. 589–601, Mar. 1997.

[230] H. B. Verheul *et al.*, “Comparison of diffusion-weighted MRI with changes in cell volume in a rat model of brain injury,” *NMR Biomed.*, vol. 7, no. 1–2, pp. 96–100, Mar. 1994.

[231] J. Ruiz-Ederra, H. Zhang, and A. S. Verkman, “Evidence against Functional Interaction between Aquaporin-4 Water Channels and Kir4.1 Potassium Channels in Retinal Müller Cells,” *J. Biol. Chem.*, vol. 282, no. 30, pp. 21866–21872, Jul. 2007.

[232] S. Murakami and Y. Kurachi, “Mechanisms of astrocytic K+ clearance and swelling under high extracellular K+ concentrations,” *J. Physiol. Sci.*, vol. 66, no. 2, pp. 127–142, Mar. 2016.

[233] A. S. Filippidis, M. Y. S. Kalani, and H. L. Rekate, “Hydrocephalus and aquaporins: the role of aquaporin-4,” *Acta Neurochir. Suppl.*, vol. 113, pp. 55–58, 2012.

[234] I. Kumagai and K. Tsumoto, “Antigen-antibody binding,” *Encycl. Life Sci.*, pp. 1–7, 2010.

[235] H. Hirayama, K. Yoshii, H. Ojima, N. Kawai, S. Gotoh, and Y. Fukuyama, “Linear systems analysis of activating processes of complement system as a defense mechanism,” *Biosystems*, vol. 39, no. 3, pp. 173–185, 1996.

[236] A. A. Korotaevskiy, L. G. Hanin, and M. A. Khanin, “Non-linear dynamics of the complement system activation,” *Math. Biosci.*, vol. 222, no. 2, pp. 127–143, 2009.

[237] A. P. van Dam *et al.*, “Complement-mediated serum sensitivity among spirochetes that cause Lyme disease.,” *Infect. Immun.*, vol. 65, no. 4, pp. 1228–1236, Apr. 1997.

[238] B. Liu *et al.*, “A computational and experimental study of the regulatory mechanisms of the complement system,” *PLoS Comput Biol*, vol. 7, no. 1, p. e1001059, 2011.

[239] J. Zhang *et al.*, “Local Inflammation Induces Complement Crosstalk Which Amplifies the Antimicrobial Response,” *PLOS Pathog.*, vol. 5, no. 1, p. e1000282, Jan. 2009.

[240] C. N. Serhan and J. Savill, “Resolution of inflammation: the beginning programs the end,” *Nat. Immunol.*, vol. 6, no. 12, pp. 1191–1197, Dec. 2005.

[241] T. A. Butterfield, T. M. Best, and M. A. Merrick, “The Dual Roles of Neutrophils and Macrophages in Inflammation: A Critical Balance Between Tissue Damage and Repair,” *J. Athl. Train.*, vol. 41, no. 4, pp. 457–465, 2006.

[242] S. A. Eming, T. Krieg, and J. M. Davidson, “Inflammation in wound repair: molecular and cellular mechanisms,” *J. Invest. Dermatol.*, vol. 127, no. 3, pp. 514–525, Mar. 2007.

[243] C. N. Serhan *et al.*, “Resolution of inflammation: state of the art, definitions and terms,” *FASEB J.*, vol. 21, no. 2, pp. 325–332, Feb. 2007.

[244] S. Kobayashi *et al.*, "Interaction of oxidative stress and inflammatory response in coronary plaque instability: important role of C-reactive protein," *Arterioscler. Thromb. Vasc. Biol.*, vol. 23, no. 8, pp. 1398–1404, Aug. 2003.

[245] T. Lawrence and D. W. Gilroy, "Chronic inflammation: a failure of resolution?," *Int. J. Exp. Pathol.*, vol. 88, no. 2, pp. 85–94, Apr. 2007.

[246] D. A. Lauffenburger and C. R. Kennedy, "Analysis of a lumped model for tissue inflammation dynamics," *Math. Biosci.*, vol. 53, no. 3, pp. 189–221, 1981.

[247] D. A. Lauffenburger and C. R. Kennedy, "Localized bacterial infection in a distributed model for tissue inflammation," *J. Math. Biol.*, vol. 16, no. 2, pp. 141–163, 1983.

[248] R. Kumar, G. Clermont, Y. Vodovotz, and C. C. Chow, "The dynamics of acute inflammation," *J. Theor. Biol.*, vol. 230, no. 2, pp. 145–155, Sep. 2004.

[249] A. Reynolds, J. Rubin, G. Clermont, J. Day, Y. Vodovotz, and G. B. Ermentrout, "A reduced mathematical model of the acute inflammatory response: I. Derivation of model and analysis of anti-inflammation," *J. Theor. Biol.*, vol. 242, no. 1, pp. 220–236, 2006.

[250] Y. Vodovotz, G. Clermont, C. Chow, and G. An, "Mathematical models of the acute inflammatory response," *Curr. Opin. Crit. Care*, vol. 10, no. 5, pp. 383–390, Oct. 2004.

[251] A. M. Smith, J. A. McCullers, and F. R. Adler, "Mathematical model of a three-stage innate immune response to a pneumococcal lung infection," *J. Theor. Biol.*, vol. 276, no. 1, pp. 106–116, 2011.

[252] J. Dunster, H. Byrne, and J. King, "The resolution of inflammation: a mathematical model of neutrophil and macrophage interactions," *Bull. Math. Biol.*, vol. 76, no. 8, pp. 1953–1980, 2014.

[253] C. Akgul, D. A. Moulding, and S. W. Edwards, "Molecular control of neutrophil apoptosis," *FEBS Lett.*, vol. 487, no. 3, pp. 318–322, Jan. 2001.

[254] A. G. Rossi and D. A. Sawatsky, "The resolution of inflammation," *Inflammopharmacology*, vol. 16, no. 2, pp. 100–102, 2008.

[255] A. Lee, M. K. Whyte, and C. Haslett, "Inhibition of apoptosis and prolongation of neutrophil functional longevity by inflammatory mediators," *J. Leukoc. Biol.*, vol. 54, no. 4, pp. 283–288, Oct. 1993.

[256] C. M. Lloyd, M. D. Halstead, and P. F. Nielsen, "CellML: its future, present and past," *Prog. Biophys. Mol. Biol.*, vol. 85, no. 2, pp. 433–450, 2004.

[257] H. Schmidt and M. Jirstrand, "Systems Biology Toolbox for MATLAB: a computational platform for research in systems biology," *Bioinformatics*, vol. 22, no. 4, pp. 514–515, 2006.

[258] R. Serban and A. C. Hindmarsh, "CVODES: An ODE solver with sensitivity analysis capabilities," Technical Report UCRL-JP-200039, Lawrence Livermore National Laboratory, 2003.

[259] T. Sumner, E. Shephard, and I. D. L. Bogle, "A methodology for global-sensitivity analysis of time-dependent outputs in systems biology modelling," *J. R. Soc. Interface*, vol. 9, no. 74, pp. 2156–2166, Sep. 2012.

[260] A. Saltelli, K. Chan, E. M. Scott, and others, *Sensitivity analysis*, vol. 1. Wiley New York, 2000.

[261] S. Tarantola and W. Becker, "SIMLAB Software for Uncertainty and Sensitivity Analysis," 2015.

[262] M. Schmidt and H. Lipson, "Distilling free-form natural laws from experimental data," *science*, vol. 324, no. 5923, pp. 81–85, 2009.

[263] D. Whitley, S. Rana, and R. B. Heckendorn, "The island model genetic algorithm: On separability, population size and convergence," *J. Comput. Inf. Technol.*, vol. 7, pp. 33–48, 1999.

[264] S. W. Mahfoud, "Niching methods for genetic algorithms," *Urbana*, vol. 51, no. 95001, pp. 62–94, 1995.

[265] M. Schmidt and H. Lipson, "Age-Fitness Pareto Optimization," in *Genetic Programming Theory and Practice VIII*, R. Riolo, T. McConaghy, and E. Vladislavleva, Eds. Springer New York, 2011, pp. 129–146.

[266] M. Canavan, G. N. Mhaille, and E. C. Mulkerrin, "Development of acute stroke units—a cost effective reconfiguration which benefits patients," *QJM*, vol. 105, no. 1, pp. 99–102, Jan. 2012.

[267] R. W. V. Flynn, R. S. M. MacWalter, and A. S. F. Doney, "The cost of cerebral ischaemia," *Neuropharmacology*, vol. 55, no. 3, pp. 250–256, Sep. 2008.

[268] U. Dirnagl, C. Iadecola, and M. A. Moskowitz, "Pathobiology of ischaemic stroke: an integrated view," *Trends Neurosci.*, vol. 22, no. 9, pp. 391–397, Sep. 1999.

[269] W. Hacke *et al.*, “Association of outcome with early stroke treatment: pooled analysis of ATLANTIS, ECASS, and NINDS rt-PA stroke trials,” *Lancet Lond. Engl.*, vol. 363, no. 9411, pp. 768–774, Mar. 2004.

[270] K. A. Hossmann, S. Sakaki, and V. Zimmerman, “Cation activities in reversible ischemia of the cat brain,” *Stroke*, vol. 8, no. 1, pp. 77–81, Feb. 1977.

[271] T. C. Sudhof, “The synaptic vesicle cycle,” *Annu. Rev. Neurosci.*, vol. 27, pp. 509–547, 2004.

[272] S. Karunanithi, L. Marin, K. Wong, and H. L. Atwood, “Quantal size and variation determined by vesicle size in normal and mutant Drosophila glutamatergic synapses,” *J. Neurosci. Off. J. Soc. Neurosci.*, vol. 22, no. 23, pp. 10267–10276, Dec. 2002.

[273] L. He and L.-G. Wu, “The debate on the kiss-and-run fusion at synapses,” *Trends Neurosci.*, vol. 30, no. 9, pp. 447–455, Sep. 2007.

[274] B. Granseth and L. Lagnado, “The role of endocytosis in regulating the strength of hippocampal synapses,” *J. Physiol.*, vol. 586, no. 24, pp. 5969–5982, Dec. 2008.

[275] L.-Y. Wang, E. Neher, and H. Taschenberger, “Synaptic vesicles in mature calyx of Held synapses sense higher nanodomain calcium concentrations during action potential-evoked glutamate release,” *J. Neurosci. Off. J. Soc. Neurosci.*, vol. 28, no. 53, pp. 14450–14458, Dec. 2008.

[276] J. D. Clements, “Transmitter timecourse in the synaptic cleft: its role in central synaptic function,” *Trends Neurosci.*, vol. 19, no. 5, pp. 163–171, May 1996.

[277] J. D. Clements, R. A. Lester, G. Tong, C. E. Jahr, and G. L. Westbrook, “The time course of glutamate in the synaptic cleft,” *Science*, vol. 258, no. 5087, pp. 1498–1501, Nov. 1992.

[278] I. A. Silver and M. Erecińska, “Intracellular and extracellular changes of [Ca2+] in hypoxia and ischemia in rat brain in vivo,” *J. Gen. Physiol.*, vol. 95, no. 5, pp. 837–866, May 1990.

[279] S. Nadkarni and P. Jung, “Modeling synaptic transmission of the tripartite synapse,” *Phys. Biol.*, vol. 4, no. 1, pp. 1–9, Jan. 2007.

[280] A. Mohan, S. Pendyam, P. W. Kalivas, and S. S. Nair, “Molecular diffusion model of neurotransmitter homeostasis around synapses supporting gradients,” *Neural Comput.*, vol. 23, no. 4, pp. 984–1014, Apr. 2011.

[281] S. A. Lipton and P. A. Rosenberg, “Excitatory amino acids as a final common pathway for neurologic disorders,” *N. Engl. J. Med.*, vol. 330, no. 9, pp. 613–622, Mar. 1994.

[282] K. Moussawi, A. Riegel, S. Nair, and P. W. Kalivas, “Extracellular glutamate: functional compartments operate in different concentration ranges,” *Front. Syst. Neurosci.*, vol. 5, p. 94, 2011.

[283] H. Osuga and A. M. Hakim, “Relationship between Extracellular Glutamate Concentration and Voltage-Sensitive Calcium Channel Function in Focal Cerebral Ischemia in the Rat,” *J. Cereb. Blood Flow Metab.*, vol. 16, no. 4, pp. 629–636, Jul. 1996.

[284] K. Fujihara *et al.*, “Neuromyelitis optica should be classified as an astrocytopathic disease rather than a demyelinating disease,” *Clin. Exp. Neuroimmunol.*, vol. 3, no. 2, pp. 58–73, May 2012.

[285] J. Kitley and J. Palace, “Therapeutic options in neuromyelitis optica spectrum disorders,” *Expert Rev. Neurother.*, vol. 16, no. 3, pp. 319–329, 2016.

[286] I. Kleiter *et al.*, “Neuromyelitis optica: Evaluation of 871 attacks and 1,153 treatment courses,” *Ann. Neurol.*, vol. 79, no. 2, pp. 206–216, Feb. 2016.

[287] A. Davies and P. J. Lachmann, “Membrane defence against complement lysis: the structure and biological properties of CD59,” *Immunol. Res.*, vol. 12, no. 3, pp. 258–275, 1993.

[288] P. F. Zipfel and C. Skerka, “Complement regulators and inhibitory proteins,” *Nat. Rev. Immunol.*, vol. 9, no. 10, pp. 729–740, 2009.

[289] H. Jiang and S. X. Sun, “Cellular pressure and volume regulation and implications for cell mechanics,” *Biophys. J.*, vol. 105, no. 3, pp. 609–619, 2013.

[290] E. R. Cohen, *Quantities, units and symbols in physical chemistry*. Cambridge, UK: Royal Society of Chemistry, 2008.

[291] E. Solenov, H. Watanabe, G. T. Manley, and A. Verkman, “Sevenfold-reduced osmotic water permeability in primary astrocyte cultures from AQP-4-deficient mice, measured by a fluorescence quenching method,” *Am. J. Physiol.-Cell Physiol.*, vol. 286, no. 2, pp. C426–C432, 2004.

[292] H. Kimelberg, “Water homeostasis in the brain: basic concepts,” *Neuroscience*, vol. 129, no. 4, pp. 851–860, 2004.

[293] H. Curtis and N. Barnes, *Biology*. New York, USA: Worth Publishers, 1989.

[294] F. Campolongo, J. Cariboni, and A. Saltelli, “An effective screening design for sensitivity analysis of large models,” *Environ. Model. Softw.*, vol. 22, no. 10, pp. 1509–1518, 2007.

[295] A. Wiese, T. Gutsmann, and U. Seydel, “Review: Towards antibacterial strategies: studies on the mechanisms of interaction between antibacterial peptides and model membranes,” *J. Endotoxin Res.*, vol. 9, no. 2, pp. 67–84, 2003.

[296] R. A. Brodsky, “Narrative review: paroxysmal nocturnal hemoglobinuria: the physiology of complement-related hemolytic anemia,” *Ann. Intern. Med.*, vol. 148, no. 8, pp. 587–595, 2008.

[297] J. Yu, T. Caragine, S. Chen, B. Morgan, A. Frey, and S. Tomlinson, “Protection of human breast cancer cells from complement-mediated lysis by expression of heterologous CD59,” *Clin. Exp. Immunol.*, vol. 115, no. 1, p. 13, 1999.

[298] J. Lundbaek and A. Hansen, “Brain interstitial volume fraction and tortuosity in anoxia. Evaluation of the ion-selective micro-electrode method,” *Acta Physiol. Scand.*, vol. 146, no. 4, pp. 473–484, 1992.

[299] E. Syková, J. Svoboda, J. Polák, and A. Chvátal, “Extracellular volume fraction and diffusion characteristics during progressive ischemia and terminal anoxia in the spinal cord of the rat,” *J. Cereb. Blood Flow Metab.*, vol. 14, no. 2, pp. 301–311, 1994.

[300] L. Li, R. Kalaga, and S. Paul, “Proteolytic components of serum IgG preparations,” *Clin. Exp. Immunol.*, vol. 120, no. 2, pp. 261–266, May 2000.

[301] P. O. Poliquin, J. Chen, M. Cloutier, L.-É. Trudeau, and M. Jolicoeur, “Metabolomics and in-silico analysis reveal critical energy deregulations in animal models of Parkinson's disease,” *PloS One*, vol. 8, no. 7, p. e69146, 2013.

[302] F. Kogan, H. Hariharan, and R. Reddy, “Chemical exchange saturation transfer (CEST) imaging: description of technique and potential clinical applications,” *Curr. Radiol. Rep.*, vol. 1, no. 2, pp. 102–114, 2013.

[303] H. Green and B. Goldberg, “The action of antibody and complement on mammalian cells,” *Ann. N. Y. Acad. Sci.*, vol. 87, no. 1, pp. 352–362, 1960.

[304] S. Höfinger *et al.*, “Structural features of aquaporin 4 supporting the formation of arrays and junctions in biomembranes,” *Biochim. Biophys. Acta BBA-Biomembr.*, vol. 1818, no. 9, pp. 2234–2243, 2012.

[305] E. A. Nagelhus *et al.*, “Aquaporin-4 water channel protein in the rat retina and optic nerve: polarized expression in Müller cells and fibrous astrocytes,” *J. Neurosci.*, vol. 18, no. 7, pp. 2506–2519, 1998.

[306] B. P. Morgan and A. L. Harris, *Complement Regulatory Proteins*. Academic Press, 1999.

[307] G. Schröder, K. Brandenburg, L. Brade, and U. Seydel, “Pore formation by complement in the outer membrane of gram-negative bacteria studied with asymmetric planar lipopolysaccharide/phospholipid bilayers,” *J. Membr. Biol.*, vol. 118, no. 2, pp. 161–170, Nov. 1990.

[308] T. V. Arumugam, I. A. Shiels, T. M. Woodruff, D. N. Granger, and S. M. Taylor, “The role of the complement system in ischemia-reperfusion injury,” *Shock Augusta Ga*, vol. 21, no. 5, pp. 401–409, May 2004.

[309] G. Ingram, S. Hakobyan, N. P. Robertson, and B. P. Morgan, “Complement in multiple sclerosis: its role in disease and potential as a biomarker,” *Clin. Exp. Immunol.*, vol. 155, no. 2, pp. 128–139, Feb. 2009.

[310] M. M. Steriade and R. W. McCarley, *Brainstem control of wakefulness and sleep*. New York, USA: Springer Science & Business Media, 2013.

[311] J. Fenstermacher and J. Johnson, “Filtration and reflection coefficients of the rabbit blood-brain barrier,” *Am. J. Physiol. Content*, vol. 211, no. 2, pp. 341–346, 1966.

[312] H. Sontheimer, E. Fernandez-Marques, N. Ullrich, C. Pappas, and S. Waxman, “Astrocyte Na+ channels are required for maintenance of Na+/K (+)-ATPase activity,” *J. Neurosci.*, vol. 14, no. 5, pp. 2464–2475, 1994.

[313] A. Sherman, J. Keizer, and J. Rinzel, “Domain model for Ca2 (+)-inactivation of Ca2+ channels at low channel density.,” *Biophys. J.*, vol. 58, no. 4, p. 985, 1990.

[314] S. Marom, H. Salman, V. Lyakhov, and E. Braun, “Effects of density and gating of delayed-rectifier potassium channels on resting membrane potential and its fluctuations,” *J. Membr. Biol.*, vol. 154, no. 3, pp. 267–274, 1996.

[315] J. Reisert, P. J. Bauer, K.-W. Yau, and S. Frings, “The Ca-activated Cl channel and its control in rat olfactory receptor neurons,” *J. Gen. Physiol.*, vol. 122, no. 3, pp. 349–364, 2003.

[316] C. Sato, M. Sato, A. Iwasaki, T. Doi, and A. Engel, “The sodium channel has four domains surrounding a central pore,” *J. Struct. Biol.*, vol. 121, no. 3, pp. 314–325, 1998.

[317] K. T. Perez, *Structure-function Relationship & Modulation Of The T-type Calcium Channel 1g*, vol. 313. Leuven, Belgium: Leuven University Press, 2004.

[318] Y. Jiang, A. Lee, J. Chen, M. Cadene, B. T. Chait, and R. MacKinnon, “The open pore conformation of potassium channels,” *Nature*, vol. 417, no. 6888, pp. 523–526, 2002.

[319] J. I. Wadiche, S. G. Amara, and M. P. Kavanaugh, “Ion fluxes associated with excitatory amino acid transport,” *Neuron*, vol. 15, no. 3, pp. 721–728, Sep. 1995.

[320] R. M. Langford, “Pain management today—what have we learned?,” *Clin. Rheumatol.*, vol. 25, no. 1, pp. 2–8, 2006.

[321] R. Leadley, N. Armstrong, Y. Lee, A. Allen, and J. Kleijnen, “Chronic diseases in the European Union: the prevalence and health cost implications of chronic pain,” *J. Pain Palliat. Care Pharmacother.*, vol. 26, no. 4, pp. 310–325, 2012.

[322] M. R. Tramèr, R. A. Moore, D. J. M. Reynolds, and H. J. McQuay, “Quantitative estimation of rare adverse events which follow a biological progression: a new model applied to chronic NSAID use,” *Pain*, vol. 85, no. 1, pp. 169–182, 2000.

[323] S. A. Schug, D. Zech, and S. Grond, “Adverse effects of systemic opioid analgesics,” *Drug Saf.*, vol. 7, no. 3, pp. 200–213, 1992.

[324] J. L. Cash, G. E. White, and D. R. Greaves, “Zymosan-induced peritonitis as a simple experimental system for the study of inflammation,” *Methods Enzymol.*, vol. 461, pp. 379–396, 2009.

[325] G. Z. Feuerstein, A. J. Hunter, B. W. Metcalf, G. Poste, and R. R. R. Jr, *Inflammatory Cells and Mediators in CNS Disease*. CRC Press, 1999.

[326] O. Soehnlein, L. Lindbom, and C. Weber, “Mechanisms underlying neutrophil-mediated monocyte recruitment,” *Blood*, vol. 114, no. 21, pp. 4613–4623, 2009.

[327] W. D. Anderson, H. K. Makadia, A. D. Greenhalgh, J. S. Schwaber, S. David, and R. Vadigepalli, “Computational modeling of cytokine signaling in microglia,” *Mol. Biosyst.*, vol. 11, no. 12, pp. 3332–3346, 2015.

[328] H. L. Malech, “The Role of Neutrophils in the Immune System,” *Neutrophil Methods Protoc.*, pp. 3–11, 2007.

[329] C. A. Gloff and R. J. Wills, “Pharmacokinetics and metabolism of therapeutic cytokines,” in *Protein pharmacokinetics and metabolism*, Springer, 1992, pp. 127–150.

[330] M. W. Lenhoff, T. J. Santner, J. C. Otis, M. G. E. Peterson, B. J. Williams, and S. I. Backus, “Bootstrap prediction and confidence bands: a superior statistical method for analysis of gait data,” *Gait Posture*, vol. 9, no. 1, pp. 10–17, Mar. 1999.

[331] A. Saltelli, S. Tarantola, F. Campolongo, and M. Ratto, *Sensitivity analysis in practice: a guide to assessing scientific models*. Ispra, Italy: John Wiley & Sons, 2004.

[332] J. Rourke, H. Dranse, and C. Sinal, “Towards an integrative approach to understanding the role of chemerin in human health and disease,” *Obes. Rev.*, vol. 14, no. 3, pp. 245–262, 2013.

[333] T. Yamamoto *et al.*, “Clinical importance of an elevated circulating chemerin level in incident dialysis patients,” *Nephrol. Dial. Transplant.*, vol. 25, no. 12, pp. 4017–4023, 2010.

[334] J. L. Cash *et al.*, “Synthetic chemerin-derived peptides suppress inflammation through ChemR23,” *J. Exp. Med.*, vol. 205, no. 4, pp. 767–775, Apr. 2008.

[335] M. Herová, M. Schmid, C. Gemperle, and M. Hersberger, “ChemR23, the receptor for chemerin and resolvin E1, is expressed and functional on M1 but not on M2 macrophages,” *J. Immunol.*, vol. 194, no. 5, pp. 2330–2337, 2015.

[336] M. Caldwell, T. Hapuarachchi, D. Highton, C. Elwell, M. Smith, and I. Tachtsidis, “BrainSignals Revisited: Simplifying a Computational Model of Cerebral Physiology,” *PLOS ONE*, vol. 10, no. 5, p. e0126695, May 2015.

[337] R. W. Albers and G. J. Siegel, “Secondary Transport Systems,” 1999.

[338] M. Nour, F. Scalzo, and D. S. Liebeskind, “Ischemia-Reperfusion Injury in Stroke,” *Interv. Neurol.*, vol. 1, no. 3–4, pp. 185–199, Sep. 2013.

[339] M. Haris *et al.*, “Imaging of glutamate neurotransmitter alterations in Alzheimer’s disease,” *NMR Biomed.*, vol. 26, no. 4, pp. 386–391, Apr. 2013.

[340] F. Büchel *et al.*, “Path2Models: large-scale generation of computational models from biochemical pathway maps,” *BMC Syst. Biol.*, vol. 7, p. 116, 2013.

[341] B. F. Trump and I. K. Berezesky, “Calcium-mediated cell injury and cell death.,” *FASEB J.*, vol. 9, no. 2, pp. 219–228, Feb. 1995.

[342] S. A. Rollins and P. J. Sims, “The complement-inhibitory activity of CD59 resides in its capacity to block incorporation of C9 into membrane C5b-9.,” *J. Immunol.*, vol. 144, no. 9, pp. 3478–3483, May 1990.

[343] B. Bondue *et al.*, “The Chemerin/ChemR23 System Does Not Affect the Pro-Inflammatory Response of Mouse and Human Macrophages Ex Vivo,” *PLOS ONE*, vol. 7, no. 6, p. e40043, Jun. 2012.